UiO : Department of Geosciences
University of Oslo

Reservoir characterization of the Triassic-Jurassic succession of the Bjarmeland Platform, Norwegian Barents Sea

Examples from the Caurus, Arenaria and Obesum discoveries

Jørgen André Hansen

Master's Thesis, Spring 2016

Reservoir characterization of the Triassic-Jurassic succession of the Bjarmeland Platform, Norwegian Barents Sea

Examples from the Caurus, Arenaria and Obesum discoveries

Jørgen André Hansen

Master Thesis in Geosciences
Petroleum Geology and Petroleum Geophysics
30 credits

Department of Geosciences
Faculty of Mathematics and Natural Sciences

UNIVERSITY OF OSLO

01.06.2016

2016

Reservoir characterization of the Triassic-Jurassic succession of the Bjarmeland Platform, Norwegian Barents Sea. Examples from the Caurus, Arenaria and Obesum discoveries.

Jørgen André Hansen

Supervisor: Nazmul Haque Mondol

http://www.duo.uio.no

Printed: Reprosentralen, University of Oslo

Preface

This thesis is part of the ‘‘Trias North - Reconstructing the Triassic northern Barents shelf” project and is submitted to the Department of Geosciences, University of Oslo (UiO), in candidacy of the M.Sc. in Petroleum Geology and Petroleum Geophysics.

This research has been performed at the Department of Geosciences, University of Oslo, during the period of January 2016 to May 2016 under the supervision of Nazmul Haque Mondol, Associate Professor, Department of Geosciences, University of Oslo, Norway.

Acknowledgements

Firstly, I would like to express my gratitude to my supervisor Nazmul Haque Mondol, for his guidance and motivation throughout this thesis work. Our discussions and his feedback have been of great value to me during this study.

I would like to thank my fellow MSc candidate Manvydas Saltis for our helpful discussions, exchange of ideas as well as giving me added motivation to improve my thesis.

I would also like to thank PhD candidates Honore Dzekamelive Yenwongfai and Mohammad Koochak Zadeh for taking time to give me valuable input, as well as Michel Heeremans for technical assistance.

Lastly I am very grateful to all my classmates and fellow students who I have made many good memories with, especially Kristoffer, Henrik and Hans-Martin who have not only been my study partners, but also great friends over the last five years. A heartfelt thank you also goes to my family for continuous support and encouragement.

Abstract

This study presents reservoir characterization of Triassic and Jurassic sandstones using petrophysical analysis, rock physics diagnostics and AVO modeling with data from eight exploration wells in and around the Bjarmeland Platform, Norwegian Barents Sea. The primary focus has been on Triassic sandstone reservoirs in the Kobbe and Snadd formations, which has been compared to Jurassic sandstone reservoirs of the Tubåen and Stø formations.

Potential reservoir intervals that have been identified and examined span over a wide range of depth levels and reservoir quality (e.g. shaliness, net-to-gross, porosity and permeability). Reservoir depths vary from around 600 to 2300 m measured depth from KB. Kobbe Formation reservoirs generally exhibit poorer quality with respect to shaliness (34.9-69.0%), porosity (2.6-16.4%) and consequently net-to-gross, but hydrocarbons are more frequently recognized than in the younger formations (i.e. Snadd, Tubåen and Stø Formations). Average effective porosity in the Snadd Formation reservoirs approach 30% at maximum, but typically varies between 10-20%. Net-to-gross ranges from 30 to 100%, and reservoirs fulfilling the net pay cutoff ($S_w < 60\%$) are identified in two wells; 7222/11-1 (Caurus) and 7222/6-1 (Obesum). The Snadd Formation thickens towards NW, and has a maximum thickness of 1406 m on the Loppa High. Across four wells, the Tubåen Formation sandstones have good reservoir quality and vary in thickness from 1-60 m. In the Stø Formation, deteriorating reservoir quality and decreasing thicknesses are observed from south to north/north-east. Well 7125/1-1 closest to the southern tip of the Bjarmeland Platform records ~120 m clean, porous sandstones in the Stø Formation, but in contrast, well 7226/11-1 on the Norsel High (eastern margin of the study area) is more shaley and encounters only a 8.1 m thick Stø Formation.

Utilization of published V_p-depth trends, uplift estimates, rock physics cement models and shear modulus-density plots has resulted in identification of transition zones from mechanical to chemical compaction and the distinction of less compacted and less cemented reservoirs in the Snadd Formation at less than ~800 m (RKB) present depth (wells 7223/5-1 and 7222/11-1). Uplift estimated using data from this study corresponds reasonably well with published values. Rock physics diagnostics in the V_p/V_s-AI and LMR domains are shown to be adequate for the current database in terms of showing lithology effects and separation of hydrocarbon-saturated intervals. They do however display low sensitivity to more specific water saturation levels, possibly due to a certain shale component frequently present in the studied reservoir sandstones.

AVO modeling has been used to compare four reservoir intervals from two of the studied wells, 7222/11-1 (Caurus) and 7224/6-1 (Arenaria), in order to observe differences of relatively deep versus shallow burial as well as spatial variations of studied sandstones. Given their depth and the information derived about their cementation and consolidation, the two Snadd reservoirs show AVO responses as generally expected. A class 3 response is inferred for a shallow, less cemented sandstone reservoir, whereas the deeply buried, well consolidated and cemented sandstone is described as class 1 AVO anomaly. Hard, high-velocity cap rocks above porous reservoirs can result in a class 4 AVO response, as interpreted in a Tubåen Formation sandstone overlain by a Fuglen Formation shale in well 7224/6-1. As sensitivity to fluid changes decreases, due to low porosity or higher cementation, AVO anomalies are harder to detect and intercept-gradient points consequently plot closer to or within the background trend. This is observed e.g. in a ~2200 m deep class 3 Kobbe reservoir in well 7222/11-1, where changes in the AVO signature due to varying fluid content is significantly smaller than for shallower reservoirs tested.

Table of contents

List of figures

List of tables

Nomenclature

AI: Acoustic Impedance

AVO: Amplitude Variation with Offset

BHT: Bottom Hole Temperature

BSF: Below Sea Floor

CMP: Common Mid-Point

(R)KB: (Relative to) Kelly Bushing

K: Bulk modulus

k: Permeability

mD: Milli Darcy

N/G: Net-to-gross ratio

V_p: P-wave velocity

V_s: S-wave velocity

V_{sh}: Shale volume

R_w: Water resistivity

S_w: Water saturation

ϕ: Porosity

μ: Shear modulus

λ: Incompressibility (Rock physics)

λ: Wavelength (AVO)

ρ: Density

ν: Poisson's ratio

Chapter 1: Introduction

1.1 Background and motivation

The greater Barents Sea is located between the coast of northern Norway, Svalbard, the island of Novaya Zemlya and the Russian coast (Figure 1.1). It covers approximately 1.4 million km^2, where the Norwegian sector of the Barents Sea (Western Barents Sea) constitutes 313 000 km^2 of water depth mostly less than 500 m (Smelror et al. 2009; Norwegian Petroleum 2016). The Barents Sea is an epicontinental sea covering large shelf areas consisting of a number of basins and highs (Faleide et al. 1984; Henriksen et al. 2011b), where the area of interest in this study is outlined by a red rectangle in Figure 1.1 representing the south-western part of the Bjarmeland platform and surrounding structural elements.

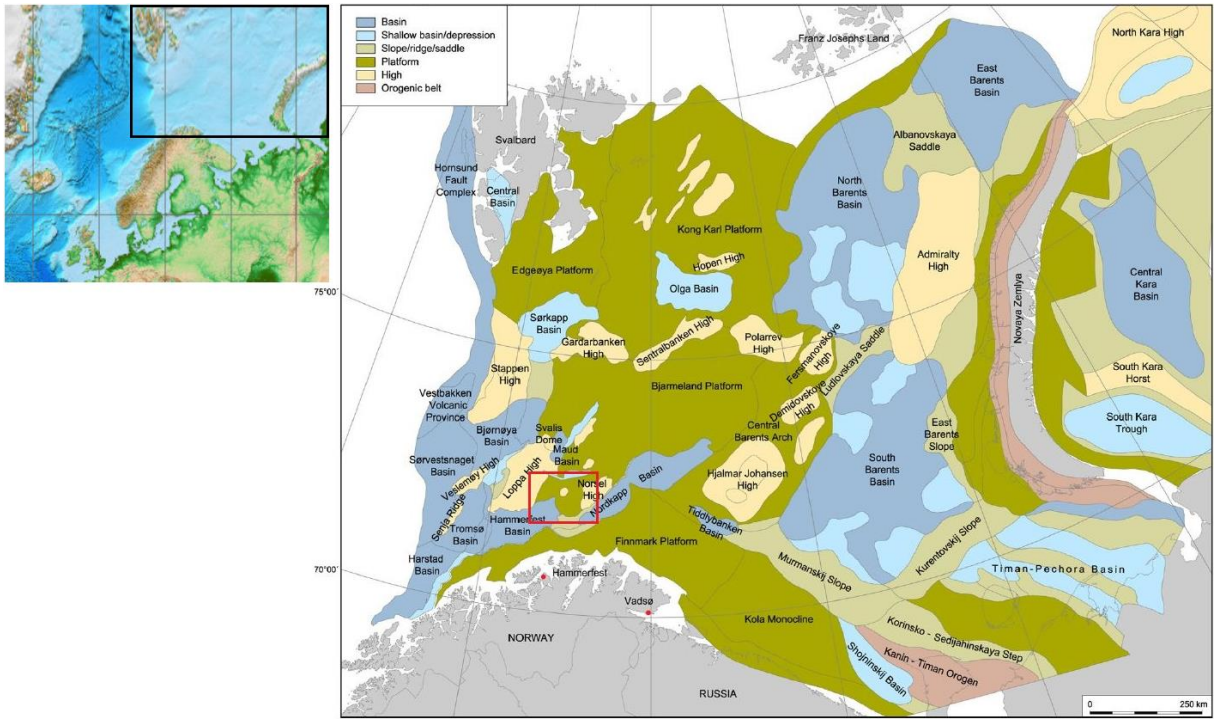

Figure 1.1. Overview of the structural elements of the Barents Sea (right, modified after Henriksen et al. 2011). Study area is highlighted by the red rectangle. Index map of regional location is also included (left, modified after Amante and Eakins 2009).

The Barents Sea is in terms of hydrocarbon exploration still highly unexplored in many areas, even though there have been activity in the area since 1980 when the area was opened for exploration, with main targets in Triassic and Middle Jurassic petroleum systems (Lundschien et al. 2014; Norwegian Petroleum 2016). It is therefore still denoted a frontier province, which is supported by the fact that the areas that have previously never been explored were included in the licensing round announced in 2015 (NPD 2015), as shown in Figure 1.2 (Norwegian Petroleum 2016). These are mainly located in the south-eastern part of the Norwegian Barents Sea (towards the Russian sector of the Barents Sea). Secondly, the entire northern Barents Sea

has yet to be opened for activity, where there is possibility of finding more resources in the future (Figure 1.2).

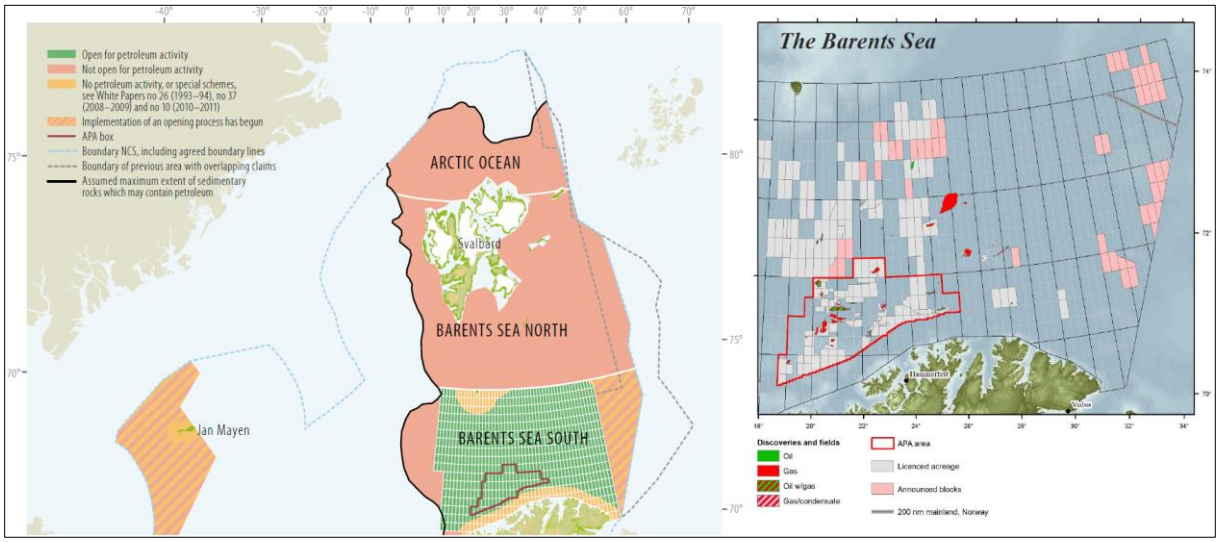

Figure 1.2. Map of areas open to exploration in the Norwegian Barents Sea (left, modified from NPD 2011). Map of license blocks in the Norwegian Barents Sea (right), the announced blocks for the 23rd licensing round are highlighted in pink (modified from NPD 2015).

Although there have been high discovery rates in the exploration wells drilled in the Norwegian Barents Sea, most have contained gas, whereas a few contain oil, and also residual oil saturation (Ohm et al. 2008). Uplift and erosion events are assumed to have largely influenced the hydrocarbon reservoirs in the Barents Sea, causing leakage and redistribution of hydrocarbons (Ohm et al. 2008). As of 2016 there are only two producing field in the region, which are the Snøhvit gas/condensate field and the Goliat oil field (Norwegian Petroleum 2016). Many smaller finds have been discovered (also oil), which at present are not commercially viable to produce due to practical challenges, e.g. distance to markets and expense of production (Ohm et al. 2008). They do, however, indicate that the Barents Sea is not only gas prone, and that more thorough exploration and new strategies can lead to more discoveries (Ohm et al. 2008).

A better understanding of the geology and variations in reservoir quality is naturally sought after both in an exploration setting and when assessing potential production of a discovery. Analysis of petrophysical logs, rock physics diagnostics and AVO modeling are useful tools to characterize a reservoir, which leads to increased knowledge about specific reservoirs as well as contributing to the understanding of the geological province as a whole. In addition, it can be implemented in risk analysis related to production. Similarities and differences between wells in various locations can also possibly be utilized in further exploration strategies.

1.2 Research objectives

The main objective of this thesis is describing the reservoir quality of Triassic-Jurassic rocks in the Bjarmeland Platform (more specifically the southern part of the platform). Examples are included from multiple discoveries, and the Caurus, Arenaria and Obesum discoveries are given the primary focus. The research tasks are focused on:

- Detail analysis of well logs to identify reservoir intervals and extract information about shale volume, porosity, water saturation, net-to-gross and net pay. Trends across wells and links to depositional environments will be discussed.
- Rock physics diagnostics to link elastic parameters to geological processes, in order to interpret sorting and diagentic trends, cement volume, compaction indicators and hydrocarbon effects. Comparisons are to be made between selected Jurassic and Triassic reservoirs rocks, as well as searching for individual formation trends.
- AVO forward modeling is employed to create an impression of how a few selected reservoirs would appear if trying to do AVO analysis of actual seismic data based on well log recordings. The most important task is to classify the reservoirs in terms of intercept and gradient, as well as investigating the sensitivity of AVO modeling to certain input parameters and conditions.
- Comments are made with regard to the sensitivity and uncertainties of the methods and the applicability of a given approach to this particular study area.

1.3 Study area

The south-western part of the Bjarmeland Platform and the surrounding area is the focus for this study, as shown in Figure 1.3. Most of the wells included in the study are positioned in relation to structural elements adjacent to or on the platform area. Bordering this section of the Bjarmeland Platform is the Loppa High to the west, the Swaen Graben in the north, Norsel High and the Nysleppen Fault Complex to the east and southeast, and the Hammerfest Basin in the south-southwest.

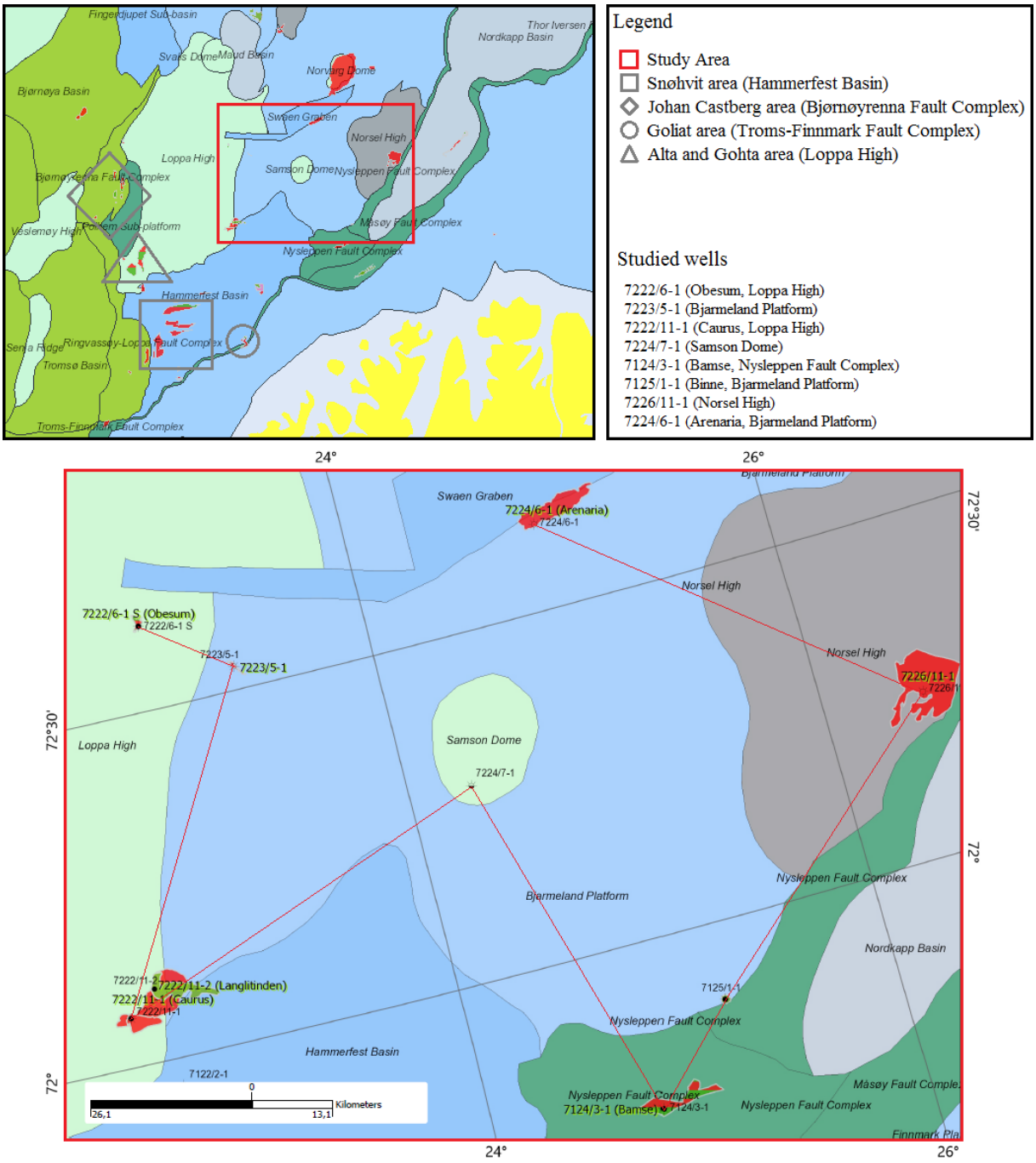

Figure 1.3. Enlarged view of study area, with the investigated wells connected by the red line [note 7222/11-2 (Langlitinden discovery) is not included in study]. The smaller map indicates regional position of the study area (modified after NPD Factmaps 2016).

1.4 Database and softwares

This study is first and foremost based on well log data from eight wells, complemented by the use of articles and published literature on the subject, as well as information from the web pages of the Norwegian Petroleum Directorate (NPD 2016).

The eight analyzed exploration wells are located as shown in Figure 1.3. Wells 7222/6-1 S and 7222/11-1 are located to the east and southeast on the Loppa High. Wells 7223/5-1 and 7224/6-1 are located in the western part of the Bjarmeland Platform and close to the Swaen Graben, respectively. Well 7224/7-1 is positioned on the Samson Dome, well 7124/3-1 in the Nysleppen Fault Complex, well 7125/1-1 on the border between the Nysleppen Fault Complex and the Bjarmeland Platform, and finally well 7226/11-1 on the Norsel High. General information about the wells is compiled in Table 1.1 (facts from NPD 2016).

Table 1.1: General information about the studied wells (NPD 2016).

Well	**7222/6-1**	**7223/5-1**	**7222/11-1**	**7124/3-1**	**7125/1-1**	**7224/7-1**	**7226/11-1**	**7224/6-1**
NS degrees	72° 37' 25.01" N	72° 32' 6.18" N	72° 4' 20.3" N	71° 45' 36.03" N	71° 53' 24.26" N	72° 17' 6.34" N	72° 14' 18.16" N	72° 37' 29.09" N
EW degrees	22° 55' 51.4" E	23° 20' 7.74" E	22° 28' 26.4" E	24° 46' 49.99" E	25° 11' 15.46" E	24° 18' 2.98" E	26° 28' 44.78" E	24° 54' 43.41" E
Year completed	2008	2009	2008	1987	1988	1988	1988	2008
Content	Oil/Gas	Gas	Oil/Gas	Oil/Gas	Oil/Gas	Shows	Gas	Gas
Discovery name	Obesum	N/A	Caurus	Bamse	Binne	N/A	N/A	Arenaria
KB [m]	23.0	23.0	23.0	23.0	23.5	23.5	23.0	23.0
Water depth [m]	364.0	340.0	356.0	273.0	252.2	269.0	237.5	266.0
Total depth [m RKB]	2895.0	2549.0	2658.0	4730.0	2200.0	3067.0	5200.0	2338.0
TVD [m RKB]	2848.0	2548.6	2625.0	4727.0	2199.0	3064.0	?	2338.0
Max. inclination [°]	24	2.5	1.3	4.7	2.1	7.3	5.8	1.6
Bottom hole temp. [°C]	89	94	92	151	64	119	143	91

Softwares used to facilitate this study are Interactive Petrophysics (IP) and Hampson-Russell Software (10.0.1) for petrophysical analysis, rock physics diagnostics and AVO modeling, as well as Petrel 2015 (Schlumberger) for well correlation and thickness maps, and Microsoft Excel for additional well log calculations, crossplotting and quality control. IP provides a greater variety of options for in-depth petrophysical analysis than the HRS software, which on the other hand is more essential in rock physics diagnostics due to better crossplot functionality. HRS also provides superior options for AVO modeling.

1.5 Chapter descriptions

Chapter 1 in this thesis contains the background and motivation for conducting this research, information about the study area and descriptions of the well logs and database that the project is based on.

The second chapter gives an introduction to the regional geologic setting of the study area, an overview of the stratigraphy, as well as describing relevant source rocks, reservoir rocks and traps in the Bjarmeland Platform area. Extent of the different key formations and effect of uplift and erosion on the petroleum system is also included in chapter 2.

Chapter 3 is intended to present relevant theories and methodologies based on published literature that this study builds upon. This includes description of the main principles of the aforementioned techniques of petrophysical analysis, rock physics diagnostics and AVO modeling, as well as providing relevant equations and empirical relations.

Furthermore, the results of the study are presented, beginning with chapter 4. In this chapter, the output generated from petrophysical analysis of the well logs are described and discussed, mainly to depict the reservoir quality of different formations and differences in wells located in diverse areas. Contents in this chapter include lithology discrimination and shale volume calculations, porosity estimation, net-to-gross, permeability prediction and calculation of water saturation.

Following in chapter 5 are the results and discussion of rock physics diagnostics which involves linking rock physics properties to the geological parameters of a rock, through crossplotting and comparison with rock physics templates (RPT's). Multiple models designed to extract different information such as cementation, sorting or hydrocarbon content are utilized and their sensitivity is evaluated.

The sixth chapter encompasses AVO modeling results and characteristic responses of selected reservoirs, as well as analysis of the sensitivity of the results to change in certain methodological approaches and parameters. Similarly to the previous two chapters, uncertainties and limitations of the approaches taken are discussed to clarify the accuracy of the obtained results.

Finally, chapter 7 consists of a summary of the work conducted in this study, as well as conclusions reached from the presented results.

1.6 Limitations and further works

This study is carried out over approximately 5 months, making time a limited resource for both analysis and writing of the thesis. Consequently, no core examination or thin-section analysis has been conducted, and more detailed sedimentological and mineralogical information must therefore rather be retrieved from published data. Core and thin-section analysis could be a relevant extension of the current work, as well as incorporating real seismic data in the workflow for a larger scale correlation or for seismic attribute and AVO analysis and quantitative inversion of seismic data. The four older wells (7124/3-1, 7125/1-1, 7224/7-1 and 7226/11-1) in the current database do not have measured shear velocity, and this property must consequently be calculated from P-wave velocity to be used in further analysis or for comparisons, e.g. in rock physics diagnostics. Specific uncertainties related to measured logs, equations, methodology and results are addressed in the relevant chapters. Log availability for the studied wells is shown in Table 1.2.

Table 1.2: Well log availability, partially indicates measurements in certain intervals only.

Well log	7124/3-1	7125/1-1	7222/11-1	7222/6-1	7223/5-1	7224/6-1	7224/7-1	7226/11-1
Caliper	✓	✓	✓	✓	✓	✓	✓	✓
Bit size	×	×	✓	✓	✓	✓	×	×
Gamma Ray	✓	✓	✓	✓	✓	✓	✓	✓
Spectral Gamma (K, Th & U)	×	×	✓	✓	✓	Partially	×	×
SP	×	×	×	×	×	×	×	×
Density	✓	✓	✓	✓	✓	✓	✓	✓
Neutron Porosity	✓	✓	✓	✓	✓	✓	✓	✓
Sonic (P-wave)	✓	✓	✓	✓	✓	✓	✓	✓
Sonic (S-wave)	×	×	✓	✓	✓	✓	×	×
Resistivity S	Partially	×	✓	✓	Partially	✓	✓	✓
Resistivity M	✓	✓	✓	✓	✓	✓	✓	✓
Resistivity D	✓	✓	✓	✓	✓	✓	✓	✓
Photoelectric	×	×	✓	✓	✓	✓	×	×
Rate of Penetration	×	×	✓	✓	✓	×	×	×
✓ indicates availability of data, × indicates lacking data								

Chapter 2: Geological setting

2.1 Regional tectonic and structural evolution

Since the Caledonian Orogeny (Ordovician to Early Devonian) the western Barents Sea Region has a complex geological history, with the most dominant episodes being three rift phases from Late Devonian-Carboniferous, Middle Jurassic-Early Cretaceous and Late Cretaceous-Palaeocene, mainly as a sheared margin, but also with zones of rifting (Figure 2.1). The earliest extensional rifting affected most of the Barents Sea area, whereas the later events mostly influenced areas further to the west/south-west (Faleide et al. 1993; Faleide et al. 2015). The Barents Sea area has also been affected by both the Caledonian and Uralian Orogenies, as well as several uplift and erosion events, which all have had an effect on subsurface geometry, clastic sediment input and the petroleum systems (Henriksen et al. 2011a; Henriksen et al. 2011b).

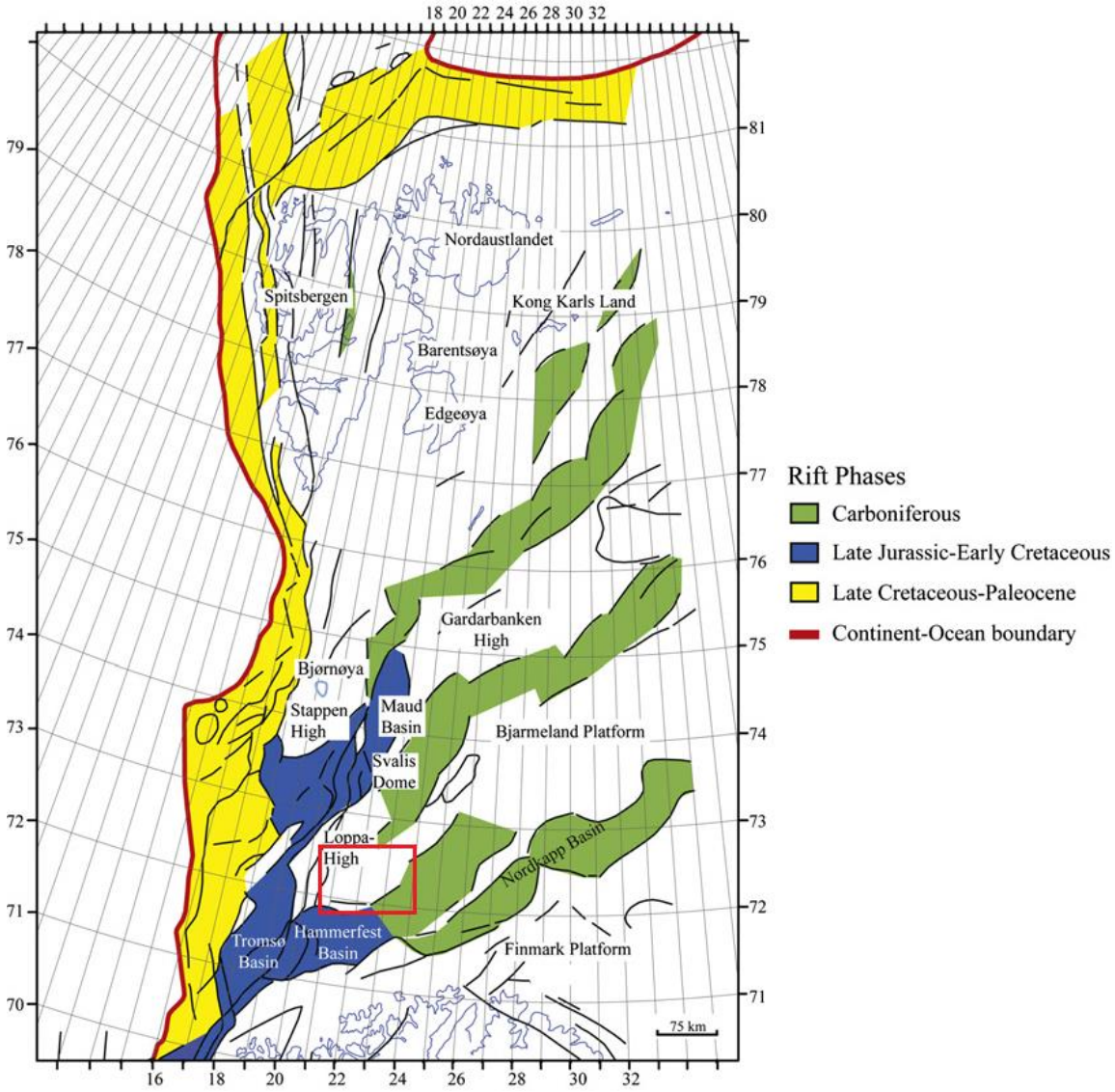

Figure 2.1. Structural timing of events affecting the western Barents Sea, with the study area indicated by the red rectangle (adapted from Glørstad-Clark et al. 2010).

The Caledonian Orogeny, resulting from the collision of Eurasia and Laurentia and consequent closing of the Iapetus Ocean, had its beginning in the Ordovician and climaxed in the Silurian. Extension in Late Palaeozoic times following the orogeny resulted in most of the Barents Shelf being covered by a regional sag basin. Uplift in the east from Permian to Early Triassic ensuing the onset of the Uralian Orogeny changed the basin physiology and sediment deposition patterns giving rise to a material influx towards the west through the Triassic (Figure 2.2) (Henriksen et al. 2011b; Lundschien et al. 2014).

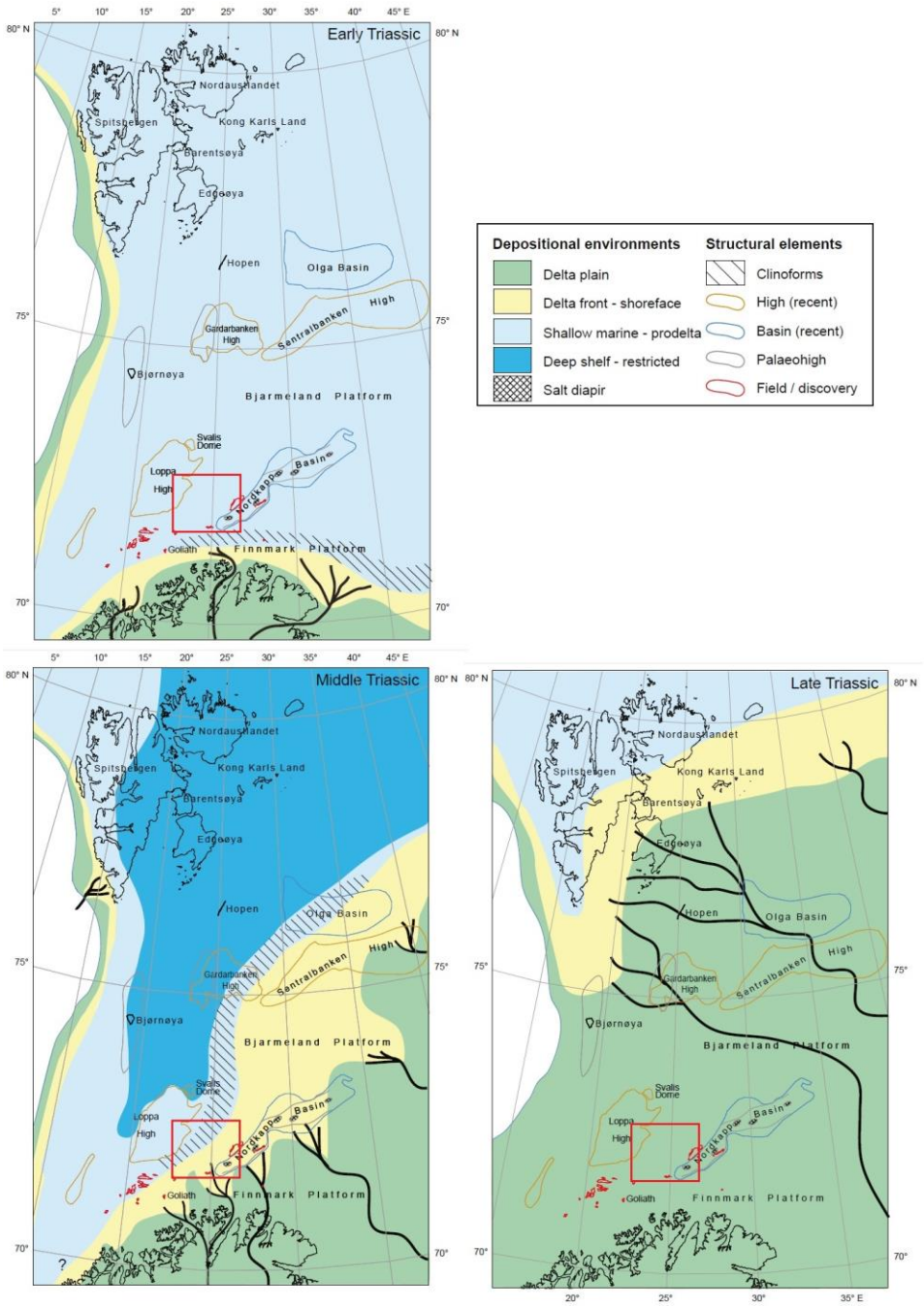

Figure 2.2. Depositional environment development through the Triassic period in the SW Barents Sea (modified from Lundschien et al. 2014). Study area is highlighted by the red rectangle.

2.2 Structural elements

The timing, trends and extent of tectonic and stratigraphic features in the south-western Barents Sea have noticeable differences between the eastern and western side of the Ringvassøy-Loppa and Bjørnøyrenna fault complexes (Figure 2.3). The western side (Harstad, Tromsø and Bjørnøya basins) are dominated by Cretaceous, Paleogene and Neogene sediments as these were periods of high tectonic activity with faults trending NNE-SSW, NE-SW and N-S (Halland et al. 2014). The eastern side on the other hand displays E-W and WNW-ESE trending faults, is dominated by Paleozoic and Mesozoic sediments and has been generally more stable since the Late Paleozoic (Halland et al. 2014; Faleide et al. 2015).

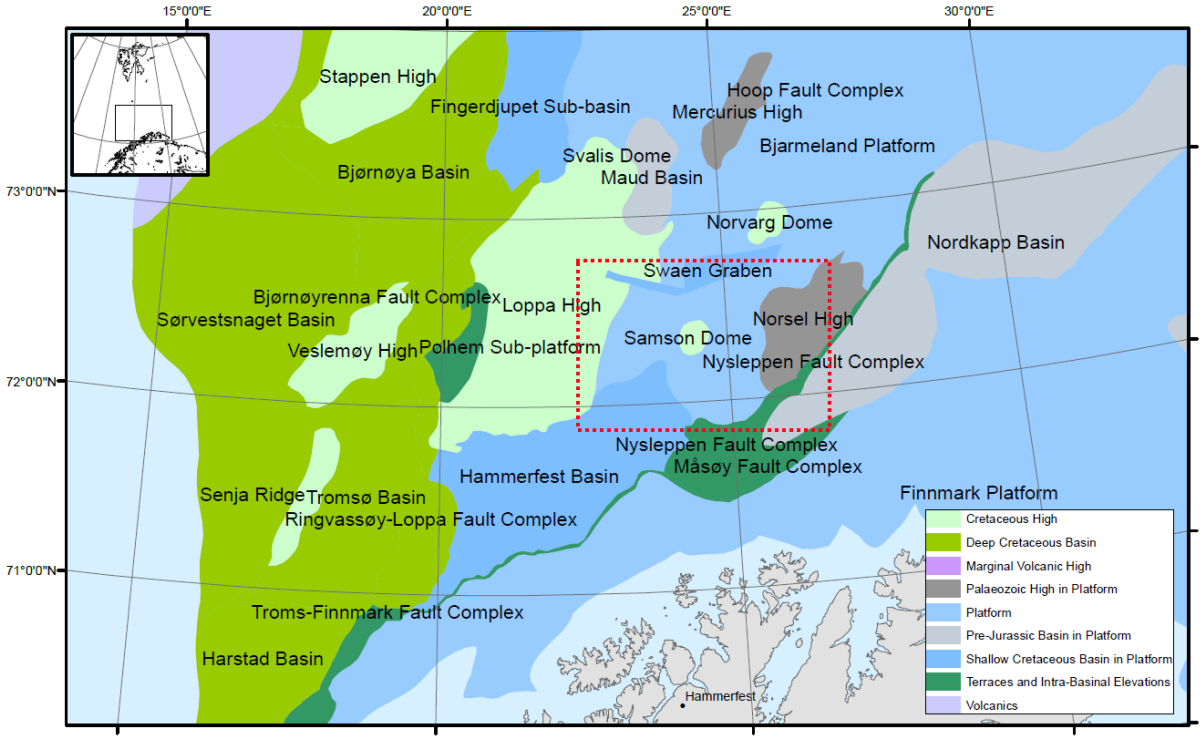

Figure 2.3. Structural elements including fault complexes in the SW Barents Sea (modified from Halland et al. 2014)

The studied Bjarmeland Platform is located on the eastern side of the western Barents Sea (Figure 2.3), and has consequently experienced a relatively low influence of regional tectonics since the Late Paleozoic. Its structural pattern is mainly shaped by subordinate highs and sub-basins created by salt tectonics and weak extension, particularly towards the more complex south-west part (e.g. Norsel High, Norvarg Dome, Samson Dome, Svalis Dome, Swaen Graben shown in Figure 2.3) (Gabrielsen et al. 1990).

At a point in time between Early Carboniferous and Late Carboniferous the Bjarmeland Platform development transitioned from pre-platform to platform, determined by the change in depositional environment from clastics to carbonates. A transition back to clastic sedimentation occurred in late Permian with origin in the uplift of the Uralian mountains (Glørstad-Clark et al. 2011). This platform area is assumed to be deposited on top of

Paleozoic and Precambrian rocks, and to have existed as a structural high from Late Permian to Early Triassic before it in Late Triassic transformed into a basin. Tectonism in the Paleogene induced dip of Paleozoic and Mesozoic sediments towards the south, with the result that younger sediments successively overlie older sedimentary layers northward (Halland et al. 2014). The Loppa High (western margin of the study area) is structural feature which has experienced several phases of uplift, subsidence, tilting and erosion (Figure 2.3). By the Early Triassic, it existed as an uplifted, tilted ridge, being onlapped by sediments up until the Middle Triassic. It is also characterized by very thick Upper Triassic sediments of the Snadd Formation.

2.3 Stratigraphy

Triassic sediments constitute the thickest sequence present on the Bjarmeland Platform, as seen in Figure 2.4. As previously mentioned, Figure 2.4 also shows that areas west of Loppa High have been severely rifted and subsided compared to the eastern side. During the Triassic the continental masses of the Earth were concentrated in one continent called Pangaea, where the Barents Sea was approximately located at 50-55^{o} N (Ryseth 2014). Erosion of the Uralian Mountain chain and a more limited source from the Fennoscandian hinterlands created a sediment influx from the south-east (Figure 2.2). Triassic sandstones on the Bjarmeland Platform is described as having an abundant plagioclase feldspar content due to the sourcing from the Uralides (Ryseth 2014). Sediments from this time are interpreted from extensive clinoform sequences as infill from a river system in the south-east, prevailing as a prograding delta system ranging from prodelta (Early Triassic) to delta plain (Late Triassic), and subsequently overlain by fluvial sediments (Lundschien et al. 2014). The depositional environments of the area through the Triassic are shown in Figure 2.2. During the Early-Middle Jurassic, the stratigraphy of the western Barents Sea is dominated by sandstones, which are more quartz-rich than Triassic feldspathic sands (Ryseth 2014; Faleide et al. 2015). Early Jurassic depositional patterns and paleogeographical setting is inferred to be similar to that of Late Triassic (Ryseth 2014).

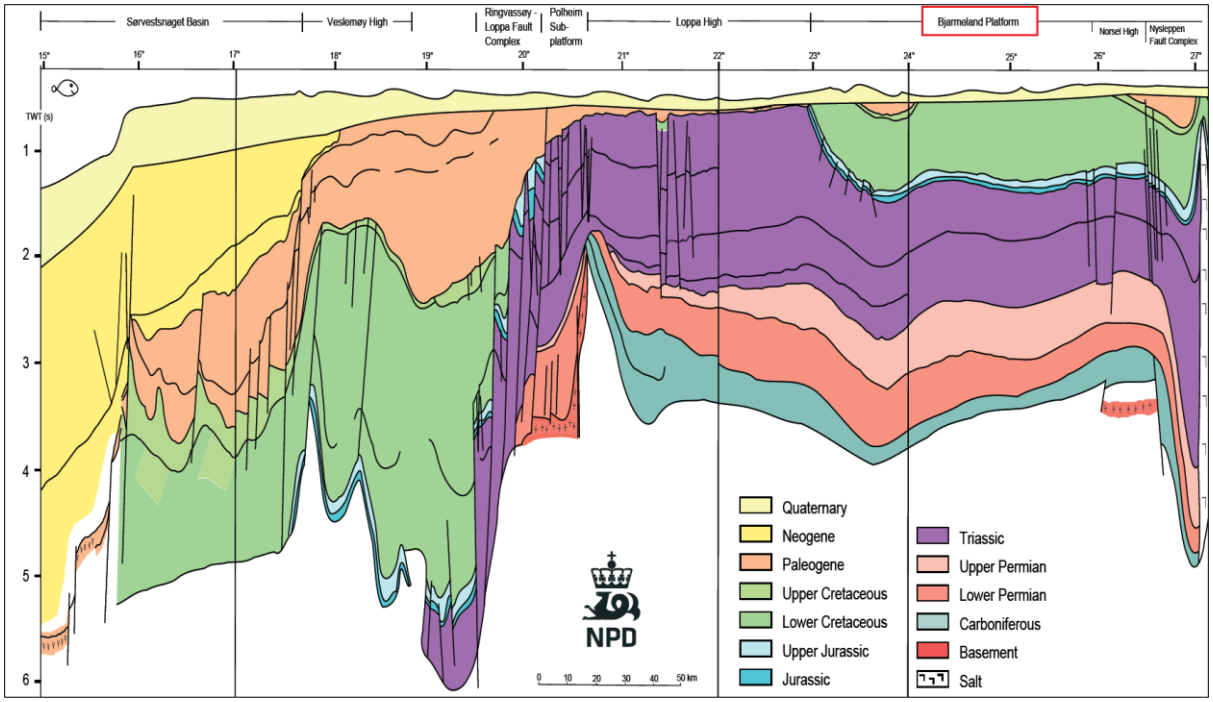

Figure 2.4. Simplified cross section of the western Barents Sea, approximately from west to east (modified from Halland et al. 2014).

As shown in the lithostratigraphic chart in Figure 2.5, the Triassic and Jurassic encompass the Sassendalen Group (Subgroup Ingøydjupet), the Kapp Toscana Group (Subgroups Realgrunnen and Storfjorden) and the lower Adventdalen Group (equivalent to Teistengrunnen Group in Dalland et al. (1988)). The Bjarmeland Platform is mainly characterized by sediments of the Sassendalen Group which has a maximum thickness of 2862 m, whereas the Realgrunnen Subgroup rarely exceeds 200 m (Halland et al. 2014). The sediments of the Sassendalen Group were mostly deposited in an open marine to shallow marine environment (Havert, Klappmyss, Steinkobbe and Kobbe), whereas parts of the Kobbe and Snadd formations were deposited in a coastal plain setting (Bergan and Knarud 1993). The Jurassic sediments are largely eroded or have not been deposited on the Bjarmeland Platform, especially towards the north of the platform and towards the Loppa High/Svalis Dome in the west. Facies equivalent to the Fruholmen, Tubåen, Nordmela and Stø formations of the Realgruppen Subgroup are deposited mostly in near-shore deltaic environments, thin towards the north and are not present in most of the platform areas (Bergan and Knarud 1993; Halland et al. 2014). The Upper Jurassic Fuglen and Hekkingen formations of the Adventdalen Group are mainly marine shales and mudstones (Halland et al. 2014).

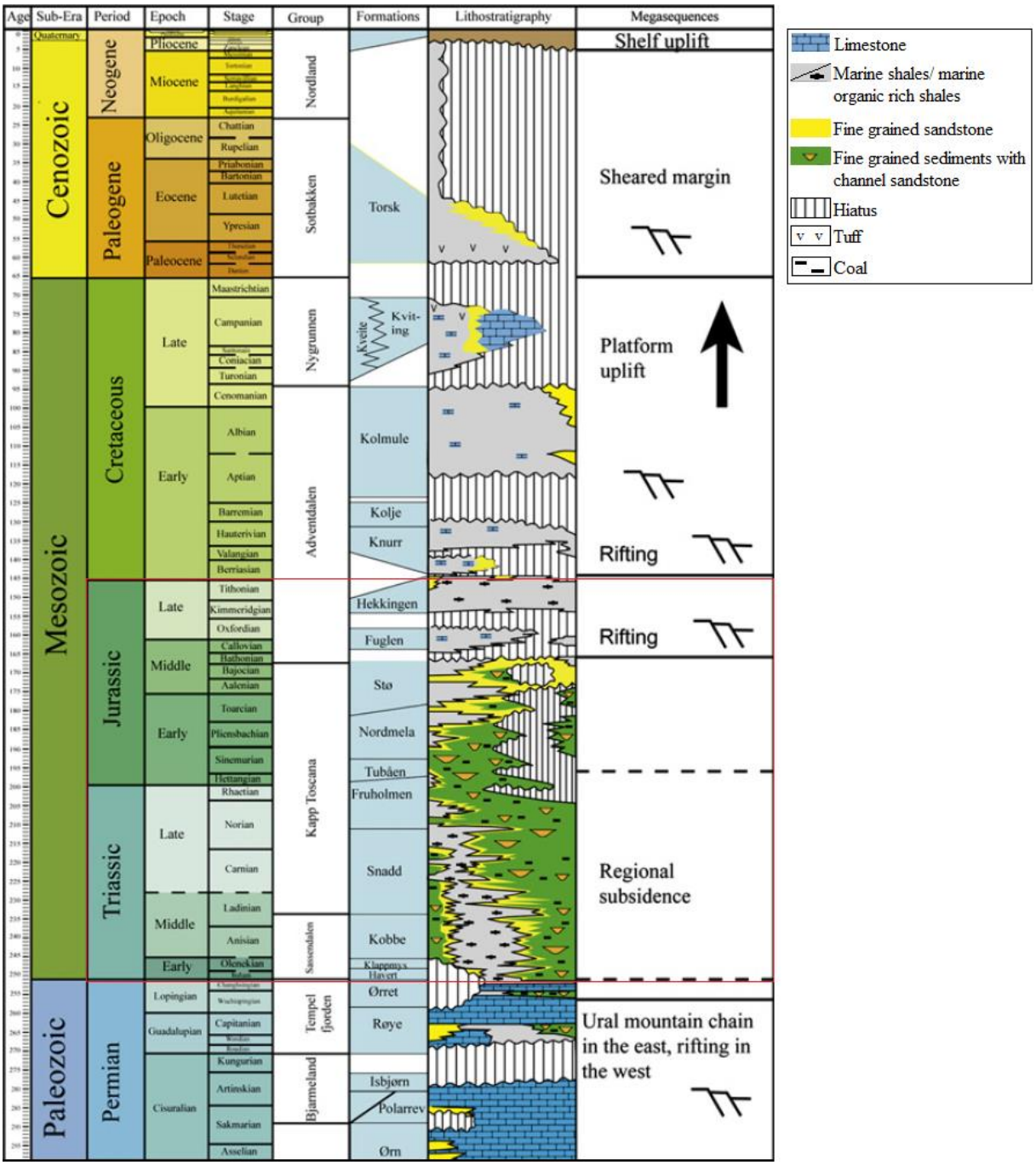

Figure 2.5. Lithostratigraphic chart representing the western Barents Sea (modified from Glørstad-Clark et al. 2010)

The deepest penetrating well in this study area is well 7226/11-1, at 5200 m, reaching Pre-Devonian basement (see Table 2.1 for depth of formations encountered in each well). Short descriptions of the formations and groups encountered that are relevant for this study are presented below.

Table 2.1: Depths (m RKB) of groups and formations encountered by the eight wells in this study. Red shading indicates that the formation is not present or eroded (source: NPD 2016).

Age	**Group,** Formation	Nysleppen Fault C.	Loppa High		Bjarmeland Platform			Samson Dome	Norsel High
		7124/3-1	**7222/6-1**	**7222/11-1**	**7125/1-1**	**7223/5-1**	**7224/6-1**	**7224/7-1**	**7226/11-1**
Neogene	**Nordland GP**	296	387	379	276	363	289	293	261
Paleogene	**Sotbakken GP**	406			391			385	
	TORSK FM							385	
Cretaceous	**Nygrunnen GP**	574			568				
	KVEITE FM	574			568				
	KVITING FM				597				
	Adventdalen GP	618			617	467	419	401	374
	KOLMULE FM	618			617	467	419	401	374
	KOLJE FM	1220			1314				
	KNURR FM				1318		890	762	1141
Jurassic	HEKKINGEN FM	1233			1344		906	792	1147
	FUGLEN FM						974	861	
	Kapp Toscana GP	1285	484	451	1399	501	1004	894	1194
	STØ FM				1399	501		894	1194
	NORDMELA FM					508		919	
	TUBÅEN FM	1285				524	1004	930	1202
Triassic	FRUHOLMEN FM	1305		589	1521	540	1064	931	1234
	SNADD FM	1438	484	636	1612	585	1166	1028	1296
	Sassendalen GP	1893	1890	2007	2105	1856	2010	1642	1878
	KOBBE FM	1893	1890	2007	2105	1856	2010	1642	1878
	KLAPPMYSS FM	2334	2464			2451		2222	2303
	HAVERT FM	2671	2674					2663	2913
Permian	**Tempelfjorden GP**	3475							3877
	ØRRET FM	3475							3877
	RØYE FM	3670							3966
	Bjarmeland GP	3900							4103
	ISBJØRN FM	3900							
	ULV FM	3952							4103
	POLARREV FM	4000							4182
	Gipsdalen GP	4271							4334
	ØRN FM	4271							4334
Pre-Devonian	BASEMENT								5137

2.3.1 Sassendalen Group (Ingøydjupet Subgroup)

This group comprises shales, siltstones and sandstones of the Havert, Klappmyss, Steinkobbe, and Kobbe formations dated Early to Middle Triassic. The sediments were deposited in costal to deltaic environments (Mørk et al. 1999). A short summary of individual formations is given below:

- **Havert Formation**

The Havert Formation is typically made up of darker shale and lighter grey silty shale deposited in a shallow marine to open marine setting (Mørk et al. 1999). On the Bjarmeland Platform it is reported to be dominated by silt and claystone with lesser sandstone inputs (Halland et al. 2014).

- **Klappmyss Formation**

The Klappmyss Formation consists mainly of medium to dark grey shales, with alterations of shale, silt and sand upwards in the formation. It is indicated to be deposited in shallow to open marine environments, influence of coastal progradation (Mørk et al. 1999). It generally thickens and gets finer northwards from the Hammerfest Basin, and is reported at around 600 m on the Bjarmeland Platform and Norsel High (well 7226/11-1 in this study) (Halland et al. 2014).

- **Steinkobbe Formation**

Although the formation is not encountered by a well included in this study, it is regarded as a potential source rock for reservoirs on the Bjarmeland Platform and therefore mentioned. It consists mainly of organic rich mudstone and contains also siltstone beds. It represents deep, open shelf environments which have been mostly restricted, and is found on the Svalis Dome with assumed limited lateral extent (Mørk et al. 1999).

- **Kobbe Formation**

The Kobbe Formation is described as having a base of shale, which changes upward to interbedding of shale, siltstone and carbonate-cemented sandstone. It is deposited after a transgression, with increasing input of clastic material by buildout of coastal areas (Mørk et al. 1999). Example core photos from a reservoir interval in well 7222/11-1 (Caurus) are shown in Figure 2.6.

Figure 2.6. Core photos from between 2233-2236 m (KB) in well 7222/11-1 of the Kobbe Formation (courtesy of Statoil ASA, previously StatoilHydro Petroleum AS).

2.3.2 Kapp Toscana Group

The Kapp Toscana Group is subdivided into the Storfjorden and Realgrunnen subgroups of Middle Triassic to Middle Jurassic age, and the main lithologies are shales, mudstones, siltstones and sandstones (Mørk et al. 1999).

2.3.2.1 Storfjorden Subgroup

The Storfjorden Subgroup includes Snadd Formation sandstones and mudstones of immature composition deposited in coastal to marine environments in Late Middle to Early Late Triassic (Mørk et al. 1999).

- **Snadd Formation**

The Snadd formation has a base of grey shales, which coarses upwards to shales with interbeds of siltstones and sandstones. Also limestone interbeds (lower part) and coaly lenses (higher part) are present, with red-brown shales defining the top of the formation. Lateral variations in lithology occur, which may cause appearance in wells to differ. Depositional environment is described as being from distal marine to deltaic progradation by Mørk et al. (1999). In Klausen et al. (2015) it is stated that the depositional characteristics is temporally and spatially varying relative to the position of the coastline and relative to sediment input source. Both a thick, widespread non-marine succession (paralic and fluvial) and a shallow marine beach facies through shelf edge to distal marine mudstone development are described. It is capped by a regional flooding of Norian age. Core photos of Snadd Formation sandstones in well 7222/11-1 and 7222/6-1 are shown in (Figure 2.7).

Figure 2.7. Core photos of Snadd Formation sandstones from well 7222/11-1 in the interval 784-787 m (left) and from well 7222/6-1 between 1640-1643 m (right, courtesy of Statoil ASA, previously StatoilHydro Petroleum AS).

2.3.2.2 Realgrunnen Subgroup

The Realgrunnen Subgroup consists of mature sandstones, shales and coal of the Fruholmen, Tubåen, Nordmela and Stø Formations deposited in a coastal plain to deltaic or shallow marine environment (Mørk et al. 1999). It is only thinly developed on the Bjarmeland Platform (Halland et al. 2014). A short description of different formations is given below:

- **Fruholmen Formation**

This formation is characterized by grey to dark grey shale at the base, which pass upwards into interbedded sandstones, shales and coals. The middle of the formation is dominated by sand in many wells (Mørk et al. 1999). The formation is further subdivided into the Akkar, Reke and Krabbe members to better represent the different lithologies present. The depositional environment transitions from open marine shales to coastal and fluvial-dominated sandstones, and finally flood-plain deposition (Halland et al. 2014).

- **Tubåen Formation**

The Tubåen Formation is characterized by sandstones, deposited in a high energy marine environment, assumingly tidal or estuarine. Also described are subordinate shales and minor coals related to more distal and lagoonal environments, respectively (Mørk et al. 1999). Core photos of Tubåen Formation sandstone in well 7124/3-1 are shown in Figure 2.8.

Figure 2.8. Core photos of a Tubåen Formation reservoir sandstone from well 7124/3-1 in the interval 1293-1298 m (modified from NPD 2016).

- **Nordmela Formation**

The Nordmela Formation consists of interbedded siltstones, sandstones, shales and mudstones, as well as minor coals. The sandstones are more dominant upwards in the formation, and the depositional environment is considered to be tidal flat to flood-plain, with estuarine and tidal channels linked to individual sandstone successions (Mørk et al. 1999).

- **Stø Formation**

The main lithology of the Stø Formation is moderate to well sorted sands, with thin units of shale and siltstones. Corresponding environments are prograding coastal regimes with regional transgressive pulses representing the shale and siltstone intervals (Mørk et al. 1999). An example of Stø Formation reservoir sand is shown in Figure 2.9 from well 7125/1-1.

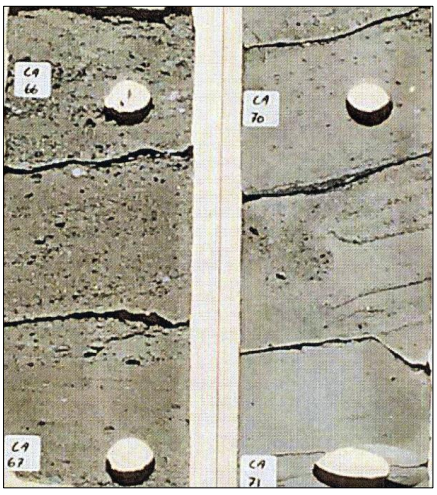

Figure 2.9. Core photos of Stø Formation reservoir sandstone from well 7125-1-1 in the interval 1421-1426 m (modified from NPD 2016).

2.3.3 Adventdalen Group

This group encompasses claystones, shales and sandstones of the Fuglen, Hekkingen, Knurr, Kolje and Kolmule Formations, where both the Fuglen and Hekkingen Formations are known source rock shales. Age of deposition is Late Middle Jurassic to Early Cretaceous (Mørk et al. 1999).

- **Fuglen Formation**

This unit contains pyritic, dark brown mudstones with thin limestone interbedding, deposited in a marine shelf environment (Mørk et al. 1999).

- **Hekkingen Formation**

Hekkingen is an organic-rich brownish to very dark grey shale characterized by high gamma ray values towards the bottom. Thin interbeds of limestone, dolomite, siltstone and sandstone is also observed (Mørk et al. 1999). It is an important source rock (better than the Fuglen Formation) for hydrocarbon as well as cap rock, and is found in thin sequences on the Bjarmeland Platform (Halland et al. 2014).

- **Knurr Formation**

The Knurr Formation encompasses mainly grey to brown mudstone with limestone and dolomite interbeds, deposited in a distal, open marine shelf environment (Mørk et al. 1999). It is thinly and more locally developed on the Bjarmeland Platform (Halland et al. 2014).

- **Kolje Formation**

The Kolje Formation is similar to the Knurr Formation in lithology and depositional environment, and is additionally interbedded with thin siltstones and sandstones towards the top. Periodical variations of good and restricted water circulation are indicated (Mørk et al. 1999).

- **Kolmule Formation**

The Kolmule Formation is characterized by grey to green mudstones and shale with siltstone interbeds and limestone and dolomite stringers present in some intervals. It is assumed to have been deposited in open marine environments (Mørk et al. 1999).

2.4 Petroleum systems

A petroleum system is defined in Magoon and Dow (1994) to include a petroleum source rock, reservoir rock, seal or cap rock in the form of a trap and overburden rock. The timing of the processes generation-migration-accumulation of hydrocarbon must occur in time and space so that organic matter in the source rock can be converted to petroleum and migrate to a sealed reservoir. Triassic to Jurassic successions have been the main exploration targets for hydrocarbons in the Barents Sea, where there are multiple candidates for both source and reservoir rocks (Lundschien et al. 2014). As indicated schematically in Figure 2.2 and Figure

2.5, the lithology of different formations can also vary laterally, so that a formation denoted as a reservoir (sandy) in one area can be deposited as more shaley (potential source rock) in other areas.

2.4.1 Source rocks

Multiple intervals and formations in the Barents Sea contains source rocks of different quality and extent, and the region has consequently been described as a multi-source rock system in Ohm et al. (2008). Sampled source rocks from the Norwegian Barents Sea and Svalbard and measures of their quality is shown in Figure 2.10, and also serves to show the abundance of possible sources in this area, including coals.

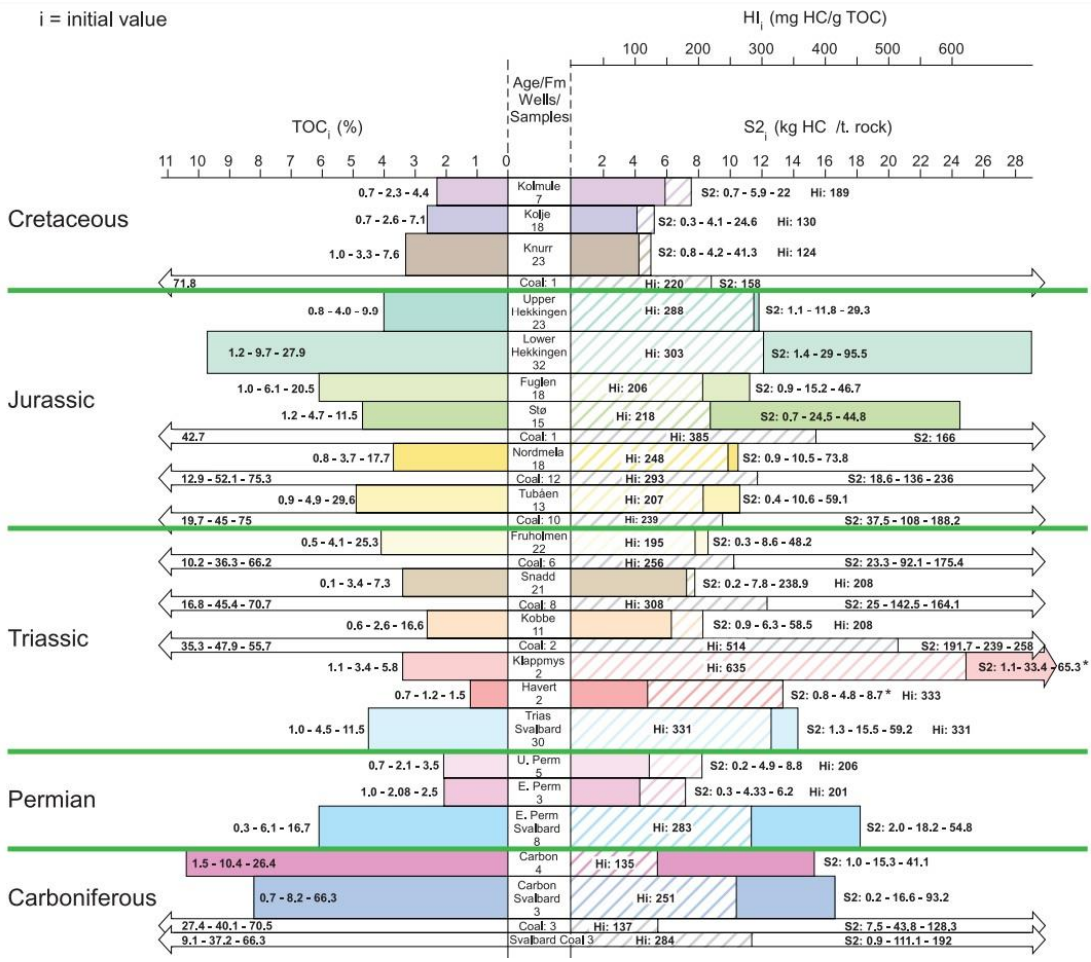

Figure 2.10. Overview of source rocks in the Norwegian Barents Sea and indications of their respective quality. Numbers (e.g.) 1.2 - 9.7 - 27.9 indicate the range and calculated average initial source rock quality values (modified from Ohm et al. 2008).

Although the Hekkingen Formation is indicated to contain the richest source rock in the area, shales in Permian, Carboniferous, Triassic and Middle to Lower Jurassic have hydrocarbon generation potential. The older intervals are however not as frequently penetrated by wells,

and there are consequently less certainty connected to evaluating the quality of the deeper source rocks (Ohm et al. 2008).

Some potential source rocks and coals were deposited in the Early to Late Carboniferous which was a sandstone and shale dominated period, before the environment changed to accommodate the deposition of dolostones and limestones in the Late Carboniferous to Late Permian. From Late Permian to Late Triassic the deposition is dominated by marine and alluvial shales with some sandstone layers, which is interpreted to represent multiple transgression and regression events. Source rock candidates from this interval are found in shales of the Tempelfjorden Group, as well as the formations Havert, Klappmyss, Kobbe, Snadd and Fruholmen, bearing in mind that these formations are also considered potential reservoir rocks. Shale of the Steinkobbe Formation is also identified as a contributing source rock to Triassic and Jurassic plays (e.g. NPD 2014).

A sandier trend is observed in the uppermost Triassic continuing through Middle Jurassic, corresponding to higher energy environments evident in the Tubåen, Nordmela and Stø deposits, resulting in lower source rock probability. Lastly, the Upper Jurassic and Cretaceous is characterized by a more distal marine environment, resulting in marine shales e.g. as seen in the Fuglen and Hekkingen formations which have high source rock potential. Formations Knurr, Kolje and Kolmule are also deposited in this period, albeit with less potential for hydrocarbon generation (Ohm et al. 2008). Correlation of potential source rocks is shown in Figure 2.11.

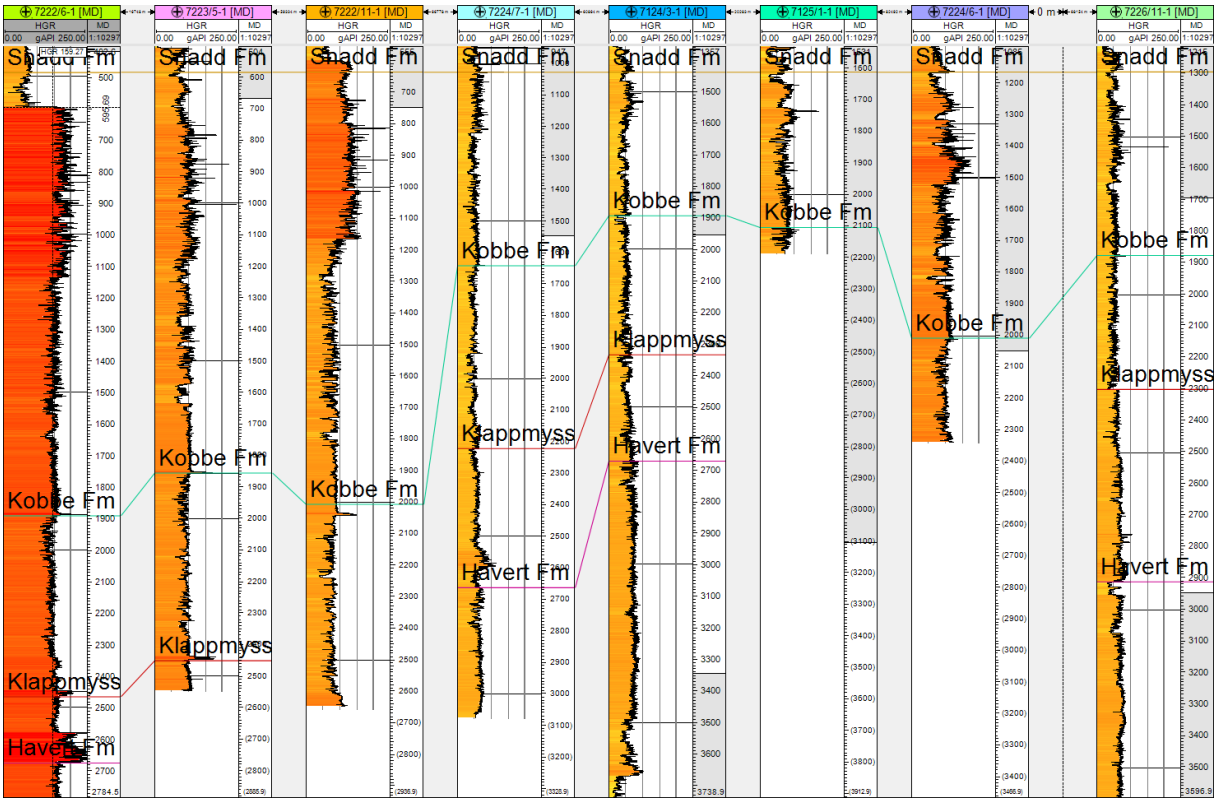

Figure 2.11. Correlation of potential source rock formations in the order indicated in Figure 1.3. Note abnormally high gamma readings in well 7222/6-1. Havert, Klappmyss, Kobbe and Snadd are also relevant as potential reservoir formations. Flattened on top Snadd.

2.4.2 Reservoir rocks

Triassic and Jurassic plays have been summarized by NPD (2014), and the extent of potential reservoirs are shown in the maps of Figure 2.12. The Snadd and Kobbe formations have been denoted the main targets in many of the exploration wells included in this study.

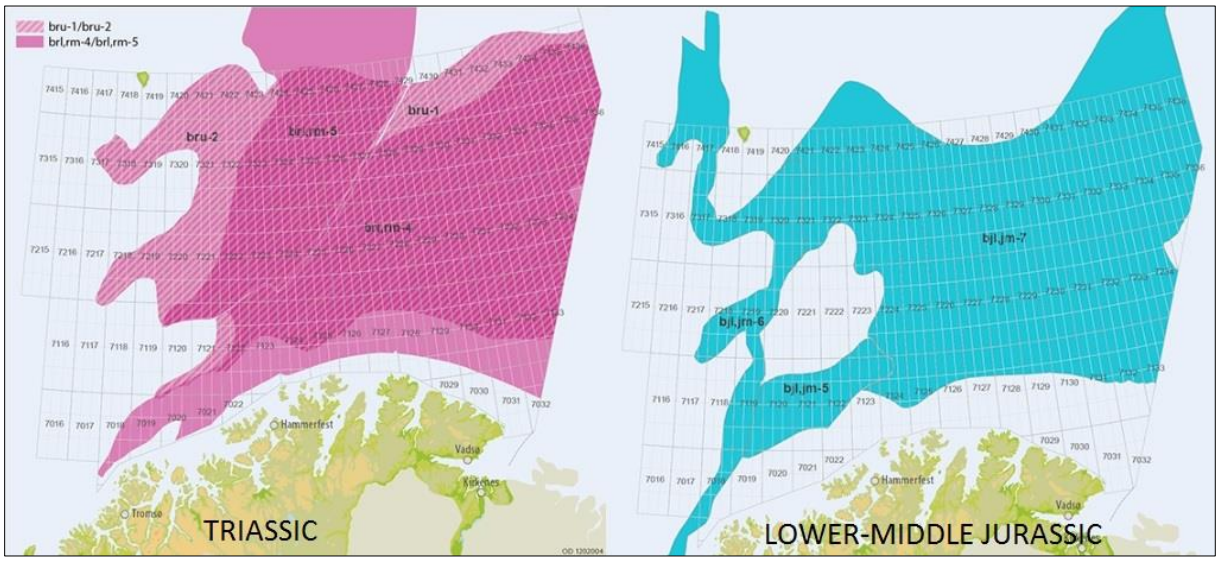

Figure 2.12. Triassic and Lower-Middle Jurassic geological plays in the western Barents Sea (modified from NPD 2014).

Triassic and Jurassic reservoir rocks in the Bjarmeland Platform area are identified in multiple levels, with the Triassic having greater thickness compared to the Jurassic. The Triassic plays named blr,rm-4 and brl,rm-5 in the overview of NPD (2014) (Figure 2.12) encompasses the Sassendalen Group, with fluvial, deltaic, shallow marine, tidal and estuarine sandstones in the formations Havert, Klappmyss and Kobbe as potential reservoirs. In plays bru-1 and bru-2 the relevant reservoir rocks are shoreface and channelized sandstones of the Snadd formation, deposited in estuarine-fluvial conditions (Henriksen et al. 2011b; NPD 2014). The Fruholmen Formation, which is part of a widespread delta progradation and contains good quality channelized sands, is mentioned in both Triassic and Jurassic plays even though it is officially placed in the Triassic part of the Realgrunnen Subgroup. It is however assumed to be somewhat diachronous (NPD 2014). Reservoir potential in the Triassic rocks is variable, related to their often fine-grained nature and effects of high maximum burial. Lower maximum burial depth, i.e. in shallower units, is described to generally increase reservoir quality simply because of less diagenesis and temperature effects. In concert with this, chlorite coating has been interpreted to improve the properties of the Snadd Formation sands, leading Henriksen et al. (2011b) to describe it as the seemingly best Triassic reservoir interval.

Considering Lower-Middle Jurassic, the play named bjl,jm-7 is most relevant for the Bjarmeland Platform when examining Figure 2.12. This play represents the Kapp Toscana Group including the formations Tubåen, Normela and Stø as reservoir rocks. These contain sandstone reservoirs of fluvial, deltaic, estuarine, tidal and shallow marine origin. Stø

Formation sandstone is a well-known reservoir rock from other areas of the Barents Sea (e.g. the Hammerfest Basin), but is often thin or absent on the Bjarmeland Platform. A correlation panel of potential reservoir rocks in the Realgrunnen Subgroup (Tubåen, Nordmela, Stø) is shown in Figure 2.13 and correlation for the Storfjorden Subgroup (Snadd) and the Sassendalen Group (Havert, Klappmyss, Kobbe) can be seen in Figure 2.11. Note that formations in Figure 2.13 displayed with a question mark is not officially named in the provided well stratigraphy from the drilling company, but is rather interpreted in this study as a possible differentiation of the Kapp Toscana Group. This is not directly influential for this thesis work (as all required logs are not recorded in this interval) but only indicated for a more complete impression of thickness variations.

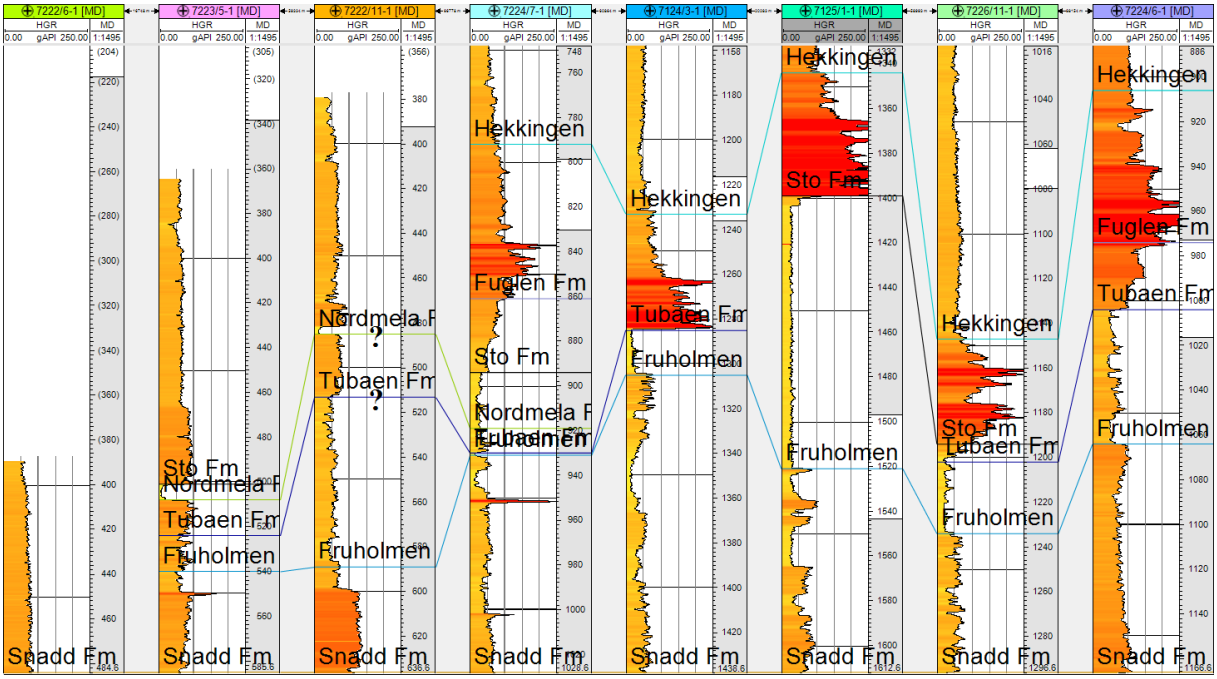

Figure 2.13. Correlation of Jurassic reservoir rock candidate formations. Flattened on top Snadd.

2.4.3 Cap rocks and traps

Common cap rocks in the Norwegian Barents Sea are the Hekkingen and Fuglen formations, but shales of older formations (e.g. intra Triassic) also have the potential to seal reservoirs (Doré 1995). A result of this can be that the cap rock varies from play to play, one example is shown in (Figure 2.14). Traps are mainly stratigraphic, but rotated fault blocks, horst structures and traps formed in relation to salt are also common (NPD 2014).

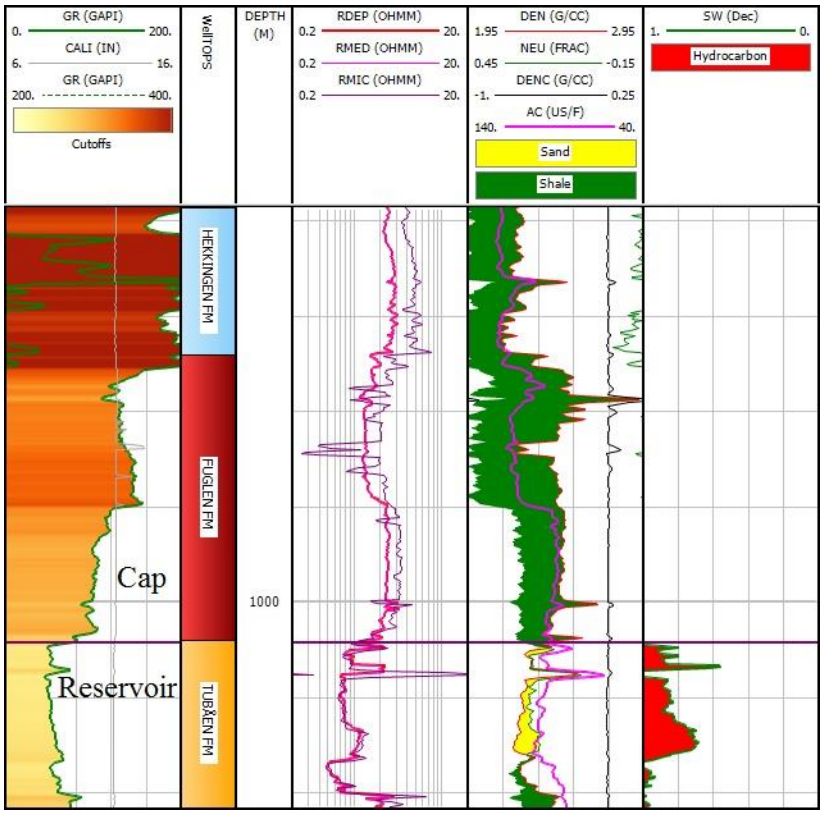

Figure 2.14. Example of the Fuglen Formation (and potentially Hekkingen Formation) from well 7224/6-1 that is acting as a cap rock above a low saturation gas reservoir in the Tubåen Formation.

2.4.4 Uplift and seal failure

As mentioned previously, the Barents Sea has been influenced by substantial periods of uplift and erosion, with the Cenozoic being particularly important in terms of effect on hydrocarbon exploration (Faleide et al. 2015). Up to 3 km of sediments are estimated to have been removed in the most affected areas - somewhat less (1.5-2 km) in the western Barents Sea - although the accuracy of timing of events and thicknesses eroded is not yet completely agreed upon (Doré and Jensen 1996; Faleide et al. 2015; Baig et al. 2016). The proposed causes of the uplift are both related to several phases of tectonics, as well as glaciation periods in the Pliocene and Pleistocene which are regarded as most important (Doré and Jensen 1996; Faleide et al. 2015). A large portion of the Paleogene and Upper Cretaceous sediments were eroded during these glaciations (Ohm et al. 2008; Baig et al. 2016). A representation of the total amount of uplift in different areas of the Norwegian Barents Sea based on vitrinite (maturity) data is shown in Figure 2.15. The possible effects this has had on the petroleum systems are not necessarily entirely negative. The positive effects could be fracturing of tight reservoirs, remigration to shallower reservoirs, relocating mature source rocks to shallower depths, and liberation of thermogenic gas from formation water. Negative effects include alteration of structures and traps which could lead to spilling of hydrocarbons or breakage of cap rocks, pressure decrease resulting in gas expansion and expulsion of oil from traps, and decreasing temperature causing source rocks to cease further generation of hydrocarbons. A poorer quality cap rock could potentially leave reservoirs more likely to retain oil if gas is

allowed to leak rather than displace oil in uplifted areas, indicated as type II and III traps in Figure 2.16 (Ohm et al. 2008). Uplifted reservoir rocks will exhibit poorer reservoir quality than expected at the present depth (Doré and Jensen 1996; Faleide et al. 2015).

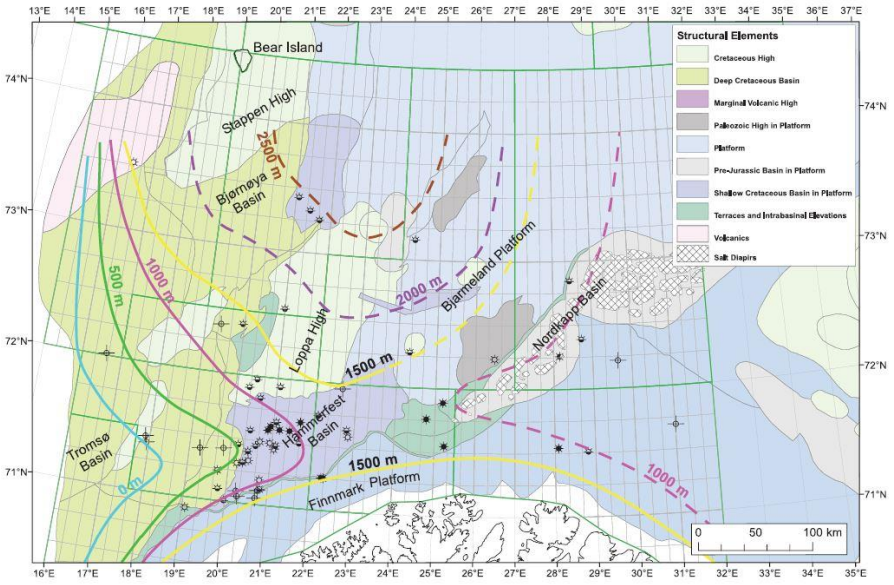

Figure 2.15. Uplift estimation based on vitrinite reflectivity values (adapted from Ohm et al. 2008).

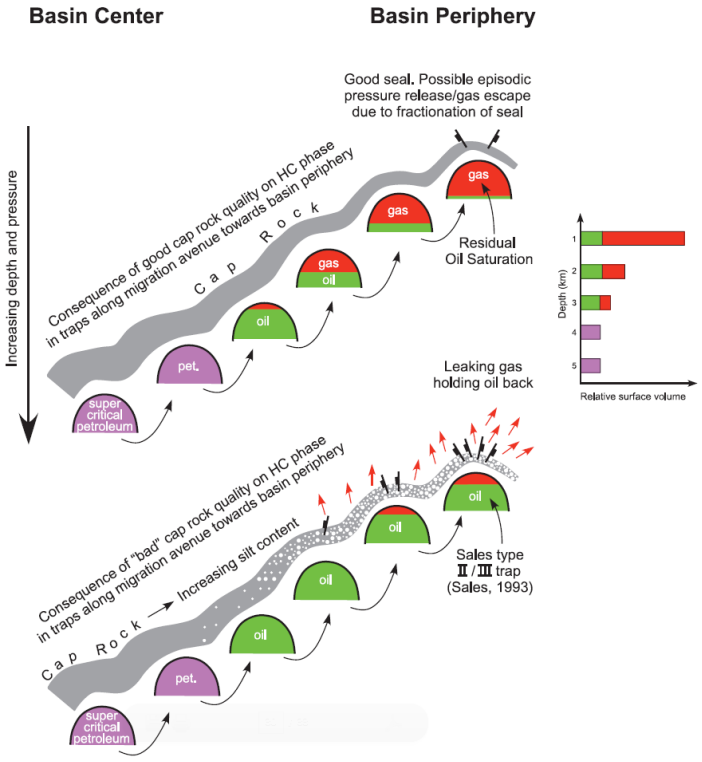

Figure 2.16. Schematical representation of hydrocarbon phase and cap rock quality (modified from Ohm et al. 2008). Good cap rock quality retains gas and can cause oil to spill.

As seen in Figure 2.15, the estimated uplift of the study area ranges from approximately 1000 m near the Norsel High and the Nysleppen Fault Complex to 2000 m near the Swaen Graben and Loppa High. Considering maximum burial depth of the sediments, this would theoretically indicate that the rocks have experienced temperatures 30-60°C higher if assuming a temperature gradient of 30°C/km. The estimates of Ohm et al. (2008) are however only based on vitrinite reflectance data, whereas in Baig et al. (2016), a combination of maturity data, shot gathers from reflection seismics, and well log data were used for estimating net uplift in the western Barents Sea. Values indicated for the Bjarmeland Platform range from ~1250-2400 m, lowest in the south-west and highest towards north-north-west, whereas in the study area the more specific estimates range from around 1150 m to around 1600 m, as seen in Figure 2.17.

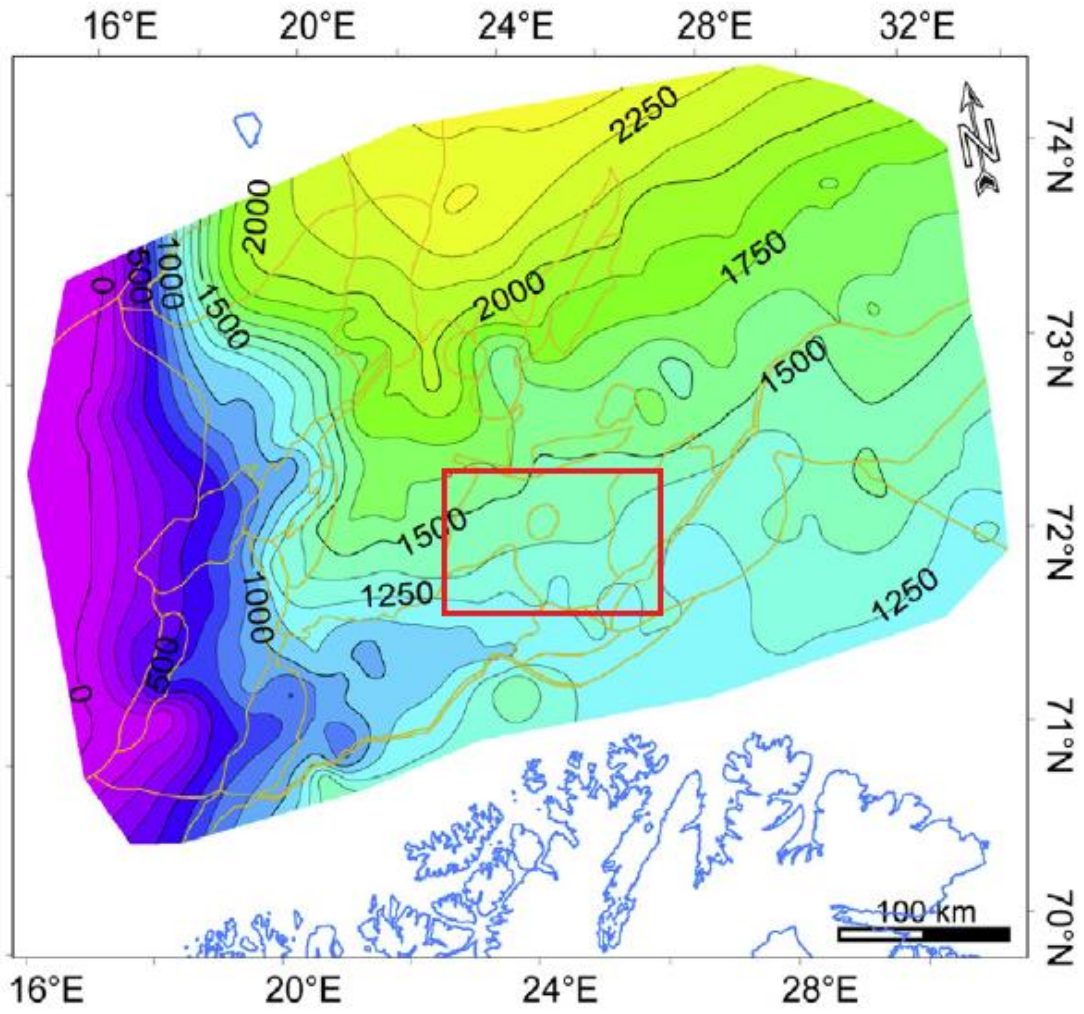

Figure 2.17. Uplift estimates in the SW Barents Sea, study area indicated in red rectangle. Note that most of the study area is captured between contours for 1250 m and 1500 m, albeit slightly more in the north-west corner near and on the Loppa High (modified from Baig et al. 2016).

Table 2.2 shows calculations made for the geothermal gradient of each well in this study. The average present day geothermal gradient based on data from these is 37.6°C, and appears to be lower in the easternmost wells 7125/1-1, 7124/3-1 and 7226/11-1. In the bottom hole temperature table of well 7222/11-1 a gradient of 41°C/km was suggested for a best possible fit to the measured temperature data, and is stated to fit well with regional observations. The gradient calculation in well 7226/11-1 is assumed to be too low, as true vertical depth is not stated for this well and total measured depth was used instead. An estimate of regional geothermal gradient is in Smelror et al. (2009) based on bottom hole temperatures and drill stem test data stated as 31-38°C, with more confidence in the higher number due to BHT estimates often being biased to lower values even with corrections. Typical geothermal gradients in sedimentary basin generally vary from 25-45°C. Both presence of salt (e.g. Samson Dome) as well as uplift and erosion can influence the geothermal gradient and heat flow of a basin (Bjørlykke 2015a) (Figure 2.18).

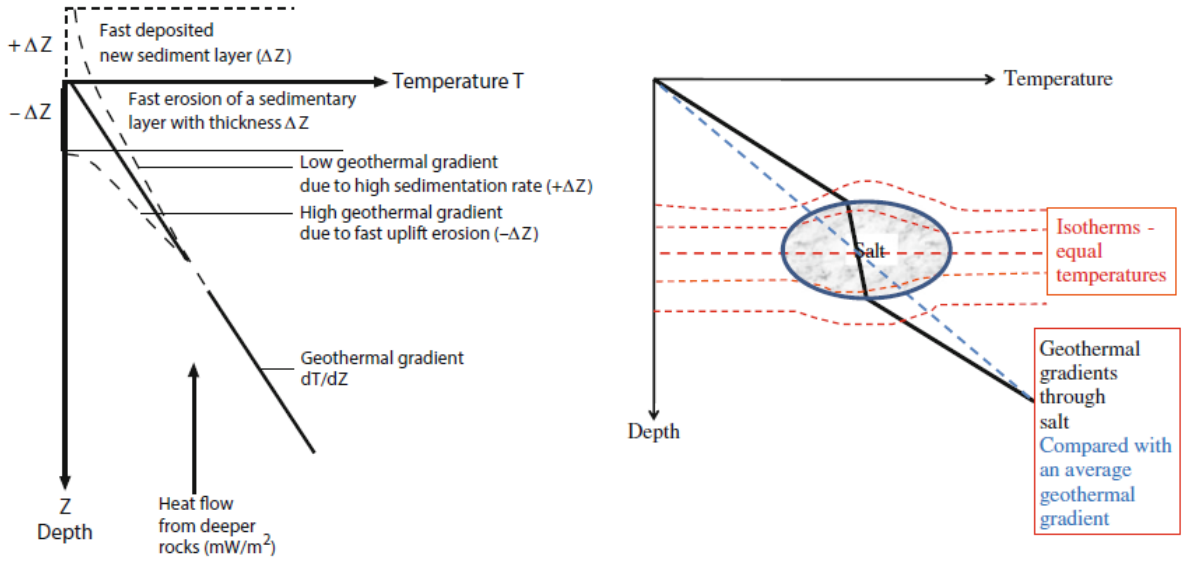

Figure 2.18. Geothermal gradient as a function of rapid uplift or subsidence (left), and the influence of salt on the geothermal gradient (right, adapted from Bjørlykke 2015a).

Table 2.2: Calculated geothermal gradient for the eight studied wells.

Well	Final vertical depth (TVD) [mRKB]	Water depth [m]	Kelly bushing [m]	Final vertical depth (TVD) [mBSF]	BHT (°C)	Geothermal gradient [°C/km]
7124/3-1	4730	273.0	23.0	4434	151	33.15
7125/1-1	2199	252.2	23.5	1923.3	64	31.20
7222/11-1	2625	356.0	23.0	2246	92	39.18
7222/6-1 S	2848	364.0	23.0	2461	89	34.54
7223/5-1	2548	340.0	23.0	2185	94	41.19
7224/6-1	2338	266.0	23.0	2049	91	42.46
7224/7-1	3064	269.0	23.5	2771.5	119	41.49
7226/11-1	5205	237.5	23.0	4944.5	143	28.11

Chapter 3: Research methodologies and theoretical background

3.1 Workflow

Figure 3.1 displays a broad overview of the workflow of this study. Generally the first task conducted is petrophysical analysis, followed by rock physics diagnostics and finally AVO modeling, with continuous comparison and quality control between the disciplines.

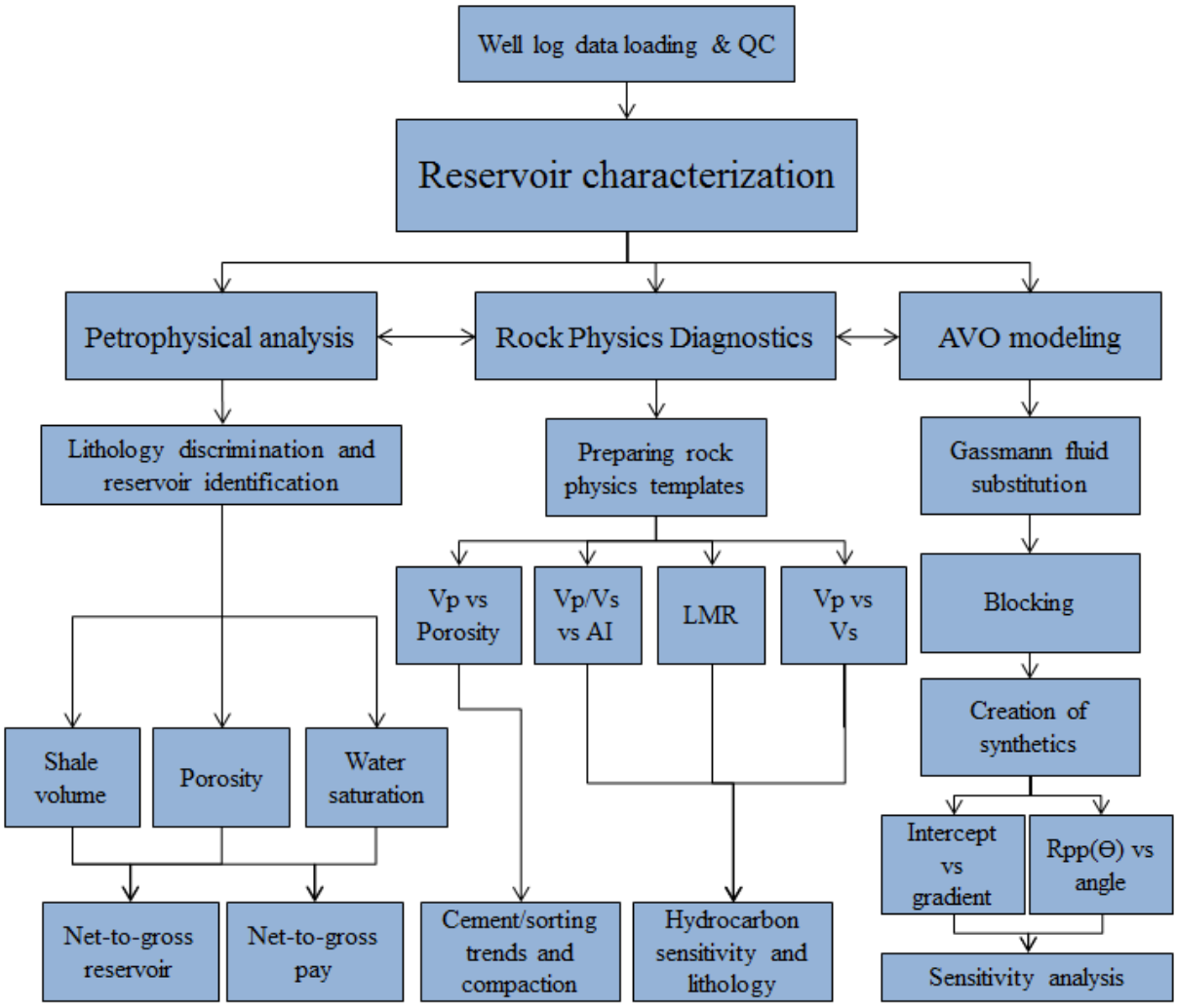

Figure 3.1. Chart showing the general workflow of the study showing the most important steps of the reservoir characterization.

3.2 Petrophysical analysis

Petrophysical analysis is the process of using well log data to describe the quality parameters of a sedimentary succession and identifying potential source, reservoir and cap rocks. This can be explored through studying the log data as they are and the relation between selected logs, but even more so through calculation of additional parameters suitable for evaluating the target reservoirs. Combining information gained from different logs is crucial for increasing confidence in the interpretations, as there are pitfalls and limitations related to practically all well logs. Parameters of special interest are e.g. shale volume (V_{sh}), porosity (ϕ), water saturation (S_w) and net-to-gross ratios. An overview of well logs available for interpretation is shown in Figure 3.2. Composite log displays of the Kobbe, Snadd, Tubåen and Stø Formations across all eight wells are included in Figure A.1 to A.21.

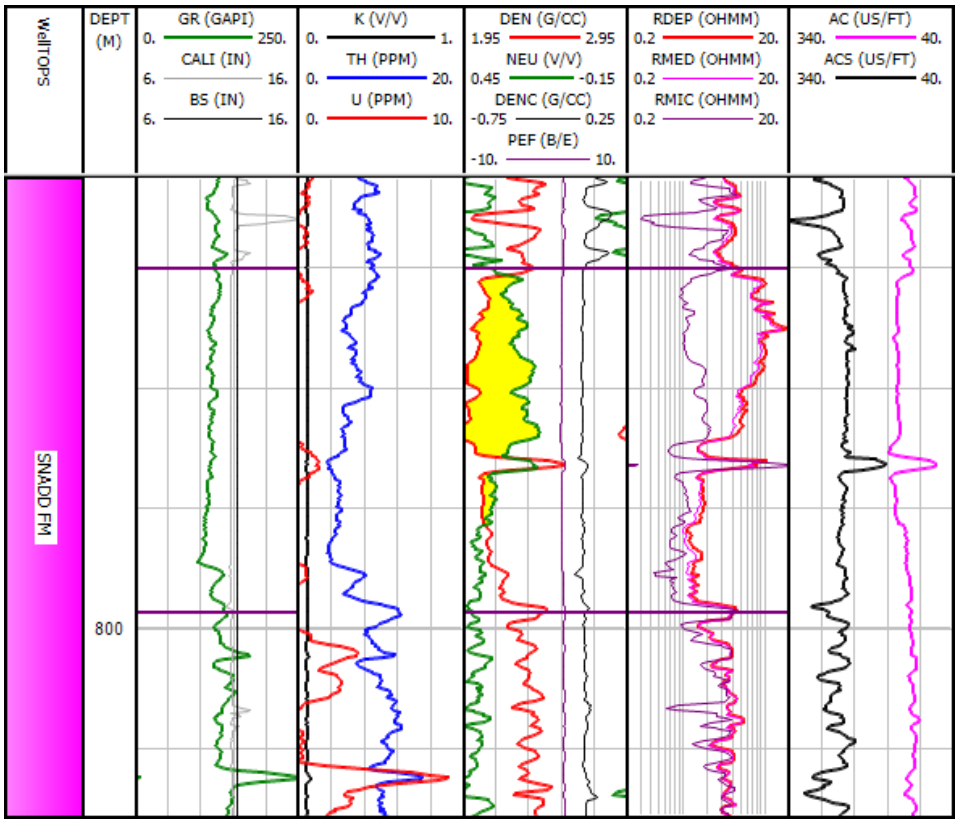

Figure 3.2. Overview of logs included in thesis work, example from well 7222/11-1. Note that S-wave acoustic log (ACS), spectral gamma, bit size (BS) and photoelectric effect (PEF) are only included in the four newest wells, and that shallow resistivity is replaced by microresistivity (RMIC).

3.2.1 Lithology discrimination and net-to-gross estimation

Lithology discrimination is mainly performed by studying the gamma ray log (GR) and neutron/density logs, but also supported by the caliper log which can show caving (brittle shale) and mudcake (permeable formation) effects. The Spontaneous Potential (SP) log could in theory also be used for identifying lithology and shaliness, but this log is not measured in

wells included in this study. A variation of the density log, the photoelectric log (with unit barns/electron or b/e, usually displayed on a scale from 1-10 b/e), records the return of low energy gamma rays and can also be used for lithology discrimination as this radiation is mostly independent on porosity and bulk density. Measured values which are used to calculate a photoelectric absorption index (P_e) can be compared to a reference Table containing common P_e values. It is not usable in holes drilled with barite mud (Mondol 2015b).

The gamma ray log is a measure of total natural gamma radiation (passive recording), and in general, sections of clean sand display the lowest GR values when considering siliciclastic rocks, whereas high GR readings indicate shaley intervals. Limestones, dolomite, coal and salts also displays low values, similarly to clean quartz sands (Mondol 2015b). Highly organic rich (black) shales are very easily distinguishable in a GR log, as it will produce the highest values due to increased content of uranium. Spectral gamma ray logs can be used to further distinguish the respective contribution of potassium, thorium and uranium to the gamma ray reading.

Net-to-gross ratio is an ambiguous term, and when calculating this parameter the quantities being used should be specifically stated. A sequential approach and definition is proposed in Worthington and Cosentino (2005) which comprises different levels of 'net' thicknesses (N) which relates to 'gross' reservoir thickness (G):

- Gross rock: All rock within the interval being evaluated (e.g. a formation)
- Net sand: Rocks that might have useful reservoir properties, defined by a shale volume (V_{sh}) cutoff value.
- Net reservoir: Includes the net sand intervals that have useful reservoir properties, defined by a porosity (ϕ) cutoff value.
- Net pay: Comprises the net reservoir intervals that have a certain level of hydrocarbons, defined by a water saturation (S_w) cutoff value.

Resulting ratios that can be expressed are consequently net-to-gross sand, net-to-gross reservoir, or net-to-gross pay (Worthington and Cosentino 2005). A pay zone is characterized by sufficiently high porosity and hydrocarbon content, as well as sufficiently low shale volume (Bjørlykke 2015b). In reservoir engineering, permeability is also a possible parameter usable for containing pay intervals. Cutoff values for porosity and shale volume should ideally be decided to fit each individual study or area, but proposed values can be used as satisfying indicators as this process is not included in or in the scope of this thesis work. Traditionally used cutoff values for sandstones are summarized in Table 3.1.

Table 3.1: Proposed cutoff values for sandstone (Worthington and Cosentino 2005).

Cutoff Parameter	Range of values
V_{sh}	<= 0.3-0.5
ϕ	>= 0.08-0.06
S_w	<= 0.5-0.6

3.2.2 Shale volume calculation

In this study, the gamma ray log and a neutron-density combination is used to estimate the shale volume (V_{sh}) in each of the wells. The goal of this is to quantify the presence of shale at different depths, in order to distinguish reservoir rocks from non-reservoir rocks (Mondol 2015b). Presence of shale or clay may influence readings in several logs, is highly important for production potential (reservoir quality), and even low amounts may affect permeability (Ellis and Singer 2008). Furthermore, the shale volume is used for estimating effective porosity and consequently water saturation, which are described in later sections.

Shale volume calculations are performed in the following manner. First it requires calculation of the gamma ray index (I_{GR}) through the following relationship:

$$I_{GR} = \frac{GR_{log} - GR_{min}}{GR_{max} - GR_{min}} \quad \text{Eq. 3.1}$$

Here, GR_{log} is the gamma ray reading at the depth of interest, GR_{min} is the minimum gamma ray reading (sand line), and GR_{max} is the maximum gamma ray reading (shale line). Assuming a linear relation between the gamma ray index and shale volume gives the maximum (most pessimistic) V_{sh} estimate, and should rather be correlated to non-linear published trends for more correct values (Asquith and Krygowski 2004a; Mondol 2015b):

Larionov (older rocks): $V_{sh} = 0.33(2^{2.0*IGR} - 1)$ Eq. 3.2

Clavier (1971): $V_{sh} = 1.7 - [3.38 - (IGR - 0.7)^2]^{1/2}$ Eq. 3.3

Stieber (1970): $V_{sh} = \frac{IGR}{3 - 2*IGR}$ Eq. 3.4

Larionov (Tertiary rocks): $V_{sh} = 0.083(2^{3.7*IGR} - 1)$ Eq. 3.5

An important uncertainty of calculating shale volume is that it heavily relies on a correct interpretation of the sand- and shale line of a well, which changes from well to well or even at different depth levels (Mondol 2015b). These values are chosen by determining a mean minimum value through a clean sandstone section, and a mean maximum value through a shale section (not including organic rich shales with abnormally high gamma readings), which in some of the wells can be challenging to decide.

The shale volume calculated from a combination of neutron and density readings is conducted by identifying a clean line and a shale point in a neutron versus density crossplot (Ellis and Singer 2008). This acts as a second shale indicator to improve confidence instead of solely relying on the gamma ray log interpretation. The formula for calculating shale volume through this method is (as stated in the Interactive Petrophysics Help Manual):

$$VshND = \frac{(DenCl2 - DenCl1)*(Neu - NeuCl1) - (Den - DenCl1)*(NeuCl2 - NeuCl1)}{(DenCl2 - DenCl1)*(NeuSh - NeuCl1) - (DenSh - DenCl1)*(NeuCl2 - NeuCl1)} \quad \text{Eq. 3.6}$$

Where DenCl1, NeuCl1, DenCl2 and NeuCl2 are density and neutron values for each end of the clean line, DenSh and NeuSh are the neutron and density values for the shale point, and Den and Neu are the density and neutron readings at the relevant depth.

From these two shale volume estimates the minimum value is chosen to represent the interval (if the values differ) as any error in any one log tend to increase the apparent shale volume (Crain 2015). E.g. in gas-bearing zones the neutron and density crossover will lead to

incorrect (negative) values, and the gamma ray estimate is preferred (Crain 2015). Figure 3.3 shows an example of shale volume calculated from the gamma ray log through the Larionov older relation and quality controlled by calculating shale volume from neutron-density, in reservoirs of the Tubåen and Snadd Formations.

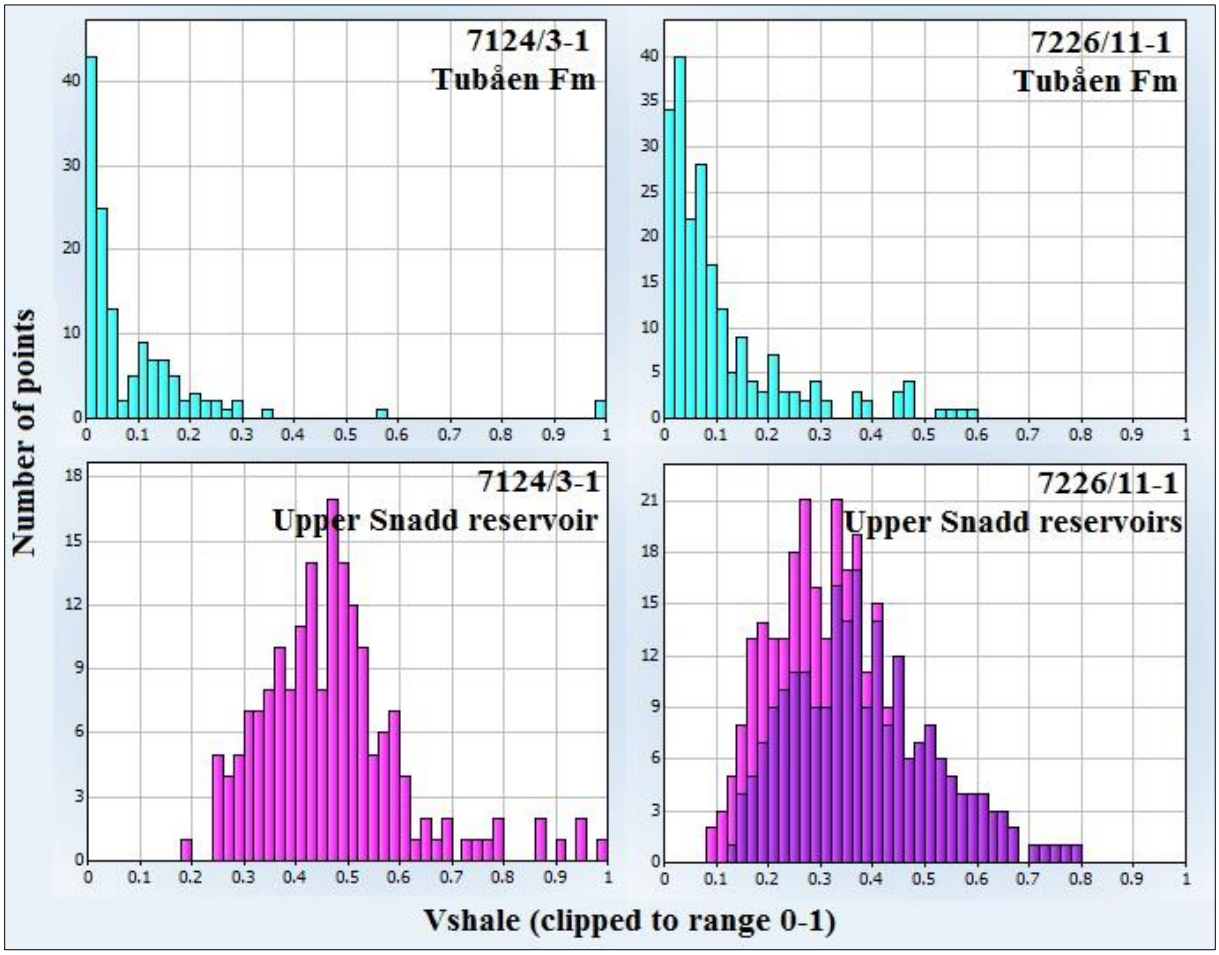

Figure 3.3. Examples of V_{sh} histograms from wells 7124/3-1 and 7226/11-1 showing the shale volume distribution from gamma ray in the reservoirs of the Tubåen and Snadd formations.

3.2.3 Porosity estimation

Four log types generally provide information about porosity:

- Neutron log (NPHI) [fraction or %]
- Density log (RHOB) [g/cm^3 or kg/m^3]
- Nuclear Magnetic Resonance (NMR, not utilized in this study)
- Sonic log (Δt) (acoustic measurement) [μs/ft]

Most porosity logs do not measure porosity directly, but infers a value from basic measurements. Measurements in the neutron, sonic and density logs are all affected by lithology when used individually, but when used in combination the logs can provide lithology information and therefore produce a more accurate porosity evaluation (Asquith and

Krygowski 2004b). When plotting the neutron and the density logs in the same track as curves or in a crossplot, the scale of the neutron log is reversed in relation to the density log, and the value range of both logs must be set to create a compatible scale overlay. A commonly used configuration is to display the logs on a limestone configuration, but a sand or dolomite configuration is also possible, depending on which is assumed to be the dominant lithology. For measurements in the correct water-filled lithology, the density and neutron porosity traces should then overlay each other and the porosity is estimated correctly. In formations of a different lithology or saturation, the neutron porosity will over- or underestimate the true porosity. Shale causes large positive separation between the curves, whereas gas creates a crossover and negative separation between the curves. The ranges for a limestone scheme are 1.95 to 2.95 g/cm^3 for density and 0.45 to -0.15 for neutron, whereas 1.9 to 2.9 g/cm^3 and 0.45 to -0.15 for density and neutron respectively are used for sandstone (Ellis and Singer 2008).

3.2.3.1 Neutron porosity (NPHI)

The neutron log is a measure of formation hydrogen content, giving an estimate of water content and consequently porosity of a rock. It is, however, affected by what is called the shale effect which gives higher porosity estimations in formations with high clay content. The reason for this is that hydrogen is present in clay minerals, and this effect is especially evident in smectite and kaolinite clays. Limestones have low hydrogen content; giving tools used a more accurate estimation of porosity, and the neutron tool is therefore commonly calibrated against limestone. Porosity underestimation occurs when pores are gas filled, as the low density of gas leads to low hydrogen content per volume. This can be advantageous in that the neutron log can be used to identify gas zones, especially when examined in combination with the density log (Asquith and Krygowski 2004b; Mondol 2015b).

3.2.3.2 Density porosity (ϕ_D or DPHI)

The density log displays a measure of bulk density (ρ_b), based on the attenuation of induced gamma radiation (higher energy gamma rays, affected by Compton scattering), which decreases with increasing porosity. The bulk density is a function of both fluid density and matrix density, which is used to estimate porosity from density measurements (Mondol 2015b):

$$\phi_D = \frac{(\rho_{matrix} - \rho_{log})}{(\rho_{matrix} - \rho_{fluid})} \quad \text{Eq. 3.7}$$

Where ϕ_D= computed density porosity, ρ_{matrix} = density of solid phase, ρ_{fluid} = fluid density and ρ_{log} = bulk density at depth of interest. As seen from the equation above, the correct matrix and fluid type must be decided in order to get accurate porosity estimations. Gas presence in the pores of a rock results in overestimation of porosity, which can be used for identifying gas zones when used in combination with the neutron porosity log (Mondol 2015b). The accompanying correction density curve (DRHO) displays the amount of correction that has been applied to the bulk density curve to counteract borehole effects like mudcake thickness. If this log's value is more than 0.20 g/cm^3, the reading of the bulk density may be incorrect (Asquith and Krygowski 2004b).

3.2.3.3 Combined neutron and density porosity

In formations of unknown or varying lithology, combinations of logs are the best way of correctly estimating porosity, circumventing the lithology effects. The technique is most commonly used with the neutron and the density porosity logs, and can be done be comparing the relative relationship of the curves or through crossplotting the values with an overlay consisting of lines representing pure sandstone, limestone and dolomite. In basins dominated by shale and sandstone, it can sensible to reference the scales to sandstone instead of limestone, although both are usable (Asquith and Krygowski 2004b).

Additionally, an average of the two porosity estimates can be calculated for a porosity curve where the lithology effects are negated as opposed to either estimation standing on its own. In a gas filled reservoir, the density porosity yields an overestimation of porosity due to lowered bulk density, and the neutron porosity is underestimated from low hydrogen concentration. This parameter can therefore be used for estimating the so-called true porosity in a gas-bearing formation, and is calculated by the following equation (Asquith and Krygowski 2004b):

$$\phi_{ND} = \sqrt{\frac{\phi_N^2 - \phi_D^2}{2}} \qquad \text{Eq. 3.8}$$

Where ϕ_{ND} is the averaged neutron and density porosity, ϕ_N is neutron porosity and ϕ_D is density porosity. In the Interactive Petrophysics software, more complex equations are designed for calculating porosity. These include many additional parameters and ties porosity to other calculations and constants, which may increase the accuracy of resulting values if utilized correctly. On the other hand, the process is largely automated and interactive, and understanding the different parameters and the correct input is highly challenging and will almost certainly lead to more sources of uncertainty. Comparing values calculated by more traditional methods with values derived in Interactive Petrophysics does not appear to yield large differences, but the confidence in knowing how these values are arrived at has diminished. The equations are, as stated in the Interactive Petrophysics help manual:

$$\phi_N = \frac{\phi_{neu} - Vcl * NeuCl + NeuMatrix + Exfact + NeuSal}{Sxo + (1 - Sxo) * NeuHyHI} \qquad \text{Eq. 3.9}$$

$$\phi_D = \frac{\rho_{ma} - \rho_b - Vcl * (\rho_{ma} - \rho_{cl})}{\rho_{ma} - \rho_{fl} * Sxo - \rho_{HyAp} * (1 - Sxo)} \qquad \text{Eq. 3.10}$$

Where ϕ_{neu} = input neutron log, Vcl = wet clay volume, NeuCl = neutron wet clay value, NeuMatrix = neutron matrix correction, Exfact = neutron excavation factor, NeuSal = neutron formation salinity correction, Sxo = flushed zone water saturation, NeuHyHI = neutron hydrocarbon apparent hydrogen index, ρ_{ma} = matrix density, ρ_b = input bulk density log, ρ_{cl} = wet clay density, ρ_{fl} = filtrate density, and ρ_{HyAp} = apparent hydrocarbon density. An example of a neutron-density crossplot is shown in Figure 3.4.

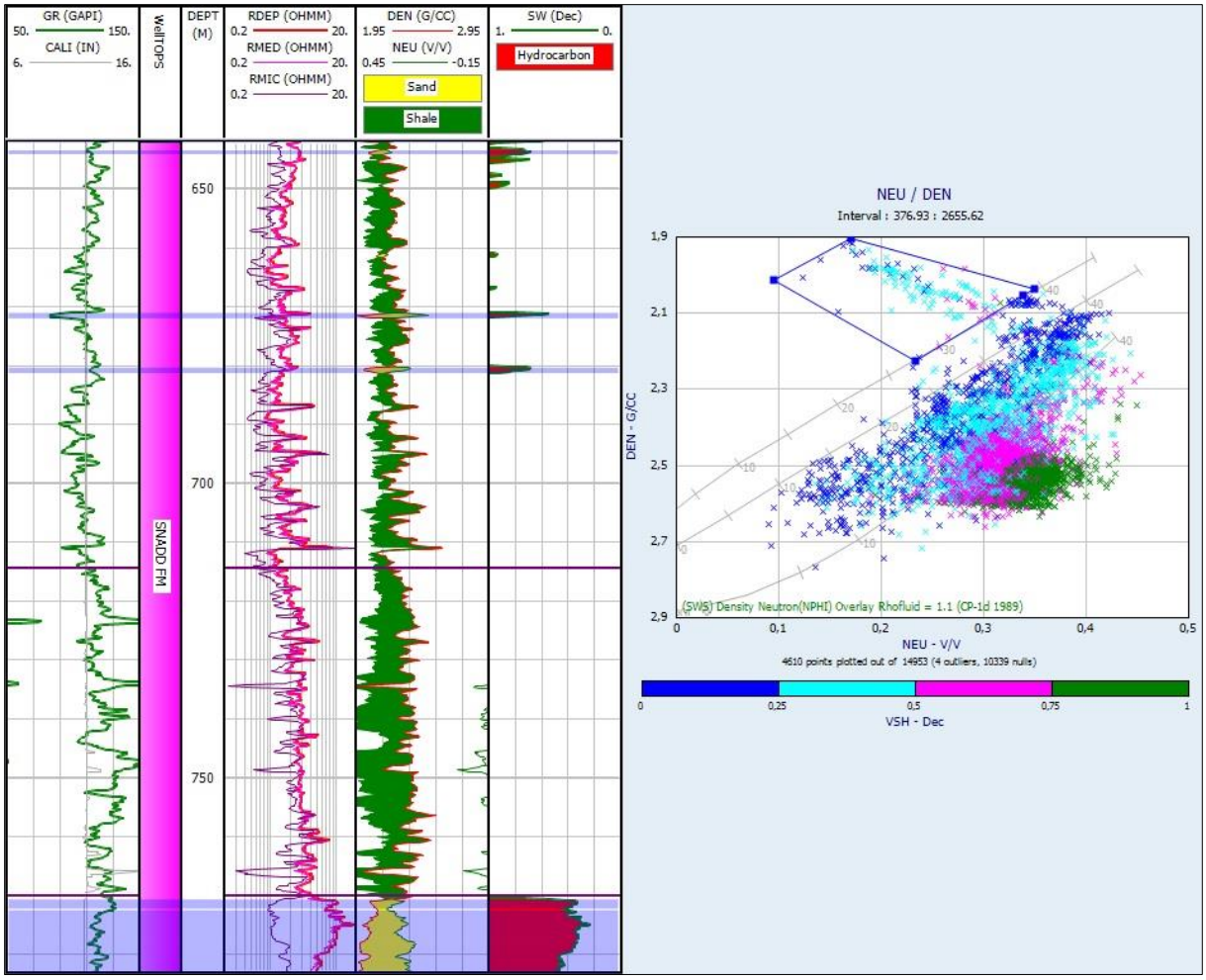

Figure 3.4. Neutron-density crossplot of all reservoir data in well 7222/11-1. Selected area in the crossplot is shown in blue shading in the logs, examplifying the hydrocarbon effect on these log types and thus identification of HC-zones. Shale points drag towards the lower right, displaying high readings of neutron porosity and density.

3.2.3.4 Sonic porosity (ϕ_S or SPHI)

The sonic log measures the slowness of a compressional sound wave which travels through a rock formation, which produces a reading of interval transit time (Δt or DT) in the unit of μs/ft. This parameter is the inverse of velocity, and the log can also be presented as velocity in m/s or km/s. Both lithology and porosity has an influence on the velocity, and correct values for matrix and fluid must be entered into the following equation in order to arrive at an accurate estimation, which is named the Wyllie (1958) time average equation (Asquith and Krygowski 2004b; Mondol 2015b):

$$\phi_S = \frac{\Delta t_{log} - \Delta t_{matrix}}{\Delta t_{fluid} - \Delta t_{matrix}} \qquad \text{Eq. 3.11}$$

Where ϕ_S is the sonic porosity, Δt_{log} is the interval transit time at the depth of interest, Δt_{matrix} is the interval transit time of the matrix, and Δt_{fluid} is the interval transit time in the formation fluid. An alternative equation is the Raymer-Hunt-Gardener equation (1980):

$$\phi_S = \frac{5}{8} * \frac{\Delta t_{log} - \Delta t_{matrix}}{\Delta t_{log}} \quad \text{Eq. 3.12}$$

Standard values used for an estimate of porosity are 55.5 μs/ft (Wyllie equation) and 56 μs/ft (RHG equation) for assumed sandstone matrix and 189 μs/ft for brine as formation fluid.

3.2.3.5 Effective porosity

Effective porosity describes the connected porosity of a rock, and is separated from total porosity in that the water bound in clay minerals which has an effect on previously mentioned estimates (e.g. neutron porosity), is not included (Hook 2003; Ellis and Singer 2008). Theoretically this is represented by the following relation from Hook (2003):

$$\phi_E = \frac{V_{pt} - V_{cbw}}{V_b} \quad \text{Eq. 3.13}$$

Where ϕ_E is effective porosity, V_{pt} is the total pore volume, V_{cbw} is the volume of clay bound water and V_b is the bulk rock volume.

The difference is taken into account by considering the calculated shale volume, and effective porosity can been calculated by the simple relation suggested in the Hampson-Russell software:

$$\phi_E = (1 - V_{sh}) * \phi_T \quad \text{Eq. 3.14}$$

Where ϕ_E is the effective porosity, V_{sh} is the estimated shale volume and ϕ_T is the total porosity, i.e. the average of the neutron porosity and density porosity. Alternatively, in the Interactive Petrophysics software, the wet clay volume is used in most calculations concerning porosity, which relates to the silt fraction and the shale volume as shown in the following equations:

$$V_{sh} = V_{cl} + V_{silt} \quad \text{Eq. 3.15}$$

and

$$V_{silt} = 1 - \frac{\phi_E}{\phi_{max}} - V_{cl} \quad \text{Eq. 3.16}$$

where V_{cl} is the wet clay volume, V_{silt} is the silt volume and ϕ_{max} is the maximum porosity in clean sand.

These relations builds on the assumption that the shale (with maximum average gamma readings) used to calculate shale volume contains the same amount of clay as the shale in zones being evaluated (Ellis and Singer 2008). The clay fraction of shale is assumed to be constant 0.7 for simplicity when using this parameter in e.g. estimation of water saturation, although the possible inaccuracy of this has been discussed in published literature, e.g. Bhuyan and Passey (1994). The same article states that the weight percent clay of average

shale ranges from 0.5-0.7. Figure 3.5 shows the difference between volume components of a rock and relevant porosity expressions.

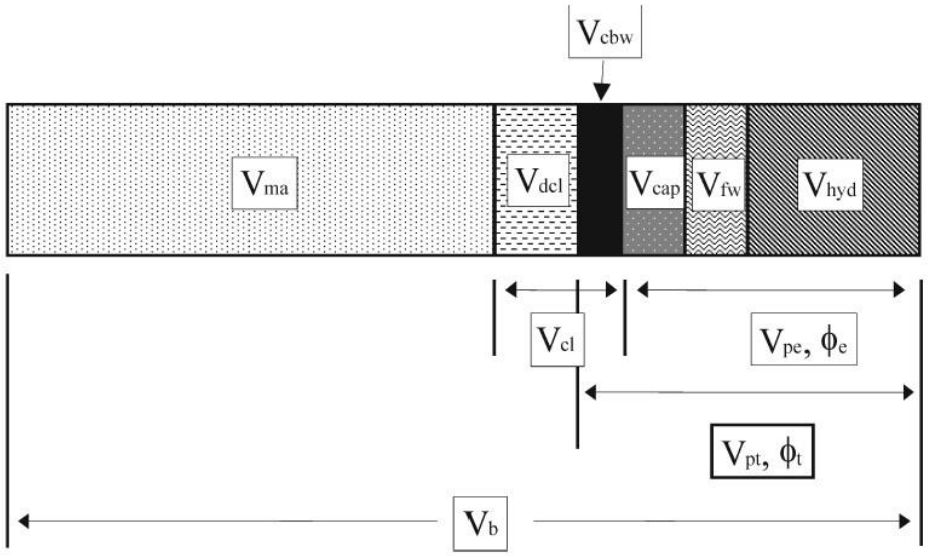

Figure 3.5. Component volumes of a rock as used by log analysts (adapted from Hook 2003). Supscripts: ma=matrix, dcl=dry clay, cl=wet clay, cbw=clay bound water, cap=capillary bound water, fw=free water, hyd=hydrocarbon, b=bulk, p/Φ=porosity, e=effective, t=total.

3.2.4 Water saturation and pay zone identification

For detecting the presence of hydrocarbons and for separating water-bearing and hydrocarbon-bearing zones, the resistivity logs are the most valuable tools. The resistivity logs mainly measure the resistance to flow of electric current in the liquid phase of a formation, as most rocks serve as insulators. Consequently, fluid content, porosity and permeability are all parameters that influence the resistivity readings. Hydrocarbons are very resistive, as opposed to brine which is highly conductive (dependent on salinity). An increase in hydrocarbon saturation will thereby yield an increase in the formation resistivity, which is visible in the deep (possibly medium) resistivity log. For determining water saturation, Archie's law is used to relate this to resistivity readings, intended for use in clean, consolidated sandstones (Asquith and Krygowski 2004c; Mondol 2015b):

$$S_w = \left(\frac{a * R_w}{R_t * \phi^m}\right)^{\frac{1}{n}} \quad \text{Eq. 3.17}$$

Where

- S_w is the calculated water saturation
- a is tortuosity factor (~1 in carbonates)
- m is cementation exponent (usually 1.8-2.0 for sandstone)
- n is saturation exponent (usually ~2)
- R_w is the formation water resistivity
- ϕ is porosity (from neutron-density average in this study)
- R_t is true formation resistivity (from deep resistivity log)

An important value which must be known in this equation is R_w (formation water resistivity). This can in theory either be calculated from the SP log, or, when SP is not present as in this study, be estimated from logs in a water-filled zone. This is done by assuming that in a 100% water filled zone, the bulk resistivity (R_0) is equal to true formation resistivity (R_t), and the formation water resistivity (as derived from a nearby zone) equals (Archie 1942; Ellis and Singer 2008; Petrowiki 2015a):

$$R_{wa} = \frac{R_t}{F} = R_t * \phi^m \qquad \text{Eq. 3.18}$$

When a micro resistivity log is available (like in the newer wells included in this study), this can be used as a measure of R_{xo}, i.e. flushed zone resistivity and subsequently be used to calculate S_{xo} (flushed zone saturation) by approximating a value for mud filtrate resistivity.

Restrictions and limitations apply to use of these equations and calculation of water saturation, e.g. when used in shaley or heterogeneous formations as clay influences the conductivity of a formation and may lead to overestimations of S_w (Ellis and Singer 2008). Temperature and different drilling muds used in the borehole has an effect on resistivity measurements, and assumptions made for the constants a, m, and n, and the formation water resistivity R_w in Archie's equation are influential for saturation calculations and may be sources of error (Mondol 2015b). A temperature gradient must also be estimated for the well (unless it is known), calculated by the following equation (Mondol 2015b):

$$G = \left(\frac{BHT - Tms}{TD}\right) x\ 100 \qquad \text{Eq. 3.19}$$

Where G is the temperature gradient in $^oC/100m$, BHT is bottom hole temperature (^oC), Tms is mean surface temperature (usually taken as 4 ^oC at sea floor), and TD is total depth, in this case meters below sea floor (mBSF).

3.2.5 Permeability estimation

Permeability, or the ability of a rock to transmit fluids, is an important characteristic of a reservoir, but is difficult to derive from well logs as only approximate relations exist to porosity. There are multiple equations that try to model permeability from porosity alone, or from porosity and irreducible water saturation. The Kozeny-Carmen equation is frequently mentioned, but requires knowledge about grain size and grain shape, which is not acquired through well log analysis alone (Kennedy 2015). Examples of other relations that exist which only consider porosity and irreducible water saturation (or porosity alone) are (Crain 2015; Petrowiki 2015b):

$$k = \frac{10^4 \phi_e^{4.5}}{S_w^2} \quad \ldots\ldots\ldots\ldots\ldots\ldots\ldots\ldots\ldots\ldots\ldots \text{Timur equation} \qquad \text{Eq. 3.20}$$

$$\log_{10} k = C \log_{10} \phi_e + D \quad \ldots\ldots\ldots \text{Logarithmic} - \text{linear for sandstones} \qquad \text{Eq. 3.21}$$

$$k = \frac{3400 * \phi_e^{4.4}}{S_w^2} \quad \ldots\ldots\ldots \text{Wylie} - \text{Rose formula (Timur parameters)} \qquad \text{Eq. 3.22}$$

$$k = \frac{62500 * \phi_e^{6}}{S_w^2} \quad \ldots\ldots. \text{Wylie} - \text{Rose formula (Morris} - \text{Biggs parameters)} \qquad \text{Eq. 3.23}$$

where k is calculated permeability, ϕ_e is effective porosity, C and D are approximate constants often equal to ~7 (Petrowiki 2015b), and S_w is irreducible water saturation which is estimated by the water saturation values in a hydrocarbon reservoir (excluding the possibility of doing calculations in water-bearing reservoirs). The general idea is that permeability is expected to increase with porosity and decrease with saturation of irreducible water (Kennedy 2015). Constants stated in these equations are by no means designed to fit this particular study area.

3.3 Rock physics diagnostics

Rock physics involves connecting geophysical measurements (elastic properties) to geological parameters and processes, and is an important part of understanding the characteristics of a reservoir and being able to quantitatively evaluate reservoirs. Examples of such geophysical parameters are acoustic impedance, P-wave to S-wave velocity ratio (V_p/V_s), bulk density and elastic moduli, which in turn can be linked to e.g. porosity, clay content, lithology, sorting and water saturation (Avseth et al. 2010). Rock physics diagnostics is commonly conducted through crossplots, where observed elastic parameters are plotted against a geological parameter and compared to published rock physics models (Avseth 2015). Color coding by a third parameter enables correlation to yet an additional measurement or calculated value (Figure 3.6).

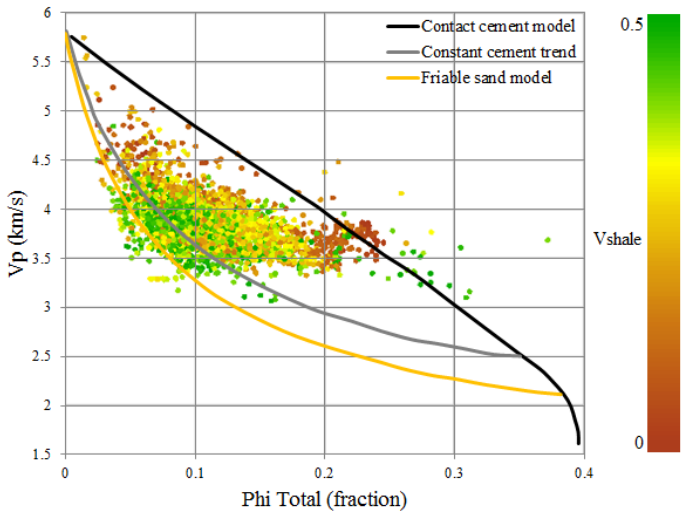

Figure 3.6. Crossplot of V_p versus porosity with data from all Kobbe Formation reservoirs across all wells. Note additional information provided by the shale volume color code.

3.3.1 Rock physics cement models

The microstructure (texture) related to cementation of a rock has an effect on the stiffness of the rock, and consequently also on velocity. The correlation between velocity and porosity is therefore not only a function of porosity and mineralogy, but can also drastically change with the disposition of the solid components at pore scale (Avseth et al. 2000). Three theoretical models are used to describe the difference between the trends of velocity-porosity in reservoir sands, namely the contact cement model, the constant cement model, and the friable sand

model (Figure 3.7). These diagnostic models can be used to infer microstructure by plotting data of velocity (or other elastic moduli) and porosity against each other and compare with velocity-porosity relations (Avseth et al. 2005; Avseth et al. 2010). When wanting to predict effective elastic moduli of a mix of grains and pores, three factors must be specified: the volume fraction of each constituent, the elastic moduli of various phases, and geometrical relations between the phases. When not specifying the geometrical relations, upper and lower theoretical bounds constrain the possibly moduli the medium can have, as the geometric details (stiff or soft pores) would determine the actual specific value. For an isotropic linear elastic medium, Hashin-Shtrikman bounds (Figure 3.8) are described as the best (Mavko et al. 2009).

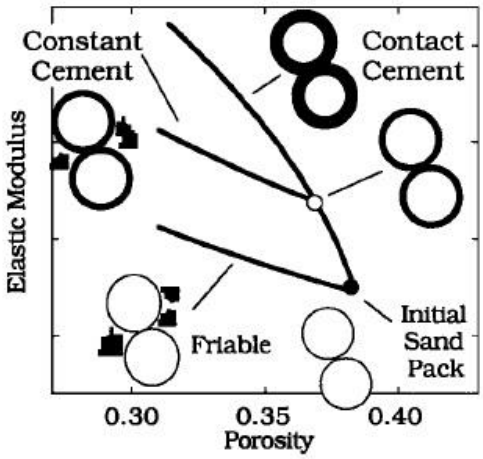

Figure 3.7. Cement models for high-porosity sands shown by elastic modus (V_p, V_s) versus porosity (Avseth et al. 2000).

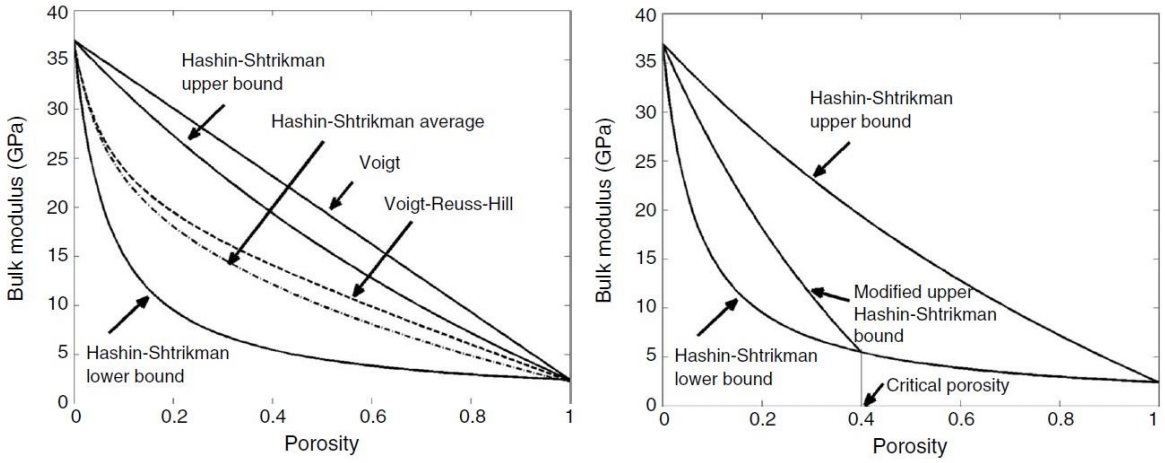

Figure 3.8. Left: Hashin-Shtrickman bounds compared to Voigt-Reuss-Hill bounds. Right: Hashin-Shtrickman bounds modified to critical porosity. Both plots represent bulk modulus in a quartz-water system (Avseth et al. 2010).

The friable-sand model, also denoted the unconsolidated line, describes change in the porosity-velocity relation as a function of deteriorating sorting. The two end members are on one side a well sorted packing of similar grains with critical porosity of typically 0.4, and on the other side a zero porosity point (i.e. moduli of the mineral). Critical porosity is the porosity at which the transition from fluid-suspended to load-bearing sediment occurs (Mavko et al. 2009). For the high-porosity limit, elastic-contact theory is used to determine the elastic properties by using Hertz-Mindlin equations for dry conditions (Eq. 3.32 and 3.33). Poorer sorting is represented by adding smaller grains in between the well sorted starting point, leading to decreased porosity and slightly increased stiffness. The line between the points is interpolated through the use of the modified Hashin-Shtrikman lower bound (Eq. 3.35 or 3.36) (Avseth et al. 2010), by firstly calculating the change in dry bulk modulus (K) or shear modulus (μ) for decreasing porosity at a certain stress level (or depth) and secondly using Gassmann fluid substitution (Eq. 3.44) to predict the behavior of water-saturated rock.

The contact cement model represents uniform cementation layers progressively depositing on grains during burial, reinforcing the stiffness of the sand due to stronger grain contacts. This yields a high increase in velocity with a small decrease in porosity from the initial state due to diagenetic quartz or clay minerals. The main limitation of this model is that it does not allow for pressure sensitivity after the cementation process begins, because of the assumption of uniform cementation (i.e. not allowing for patchy cementation) (Dvorkin and Nur 1996; Avseth et al. 2010). This model represents initial stage of cementation in high porosity sands, and more cemented sandstones should be modeled by the modified Hashin-Shtrikman upper bound instead.

The constant cement model is in theory a combination of the friable sand model and the contact cement model, and assumes that decreasing porosity is a result of deteriorating sorting, but sands of various sorting all have equal amounts of contact cement. This is often correct when assessing a constrained reservoir, as cement variations are mainly related to depth. Multiple lines can be drawn of this model to represent varying percentages of cement and considered to be "constant-depth" lines (Avseth et al. 2005).

Marcussen et al. (2010) derived a linear relation between V_p and quartz cement from well log data which shows good correlation for the Etive Formation in the northern North Sea. Cement volume (%) can be estimated from the equation (derived from digitized data):

$$\text{Cement volume} = \frac{\text{Vp} - 2775}{84.825} \qquad \text{Eq. 3.24}$$

3.3.2 V_s prediction

As only the four newer wells (7222/6-1, 7222/11-1, 7223/5-1 and 7224/6-1) in this study have shear wave velocity (V_s), an estimate of this parameter must be computed in order to perform e.g. rock physics diagnostics, Gassmann fluid substitution, and to make use of the V_p/V_s ratio. Equations used to predict V_s from P-wave velocity (V_p) are numerous, many of them discussed in Dvorkin (2008), V_p and V_s in listed equations are given in km/s.:

- Castagna et al. (1993):
  $V_s = 0.804V_p - 0.856$ (Clastic rocks)
- Castagna et al. (1985):
  $V_p = 1.16V_s + 1.36$ (Mudrock line), equal to $V_s = 0.862V_p - 1.172$
- Han (1986):
  $V_s = 0.794V_p - 0.787$
- Mavko et al. (1998), based on data from Han (1986) and high porosity unconsolidated sands:
  $V_s = 0.754V_p - 0.657$ (Rocks with clay content <0.25)
  $V_s = 0.842V_p - 1.099$ (Rocks with clay content >0.25)
  $V_s = 0.853V_p - 1.137$ (Porosity <0.15)
  $V_s = 0.756V_p - 0.662$ (Porosity >0.15)
- Williams (1990):
  $V_s = 0.846V_p - 1.088$ (Water-bearing sands)
  $V_s = 0.784V_p - 0.893$ (Shales)

Also, directly from respective sources:

- Greenberg and Castagna (1992):
  $V_s = 0.80416V_p - 0.85588$ (Sandstone)
  $V_s = -0.05508V_p^2 + 1.01677V_p - 1.03049$ (Limestone)
  $V_s = 0.58321V_p - 0.07775$ (Dolomite)
  $V_s = 0.76969V_p - 0.86735$ (Shale)
- Krief et al. (1990):
  $V_p^2 = 2.213V_s^2 + 3.857$ (Water-bearing sandstone)
  $V_p^2 = 2.282V_s^2 + 0.902$ (Gas-bearing sandstone)
  $V_p^2 = 2.033V_s^2 + 4.894$ (Shaley sandstone)
  $V_p^2 = 2.872V_s^2 + 2.755$ (Limestone)

By comparing all data from the four studied wells that have both P- and S-wave velocity measurements, a linear regression line that indicates the relationship between the parameters can be created. V_p and V_s data with Castagna's mudrock line and Han's equation included for comparison is shown in Figure 3.9. This yields a locally derived V_p-V_s relation ($V_s = 0.712V_p - 0.663$, represented by the black line) that can be used to estimate V_s from V_p in the four wells lacking V_s measurements. Other published empirical relations have been included in Figure 3.10 to show the discrepancy between data from this area and the different equations. The data points in this study appear to plot higher than the published lines, with the shale lines of Williams (1990) and Greenberg and Castagna (1992) being the seemingly closest fits. A wide spread of the data around the lines indicates the difficulty of adequately capturing all variations in the V_p-V_s relationship with a simple linear approximation. Areas of high V_p and V_s values is particularly poorly captured by the published relations.

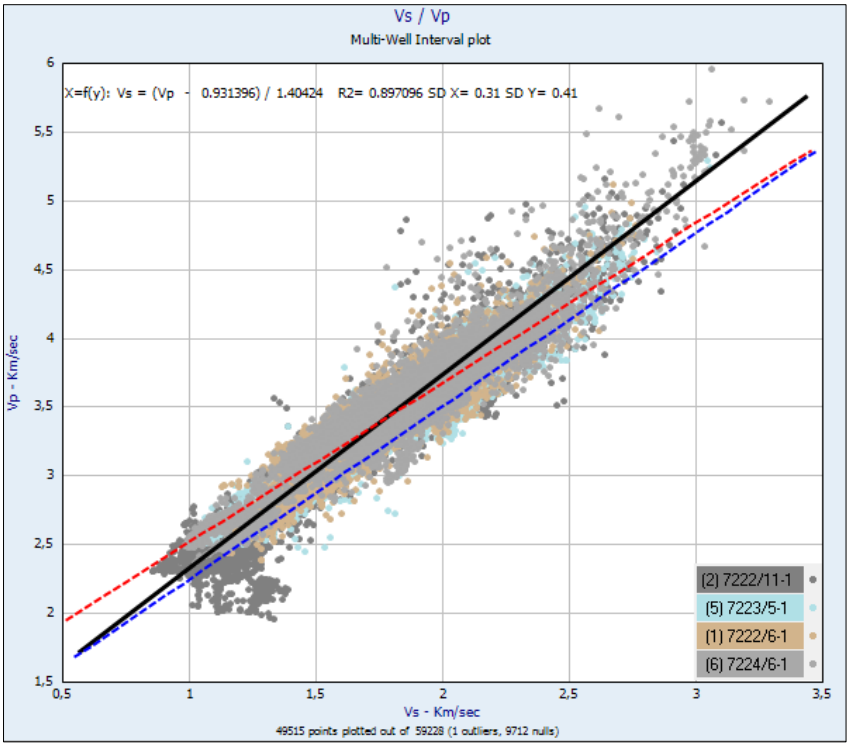

Figure 3.9. Crossplot of V_p versus V_s data from wells 7222/6-1, 7222/11-1, 7223/5-1 and 7224/6-1. Castagna (1985) mudrock line (red) and Han's (1986) line (blue) included for comparison.

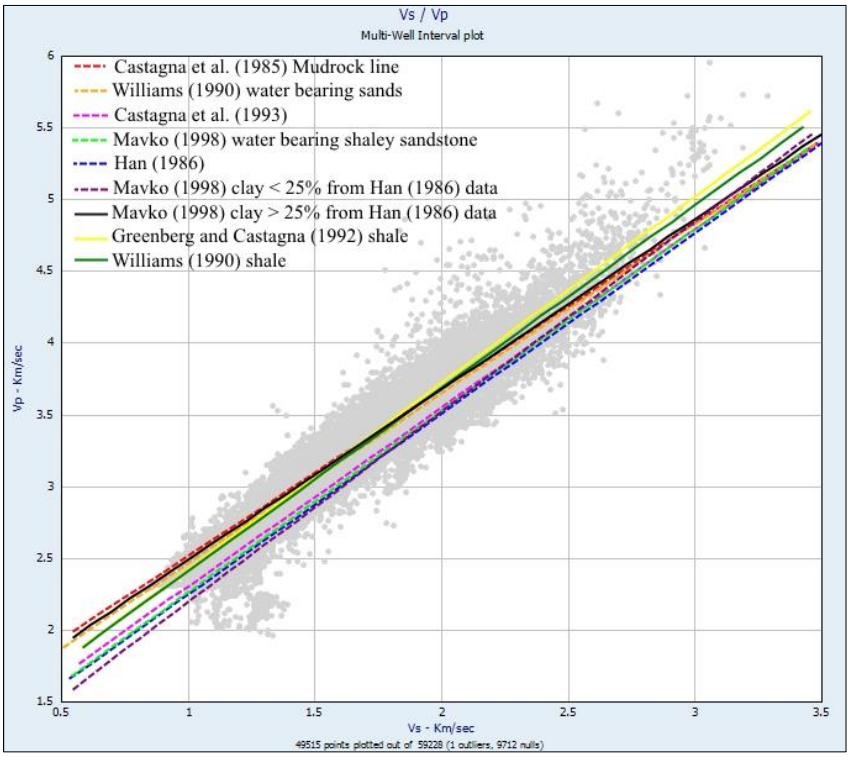

Figure 3.10. Crossplot of V_p versus V_s data from wells 7222/6-1, 7222/11-1, 7223/5-1 and 7224/6-1 compared to published empirical relations estimating V_s from measured V_p.

3.3.3 Calculation of elastic parameters

Under the assumption of an isotropic, linear elastic material, two elastic constants known as the Lamé's parameters are required to describe relation between stress and strain. The parameters are μ (shear modulus) and λ (pure incompressibility). λ = K - 2μ/3, where K is the bulk modulus (a material's resistance to volume change). These moduli are related to V_p and V_s through the following equations, where ρ is the bulk density of the rock (Avseth 2015):

$$V_p = \sqrt{\frac{K+4\mu/3}{\rho}} \quad \text{Eq. 3.25}$$

$$V_s = \sqrt{\frac{\mu}{\rho}} \quad \text{Eq. 3.26}$$

$$\rho = \phi\rho_{fluid} + (1-\phi)\rho_{mineral} \quad \text{Eq. 3.27}$$

Rearranged for calculation of K and μ (Gelius and Johansen 2010):

$$K = \rho(V_p^2 - \frac{4}{3}V_s^2) \quad \text{Eq. 3.28}$$

$$\mu = \rho V_s^2 \quad \text{Eq. 3.29}$$

Poisson's ratio (ν, relation between transverse contraction to longitudal extension in stretching of a material) can be related to the V_p/V_s ratio and calculated on the form (Gelius and Johansen 2010):

$$\nu = \frac{0.5(V_p/V_s)^2 - 1}{(V_p/V_s)^2 - 1} \quad \text{Eq. 3.30}$$

Alternatively, when expressed in terms of K and μ (Avseth et al. 2005):

$$\nu = \frac{3K-2\mu}{2(3K+\mu)} \quad \text{Eq. 3.31}$$

The aforementioned Hertz-Mindlin equations for calculating bulk (K_{HM}) and shear (μ_{HM}) moduli of the dry, well-sorted end member when computing cement models are (Avseth et al. 2005):

$$K_{HM} = \left[\frac{n^2(1-\phi_c)^2\mu^2}{18\pi^2(1-\nu)^2}P\right]^{1/3} \quad \text{Eq. 3.32}$$

$$\mu_{HM} = \frac{5-4\nu}{5(2-\nu)}\left[\frac{3n^2(1-\phi_c)^2\mu^2}{2\pi^2(1-\nu)^2}P\right]^{1/3} \quad \text{Eq. 3.33}$$

where ϕ_c is critical porosity, μ and ν are the shear modulus and Poisson's ratio of the solid phase (often assumed as pure quartz when modeling sandstone), P is effective pressure in GPa, and n is the coordination number which is approximated as follows (Avseth et al. 2005):

$$n = 20 - 34\phi + 14\phi^2 \quad \text{Eq. 3.34}$$

Interpolation between the high-porosity member and the mineral point is calculated by using equations for Hashin-Shtrikman bounds. The lower bound is used when modeling the friable sand model, which is the only model manually computed in this study (Avseth et al. 2005):

$$K_{dry} = \left[\frac{\phi/\phi_c}{K_{HM}+4\mu_{HM}/3} + \frac{1-\phi/\phi_c}{K+4\mu_{HM}/3}\right]^{-1} - \frac{4}{3}\mu_{HM} \quad \text{Eq. 3.35}$$

$$\mu_{dry} = \left[\frac{\phi/\phi_c}{\mu_{HM}+z} + \frac{1-\phi/\phi_c}{\mu+z}\right]^{-1} - z \quad \text{Eq. 3.36}$$

where

$$z = \frac{\mu_{HM}}{6}\left(\frac{9K_{HM}+8\mu_{HM}}{K_{HM}+2\mu_{HM}}\right) \quad \text{Eq. 3.37}$$

Here, K_{dry} and μ_{dry} are moduli of the dry friable sand mix, and K and μ are the mineral bulk and shear moduli. Finally, Gassmann fluid substitution is used to calculate the corresponding moduli for fluid saturated rock (Eq. 3.42 and 3.44). From the saturated moduli, calculated models can be combined with density and transformed to velocity as shown above in this subchapter.

3.3.4 Construction of rock physics templates (RPTs)

Rock physics templates are ideally local specific background trends displaying rock physics models, and are used for predicting lithology, depositional trends and compaction trends as previously discussed in chapter 3.3.1 (cement models). Commonly used RPTs are described in the following sub-chapters. The general process of generating rock physics models is shown in Figure 3.11, i.e. the combination of Hertz-Mindlin theory, modified Hashin-Shtrikman bounds (upper or lower, depending on cement model) and Gassmann fluid substitution. Moduli values can subsequently be converted to velocity through the equations described above.

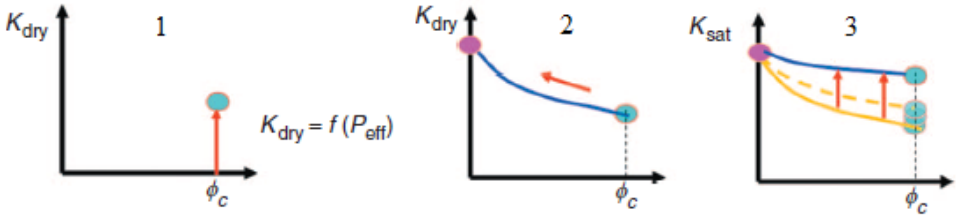

Figure 3.11. The process of generating rock physics models, example for sandstones (modified from Avseth et al. 2010).

The construction of, or use of, following rock physics templates (that are not digitized) are based on published values of moduli, density and velocities of minerals as shown in Table 3.2:

Table 3.2: Mineral moduli, velocities, density and Poisson's ratio. Modified from Mavko et al. (2009).

Mineral	V_p (km/s)	V_s (km/s)	K - bulk modulus (GPa)	μ - shear modulus (GPa)	Density (g/cm3)	Poisson's ratio
Quartz (Carmichael 1989)	6.05	4.09	37.0	44.0	2.65	0.08
Quartz with clay (Han 1986)	5.59	3.52	39.0	33.0	2.65	0.17
Clay (Tosaya 1982)	3.81	1.88	21.0	7.0	2.6	0.35

Caution must be taken especially when utilizing generalized values for clay minerals, as different compositions of clay can have largely varying properties and there exists no set value (Avseth et al. 2005).

3.3.4.1 Porosity/density versus V_p/V_s/IP/K/μ

Plotting porosity estimations against elastic parameters, such as V_p, V_s, acoustic impedance, bulk modulus (K) or shear modulus (μ), can give information about sorting and cementation of a reservoir rock. Velocity-porosity trends are used to interpret microstructure of a rock, i.e. as described under cement models above. Han (1986) introduced the following equations to describe the influence of clay on velocity-porosity trends for shaley sandstones at confining pressure of 40 MPa and pore pressure 1 MPA, with consideration of clay content C ($0 < C < 0.5$):

$$V_p = 5.59 - 6.93\phi - 2.18C \quad \text{Eq. 3.38}$$

$$V_s = 3.52 - 4.91\phi - 1.89C \quad \text{Eq. 3.39}$$

Similar equations with slightly different coefficients are also derived for lower confining pressures, giving the possibility to correlate more closely to reservoirs at variable depth levels. Figure 3.12 shows a plot of V_p versus total porosity with empirical relations from Han (1986) superimposed as lines divided into clay fractions, and corresponding data from this study. The data includes all reservoir intervals in the four formations investigated across eight wells where shale volume is estimated to be below 50%.

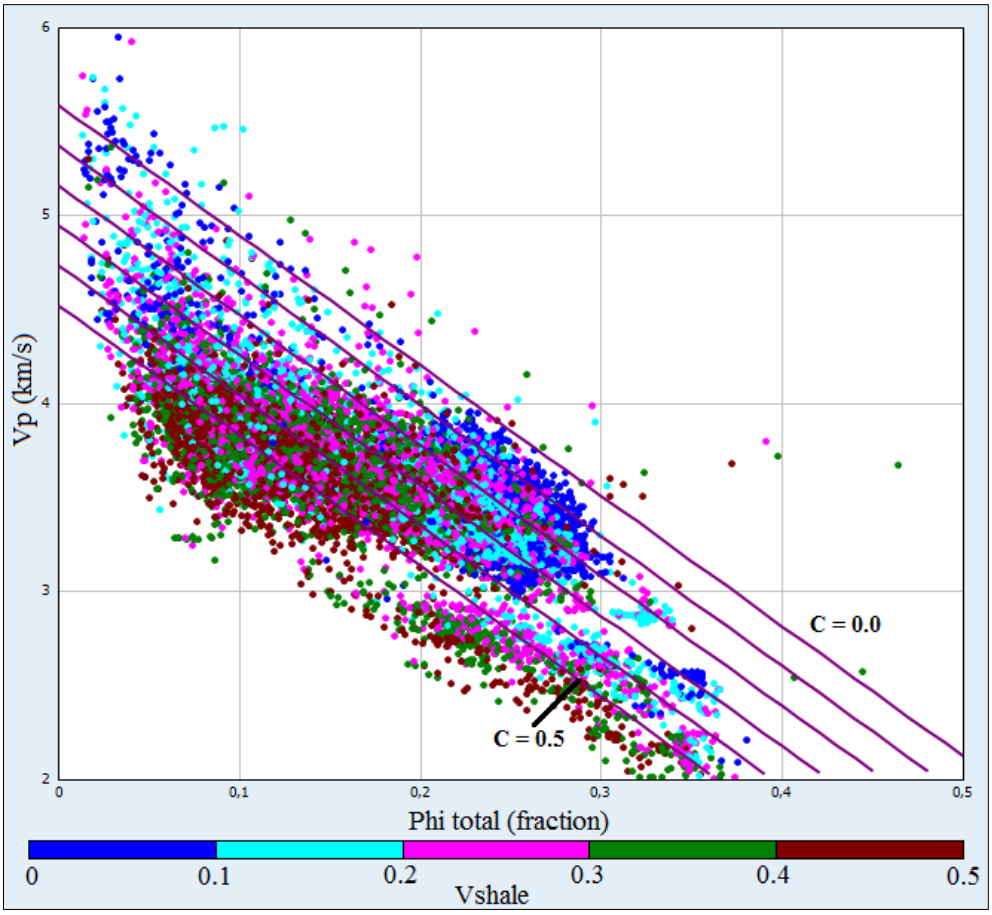

Figure 3.12. Crossplot of V_p versus total porosity, with equations from Han (1986) superimposed showing V_p calculated as a function of porosity and clay content.

Templates for rock physics cement models in the V_p-porosity domain (Figure 3.6) are digitzed from Avseth et al. (2005), and templates for V_s-porosity are retrieved from Avseth et al. (2010).

Plots of shear modulus (μ) versus density or porosity (Figure 3.13) are described in e.g. Storvoll and Brevik (2008) and Baig et al. (2016) as a suitable domain for identifying the transition from mechanical to chemical compaction by identifying a bend or knee-point in the data trend.

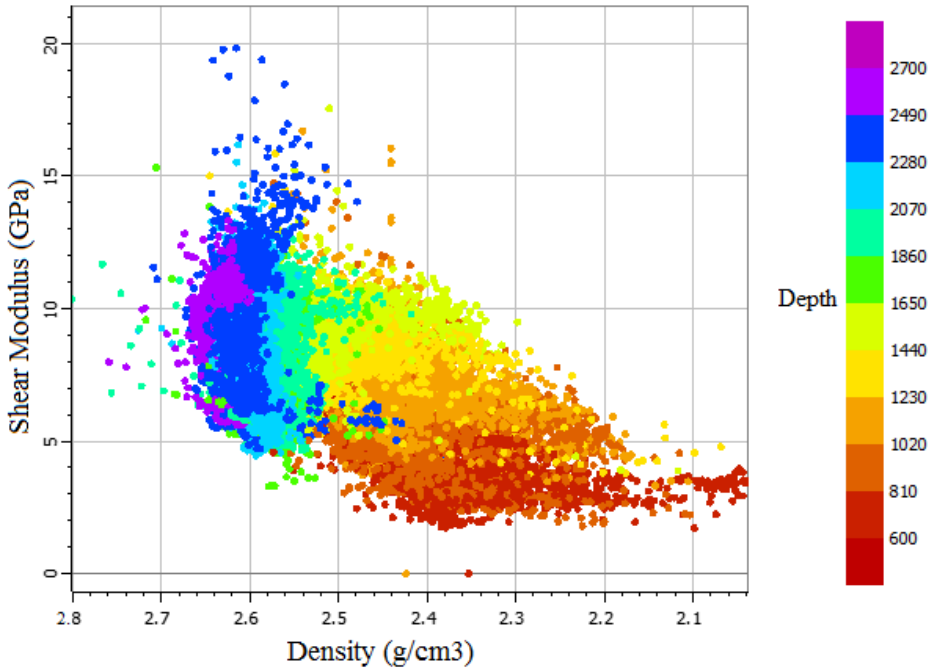

Figure 3.13. Crossplot of shear modulus versus density, with data from all wells with measured V_s (7222/11-1, 7222/6-1, 7223/5-1 and 7224/6-1). Only data that include mainly shale is plotted.

3.3.4.2 V_p versus V_s

Published equations for V_p-V_s relationships are numerous, and many of them are mentioned previously in this chapter. When plotting P-wave velocity versus S-wave velocity, one or multiple of these relations can be used as background trends for the plot, chosen adequately to lithologies expected to be present. E.g. when plotting data from what is assumed to be clean sandstone, equations that describe brine-filled and/or gas-filled sandstone trends should be used as the template. Data that deviates from the assumed trends consequently represents anomalies from the template, and can contain information about the fluid content or lithology differences. When plotting larger, heterogeneous intervals of a log, it may be sensible to include more than one trend in order to capture more of the relation between sandy and shaley intervals. Figure 3.14 shows crossplots of V_p versus V_s in the four wells with measured S-wave velocity, restricted by estimated shale volume less than 50%. Color coding to saturation gives an impression of the separation that occurs between water-saturated and hydrocarbon-influenced intervals, with the red and blue line being inferred from only water-sands and only hydrocarbon-saturated sands. Separation between the two would very hard to observe with certainty if saturation was not already estimated by petrophysical analysis. Well 7222/11-1 displays slightly better discrimination of a hydrocarbon-filled reservoir in the upper part of the Snadd Formation. This plot is not useable in wells where V_s is estimated from V_p, as they would plot in a linear manner.

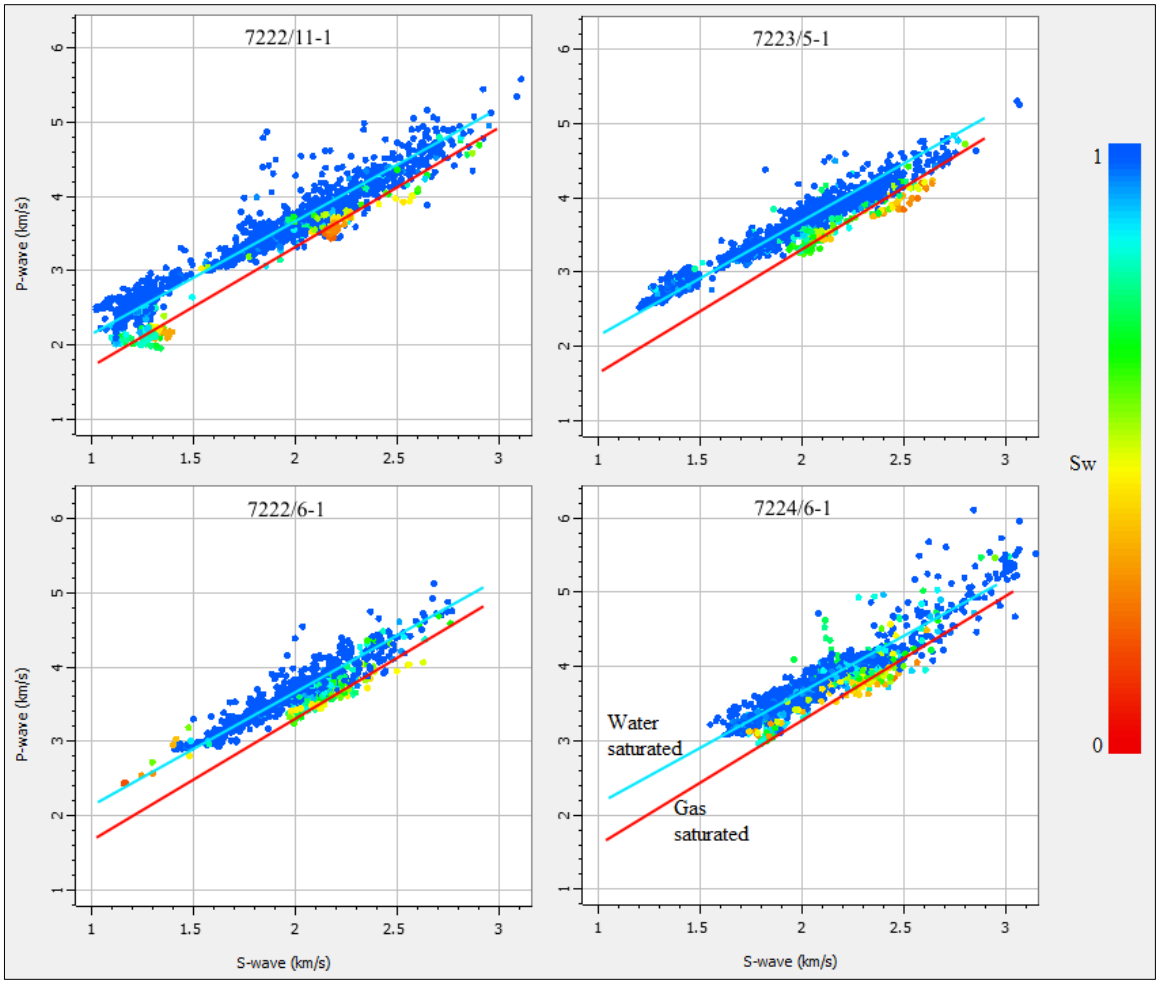

Figure 3.14. V_p versus V_s with all reservoir data from wells with measured V_s showing effect of hydrocarbon saturation. Guiding water and hydrocarbon lines are inferred from data from all four wells for easier comparison of the separation. Note poorer separation in deep reservoirs (i.e. in areas of high V_p and V_s).

3.3.4.3 V_p/V_s versus AI

Plotting the V_p/V_s ratio versus acoustic impedance (denoted IP or AI) can be used to discriminate oil- or gas bearing sands from brine-filled sands as well as describing lithology and porosity. The separation is largest in unconsolidated, homogeneous sands, and the fluid sensitivity decrease with increasing cementation which may lower the V_p/V_s ratio of a brine sand to make it similar to oil-bearing unconsolidated sands. Low net-to-gross ratio will potentially move oil-sands to an area of higher V_p/V_s, mimicking brine sands (Avseth 2015). This concept was first introduced by Ødegaard and Avseth (2004).

The brine sand line, gas sand line and shale line (assumed simplistically as 100% clay) are modeled using standard values for elastic properties and densities as stated in Table 3.2 to create the rock physics template used in this study. The Hampson-Russell software was used to create the models. Depending on which effective pressure is chosen in the modeling, the templates look slightly different. An RPT of V_p/V_s versus AI with conceptual geologic trends indicated by arrows is shown in Figure 3.15.

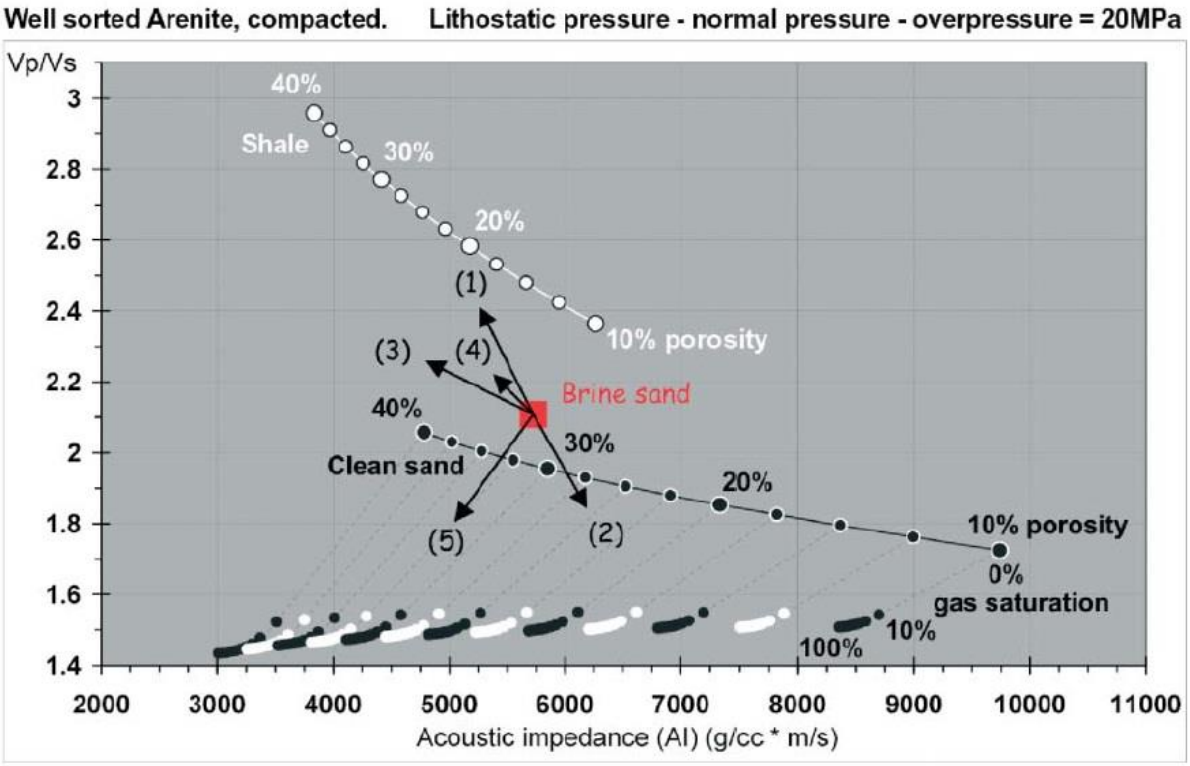

Figure 3.15. An example of a rock physics template of V_p/V_s versus AI, arrows indicating: (1): Increasing shaliness, (2): Increasing cement volume, (3): Increasing porosity, (4): Decreasing effective pressure and (5): Increasing gas saturation (adapted from Ødegaard and Avseth 2004).

Models used in this study are shown in Figure 3.16, which shows also the difference in values for pressure used in the generation of the template. The 20 MPa model appears to capture the boundary between water saturated and hydrocarbon influenced data points, if comparing with the color coding of water saturation.

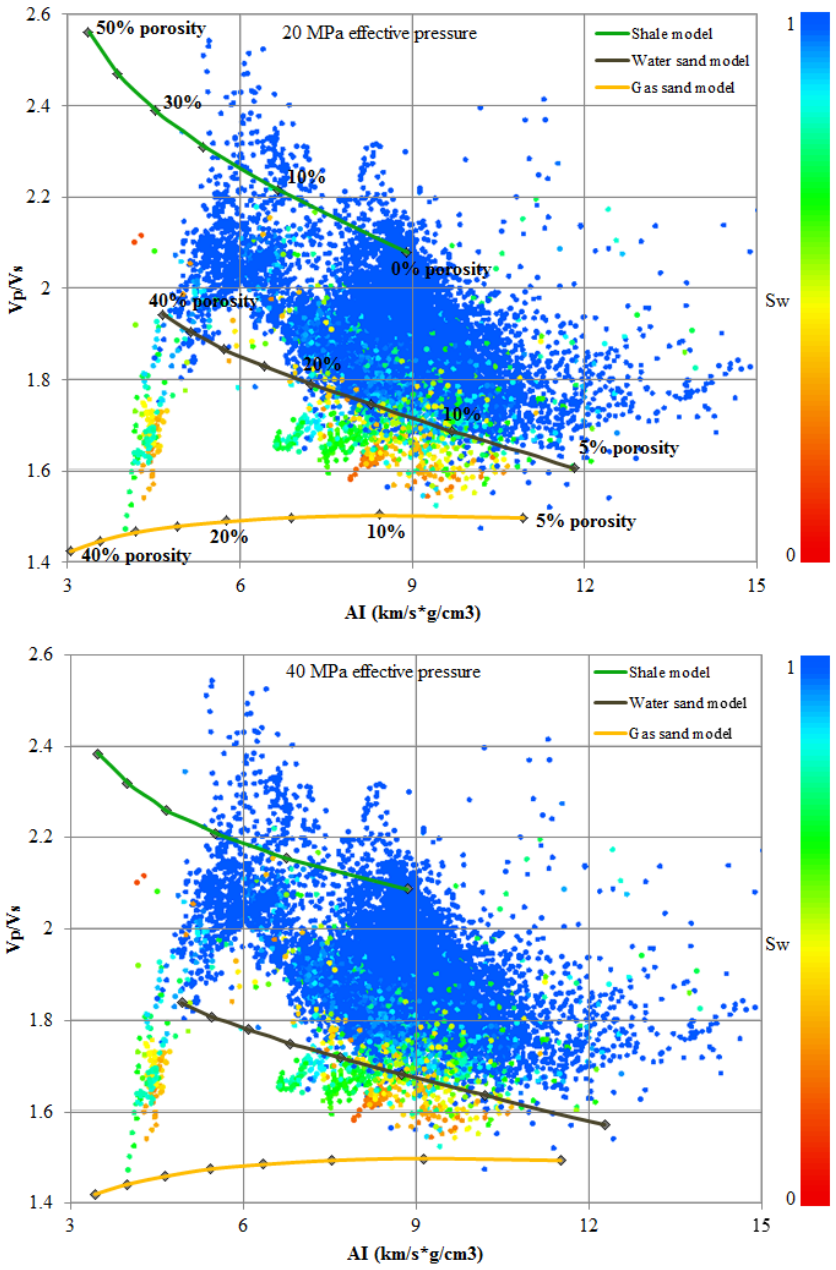

Figure 3.16. RPTs of V_p/V_s versus AI modelled at 20MPa and 40MPa effective pressure. All reservoir data from the four wells with measured V_s are shown (7222/11-1, 7222/6-1, 7223/5-1 and 7224/6-1). Colored by water saturation.

3.3.4.4 λρ versus μρ

Lambda-Mu-Rho (LMR) crossplots are based on the Lamé parameters of rigidity (μ) and pure incompressibility (λ). Along with density (ρ) they are related to velocities V_p and V_s through impedance, as shown in the equations (Goodway 2001):

$$\lambda\rho = Ip^2 - 2Is^2 \qquad \text{Eq. 3.40}$$

$$\mu\rho = Is^2 \qquad \text{Eq. 3.41}$$

where Ip is the P-impedance ($\rho*V_p$), Is is the S-impedance ($\rho*V_s$), and $\lambda\rho$ and $\mu\rho$ is LambdaRho and MuRho respectively (the Lamé impedances). A rock physics template built on this model (Figure 3.17) is meant to give an enhanced sensitivity to pore fluids and thereby be able to improve reservoir identification and lithology discrimination independent on fluid effects (Goodway 2001). All data from reservoirs with measured shear wave velocity is shown in Figure 3.18 together with the threshold for porous gas sand as seen in Figure 3.17. Data is colored by shale volume in the left plot and water saturation in the right plot.

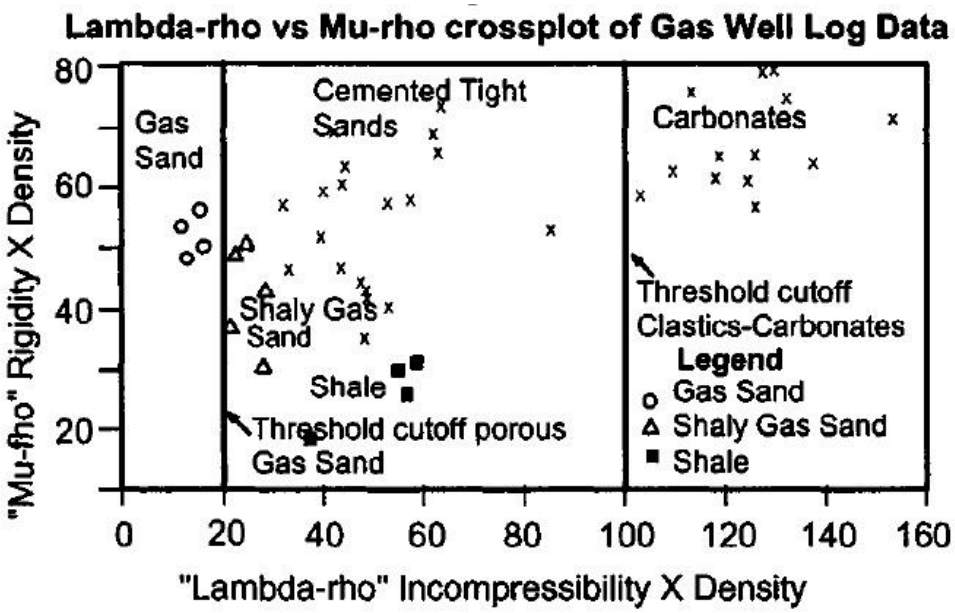

Figure 3.17. LambdaRho versus MuRho crossplot of Gas Well Log Data (adapted from Goodway et al. 1997).

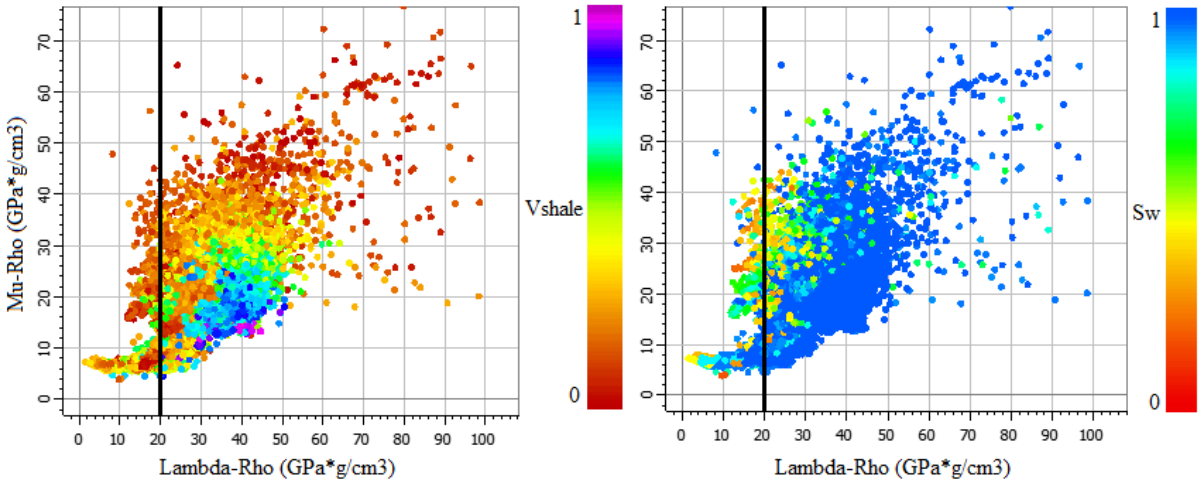

Figure 3.18. LMR crossplot of all data in reservoirs from wells with measured V_s (7222/6-1, 7222/11-1, 7223/5-1 and 7224/6-1). Note data points estimated to describe hydrocarbon-saturated intervals plot on both sides of the gas sand threshold.

3.4 AVO modeling

AVO (Amplitude Variation with Offset – or AVA, Amplitude Variation with Angle) is originally based on variation in the reflectivity of gas sands overlain by shales with different offset in pre-stack seismic data (Avseth 2015). The technique has been used as a direct hydrocarbon indicator, but suffers in that respect to ambiguities and pitfalls related to rock properties and the acquisition and processing of seismic data. More modern uses of AVO are aimed at attempting to describe differences in lithology and fluid above and below a reflector, as well as identifying and classifying gas sands that do not appear as typical "bright spots". AVO modeling is a tool to link rock properties to offset-dependent amplitude responses which involves the creation of synthetic seismic CMP-gathers from well log data, and subsequent analysis of these (Li et al. 2007). Synthetics can be created from in-situ well log data or from logs created by using Gassmann fluid substitution techniques to represent pre-defined fluid contents for reference. If available, results of this process should ideally be used as a validation tool to be compared to real pre-stack seismic data of the same location as they provide independent information (Li et al. 2007; Chopra and Castagna 2014).

3.4.1 Gassmann fluid substitution

Sensitivity to fluids in seismic is a function of porosity and stiffness of pores, where a stiffer rock is less sensitive to fluids at equal porosities (Avseth 2015). The Gassmann theory aims to describe the effective elastic properties of a porous rock with a given pore fluid, from knowing the bulk modulus of the solid constituent, the frame bulk modulus (dry, porous rock) and the bulk modulus of the fluid in the pores. It is limited by certain assumptions, namely that all pores are connected, that all grains have the same physical properties, that the pore fluid is homogeneous and fully saturates the pore volume, and that the wavelength is much larger than the maximum size of pores and grains. When considering more than one solid constituent, effective medium modeling can be used to represent a single effective solid (Gelius and Johansen 2010). Seeing as open (connected) porosity is assumed, the shear modulus of dry rock (μ_{dry}) and fluid saturated rock (μ_{sat}) are equal:

$$\mu_{dry} = \mu_{sat} \qquad \text{Eq. 3.42}$$

An arrangement of Gassmann's equation which expresses the effect of the fluid bulk modulus is (Gelius and Johansen 2010):

$$K^* = K_d + \frac{(1-\frac{K_d}{K_s})^2}{\frac{\phi}{K_f}+\frac{1-\phi}{K_s}+\frac{K_d}{K_s^2}} \qquad \text{Eq. 3.43}$$

Where K* is the effective bulk modulus of the saturated rock, K_d is the dry rock bulk modulus, K_f is the fluid bulk modulus, K_s is the solid (mineral) bulk modulus and ϕ is porosity.

For fluid substitution, i.e. estimating the effective bulk modulus of a rock (K_2^*) saturated with one fluid (K_{f2}), from the known effective bulk modulus of a rock (K_1^*) saturated with another pore fluid (K_{f1}), a different formulation can be utilized:

$$\frac{K_1^*}{K_s - K_1^*} - \frac{K_{f1}}{\phi(K_s - K_{f1})} = \frac{K_2^*}{K_s - K_2^*} - \frac{K_{f2}}{\phi(K_s - K_{f2})} \qquad \text{Eq. 3.44}$$

3.4.2 Generation of synthetic seismogram

Creating synthetic seismograms (or synthetics) from well logs can be a way of showing the expected AVO/AVA effect of a reservoir for different fluid types (Chiburis et al. 1993). A seismic trace (S) recorded during seismic acquisition can be expressed as a convolution (denoted * here) of the created source signal wavelet (W) and the reflectivity series of the earth (R), in addition to noise (Mondol 2015a):

$$S = W * R + \text{Noise} \qquad \text{Eq. 3.45}$$

A wavelet is a mathematical function which is used to divide a given function into frequency components of a matching resolution (Mondol 2015a), and for creating synthetics a constant wavelet can be used for simplicity (Figure 3.19).

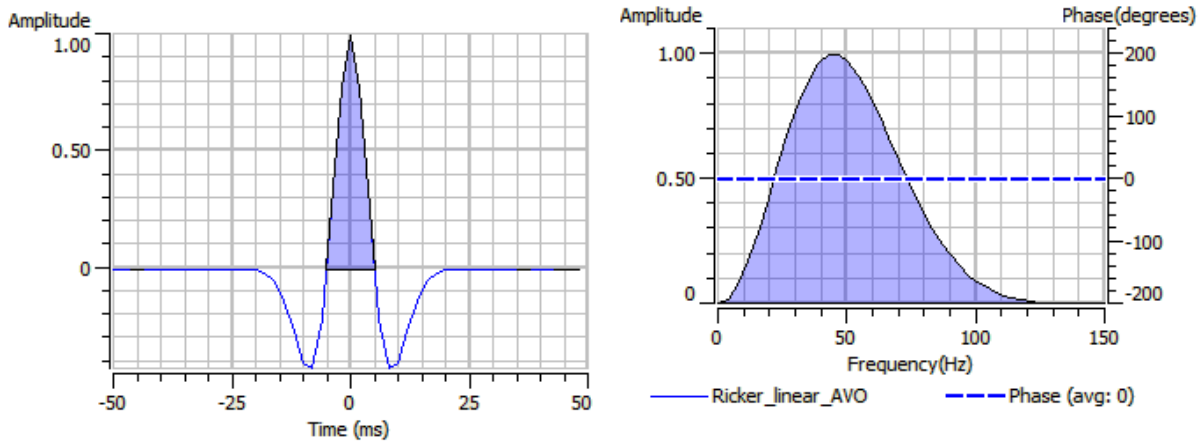

Figure 3.19. Linear phase Ricker wavelet used in this study. Dominant frequency = 45 Hz, wavelet length = 100 ms, samle rate = 2 ms.

Synthetics are created by convolving the reflection coefficient series derived from upscaled acoustic impedances recorded in the wells (density multiplied with velocity) with the chosen wavelet, as shown in Figure 3.20.

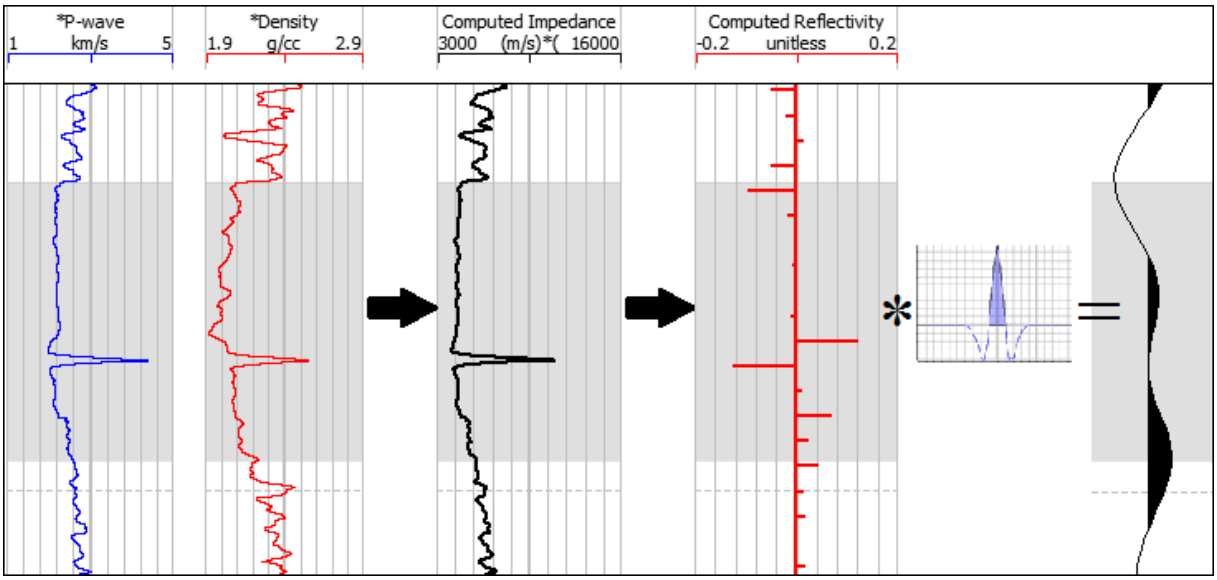

Figure 3.20. A zero-offset synthetic seismic trace created by convolution of a reflectivity series with a wavelet.

Creation of synthetic seismograms comes with assumptions of upscaled logs being representative of larger changes in the subsurface layers, and multiples are not modeled.

3.4.3 Angle dependent reflection coefficient

At a boundary between two layers (media of different velocities), an angled incident seismic wave will generate both reflected and transmitted (refracted) waves (both P and S, i.e. mode conversion), as shown schematically in Figure 3.21 (Mondol 2015a).

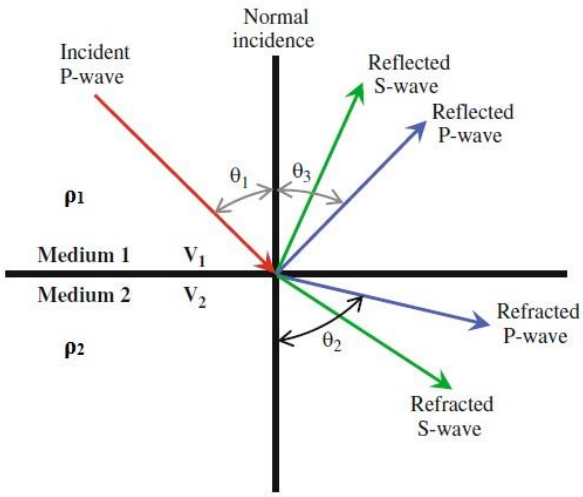

Figure 3.21. Schematic representation of reflected and refracted waves created at a layer interface (modified from Mondol (2015a)).

These waves are related through Snell's law (Gelius and Johansen 2010):

$$p = \frac{\sin\theta_1}{V_1} = \frac{\sin\theta_2}{V_2} \quad \text{Eq. 3.46}$$

where θ_1 is the incident angle, θ_2 is the transmitted angle and V_1 and V_2 are the layer velocities (P- or S-wave velocity). The zero-offset reflection coefficient (R_p) at an interface, i.e. how much of the energy is reflected with no incident angle, is defined as (Gelius and Johansen 2010):

$$R_p = \frac{Ip_2 - Ip_1}{Ip_2 + Ip_1} = \frac{V_{p2}\rho_2 - V_{p1}\rho_1}{V_{p2}\rho_2 + V_{p1}\rho_1} \quad \text{Eq. 3.47}$$

Where Ip is the P-wave impedance, V_p is P-wave velocity and ρ is density, subscripts 1 and 2 denoting upper and lower layer, respectively. The same applies for S-wave velocities (except for fluid layers). For angled incidences however the amplitudes of the reflected P-wave (R_{pp}) is described as a function of angle (θ), originally through what is known as the Zoeppritz equations, which are complex. Even when only measuring P-P events, S-wave information can also indirectly be extracted from this as they are related through the mentioned mode-conversion at the boundary of two elastic media (Gelius and Johansen 2010). Simplified expressions have been introduced for physical insight and practical applicability, notable simplifications being the Aki and Richards (1980) approximation, Wiggens' or Gelfland's (1986) approximation, and the Shuey (1985) approximation.

The Aki-Richards' formulation is a linearized approximation on the form (Gelius and Johansen 2010):

$$R_{pp}(\theta) = \frac{1}{2}\left[\frac{\Delta V_p}{V_p} + \frac{\Delta\rho}{\rho}\right] - 2\left(\frac{V_s}{V_p}\right)^2\left[2\frac{\Delta V_s}{V_s} + \frac{\Delta\rho}{\rho}\right]\sin^2\theta + \frac{1}{2}\frac{\Delta V_p}{V_p}\tan^2\theta \quad \text{Eq. 3.48}$$

Where $\Delta V_p = V_{p2} - V_{p1}$ and $V_p = \frac{1}{2}(V_{p1} + V_{p2})$, and the same for the V_s equivalents.

If assuming small angles, as done in Wiggens' or Gelfand's approximation, i.e. tan θ ≈ sin θ and $V_p/V_s = 2$, the equation simplifies to (Gelius and Johansen 2010):

$$R_{pp}(\theta) = R_p + G\sin^2\theta \quad \text{Eq. 3.49}$$

Where $G = R_p - 2R_s$, and R_p and R_s are the zero-offset P- and S-wave reflection coefficients calculated as follows:

$$R_p = \frac{1}{2}\left[\frac{\Delta V_p}{V_p} + \frac{\Delta\rho}{\rho}\right] \quad \text{Eq. 3.50}$$

$$R_s = \frac{1}{2}\left[\frac{\Delta V_s}{V_s} + \frac{\Delta\rho}{\rho}\right] \quad \text{Eq. 3.51}$$

The zero-offset reflection coefficient R_p is called the AVO intercept, and the G is the called the AVO gradient describing change in amplitude with increasing offset as when picked from a top reservoir reflection in a NMO-corrected CMP-gather. These amplitude values can be plotted as a function of offset or angle of incidence and used to classify gas sands (Gelius and Johansen 2010).

The approximation of Shuey (1985) describes that a change in Poisson's ratio can be estimated from having estimates of R_p and G (Gelius and Johansen 2010). As mentioned, Poisson's ratio is related to the V_p/V_s ratio:

$$\nu = \frac{0.5(V_p/V_s)^2 - 1}{(V_p/V_s)^2 - 1} \qquad \text{Eq. 3.52}$$

which can be differentiated:

$$\Delta\nu = \frac{\left(\frac{V_s}{V_p}\right)^2 \left(1 - 2\nu\left[\frac{\Delta V_p}{V_p} - \frac{\Delta V_s}{V_s}\right]\right)}{\left[\left(\frac{V_s}{V_p}\right)^2 - 1\right]} \qquad \text{Eq. 3.53}$$

Lastly, by assuming $V_p/V_s = 2$ and $\nu = 1/3$, the form of the approximation reads:

$$\Delta\nu = (R_p + G)\frac{4}{9} \qquad \text{Eq. 3.54}$$

All of these described approximations has been compared to the exact Zoeppritz formulation, shown in e.g. Gelius and Johansen (2010) as displayed in Figure 3.22. It was noted that all approximations were within 2% accuracy up to 20 degrees offset, that Gelfand's or Wiggen's approximation was best up to 35 degrees, and that Shuey's approximation gave the overall most accurate result when considering all angles. The Hampson-Russell software provides the opportunity to utilize the full Zoeppritz equations, an option which has been utilized when doing AVO modeling in this study.

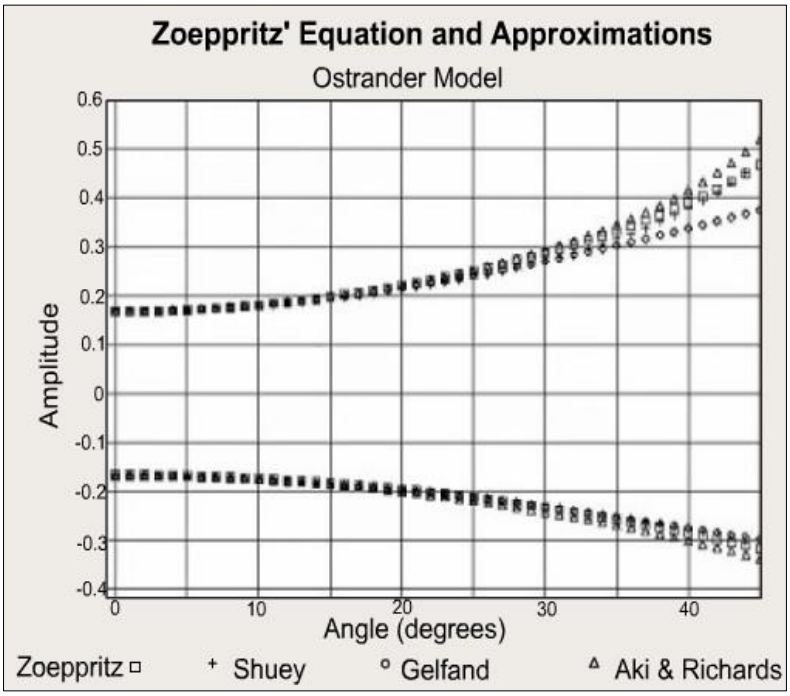

Figure 3.22. Comparison of approximations to original Zoeppritz equation (modified from Gelius and Johansen 2010).

3.4.4 AVO classification of reservoir sands

As mentioned, the P-P reflection coefficient values ($R_{pp}(\theta)$) picked from a reflection interface corresponding to the top of a reservoir can be plotted versus offset (or angle) and be classified by the behavior of the subsequent line plotted (Rutherford and Williams 1989) (Figure 3.23).

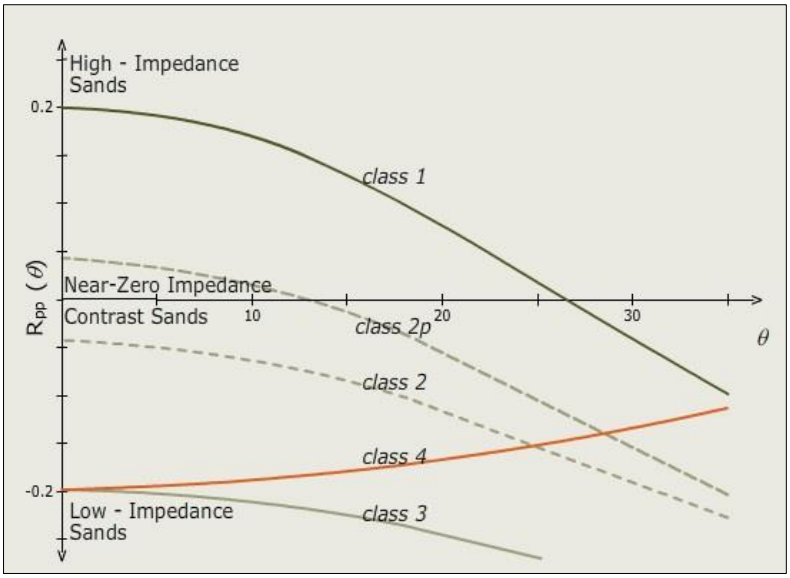

Figure 3.23. Gas sand classification: $R_{pp}(\theta)$ versus angle of incidence (adapted from Gelius and Johansen 2010).

A similar and common way of classifying gas sands is to crossplot the zero-offset reflectivity R_p (equal to $R_{pp}(0)$) versus the AVO gradient (Figure 3.24). This plot is recommended to have a background trend from brine saturated clastic rocks within a limited depth range in order to determine deviations from this trend and thereby identify hydrocarbons (Castagna and Swan 1997; Avseth 2015). A commonly used background trend for this plot is based on constant V_p/V_s ratio of 2 (Castagna et al. 1998), and is intended to represent where brine-sand data generally should plot, in order to be able to interpret deviations ideally related to the presence of hydrocarbon (with gas sand providing the most clear contrast). Reflections from top of gas sand intervals should generally plot beneath the trend line, whereas bottom gas sand data should plot above it.

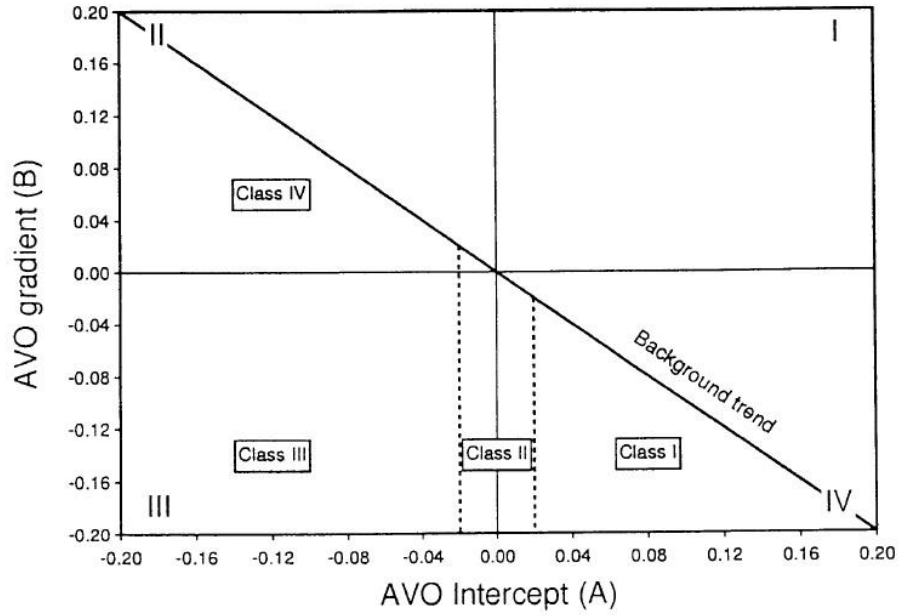

Figure 3.24. R_p (A in figure) versus G (B in figure), and determination of gas sand classes (adapted from Castagna and Swan 1997).

The classification of gas sands was originally suggested by Rutherford and Williams (1989) and contained three classes (I, II and III), it was later expanded by Castagna and Swan (1997) to include a fourth class, and additionally a variation of class II has been added since the initial scheme (Ross and Kinman 1995):

- Class I – Positive intercept, negative gradient. Sand impedance is higher than surrounding shale, and is often associated with high impedance sands of moderate to high compaction.
- Class II & IIp – Slightly positive (IIp) or slightly negative (II) intercept, negative gradient. Sand impedance is close to surrounding material, indicating moderate compaction and consolidation.
- Class III – Negative intercept, negative gradient. Sand impedance is lower than surrounding medium, and is associated with marine, unconsolidated or little compacted sands. Amplitude increase (more negative) with offset.
- Class IV – Negative intercept, positive gradient. Of similar origin as class 3, except that the reflection amplitude decrease (less negative) with offset.

Chapter 4: Petrophysical analysis

4.1 Results

A summary of the thickness and presence of formations which are utilized to characterize target reservoirs is presented in Table 4.1. Regarding the Triassic succession, only the Snadd and Kobbe formations are present in all studied wells, culminating in the most results available for analysis and are subsequently the most thoroughly investigated formations. These formations are described as main targets by the drilling company of multiple wells in the study. The Fruholmen Formation is also present in five wells but not given focus during this thesis work. As for the Jurassic interval, the Stø and Tubåen formations are present in the highest number of wells and will serve to address the quality of the Jurassic reservoirs. The Stø Formation is generally known as a high quality reservoir in the Barents Sea, well known from the Hammerfest Basin. Concerning the remaining reservoir candidates mentioned in the previous chapters, the Nordmela Formation is only present thinly in two wells (7224/6-1 and 7224/7-1) with adequate well logs recorded. The Klappmyss and Havert formations are present in five and three wells, respectively, but generally display very high shale volume values and seemingly poor reservoir quality in general. Hydrocarbon has however been proven in the Havert formation, e.g. in well 7226/11-1 in the current database.

Table 4.1: Overview of depth and thickness of main formations analyzed in this study.

Well	Possible Target Fm	Start Depth (m RKB)	End Depth (m RKB)	Thickness (m)
7124/3-1	Tubåen	1285	1305	20
	Snadd	1438	1893	455
	Kobbe	1893	2334	441
7125/1-1	Stø	1399	1521	122
	Snadd	1612	2105	493
	Kobbe	2105	2177*	72^{+}
7222/11-1 (Caurus)	Snadd	636	2007	1371
	Kobbe	2007	2644*	637^{+}
7222/6-1S (Obesum)	Snadd	484	1890	1406
	Kobbe	1890	2464	574
7223/5-1	Snadd	585	1856	1271
	Kobbe	1856	2451	595
7224/6-1 (Arenaria)	Tubåen	1004	1064	60
	Snadd	1166	2010	844
	Kobbe	2010	2328*	318^{+}
7224/7-1	Stø	894	919	25
	Tubåen	930	931	1
	Snadd	1028	1642	614
	Kobbe	1642	2222	580
7226/11-1	Stø	1194	1202	8
	Tubåen	1202	1234	32
	Snadd	1296	1878	582
	Kobbe	1878	2303	425
*max. penetration of well, $^{+}$the actual thickness is higher				

All relevant formations of the Triassic-Jurassic interval are considered when conducting lithology discrimination. From the initial overview, obvious shale intervals and non-prospective sections within the formations are excluded and the remaining potential reservoir intervals are investigated further. These reservoir zones have been chosen based on interpretation of available logs used for lithology discrimination, e.g. the relative relations of neutron-density readings, and information from the well summaries provided by the oil companies to the Norwegian Petroleum Directorate (NPD 2016). The reasoning behind this is that the formations are often very thick and varied, especially in the Triassic, which means that much of each formation does not act as a reservoir interval and is therefore excluded from analysis. As the formations are varied in composition these chosen reservoir sections may still include a substantial amount of shale. Correlation panels showing all evaluated formation intervals of the Snadd and Kobbe formations are included in the appendix (Figure B.1 and B.2). In the Tubåen and Stø formations, the whole formation is evaluated as a reservoir (Figure B.3).

Furthermore, shale volume is estimated from the Larionov equation (valid for older rocks, Eq. 3.2), quality controlled by calculating shale volume from the neutron-density combination (Eq. 3.6), and constrained to the selected potential reservoir intervals. Porosity, and subsequently net-to-gross reservoir, is then estimated in the reservoir zones, by using a neutron-density combination corrected for shale volume in the porosity estimates, denoted effective porosity. Water saturation is calculated and presented in the reservoirs assumed or known to contain hydrocarbons (i.e. pay zones). Water saturation has been estimated in identified reservoirs through Archie's equation by deducing an apparent formation water resistivity through one or more brine-filled, and preferably clean, reservoir interval(s). All calculated quantities are presented as averages for each reservoir interval in each formation in tables 4.2 to 4.5. The utilized cutoff values (V_{sh} <= 0.5, ϕ >= 0.06, and S_w <= 0.6) for net reservoir and net pay are chosen in order to be able to also include less than excellent reservoirs in further assessments. Kennedy (2015) uses these values in general examples, stating that even though they are not universally applicable, they are acceptable for the sake of comparing wells to each other.

4.1.1 Kobbe Formation

Results of the petrophysical analysis of the Kobbe Formation are presented in Table 4.2. The results show that the values of average shale volume are close to or more than 50%, except for three reservoir intervals encountered in wells 7124/3-1, 7224/6-1 and 7226/11-1. The maximum formation thickness is in well 7223/5-1 where it measures 595 m. Average effective porosity values range from acutely low at 0.026 in well 7223/5-1 to fairly high at 0.164 in well 7124/3-1. Combined with shale volume estimates, this yields low net-to-gross reservoir values in almost all reservoir zones, varying between 0.056 and 0.382. Exceptions are in well 7124/3-1 and 7226/11-1 due to lower shale volume and relatively high porosity in which respective N/G values are 0.601 and 0.680.

Table 4.2: Characteristics and average values of the reservoir zones in the Kobbe Formation.

KOBBE FORMATION									
Well	**Reservoir depth (mRKB)**	**Gross reservoir [m]**	**GR_{min} - GR_{max} [API]**	**V_{sh}**	**Eff. Porosity**	**N/G reservoir**	**Net res. [m]**	**S_w in pay**	**Net pay [m]**
7222/6-1	1915-2060	145.1	108-150	0.546	0.037	0.214	31.1	0.489	7.2
7223/5-1	1870-2025	154.7	55-108	0.522	0.056	0.212	32.8	0.483	2.9
	2231-2348	116.1	55-108	0.566	0.026	0.056	6.6	0.359	5.8
7222/11-1	2101-2137	36.7	30-85	0.634	0.037	0.137	5.0	0.482	1.4
	2210-2243	33.5	30-85	0.472	0.069	0.382	12.8	0.303	9.3
7224/7-1	1662-1764	102.0	15-60	0.561	0.081	0.326	33.2	0.518	9.5
	1920-2030	109.7	15-60	0.475	0.044	0.253	27.7	0.452	14.8
7124/3-1	1894-1923	28.8	15-60	0.349	0.164	0.601	17.3	-	-
	2221-2291	70.0	15-60	0.612	0.056	0.312	21.8	-	-
7125/1-1	2105-2162	56.7	24-92	0.596	0.055	0.263	14.9	0.470	4.9
7226/11-1	1878-2275	397.5	18-65	0.690	0.067	0.159	63.1	-	-
	2275-2303	27.6	18-65	0.393	0.092	0.680	18.8	-	-
7224/6-1	2009-2120	110.6	55-115	0.559	0.043	0.154	17.1	0.415	10.7
	2247-2258	11.3	55-115	0.386	0.048	0.324	3.7	0.415	1.7

The Kobbe Formation has proven hydrocarbons in six out of eight wells, with a maximum (cumulative) pay zone thickness estimated in the lower reservoir of well 7224/7-1 of 14.8 m. Core and pressure tests made by the drilling operator did however show that the reservoirs in this well had very low permeability, and the lower intervals were only described as hydrocarbon shows (NPD 2016). The maximum continuous pay zone established is found in well 7222/11-1 (Caurus) of around 10 m (Figure 4.1). In well 7226/11-1 the Kobbe Formation is dominantly shaley, but contains thin sandstones throughout the formation. Thus, the entire formation contains potential small reservoir intervals, but overall net-to-gross is very low and shale volume fraction is high. As it is difficult to separate narrower good reservoir zones, the full formation has been included as “reservoir”, with the most promising section in lowermost Kobbe separated from the rest of the formation to indicate the interval of highest potential (Figure A.7 and B.1).

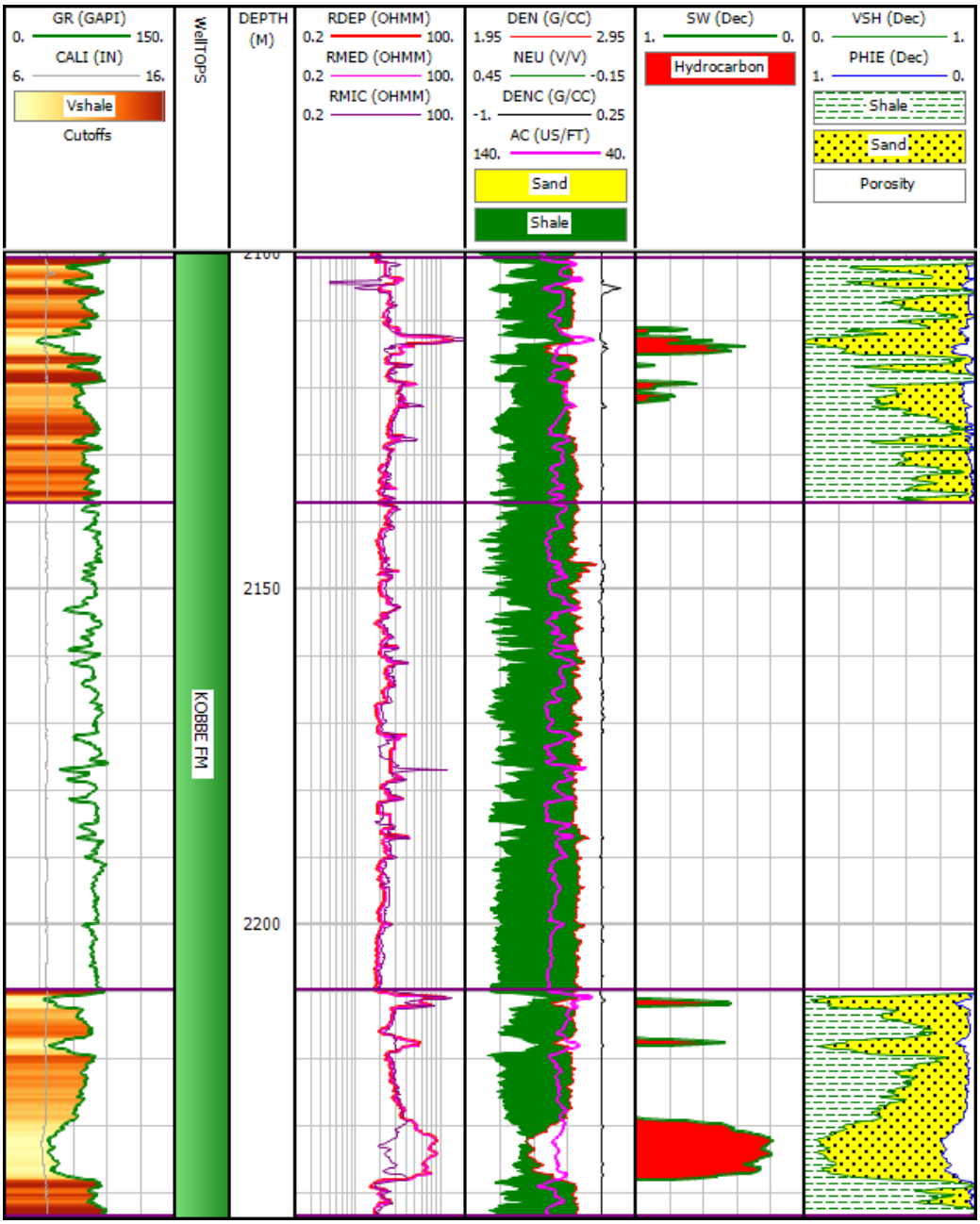

Figure 4.1. Composite log display of the Kobbe Formation reservoirs in well 7222/11-1. The intervals shows typical thin sandstones interbedded in shale.

4.1.2 Snadd Formation

Results of the petrophysical analysis of the Snadd Formation are presented in Table 4.3. The Snadd Formation constitutes the thickest recorded interval in six out of eight wells, and has a maximum thickness in well 7222/6-1S of 1406 m. The overall best quality reservoirs based on the present calculations are found in well 7125/1-1, 7226/11-1, 7224/6-1 and 7223/5-1, exhibiting shale volume values among the lowest (18-27%) and relatively high average effective porosities (around 15-23%).

Table 4.3: Characteristics and average values of the reservoir zones in the Snadd Formation.

SNADD FORMATION									
Well	**Reservoir depth (mRKB)**	**Gross reservoir [m]**	**GR_{min} - GR_{max} [API]**	**V_{sh}**	**Eff. Porosity**	**N/G reservoir**	**Net res. [m]**	**S_w in pay**	**Net pay [m]**
7222/6-1	1134-1423	289.1	114-165	0.548	0.102	0.302	87.2	-	-
	1518-1648	129.8	114-160	0.500	0.096	0.493	64.0	0.553	11.3
7223/5-1	657-727	69.5	55-108	0.259	0.214	0.985	68.4	-	-
	1176-1454	278.4	55-108	0.512	0.135	0.443	123.3	-	-
	1575-1635	59.3	55-108	0.272	0.167	0.778	46.1	-	-
7222/11-1	636-715	78.6	88-135	0.348	0.19	0.791	62.2	-	-
	770-799	28.5	95-145	0.305	0.299	0.864	24.6	0.381	12.0
	1277-1802	525.0	40-95	0.576	0.093	0.290	152.3	-	-
7224/7-1	1201-1352	151.2	15-60	0.581	0.096	0.341	51.5	-	-
	1452-1478	25.8	15-60	0.573	0.061	0.118	3.1	-	-
7124/3-1	1438-1465	27.3	15-60	0.470	0.14	0.648	17.7	-	-
	1591-1708	116.7	15-60	0.498	0.1	0.349	40.7	-	-
7125/1-1	1612-1640	28.5	24-92	0.182	0.171	0.995	18.4	-	-
	1774-1872	98.2	24-92	0.513	0.086	0.314	30.8	-	-
7226/11-1	1296-1308	11.6	18-65	0.241	0.224	1.000	11.6	-	-
	1352-1386	33.8	18-65	0.381	0.166	0.802	27.1	-	-
	1644-1682	38.3	18-65	0.384	0.17	0.693	26.5	-	-
7224/6-1	1166-1233	67.2	45-125	0.217	0.156	0.931	62.6	-	-
	1288-1398	110.3	45-125	0.522	0.106	0.406	44.8	-	-
	1699-1838	139.1	45-125	0.433	0.089	0.436	60.7	-	-

Examples of reservoir shale volumes in the Snadd Formation compared to the Kobbe Formation are shown in Figure 4.2. Shale volume range from 0.182-0.581, porosity varies from 0.061-0.299, and net-to-gross values are between 0.302 and 1. One of the two reservoirs in the study interpreted to contain hydrocarbon of sufficient quantities based on stated cutoff values is found in well 7222/11-1 (Caurus) where a 28.5 m thick gross reservoir is estimated to contain 12 m of pay sand with an average water saturation of 0.381 (Figure 4.3). This reservoir as a whole also exhibits high porosity (29.9%), and the shale volume estimate is about 30%. The other reservoir with good hydrocarbon indication (7222/6-1 S Obesum) appears to have less favorable reservoir properties. Multiple other reservoir zones investigated

in the Snadd Formation are also proven to contain hydrocarbons (NPD 2016), but low saturation or poor reservoir quality inhibits their potential.

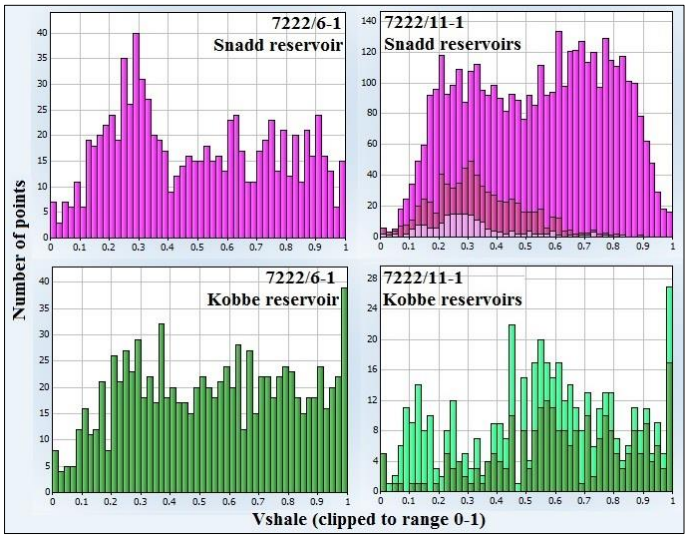

Figure 4.2. Comparison of Snadd and Kobbe reservoirs shale volume in wells 7222/11-1 and 7222/6-1. Note lower shale volume estimated in the two smaller, upper Snadd Formation reservoirs in well 7222/11-1.

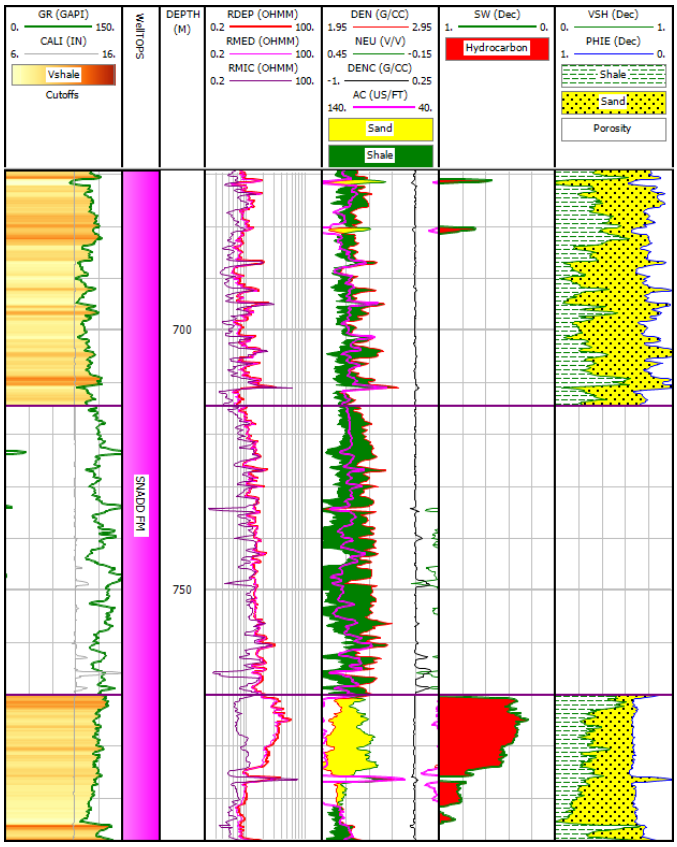

Figure 4.3. Composite log display of two upper Snadd reservoir in well 7222/11-1.

4.1.3 Tubåen Formation

Results of the petrophysical analysis of the Tubåen Formation are presented in Table 4.4. The Tubåen Formation generally displays the lowest estimated shale volumes of all reservoir intervals, except for the Stø Formation encountered in well 7125/1-1. Values range from a shale volume of 0.089 in well 7124/3-1 to 0.110 in well 7226/11-1 and roughly the same in well 7224/6-1, with a maximum thickness of 60 m in the latter.

Table 4.4: Characteristics and average values of the Tubåen Formation.

TUBÅEN FORMATION									
Well	**Reservoir depth (mRKB)**	**Gross reservoir [m]**	**GR_{min} - GR_{max} [API]**	**V_{sh}**	**Eff. Porosity**	**N/G reservoir**	**Net res. [m]**	**S_w in pay**	**Net pay [m]**
7224/7-1	930-931	0.9	15-60	0.020	0.252	1.000	0.9	-	-
7124/3-1	1285-1305	19.9	15-60	0.089	0.239	0.981	19.5	0.221	13.9
7226/11-1	1202-1234	32.0	18-65	0.110	0.204	0.983	31.5	-	-
7224/6-1	1004-1064	60.1	45-125	0.107	0.216	0.997	59.9	-	-

A comparison of shale volume distribution with upper Snadd reservoirs in two wells was shown in Figure 3.3. The shale volume is estimated to be even lower in well 7224/7-1, but accurate analysis is restricted as the formation is less than a meter thick and there are consequently very few data points from this well. As with the Stø Formation, Tubåen is recorded in well 7223/5-1 with gamma measurements. The resulting average value from estimating shale volume from gamma ray is 0.275 through a 16 m interval. Average porosity values are high in all four encountering wells, with more than 20% porosity being estimated in all cases. Resulting net-to-gross reservoir values are therefore very high, being very close to 1 in each of the wells. A comparison of the Stø Formation and the Tubåen Formation in the neutron-density domain is shown in (Figure 4.4). The crossplot shows a clear hydrocarbon effect in points from well 7124/3-1. In well 7124/3-1 (Bamse) the Tubåen Formation contains a good quality reservoir of 19.5 m, with approximately 14 m of hydrocarbon-bearing sand which averages an estimated 22.1% water saturation, i.e. 77.9% hydrocarbon saturation (Figure 4.5). High gamma ray readings and simultaneous negative crossover in the neutron-density log are observed in the base of the Hekkingen Formation in Figure 4.5, which provides contrasting information about the exact thickness extent of the sandstone reservoir. This could possibly be an effect of differences in the vertical resolution of gamma ray, neutron and density logs (Mondol 2015b).

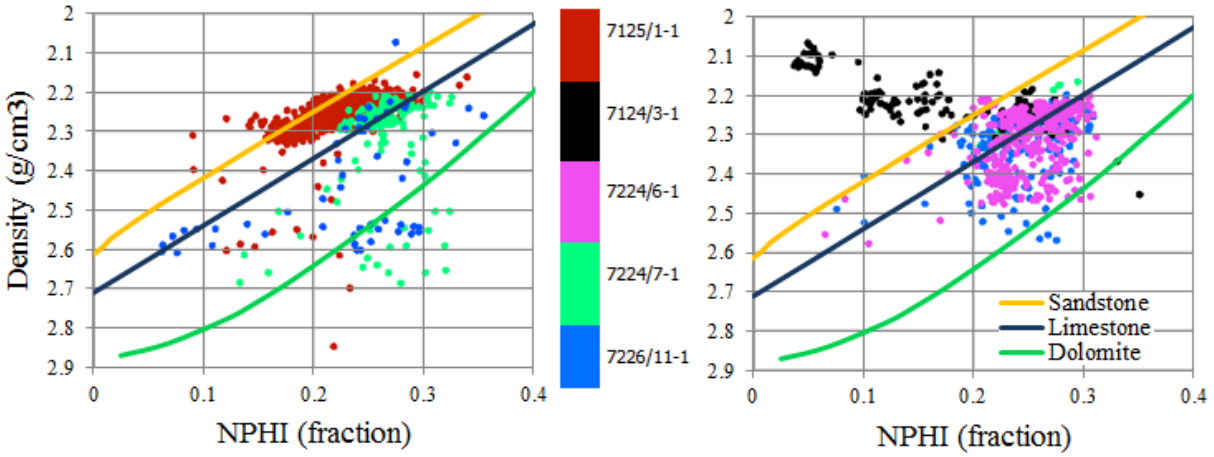

Figure 4.4. Neutron-density crossplots showing data from the Stø (left) and Tubåen (right) formations in all wells present. Data is color coded by well.

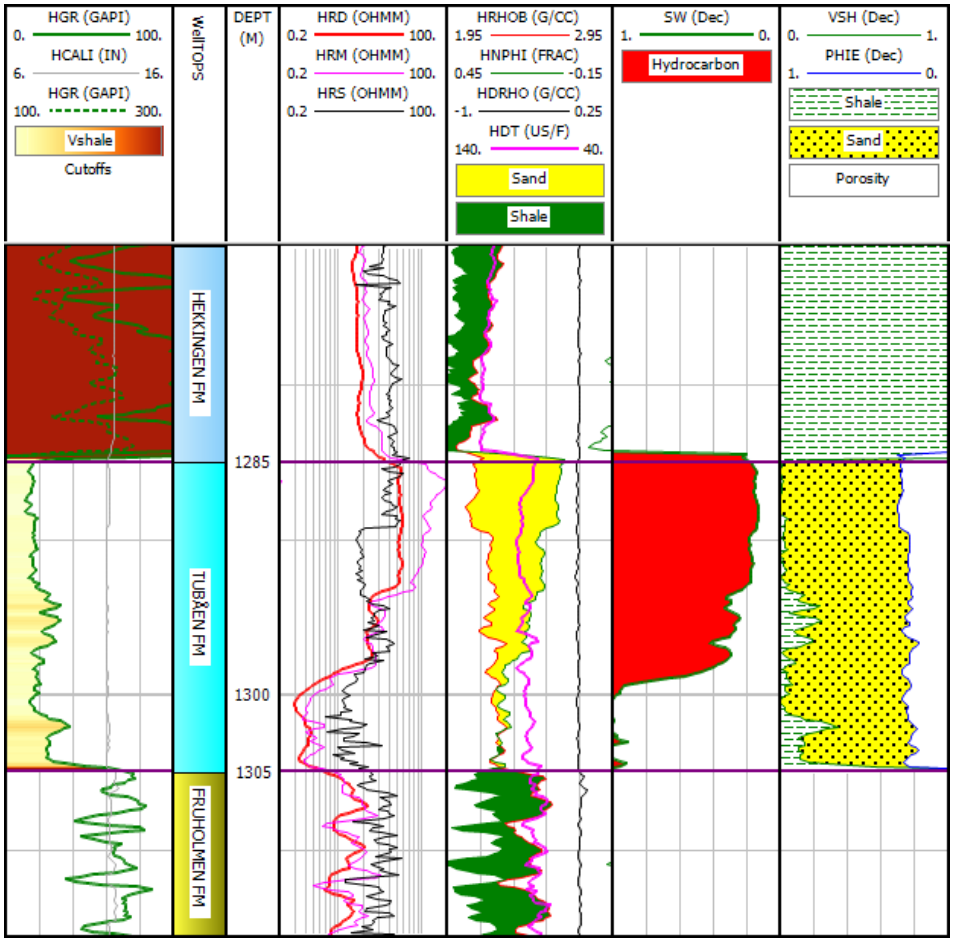

Figure 4.5. Composite log display of the Tubåen reservoir in well 7124/3-1 capped by the Hekkingen Formation.

4.1.4 Stø Formation

Results of the petrophysical analysis of the Stø Formation are presented in Table 4.5. Average shale volume in the Stø formation varies from 0.551 in well 7226/11-1 at the poorest to 0.038 in well 7125/1-1. In the latter well Stø is also at its thickest considering the studied wells, measuring 122 m. An intermediate value is registered in well 7224/7-1 at 0.188.

Table 4.5: Characteristics and average values of the Stø Formation.

STØ FORMATION									
Well	**Reservoir depth (mRKB)**	**Gross reservoir [m]**	**GR_{min} - GR_{max} [API]**	**V_{sh}**	**Eff. Porosity**	**N/G reservoir**	**Net res. [m]**	**S_w in pay**	**Net pay [m]**
7224/7-1	894-919	24.8	15-60	0.188	0.206	0.862	21.4	-	-
7125/1-1	1399-1521	121.6	24-92	0.038	0.246	0.990	120.4	0.407	2.6
7226/11-1	1194-1202	8.1	18-65	0.551	0.127	0.349	2.8	-	-

A comparison of the Stø Formation and reservoirs of the Kobbe Formation with respect to shale volume is shown in Figure 4.6. In well 7223/5-1 the Stø Formation is recorded with gamma ray measurements, but lack values from both the neutron and density log. Thus, only shale volume was estimated which yielded 7 m of clean sand (0% shale), although further analysis is not performed.

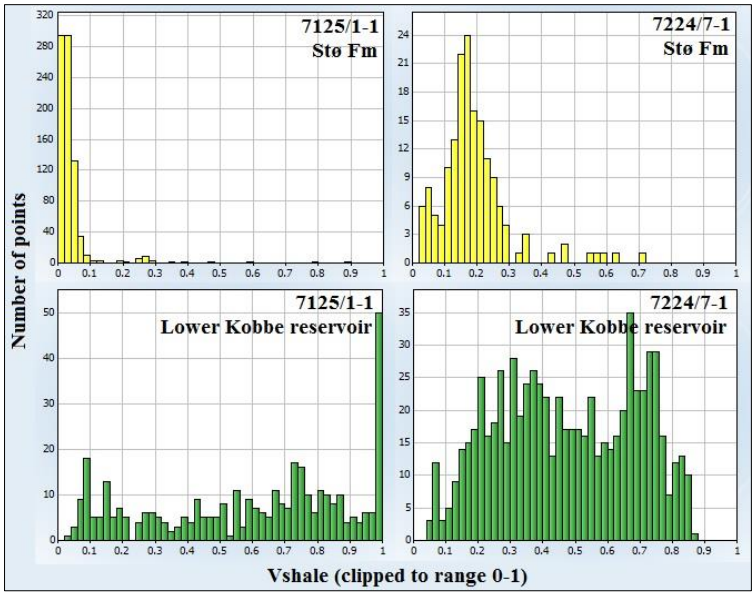

Figure 4.6. V_{sh} histograms for comparison of reservoirs in the Kobbe and Stø formations in wells 7125/1-1 and 7224/7-1.

A similar trend is observed in the porosity values of the three wells that encounter the Stø Formation as in the shale volume estimates, where the highest value is found in well 7125/1-1 with the average effective porosity of 0.246, an intermediate value of 0.206 in well 7224/7-1

and lowest at 0.087 in 7226/11-1. Both the former wells display good net-to-gross reservoir values of 0.990 and 0.862 respectively, which indicates that Stø in both wells contain excellent reservoirs. The net-to-gross reservoir value of the thin reservoir in well 7226/11-1 is much lower. Different behavior of data points from the three wells in the neutron-density crossplot corresponds well to observations about reservoir cleanliness (i.e. proximity to the sandstone line) and a slight hydrocarbon effect being observable in the red data points (Figure 4.4, above the sandstone line). Hydrocarbon is encountered in one of three wells, 7125/1-1 (red data points in crossplot), albeit only a thin interval of maximum thickness 2-3 m and estimated average water saturation of 0.407 (Figure 4.7).

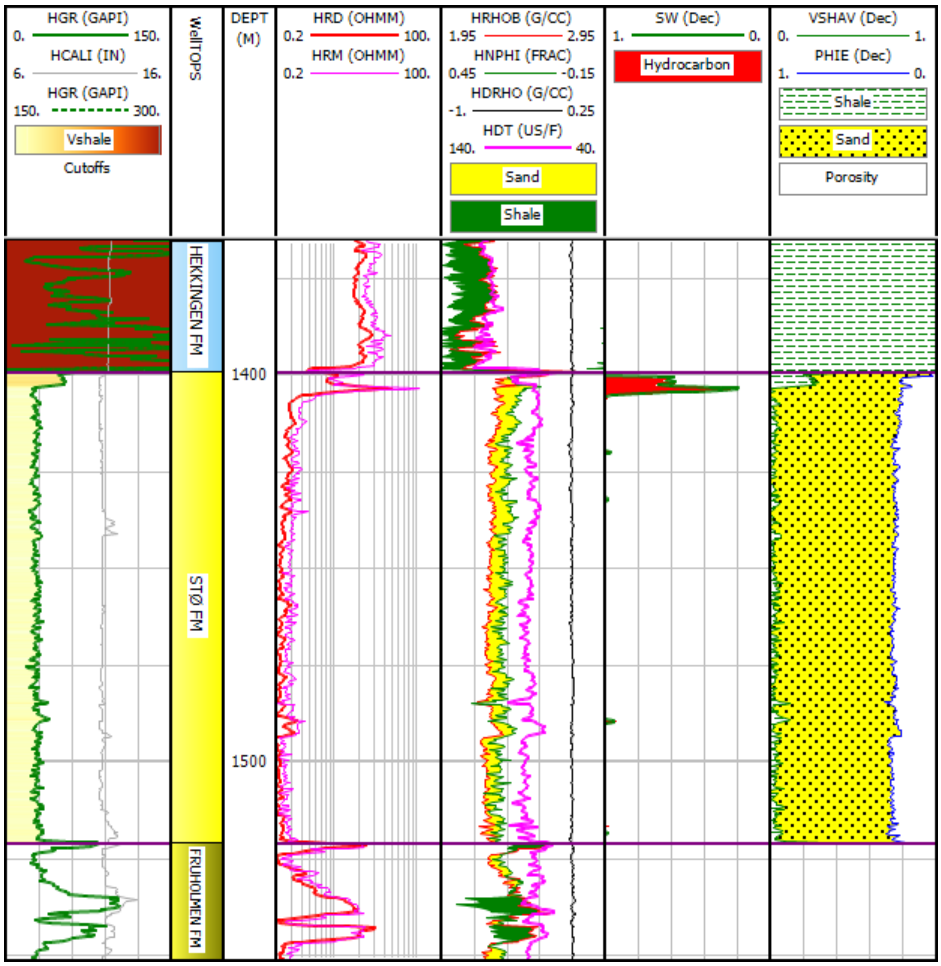

Figure 4.7. Composite log view of the Stø Formation in well 7125/1-1 showing a very clean sandstone reservoir with a thin hydrocarbon leg at the top, capped by the Hekkingen shale.

4.1.5 Estimates of permeability

Two examples of permeability estimates through four different relations are shown in Figure 4.8. The data in the left plot is from within the lowermost Kobbe Formation reservoir with oil and gas in well 7222/11-1 (2229-2238 m). In the right plot, data from the mostly gas-filled reservoir in the Tubåen Formation in well 7124/3-1 is used (1285-1298 m). Composite log views of these reservoirs are shown in Figure 4.1 and Figure 4.5.

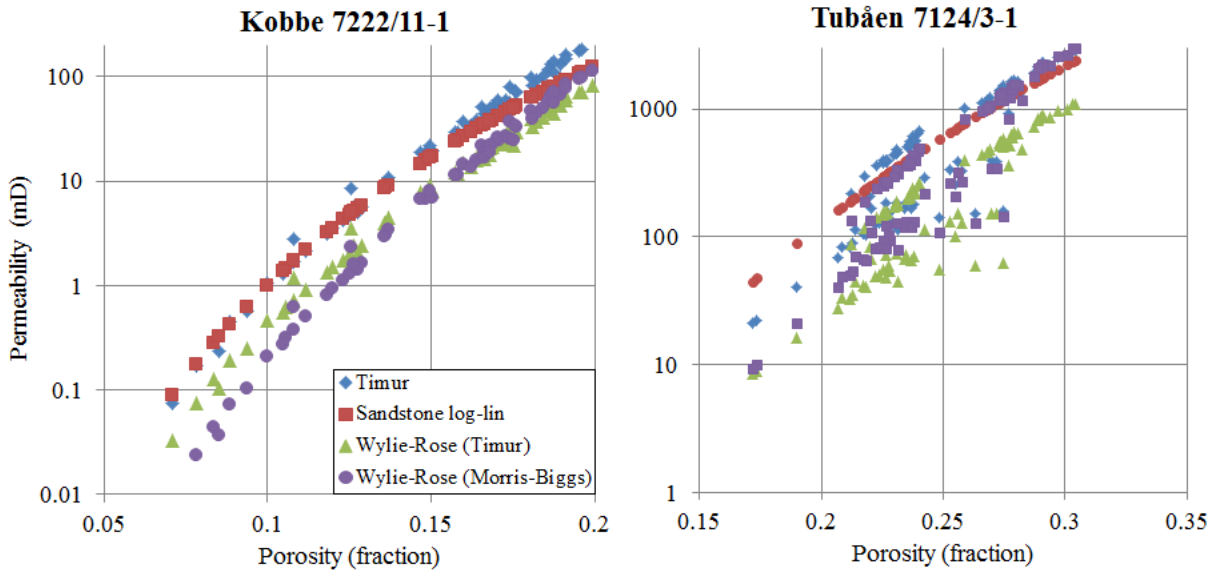

Figure 4.8. Crossplot of estimated permeability versus porosity, with data from the Kobbe Formation in well 7222/11-1 and the Tubåen Formation in well 7124/3-1. Note different scales on both axes.

In the Kobbe reservoir plot on the left, the Wylie-Rose equations give the lowest estimates of permeability, whereas the Timur equation and the logarithmic-linear equation yield the highest values. Values range from around 0.02-0.1 mD to 95-170 mD in the low and high porosity range, respectively. As much as ~100 mD separate the maximum and minimum estimate when porosity approaches 20%. R^2-values for exponential best fit lines (not shown) are around 0.98 for all four relations. Permeability estimates in the Tubåen Formation saturated with gas (and a thin oil zone) range from ~10-45 mD at 17% porosity to ~900-2500 mD at 30% porosity. Data points plot with less clear linear trends (when the y-axis is logarithmic) in this plot than what is apparent in the Kobbe data. R^2-values (lines not shown) are around 0.78-0.8 for the Timur and Wylie-Rose relations and for the logarithmic-linear relation it is about 0.99.

4.2 Discussion

At a glance, it seems apparent that the Jurassic Stø and Tubåen Formations are the superior reservoir candidates, as they display high values of porosity and net-to-gross reservoir compared to most of their Triassic counterparts. The thicknesses of these formations are however rather limited in the studied Bjarmeland Platform area, and are in some wells absent, e.g. in well 7222/6-1 located near the edge of Loppa High where neither Stø nor Tubåen are present. This is consistent with the structural and stratigraphic information derived from published literature discussed in chapter 2, as indicated in e.g. Figure 2.4 showing the absence of Jurassic sediments on the Loppa High. The Triassic interval is contrarily thicker on the Loppa High than on the Bjarmeland Platform, corresponding to the great thickness of both the Snadd and Kobbe formations in the westernmost studied wells 7222/6-1, 7222/11-1 and 7223/5-1. Even though many of the studied reservoir intervals of Triassic age display relatively high average values for shale volume, this is often a result of shale-sandstone fluctuations and does not exclude the formations from containing intervals of good reservoir quality, in e.g. channelized sands or sandstone stringers. This is also reflected in net-to-gross ratio estimates. Thick reservoir intervals tend to have been chosen partly in Kobbe and lower Snadd, and especially around the middle of the Snadd Formation. The reasoning for picking larger zones is that there are often frequent variations between sand and shale, and not necessarily one thick, clean continuous zone of sandy lithology. This has consequently had an effect on the total reservoir characteristics and apparent reservoir condition.

4.2.1 Triassic reservoirs

The Kobbe Formation is commonly high in shale content, and identified reservoirs which display promising overall properties are thin, i.e. less than 30 m gross reservoir as seen in Table 4.5. Even with seemingly poor reservoir potential at the initial glance, the Kobbe Formation has the highest number of hydrocarbon occurrences of the four formations analyzed. The thickest continuous hydrocarbon-filled sand interval identified is less than 10 m thick (lowermost zone in well 7222/11-1, Caurus discovery), which demonstrates the pay zone thickness limitation of the Kobbe reservoirs. When estimating permeability using porosity and water saturation values from this reservoir (Figure 4.8), the values reach up to 95-170 mD at maximum. Being described as having poor permeability by the drilling company (NPD 2016), values from the higher porosity range can therefore possibly be assumed to be overestimated, depending on local permeability cutoff values. Another factor that can affect the porosity-permeability relationship is grain size, which is not accounted for in the equations tested (Crain 2015).

The depositional trend in the Kobbe Formation of Middle Triassic age on the Bjarmeland Platform is described in Worsley (2008) as a NNW trending prograding coastline, giving rise to the possibility of sandy deposition in a delta-front/shoreface setting (see also Figure 2.2). Sand intervals in well 7222/6-1 (Obesum discovery) are interpreted to be deposited in this environment. Lundschien et al. (2014) also comments that the creation of reservoirs in the Kobbe Formation on the Bjarmeland Platform is made possible by deposition of fluviodeltaic and shallow marine sediments. The main trend of the Kobbe Formation appears to be, as seen in e.g. Figure 4.1, that rather thin sandy reservoir intervals are situated in generally shaley successions. There does not appear to be a trend in quality specifically towards upper or lower formation zones. If interpolating the thickness distribution of the Kobbe Formation (Figure

4.9), more complex variations are seen than in the thickness map of the Snadd Formation (Figure 4.12). The main trend is still observable as the formation appears to be thickest towards the north-west (Loppa High) and thinnest towards the Nysleppen Fault complex in the south-east. Base Kobbe was penetrated in only five of eight wells, making the thickness map less complete and with increased possibility of errors in the interpolation. If knowing the thickness of the Kobbe Formation in wells 7222/11-1, 7224/6-1 and 7125/1-1 the resulting map would appear different. Trends between wells 7226/11-1 and 7124/3-1 (east and south in the study area respectively) and the north-west part of the study area can assumedly still be correctly observed.

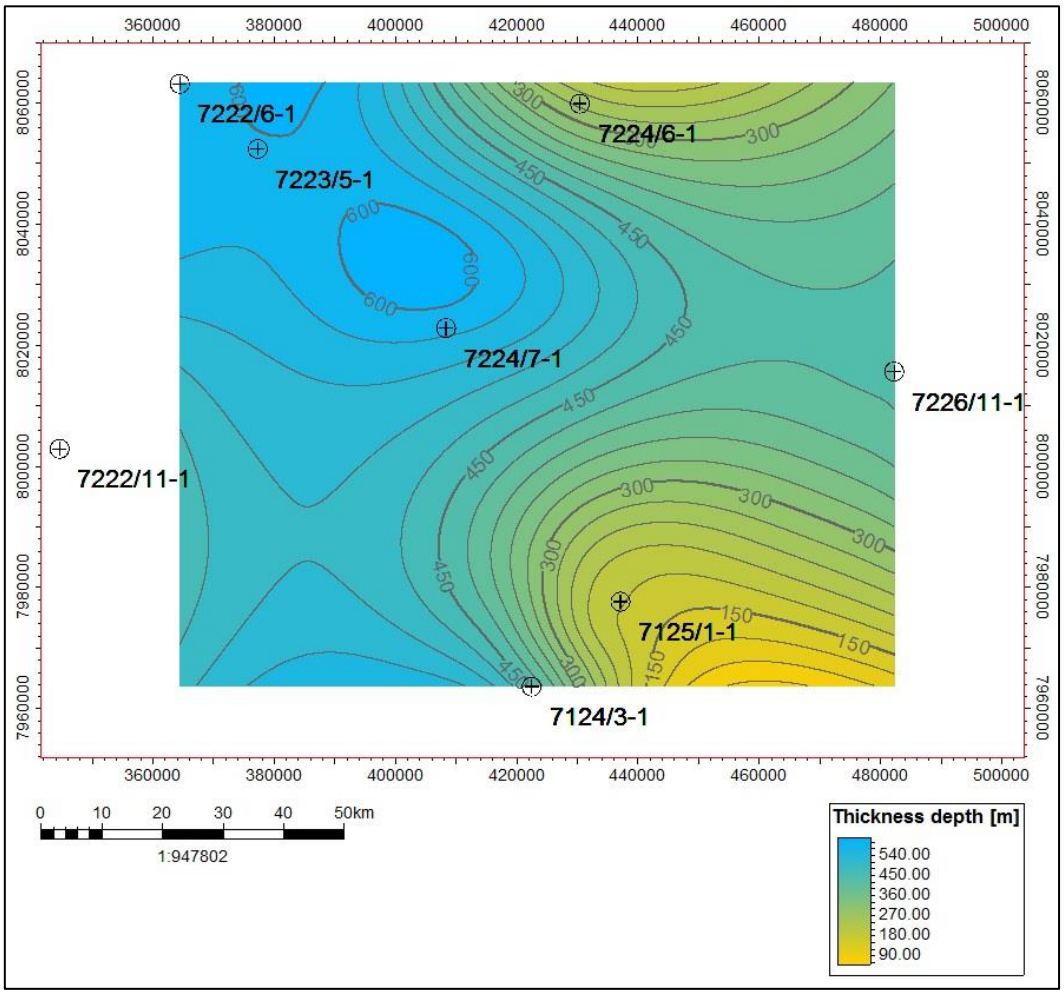

Figure 4.9. Contour map showing thickness between the Kobbe and Klappmyss formations. Note additional uncertainty as the Klappmyss Formation is only penetrated in 5 wells, i.e. not reaching bottom Kobbe.

Chlorite coating and the presence of ductile, lithic rock fragments have been indicated to preserve the quality of Snadd and Kobbe reservoirs even at deep burial depths (Figure 4.10). Ductile rock fragments reduce mechanical compaction due to less crushing of brittle grains which reduces the inter-granular volume (IGV). In the Kobbe Formation, fine grain sizes also reduce compressibility due to a higher number of grain contacts (Bjørlykke and Jahren 2015; Line 2015). Efficient chlorite coating is described to inhibit quartz cementation at burial more

than 2.5 km, and can therefore contribute to preservation of porosity. The quality of chlorite coating is suggested to be dependent on grain size and facies, based on studies of the Snadd and Kobbe formations in closely related areas (e.g. well 7222/11-2 Langlitinden) (Line 2015). Chlorite coating proven in this neighboring well in the Kobbe Formation is shown in Figure 4.11.

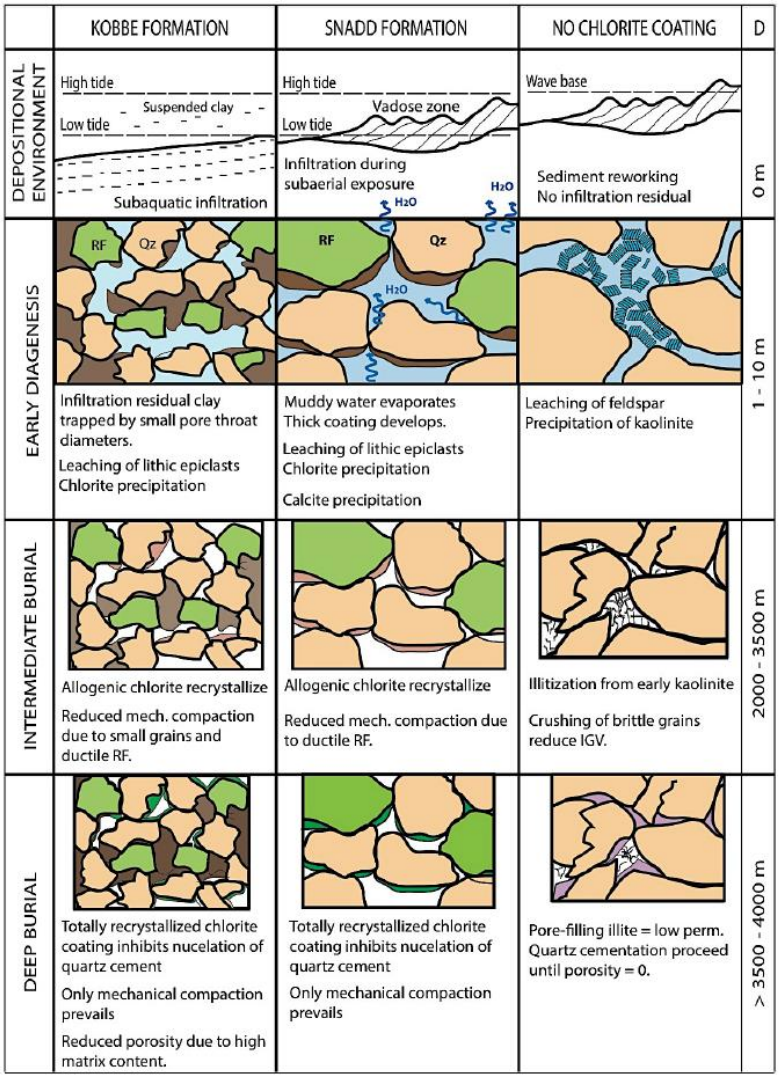

Figure 4.10. Effects of chlorite coating and ductile framework grains on the reservoir quality of Snadd and Kobbe, compared to a non-coated sandstone. After Line (2015).

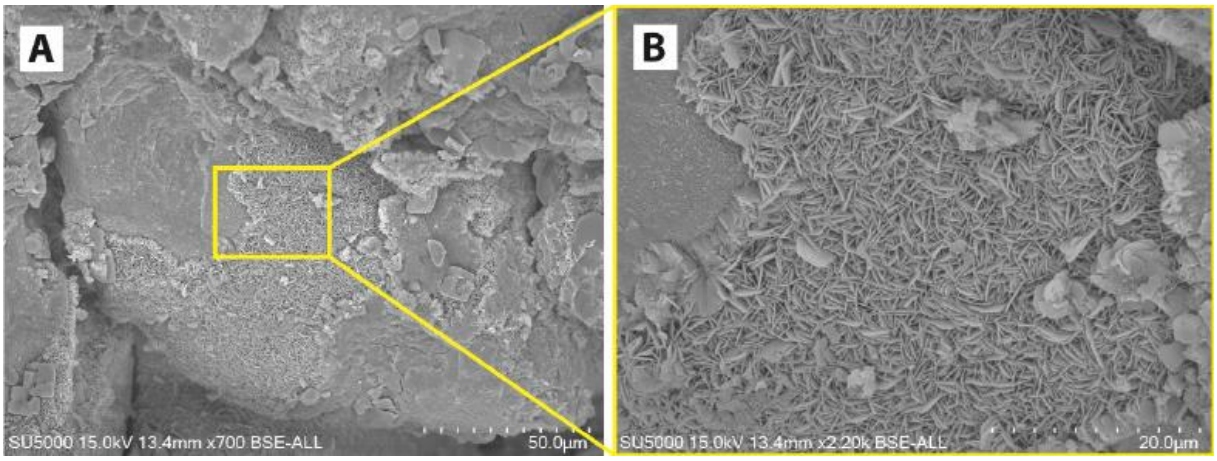

Figure 4.11. Authigenic, continously distributed chlorite coating in the Kobbe Formation in well 7222/11-2. Figure from Line (2015).

A contour map showing the thickness of the Snadd Formation throughout the study area is shown in Figure 4.12. This map is constructed by creating surfaces of the Snadd Formation and the underlying Kobbe Formation from corresponding well tops, on which the depth variations of each formation have been interpolated in-between wells. This interpolation method obviously results in uncertainties related to the spatial accuracy of depths and consequently thicknesses derived, but serve as a good indicator for the directions of thickness trends. Westward thickening of the Carnian strata (i.e. Snadd Formation) is described in Smelror et al. (2009) and is attributed to an increased sediment infill from the Fennoscandian shield and a possible additional Laurentian source from the west, marking a change in the Barents Shelf palaeogeography. Although this description is on a more regional scale, the same westward thickening is observed in Figure 4.12.

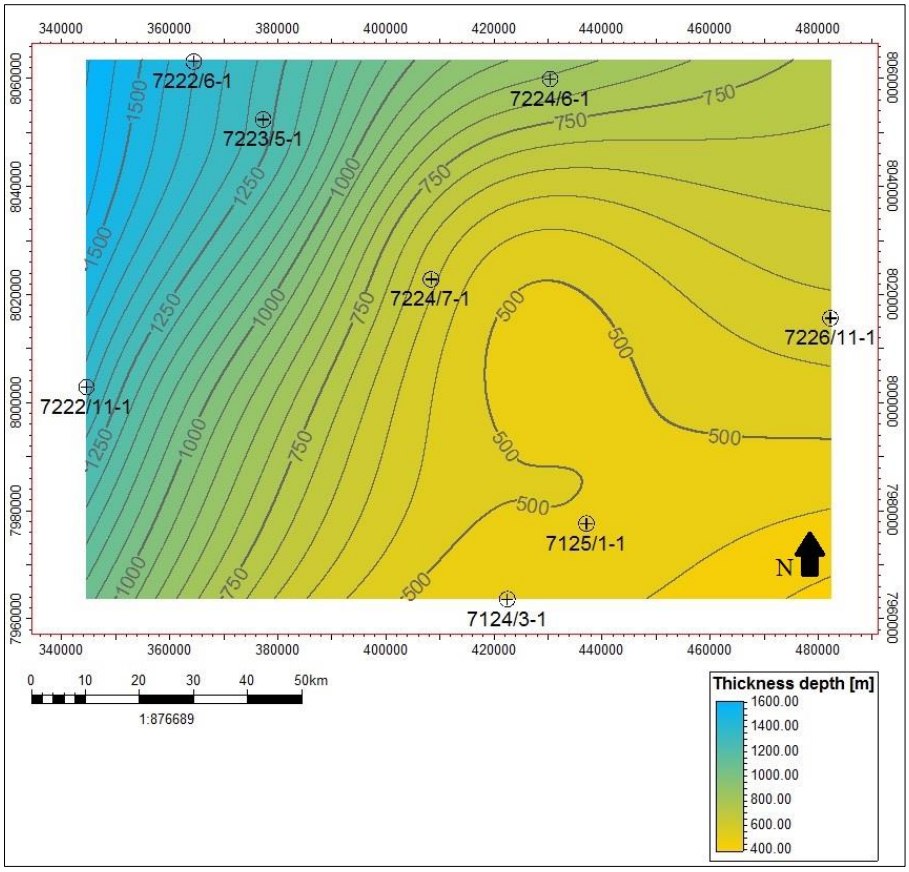

Figure 4.12. Contour map showing the thickness of the Snadd Formation, i.e. the difference in depth between the Kobbe and Snadd formations. Aside from interpolation method uncertainty, note trend of thickening towards the west/north-west in the Loppa High area.

An observable trend from the analysis of the Snadd Formation is that the reservoir intervals displaying the most favorable values for shale volume, porosity and net-to-gross reservoir are situated in the upper part of the formation. This trend appears to hold true in all wells except for 7222/6-1 and 7224/7-1 where there have not been identified reservoirs of good quality. Another clear exception to the trend is found in well 7223/5-1 where a good reservoir of 60 m is found in the lower part of the formation. This well is drilled on the same prospect as 7222/6-1 (Obesum), but sufficient hydrocarbon saturation levels were not interpreted in what is assumed to be the equivalent reservoir intervals to the 7222/6-1 pay zone. Reservoirs of fair quality and thickness (up to ~40 m of sandier intervals) can be identified in lower levels also, e.g. in well 7224/6-1, partly in the lowermost reservoir in well 7222/11-1, in well 7226/11-1, and in well 7222/6-1 which contains indications of hydrocarbons. These do however not exhibit the same apparent quality of reservoir properties when compared to the upper part of the formation.

Depositional development and facies discrimination of the Snadd Formation has been interpreted in Klausen et al. (2015) and compared to this study for a better understanding of the intervals that usually contain higher quality reservoirs. An example excerpt from well 7222/11-1 in this study displayed alongside the published facies interpretation (Figure 4.13) gives good correlation between cleaner intervals of the reservoirs analyzed and sandy facies, i.e. marginal marine and shoreface facies, and fluvial channel deposits within a coastal plain

setting. Larger scale upwards coarsening successions can be identified and correlated to transitions from marine/shelf deposition to shallow marine deposits (one example indicated in Figure 4.13). Conspicuous spikes in the neutron and density log of the Snadd Formation e.g. in well 7226/11-1 could be attributed to coal layers, which have very low density compared to sand and shale. The intervals containing these spikes are often consistent with interpreted floodplain facies depth levels from Klausen et al. (2015). Figure 4.13 also shows the temporal fluctuations of the depositional environment of the Snadd Formation, i.e. multiple changes from marine to non-marine deposition. The mentioned trend of good upper Snadd reservoirs can seemingly often be related to shallow marine and fluvial/coastal plain depositional environments interpreted to be present in the location of multiple wells prior to a regional Norian flooding. Correlation of good quality reservoirs across wells can prove challenging, especially when considering fluvial sandstone bodies that is not necessarily present continuously over large areas. As an example of the local extent, a seismic amplitude map showing the channelized sandstone bodies in the Upper Snadd Formation of the Loppa High and the location of well 7222/11-1 is included in (Figure 4.14). The width of the channel is approximately 1000 m, and the sandstone body is interpreted as deposition in a major distributary channel in a lower delta plain environment (Ryseth 2014).

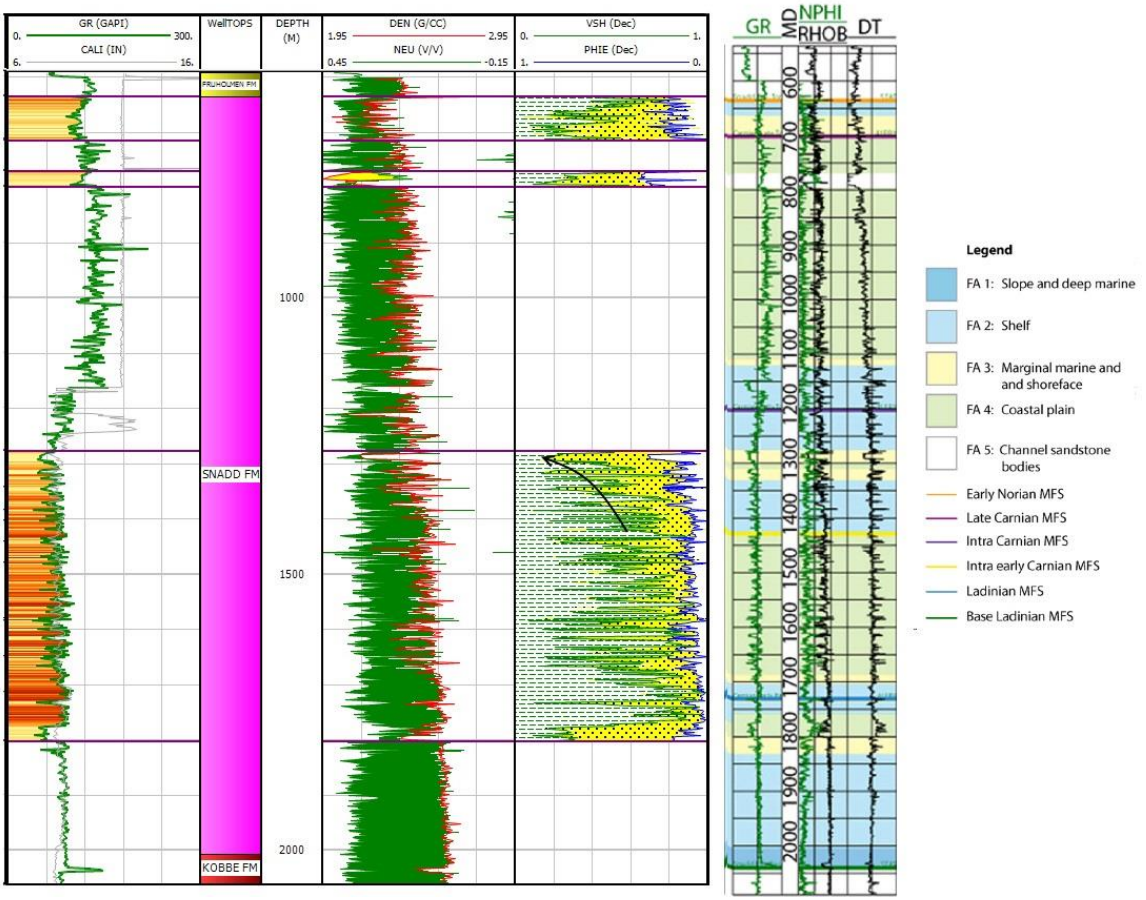

Figure 4.13. Snadd Formation facies interpretations compared to reservoir intervals in well 7222/11-1. Facies interpreted log and legend modified from Klausen et al. (2015).

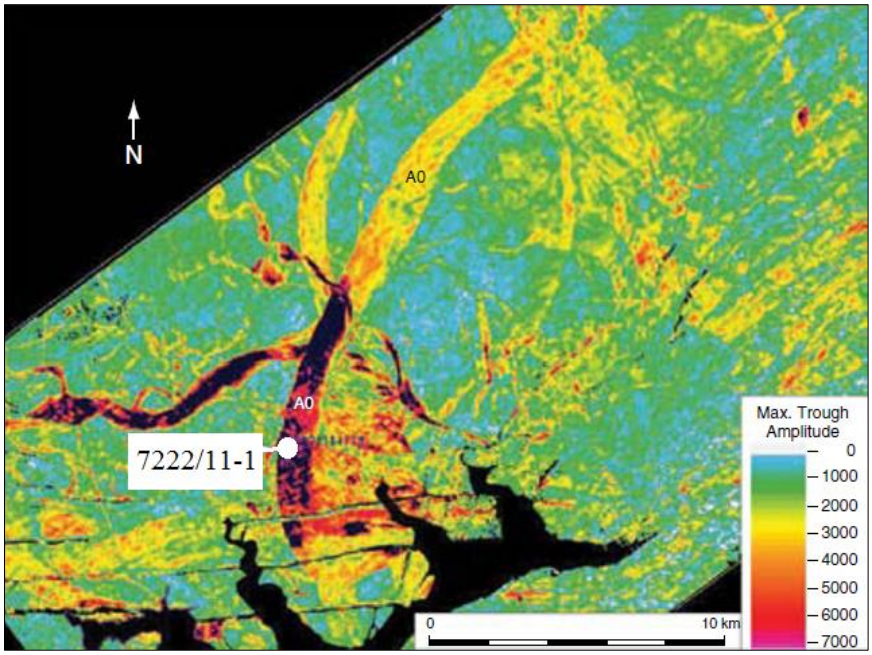

Figure 4.14. Seismic amplitude map showing upper Snadd channel sandstone bodies, south-east Loppa High (modified from Ryseth et al. 2014).

4.2.2 Jurassic reservoirs

The Stø reservoir in well 7125/1-1 is the reservoir of highest apparent quality in the present study, which basically consists of 122 m of clean sandstone with high porosity. The Tubåen Formation is however more consistently excellent with regard to petrophysical properties across all encounters in analyzed wells, whereas the Stø Formation appears to both deteriorate and thin towards the north and east based on the interpretation of wells 7224/7-1 and 7226/11-1. Tubåen is described to be of fluvial, deltaic origin, and the main sandstone bodies result from diverse high-energy fluvial and distributary channels (Ryseth 2014). Both formations are recorded in well 7223/5-1 although with insufficient data for a thorough analysis, in which the Stø Formation appears to constitute a thin (7 m), clean section, and Tubåen appears as a slightly thicker (16 m) and more shaley section. As a whole, the Tubåen Formation appears to thin towards the south or south-west. An undifferentiated section of the Kapp Toscana Group in well 7222/11-1 of 138 m indicates that Stø and Tubåen could both have a presence in the south-eastern edge of the Loppa High near the Hammerfest Basin.

With regard to permeability, the Tubåen reservoir in well 7124/3-1 yields higher estimates for permeability in comparison to the Kobbe reservoir (Figure 4.8) due to higher porosity. The reason for the logarithmic-linear relation displaying an almost perfectly linear trend in the porosity-permeability domain is that irreducible water saturation is not an input parameter in the equation, i.e. porosity is the only variable. Higher spread in the data for the three remaining equations does however not seem to be explained by the water saturation, as the span in values for this parameter is larger in the Kobbe reservoir.

4.3 Uncertainties

Many uncertainties arise when doing petrophysical analysis, as it involves multiple equations and estimations which attempt to relate measured properties to geological parameters. Results and subsequent discussion of the findings are based on the assumption that values and estimates are adequate approximations to reality.

4.3.1 General uncertainties

- Overall accuracy of well log measurements and following calculated properties is not perfect even when measured in good conditions, e.g. according to Chopra and Castagna (2014) porosity is commonly known only within ±2 porosity units, and water saturation is frequently estimated with an error of up to 20%.
- The gamma ray log can be affected by borehole conditions and radioactive elements.
- The fraction of clay in shale is assumed as a constant value of 0.7, which is as mentioned a simplification (Bhuyan and Passey 1994).
- Bias is a factor in the interpretation and selection of shale and sand baselines.
- The density log can display invalid readings in rough boreholes or when using heavy drilling muds (Asquith and Krygowski 2004b).
- S_w calculations are not accurate as they are dependent on a number of uncertain factors, like the use of apparent formation water resistivity, apparent mud filtrate resistivity, as well as choice of the neutron and density values for pure shale which is integrated in porosity calculations.
- Equations used for permeability are simplified and does not take more complex parameters into account which influence permeability like coordination number, pore shape/size, tortuosity, etc. If utilizing more advanced equations, e.g. the Kozeny-Carman equation (Mondol et al. 2008), more parameters could be included but the complexity of the equation and of choosing input values increases. Methods for predicting permeability should be calibrated to core to be reliable (Crain 2015).
- Variations in drilling mud used can influence what is recorded in the logs, as the depth of investigation is not the same for all measuring devices. Drilling fluid used may vary from well to well or at different depth levels within the same well. Corrections that are applied to negate these effects can introduce uncertainty (Mondol 2015b).

4.3.2 Study-specific uncertainties

In well 7226/11-1 the porosity estimates were in some areas influenced by the neutron and density log displaying erratic values unrealistic for shale-sand sequences. This can possibly be due to presence of coal layers. The caliper log in well 7124/3-1 shows lots of erroneous readings, meaning that the trustworthiness of other measurements could be compromised and the accuracy of further calculations is less certain.

Generally in the Snadd Formation, larger reservoir zones are often picked in middle parts of the formation due to the heterogeneity of the rocks, which can contribute to increase average shale volume values and decrease porosity and net-to-gross. In addition to the presented reservoir zones, a good possibility exists for small potential reservoirs to have been overlooked. E.g. in well 7226/11-1 only relatively small zones of potentially sufficient

reservoir quality have been analyzed, but the formation contains additional thin stringers of sandy lithology which possibly could be prospective within the dominantly shaley formation. Individually, they are deemed of insufficient thickness to be included in subsequent analysis.

Chapter 5: Rock Physics Diagnostics

In this chapter, the results of the rock physics diagnostics are presented and discussed. The main objectives are to link elastic properties such as V_p, V_s, and acoustic impedance to porosity, microstructure of the reservoir rocks of different formations and depths, and fluid effects. Theoretical background behind all models and templates utilized in this study are described in more detail in chapter 3. The uplift history of the SW Barents Sea introduces uncertainty to the use of standard templatesd due to maximum burial being greater than the present burial depth. The intention of this approach is to compare with these standard models in order to understand their validity for use in this study area. It is also important to keep in mind that predicted V_s (estimated from measured V_p) is used in half of the studied wells, as well as each model's validity for only certain rock types (e.g. only for reservoir sandstones). Results will be compared to the interpretations made during the petrophysical analysis for validation of the consistency of these two different but closely linked approaches.

5.1 Results

5.1.1 V_s estimation

Published V_p-V_s relations such as Castagna et al. (1985) and Krief et al. (1990) yield similar results as when using the relation derived from the data in this study (red curves in Figure 5.1). These all correspond reasonably well with measured V_s (blue curve) in both shaley and sandy intervals, but differ in hydrocarbon saturated intervals (Figure 5.1). V_s predicted from data in this study is closest to measured V_s in the hydrocarbon interval in the left example (7222/11-1), whereas the Krief relation is slightly closer in the right example (7224/6-1).

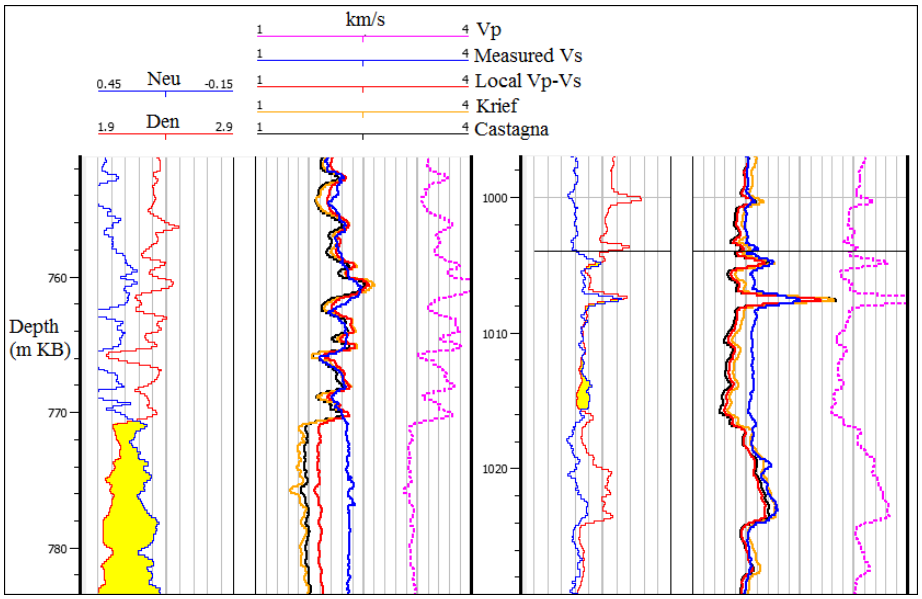

Figure 5.1. Difference in relations used to estimate V_s shown in both water-bearing and gas-bearing rocks. The V_s relation derived from the data in this study is reasonably well suited to predict V_s in both examples, except for in the hydrocarbon reservoir.

Estimated V_s is still not properly useable in crossplots and templates requiring measured V_s data, as information about the relation between P- and S-wave velocities is not available and subsequent hydrocarbon effects and most lithology variations are not observable. This leaves the wells not containing measured V_s to mainly be interpretable in the velocity-porosity domain.

5.1.2 Velocity versus porosity relationship

5.1.2.1 Han's (1986) empirical relations for shaley sandstones

Figure 5.2 shows data from all reservoir intervals of the Kobbe, Snadd, Tubåen and Stø Formations, overlain by Han's lines for V_p relations to porosity considering variable clay volume. The shallower Jurassic reservoirs plot to the lower right in this plot, the data points of the Kobbe reservoir drag towards the upper left, whereas the large amount of data points from Snadd reservoirs spreads widely both in porosity range and across the theoretical lines. Large portions of the Snadd and Kobbe reservoirs also plot significantly lower than Han's estimated 50% clay volume line, even though all plotted points are estimated from the petrophysical analysis to contain less than 50% shale. The green and red line below the purple Han lines in the Kobbe Formation frame indicate a clay volume of 50% with Han's relations for pressures of 20 MPa and 10 MPa, respectively. All data points are still not captured when attempting to vary the pressure assumptions of the model (see Figure D.1 for depth color code).

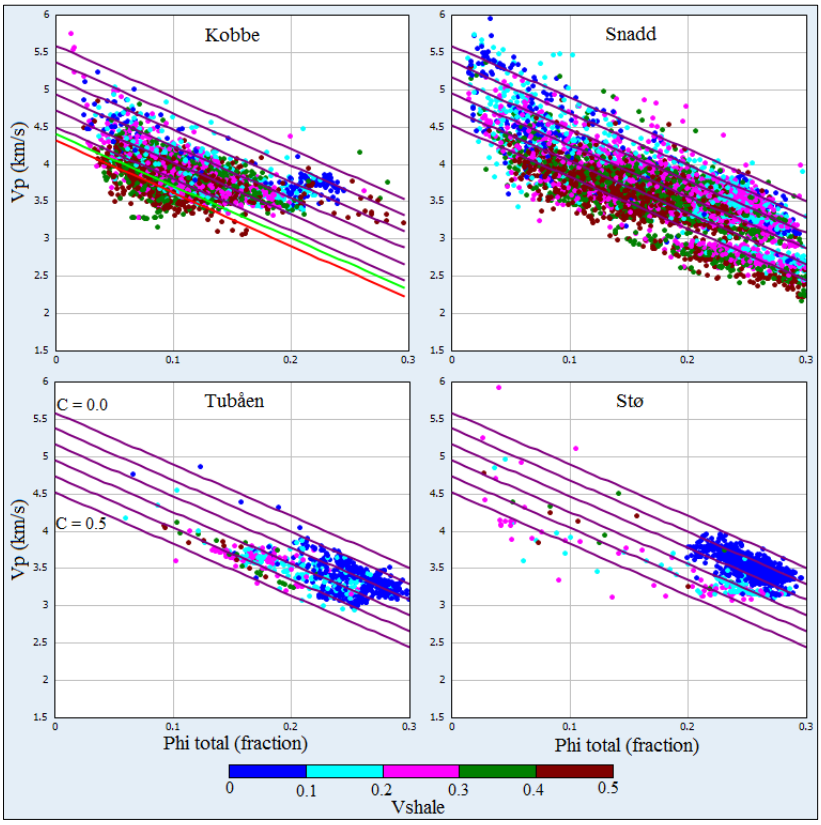

Figure 5.2. Comparison of all reservoirs separated into formations, relative to Han's (1986) empirical equations. Color coded by V_{sh} estimated in petrophysical analysis.

5.1.2.2 Rock physics cement models

Rock physics cement models are used to infer microstructure of rocks from velocity-porosity data. If plotting velocity against porosity for sands and shales at different burial depth, the effects of diagenesis and sorting can be observed (Avseth et al. 1999). Figure 5.3 shows a plot of one relatively clean upper Snadd reservoir with overlying shale and one more heterogeneous Kobbe reservoir of multiple upwards-coarsening sequences in well 7223/5-1. The lower right cluster of points represents the shallow sand and shale of the Snadd Formation, at depth level ~600-700 m. The upper left cluster consists of points from the Kobbe Formation representing deeper sandstones where depth varies between 2230 and 2340 m.

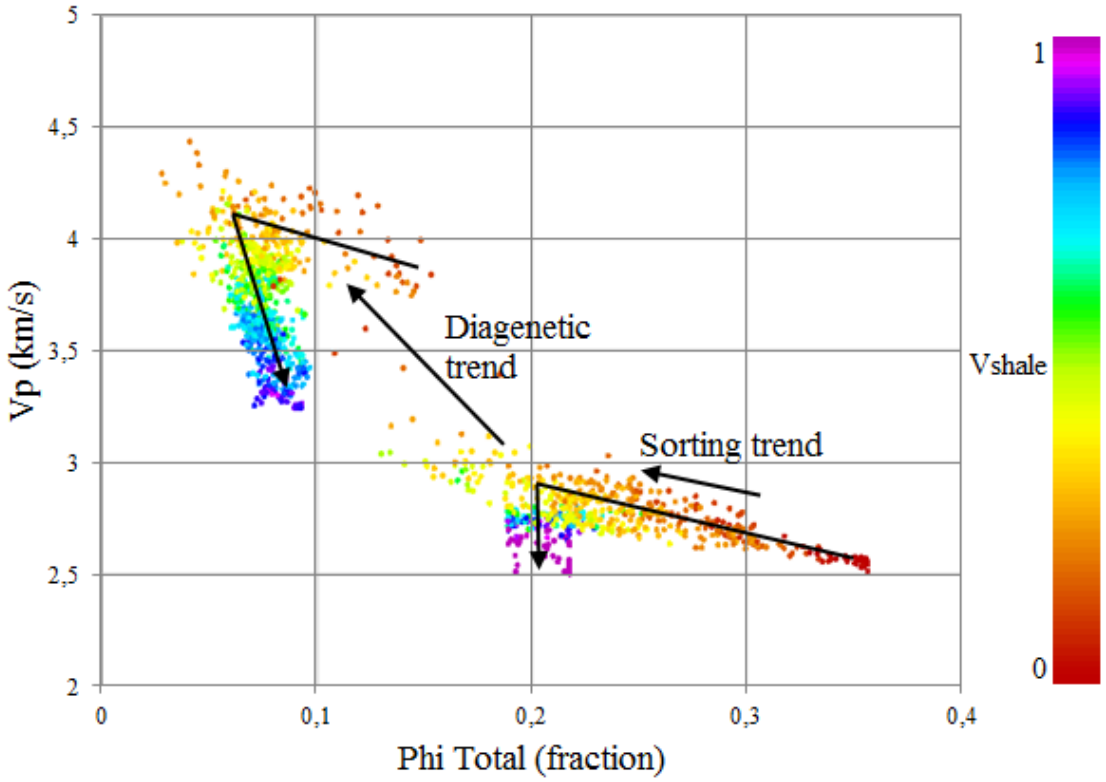

Figure 5.3. Crossplot of V_p versus porosity with data from Snadd and Kobbe in well 7223/5-1, showing diagenetic and sorting trends. Color coded by V_{sh} estimated by petrophysical analysis.

Arrows through the clusters represent increasing shale content. The drop in velocity when increasing shale volume from around 50% to 100% is larger in the deeply buried reservoir than in the shallow one. Sandy points of either cluster display slightly increasing velocity with lower porosity, i.e. an effect of increasing shale volume and/or deteriorating sorting, corresponding to the arrow showing the sorting trend (Avseth et al. 1999). The separation of each unit as a whole can be interpreted as an effect of difference in depth, reflecting burial compaction and cementation. This is represented by the arrow showing the diagenetic trend. These two trends shown are the essence of velocity-porosity models and templates used to

evaluate sorting, cementation and compaction of studied reservoirs, and also gives an idea where given reservoirs should plot relative to each other based on burial depth.

If plotted together with an overlay of cement models (Figure 5.4), the shallow Snadd reservoir can be seen plotting along a constant cement trend, but only up to a certain fraction of shale content (left plot). The deviation is not unexpected as the models are designated to capture only certain sandstone trends (Avseth et al. 2005). Reducing the data range to include only sandy lithology, i.e. V_{sh} <= 50%, the trend in this shallow reservoir is more apparent (right plot). Approximately half of the deeper Kobbe reservoir plots above the upper constant cement trend line, with the shalier sand shifted towards lower porosity in between the lines.

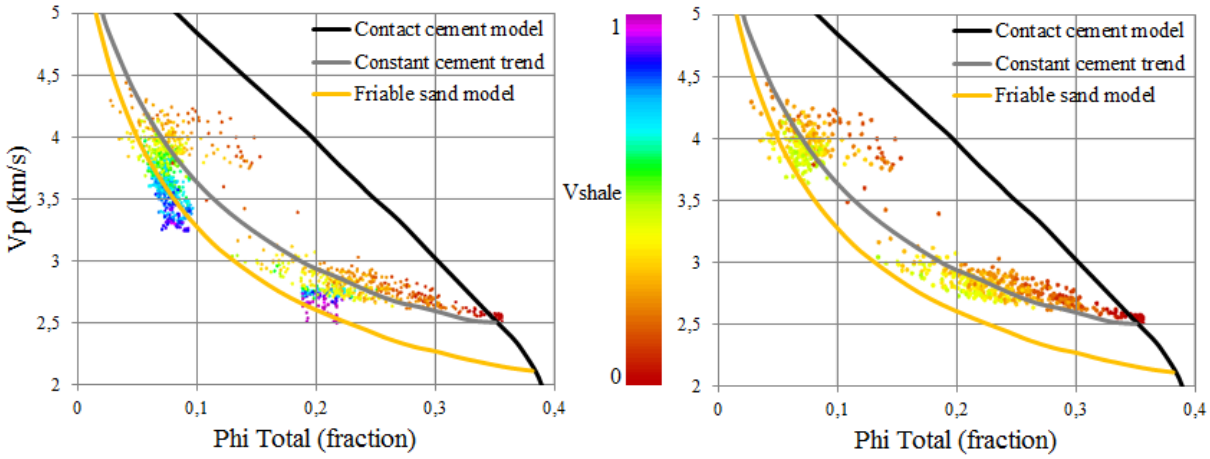

Figure 5.4. Crossplot of V_p versus porosity for the Snadd and Kobbe reservoirs and shale from well 7223/5-1, with superimposed rock physics cement models. Note drop in velocity in shaley points, as well as how Kobbe reservoir data could be captured if trend lines representing higher cement percentages were included.

A slightly different approach taken to examine reservoir trends is taken in Figure 5.5, where reservoir intervals are plotted according to present burial depth without age being taken into account, i.e. not segregating different formations. Here data from the intervals 600-800 m and 2200-2400 m are shown, and are clearly separated. The data is displayed in both a V_p-porosity plot and a V_s-porosity plot, with corresponding cement model templates. Points can be observed plotting slightly different in the V_s-porosity domain, especially in the higher shale volume fraction. Data from 600-800 m drag below the friable sand model line in the lower plot, whereas in the upper plot the data follows the constant cement trend more closely. Parts of the data from the reservoirs between 2200 m and 2400 m plot below the friable sand model line in the lower crossplot.

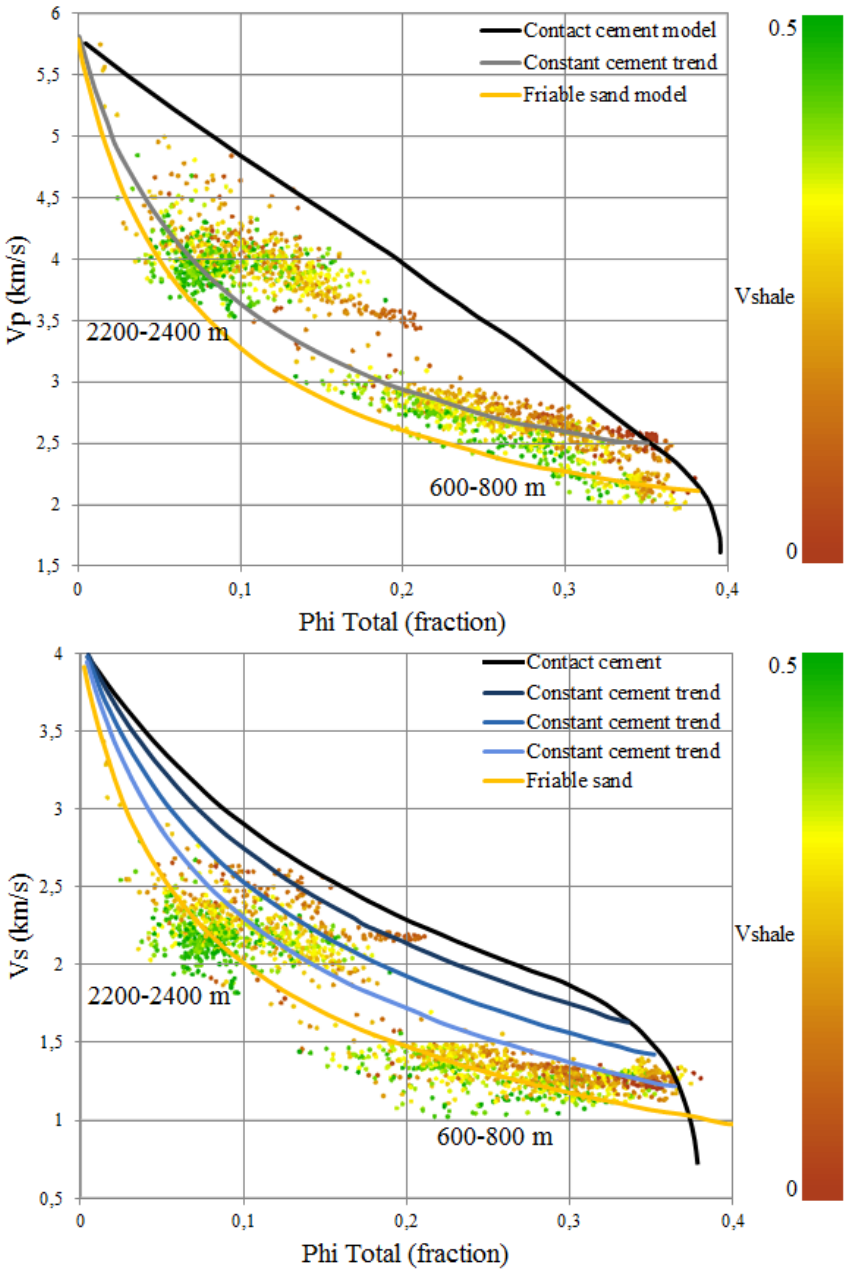

Figure 5.5. Crossplots with all reservoir data from 600-800 m and 2200-2400 m, in the V_p-porosity domain (top) and V_s-porosity domain (bottom). Corresponding rock physics cement models are superimposed, and data is colored by shale volume.

Extending the range, all data with estimated shale volume below 50% is plotted in Figure 5.6, in the V_p-porosity domain. Data is color coded by depth in the lower plot, and in the upper plot the data is colored by shale volume and the cement models template is included. A large portion of the data plots above a V_p of 3 km/s and is indistinguishable from each other, but a lower cluster is separated from the rest of the data, outlined in the blue ellipse in the upper plot. These are shallow reservoirs of the Snadd Formation in wells 7222/11-1 and 7223/5-1, situated between 600 and 800 m depth. Note that the lowermost part of this cluster, which plots along the friable sand model, is data from hydrocarbon-influenced intervals which

generally results in additionally lowered P-wave velocity. A possible interpretation of the separation between reservoirs influenced by mechanical (or a low degree of chemical compaction) and a significantly higher degree of chemical compaction is shown by the stippled black line.

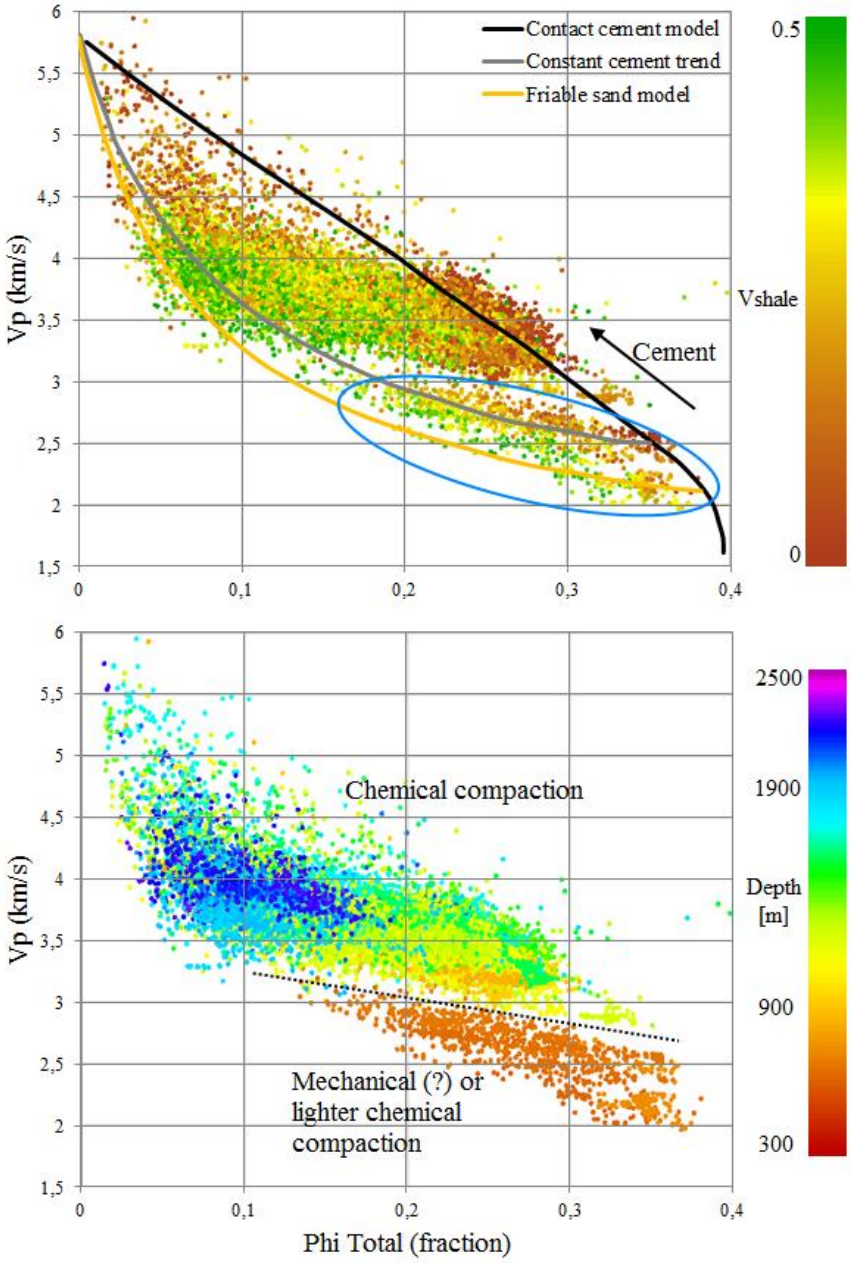

Figure 5.6. Crossplot of V_p versus porosity of all reservoir data with shale volume estimated below 50%. Note separation between lower cluster below ~3 km/s velocity. Stippled line indicates border between mechanically compacted or more likely lightly cemented rocks and rocks that are more heavily influenced by chemical compaction and cementation.

Further search for the transition between mechanical and chemical compaction is conducted in crossplots of shear modulus versus density, with shale data from well 7224/6-1 (Arenaria,

Figure 5.7). A knee-point in the data trend is identified and roughly indicated with stipled black lines, assumed to be descriptive of difference in compaction trends. An identical plot only with all data from well 7222/11-1 (Caurus) is shown in Figure 5.8. Thick shale sequences of almost uniform density around 2.6 g/cm^3 characterize the lower part of the Snadd Formation and the Kobbe Formation in well 7222/11-1 (approximately 1800 m to TD). This explains the straight line behavior of data points of the deeper intervals in the crossplot (blue and magenta points, Figure 5.8).

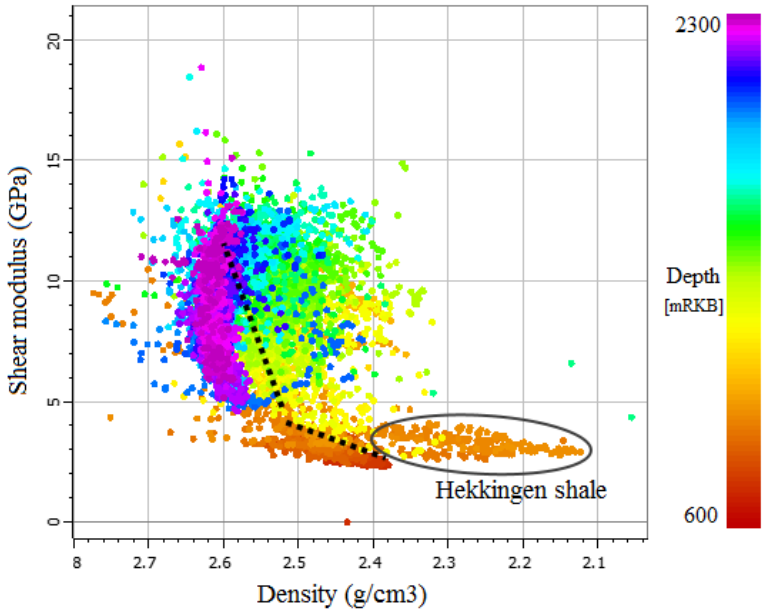

Figure 5.7. Crossplot of shear modulus versus density, with data from mainly shales in well 7224/6-1. Data is color coded by depth.

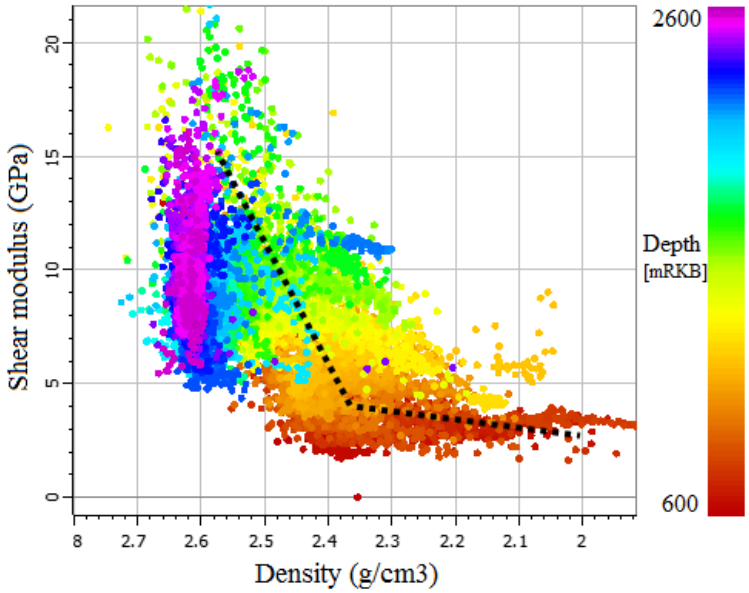

Figure 5.8. Crossplot of shear modulus versus density, with data from well 7222/11-1 between 600 and 2600 mRKB. All data is included, and is color coded by depth.

Marcussen et al. (2010) suggested a linear relation between velocity and cement volume (Eq. 3.24) for Etive sandstones in the North Sea. By using this relation, although with the difference in geological setting and sediment composition in mind, an expression of cement volume can be calculated from P-wave velocity data to compare with the findings in this study. In Figure 5.9 the estimated cement volume has been used as color code in a crossplot of V_p versus porosity. By examining the color coding, data below ~3 km/s velocity is indicated to contain less than 2% cement. Above 3 km/s, cement volume increases gradually in the direction of higher burial depth.

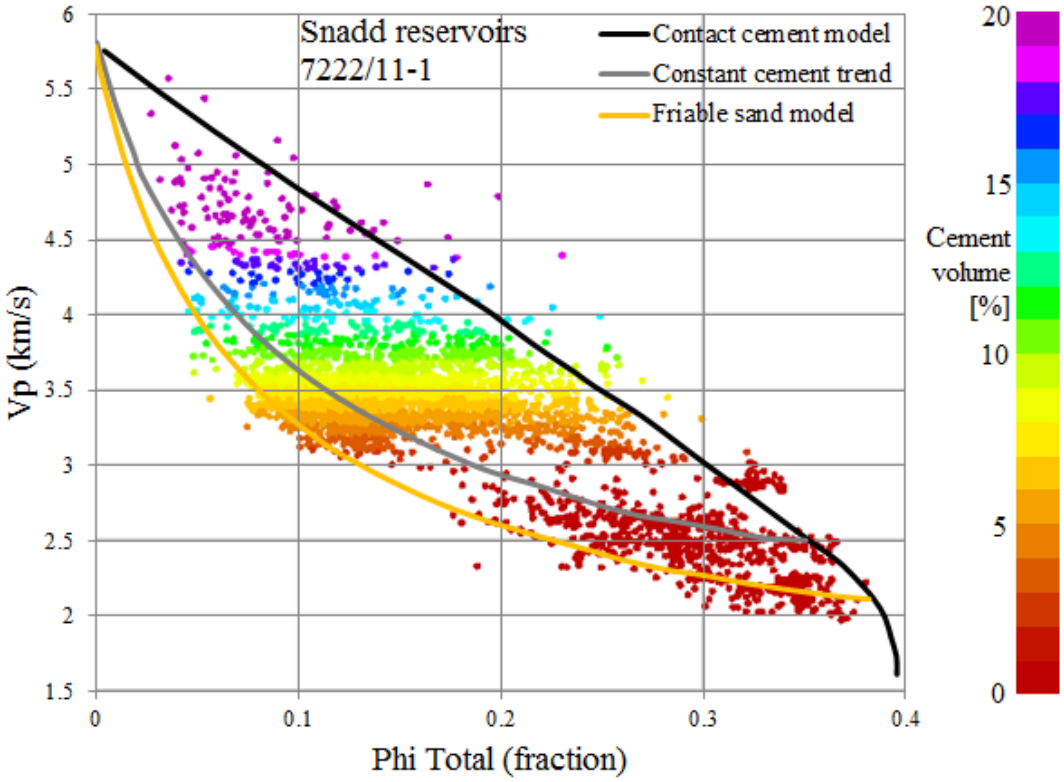

Figure 5.9. Crossplot of V_p versus porosity, with data from the Snadd Formation reservoirs in well 7222/11-1. Data is color coded by cement volume derived from the relation of Marcussen et al. 2010.

Identification of diagenetic and sorting trends is a crucial goal of using cement model templates. If investigating the difference between the clean Tubåen Formation and sand from the lowermost part of the Kobbe Formation, both in well 7226/11-1, data plots as shown in Figure 5.10.

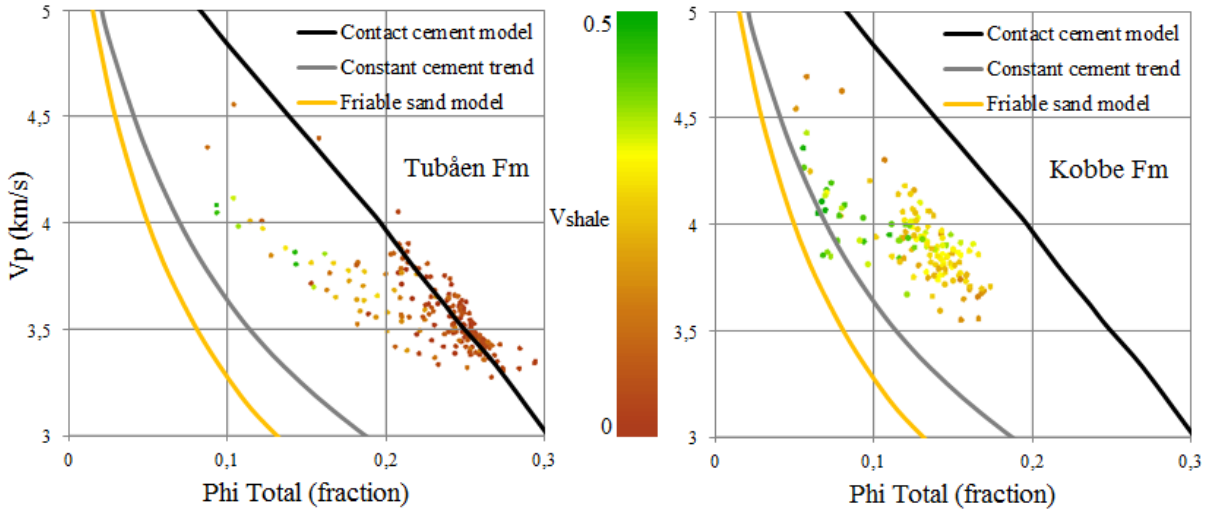

Figure 5.10. V_p versus porosity crossplot of data from the Tubåen Formation and the lowermost Kobbe reservoir in well 7226/11-1. Data is colored by V_{sh} and restricted to below 50%.

The difference in sorting or cleanliness, indicated by lowered porosity and slightly higher velocity is observable but not striking. There is approximately 1000 m separating the bottom of Tubåen from the top of this Kobbe reservoir, and Tubåen velocities range from ~3.3-4.0 km/s whereas most of the Kobbe data points in the right plot range from ~3.6-4.5 km/s. Respective total porosity values vary from 9 to 29% for Tubåen and 5% to 17% for Kobbe. If plotting data from the Stø Formation in well 7125/1-1, close to all data points plot along the contact cement model line and is indicated by the color code to be mostly homogeneous with regard to shale volume (Figure 5.11). If examining the right plot, the color coding reveals that deeper points plot more towards the lower right, i.e. lower along the contact cement line than the shallower points.

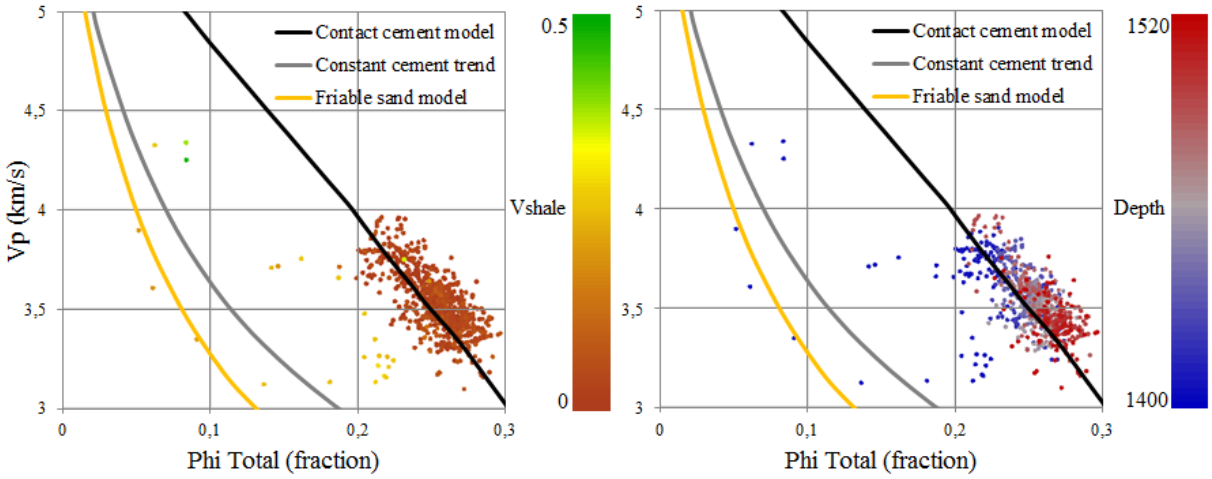

Figure 5.11. V_p versus porosity crossplot of data from the Stø Formation in well 7125/1-1. The left plot is color coded by V_{sh} and the right is color coded by depth. Note trend in depth along the contact cement line.

5.1.3 V_p versus V_s relationship

In Figure 5.12 a crossplot of V_p versus V_s is shown with data from wells 7222/11-1 (Caurus) and 7223/5-1 of one deep and one shallow Snadd Formation reservoir, exemplifying the effect of hydrocarbon in sands. The shallower reservoir (~800 m) shows more separation between brine and hydrocarbon sands than the deeper reservoir (~1600 m), which additionally is assumed to have lower hydrocarbon saturation.

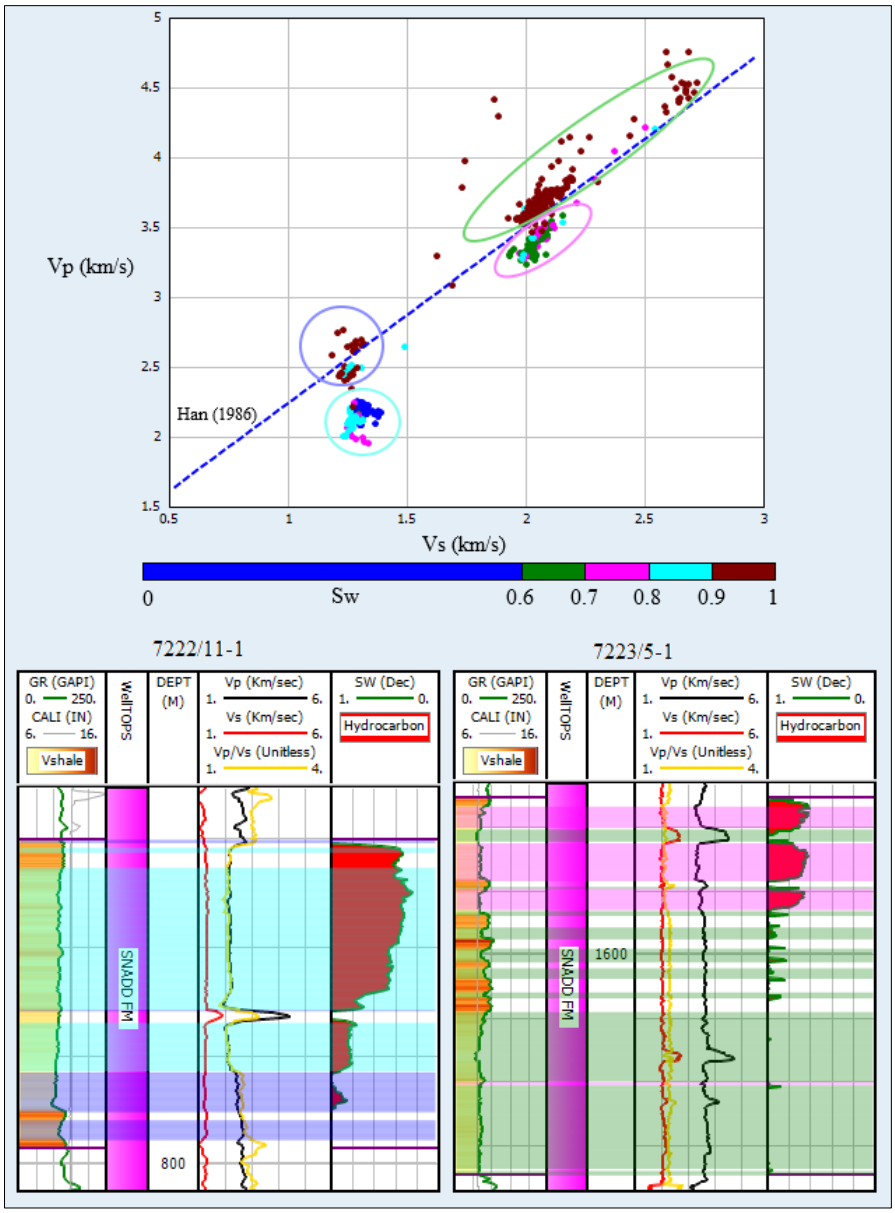

Figure 5.12. Crossplot of V_p versus V_s with data from one shallow and one deep Snadd reservoir, from well 7222/11-1 and 7223/5-1, respectively. Data is color coded by water saturation, with a scale intended to emphasize the effect only a small amount of hydrocarbon can have on the position of data points.

5.1.4 V_p/V_s versus AI relationship

The initial step of creating this rock physics template is computing moduli of the dry rock frame at critical porosity using Hertz-Mindlin theory. By calculating bulk modulus, shear modulus and density as a function of porosity and saturation (over a range of ϕ and S_w values), corresponding velocity values can be calculated for each porosity and water saturation. Finally, the V_p/V_s ratio and P-impedance ($\rho*V_p$) can be computed and plotted according to each possible porosity and saturation scenario. This process is conducted in the Hampson-Russell software, providing a "standard" template used consistently in all following crossplots. If once again plotting all data points with measured V_s as in Figure 3.16, the shale model in the RPT created for 20 MPa appears to be slightly better correlated with the shaley datapoints than the 40 MPa model, although still not perfectly as seen in Figure 5.13. Similar observations were made with regard to the models' ability to capture change in fluid saturation, and following figures are presented with templates related to 20 MPa effective pressure.

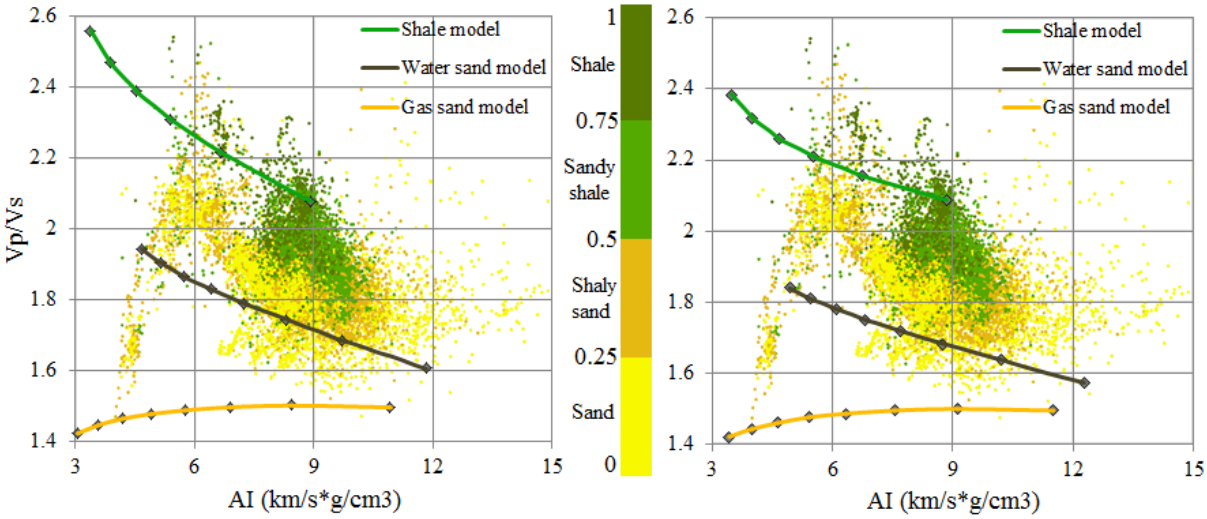

Figure 5.13. Crossplot of V_p/V_s versus acoustic impedance (AI), with data from all reservoirs in wells that have measured V_s (7222/6-1, 7222/11-1, 7223/5-1 and 7224/6-1). Left: template modelled for effective pressure 20 MPa. Right: 40 MPa. Data is color coded by shale volume (facies).

When picking two reservoirs of assumed low hydrocarbon saturation, one from the Snadd Formation in well 7223/5-1 (1575-1635 m) and one from the Tubåen Formation in well 7224/6-1 (1004-1064 m), both show separation between brine-saturated sections (plotting near the water-sand model) and gas saturated sections (plotting between the water-sand and gas-sand models). The cluster of water-sand data from Snadd plots mainly between AI = 8-9 km/s*g/cm^3 with a few data points dragging to higher impedance values, and between 1.7-1.9 for V_p/V_s ratio. The cap rock related to the Tubåen reservoir is the Fuglen Formation, and plots in the vicinity of the shale model. The intra Snadd cap rock in well 7223/5-1 plots between the water-sand model and the shale model (Figure 5.14).

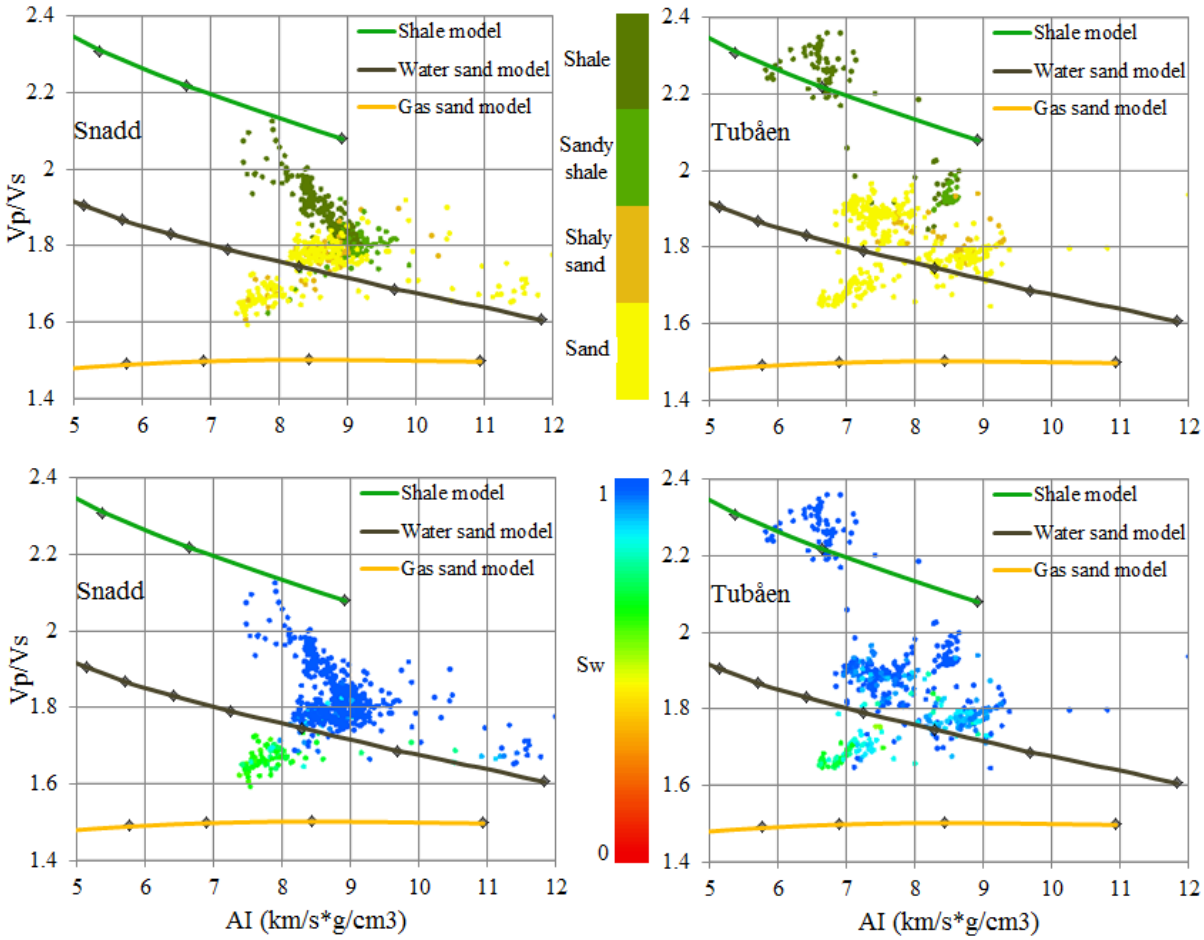

Figure 5.14. Crossplot of V_p/V_s versus acoustic impedance (AI), with data from reservoirs interpreted to have low levels of hydrocarbon saturation. Left plots correspond to a reservoir (1575-1635 m) of the Snadd Formation in well 7223/5-1, and the plots to the right represents a Tubåen reservoir (1004-1064 m) from well 7224/6-1. Data points are color coded by shale volume (facies) in the top row, and in the bottom row by water saturation.

A discrimination of oil and gas saturated intervals does not appear to be straightforward in the studied wells, even though an attempt was made to define an oil model to be included in the rock physics template. An example of a Kobbe Formation reservoir in well 7222/11-1 (Caurus discovery) is shown in Figure 5.15, where points from the oil and gas leg of the same reservoir plot practically on top of each other. The discrimination in color is based on a report of the gas-oil contact from the drilling company. Dark green and red points are oil and gas from the reservoir at 2210-2242 m depth, and light green points are from a thin oil leg in a reservoir ~100 m shallower, from 2100-2137 m. Some of these upper reservoir oil points also overlay gas points from the lower reservoir. Grey points are from more shaley, water-bearing surrounding rocks.

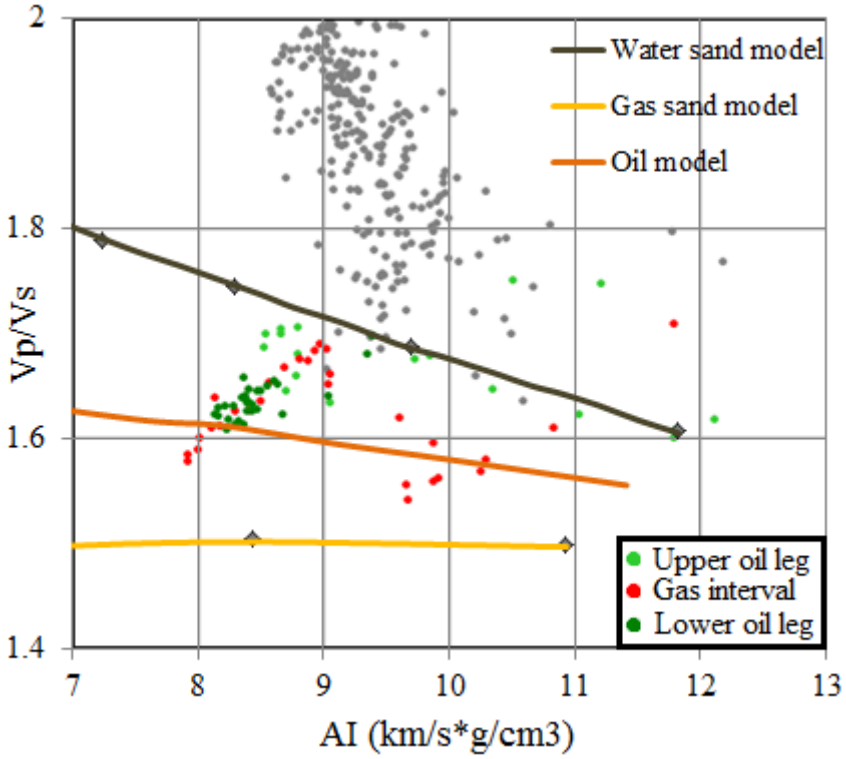

Figure 5.15. V_p/V_s versus acoustic impedance crossplot of data from oil and gas legs of the Kobbe Formation reservoirs in well 7222/11-1. Note – zoomed view, shale model not included.

When displaying data in the V_p/V_s versus P-impedance domain using estimated V_s as input, the data shows a clear trend of decreasing V_p/V_s ratio with increasing impedance, and has very little spread in the y-direction as expected. Figure 5.16 shows comparisons of using measured (right) and predicted (left) S-velocity as input, exemplified by data from the Kobbe Formation in well 7222/11-1 and the Snadd Formation in well 7223/5-1. Note ellipses in the lower plots which indicate deviating positioning of an assumedly low shale volume data. The effect of increasing cement as described in Ødegaard and Avseth (2004) is shown with the arrow in the lower right frame. Apparent trends of shaley and sandy data with decreasing impedance in the event of using predicted V_s is shown in the upper right frame. A certain gradual transition between the end-member lithologies is observable in the right plots with the help of color coding, and a slight separation in the data points is noticeable, though only below impedance values of 8-9 km/s*g/cm^3. Above this value the data is basically inseparable when trying to utilize estimated shear wave velocity. Separation in data points because of hydrocarbon effects is not visible in the right plots, only in the left plots where measured V_s data is used. Clean wet sand data (based on petrophysical analysis) plots along a trend slightly higher than the clean water-sand model in the lower left plot of the Snadd reservoir. In the upper left plot representing the Kobbe reservoir, the clean sand points are interpreted to be hydrocarbon-bearing from petrophysical analysis and plots below the water-sand line, the largest cluster positioned between ~8-9 km/s*g/cm^3. More shaley data points plot above the water sand line, towards increasingly higher V_p/V_s ratio and lower impedance with increasing shale volume. The respective clean water sand data in the plots on the right is positioned distinctly further above the water sand model.

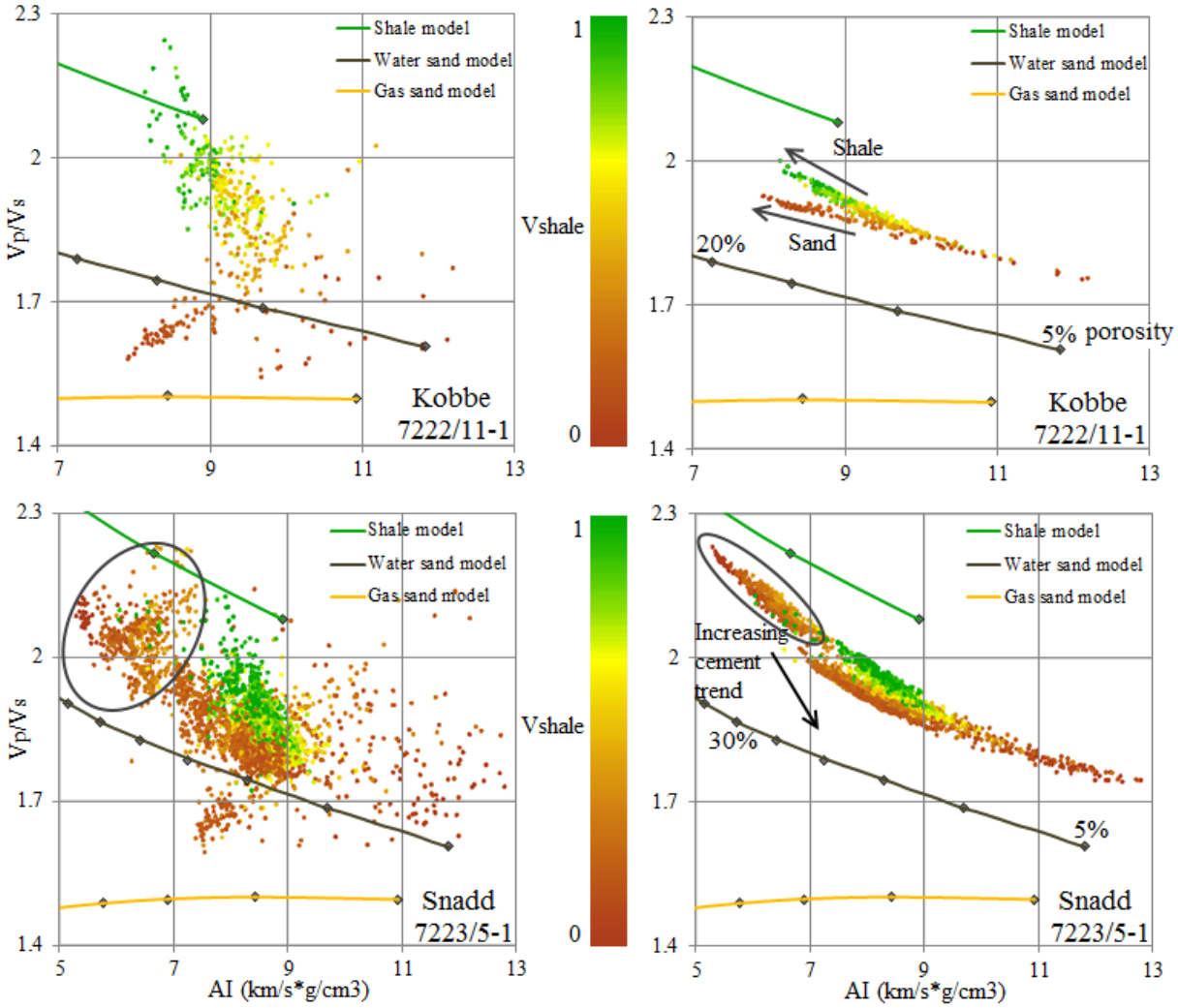

Figure 5.16. Crossplot of V_p/V_s versus AI, with data from all Kobbe reservoir data in well 7222/11-1 and all Snadd reservoir data in well 7223/5-1. Note different x-axis scale on lower plots. Ellipses indicate sandstone data which plot differently than what appears to be the general sandstone-trend. Increasing cement trend from Ødegaard and Avseth (2004).

The same Snadd Formation data from well 7223/5-1 is plotted in Figure 5.17 with color code according to cement volume estimated from the relation of Marcussen et al. (2010). Low cement volume is observed in the data points marked by the ellipses in Figure 5.16.

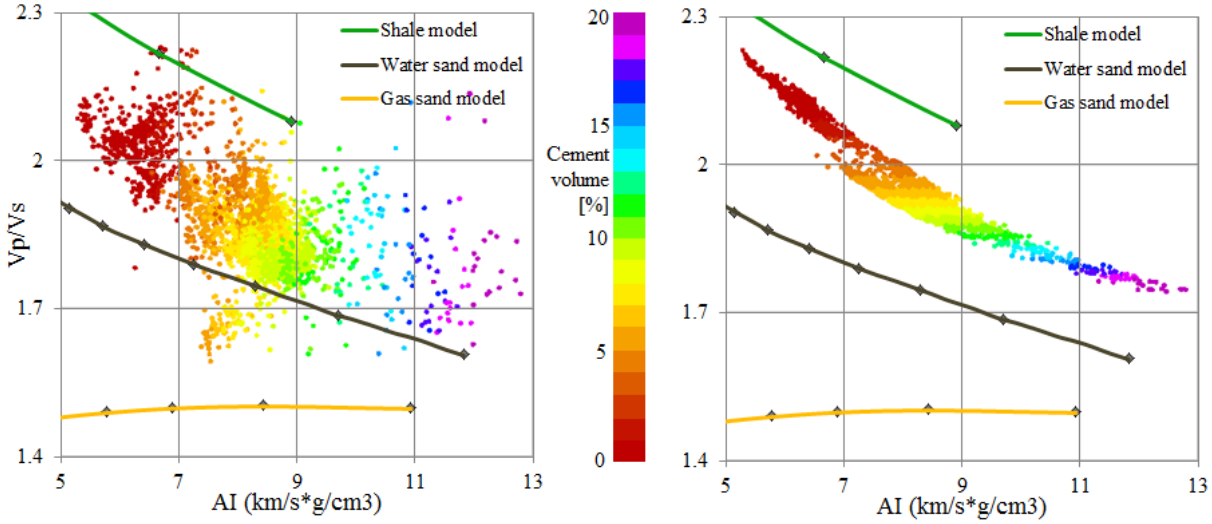

Figure 5.17. Crossplot of V_p/V_s versus AI, with data from all Snadd reservoir data in well 7223/5-1. Input V_s is measured (left) and predicted from V_p (right).

If more closely adapting the rock physics template to one particular reservoir, correlation between porosity calculated in petrophysical analysis versus what is inferred from the template, as well as the quantity of hydrocarbon saturation can be examined. Data from a shallow, hydrocarbon-bearing Snadd reservoir from the Caurus discovery in well 7222/11-1 displays color coded porosity approximately 5% higher than if interpreting template values (Figure 5.18). Only few points plot in areas of >10% gas saturation, whereas petrophysical analysis indicated average pay zone hydrocarbon saturation around 60%.

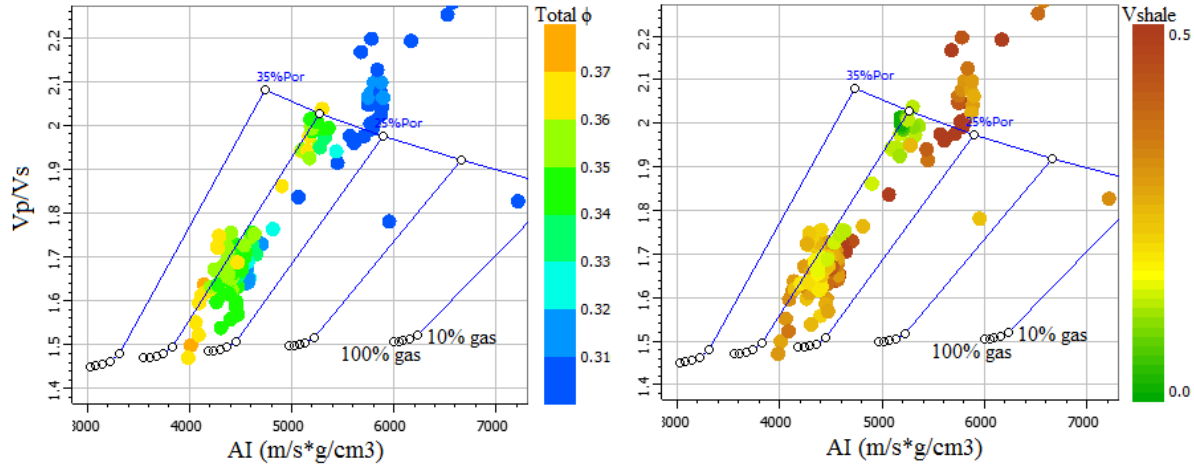

Figure 5.18. V_p/V_s versus AI crossplot with data from the Snadd Formation sandstone reservoir from 770-799 m (RKB) in well 7222/11-1. The reservoir is mostly gas-saturated with a lower thin zone of brine and oil shows. Data is color coded with porosity (left) and shale volume (right).

5.1.5 LMR crossplot

Crossplots of Lambda-Rho versus Mu-Rho display slight distinction between shaley and sandy intervals in the wells with measured V_s, although the transition is gradual and many points largely overlay each other (see Figure 3.18 in chapter 3). Points estimated in the petrophysical analysis to describe hydrocarbon-bearing intervals plot both in the theoretical regions of porous gas sand and shaly gas sand, i.e. below and above 20 GPa*g/cm^3 on the x-axis, respectively. In wells where V_s is estimated from the locally derived relation between V_p and V_s, data points plot in a constrained, almost linear manner, as the S-wave impedance in an input in the calculation of μρ ($Is = \rho * V_s$) and consequently provides little information in the LMR domain. If reducing the data volume, separation of shale, cemented sand, less cemented/shaley sand and gas sand points become clearer, as in Figure 5.19. This figure shows nice separation between shaley data points from the cap rock interval (Fuglen Formation), and sand data from the reservoir in the Tubåen Formation in well 7224/6-1 (all data between 980-1064 m). Clean, porous gas sand data points are separated from more shaley gas sand and sands of negligible hydrocarbon saturation.

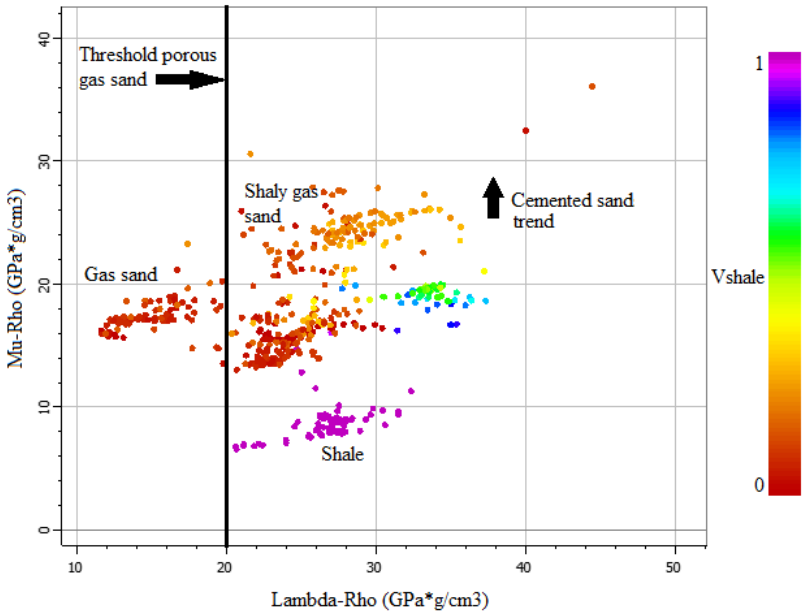

Figure 5.19. LMR crossplot of the Tubåen Formation in well 7224/6-1, with data from the overlying Fuglen Formation cap rock included. This reservoir is estimated to contain low saturation gas, a claim supported with information from the drilling company (NPD 2015b). Data is color coded by shale volume.

Data from two upper Snadd Formation reservoirs in well 7222/11-1 (Caurus) are plotted in Figure 5.20, with the left plot showing data from 636-715 m depth and the right plot representing data from 770-799 m. Both plots show data in proximity of the porous gas sand cutoff line from Goodway et al. (1997), in areas of low Mu-Rho and Lambda-Rho values.

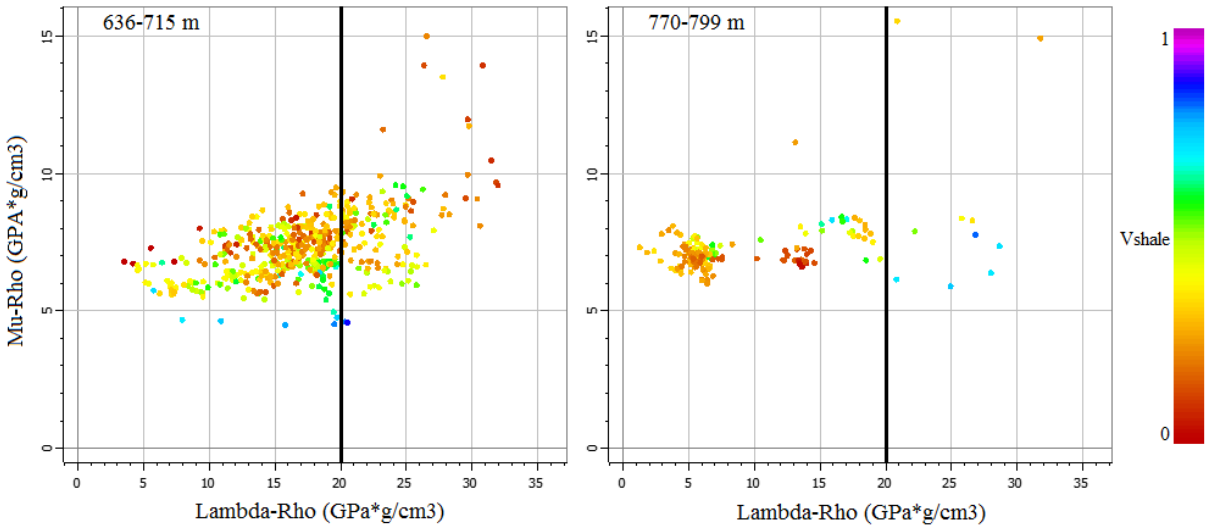

Figure 5.20. LMR crossplot with data from the two upper Snadd reservoirs in well 7222/11-1. The left plot represents the upper reservoir (636-715 m) and the right plot shows data from the lower reservoir (770-799 m). Note small scale compared to original template shown in chapter 3. Data colored by shale volume.

For investigating cementation across wells, the sandy part (V_{sh} < 0.5) of all Snadd Formation reservoir intervals has been plotted for each well with measured V_s in Figure 5.21, and color coded with cement volume estimated from Eq. 3.24 (Marcussen et al. 2010). More cemented sand is assumed to plot higher in the plot (increased Mu-Rho) than less cemented rocks (Goodway 2001). At the same time, if examining the color code cement trend based only on P-velocity, cement volume appear to increase from the lower left to the upper right. This trend is even more pronounced if displaying all data (both shale and sand) of the Snadd and Kobbe formations as in Figure 5.22. Data from well 7222/11-1 in Figure 5.21 displays the highest spread in data, but also the largest fraction of low estimated cement volume. Well 7224/6-1 data also plots within a wide Mu-Rho interval, and displays mostly intermediate to high estimated cement values. Well 7223/5-1 and 7222/6-1 shows relatively similar behavior to each other, plotting mainly below $\mu\rho$ = 50 GPa*g/cm^3, yet the former indicates a somewhat larger portion of low-cement data points through the coloring (reddish colors).

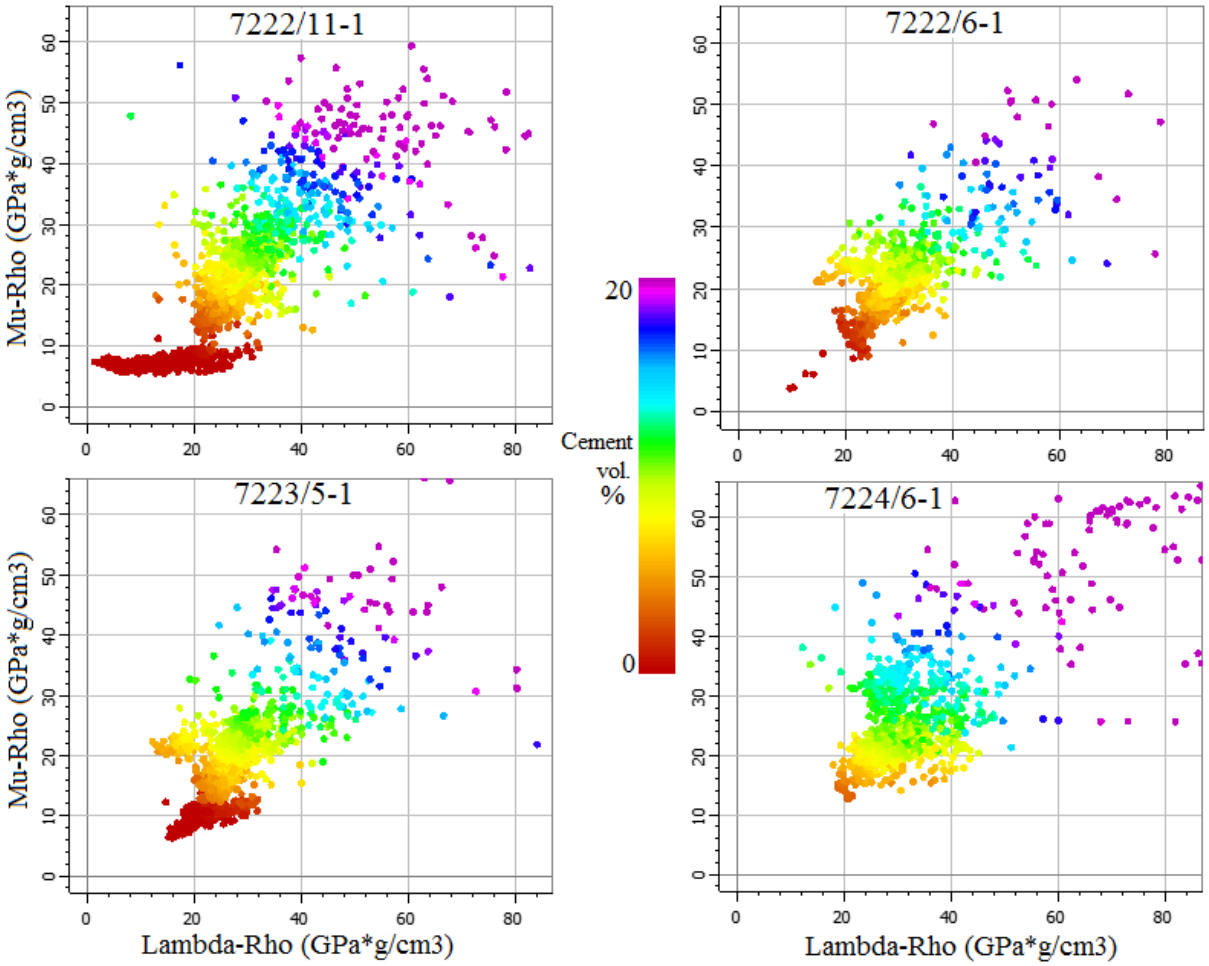

Figure 5.21. LMR crossplot of reservoir sandy data (V_{sh} < 0.5) of the Snadd Formation from wells with measured shear velocity. Data is color coded by cement volume after the relation between V_p and cement volume by Marcussen et al. (2010).

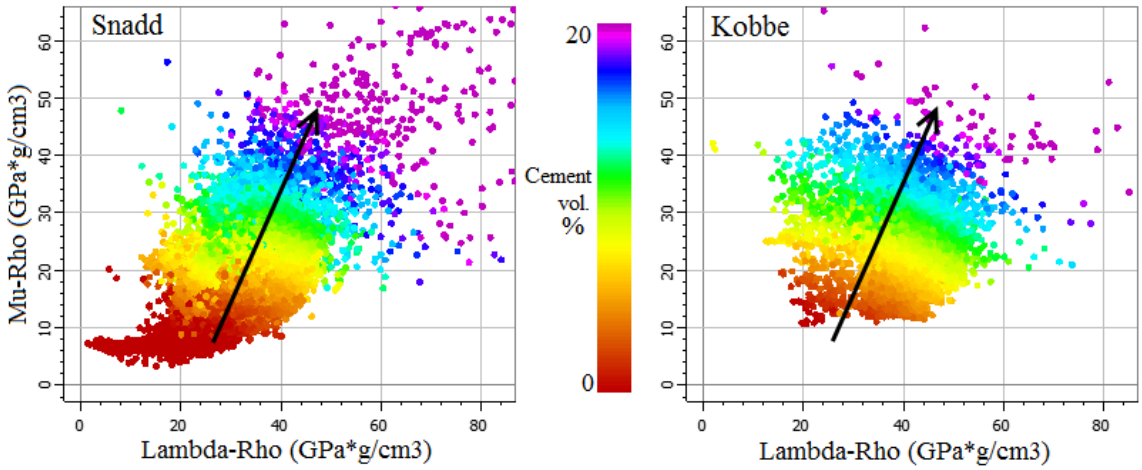

Figure 5.22. LMR crossplot of all data of the Snadd and Kobbe formations from wells with measured shear velocity, showing the color code trend of increasing cement volume after Marcussen et al. (2010).

Similarly, all Kobbe reservoir sands (V_{sh} < 0.5) are plotted in the LMR domain in Figure 5.23 and color coded by estimated cement volume.

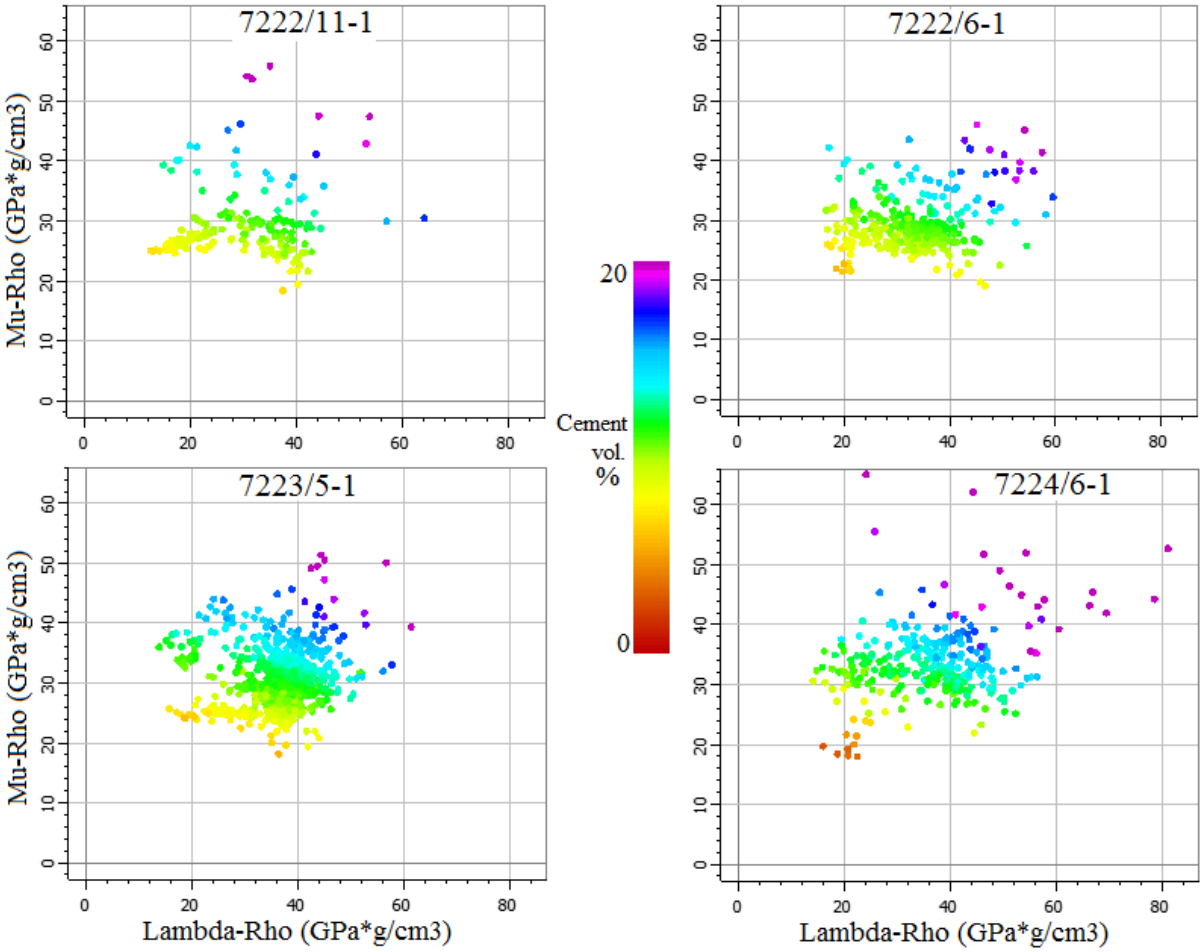

Figure 5.23. LMR crossplot of reservoir sandy data (V_{sh} < 0.5) of the Kobbe Formation from wells with measured shear velocity. Data is color coded by cement volume.

A lower amount of sandy data exists within the Kobbe Formation, related to thinner and fewer reservoir intervals having been identified. Opposed to the observations made about the Snadd Formation, all four wells indicate higher overall cement volume in the Kobbe reservoirs both by plotting higher relative to the y-axis and judging from the estimated cement volume coloring. Approximately all data plots between Mu-Rho values of 20 to 50 GPa*g/cm^3.

5.2 Discussion

5.2.1 Han's clay lines, sorting and shale volume

If examining Figure 5.2 showing Han's (1986) clay volume lines in the V_p-porosity domain, there is a certain trend in increasing shale volume towards the lower left, but it does by no means correspond very well to the superimposed divisions. The trend is most evident in the plot of the Stø Formation, but also in plots of the Kobbe and Snadd formations. Even though the lines of Han (1986) are meant to describe shaley sands, one reason for the discrepancy could be that shale volume from the petrophysical analysis is not necessarily in accordance with the definition of the variable "clay volume" from Han's paper. Alternatively, the predicted shale volume could in reality higher than what is interpreted in the petrophysical analysis. If interpolating clay volume from this plot alone, the Kobbe Formation reservoirs indicate practically no data with less than 10% clay, as only a few points plot between the 0% and 10% line. Most of the data plots from 20% clay and higher. The majority of the Tubåen and Stø reservoir data points plot between 10%-40% and 0%-30%, respectively, whereas the petrophysical analysis generally yielded lower estimates of shale (0-10%), especially in the Stø Formation. Increasing shale volume in the Tubåen reservoirs seem to rather shift points across the clay lines towards the left, similar to the sorting trend described in Figure 5.3.

Increasing shale volume from shaley sands to purer shales results in a drop in velocity which is, as described in Avseth et al. (1999), related to going from grain supported to clay supported sediments. This is observed as expected in data from this study in Figure 5.3 (bend in the arrows showing increasing shale volume). When extending the interpretation to include cement templates as in Figure 5.4, the Kobbe reservoir points could be captured by either a constant cement trend related to a higher degree of cement, or a contact-cement line representing poorer initial sorting and thereby lower critical porosity. The gradient of the trend in the data could decide which solution fits better. Furthermore, Figure 5.10 shows that even with difference in depth of 1 km, data from two different reservoirs (from the Kobbe and Tubåen Formations) plotted are to a large degree separated by difference in sorting/porosity. An implication of this is that the V_p-porosity domain can be useful to distinguish reservoirs of varying sorting from each other. However, the difference in velocity is more subtle, which means that if the sands had been of similar sorting/quality, they would plot in very similar areas. This could be an indication that identifying differences in cementation/diagenesis is more challenging unless the contrast between reservoirs are high, i.e. that they are at very different depth levels, perhaps ideally more than 1 km, or in different stages of cementation.

The Stø Formation in well 7125/1-1 is interpreted as a clean, thick sand interval which is similar in quality to the Tubåen Formation in well 7226/11-1. An interesting observation from Figure 5.11 is that the local depth trend in this formation seems opposite of what is expected, in terms of deeper points plotting in areas of higher porosity and lower velocity than data points representing rocks ~100 m shallower. Additionally the formation can be interpreted as well sorted, from the argument that points plot along the constant cement trend line, indicating that porosity loss and velocity increase is solely due to cementation. These interpretations are to an extent supported by examining core photos (Figure 5.24) and accompanying interpretation from the drilling company (NPD 2016), where the formation is described as predominantly fine to medium grained and well- to moderately-well sorted.

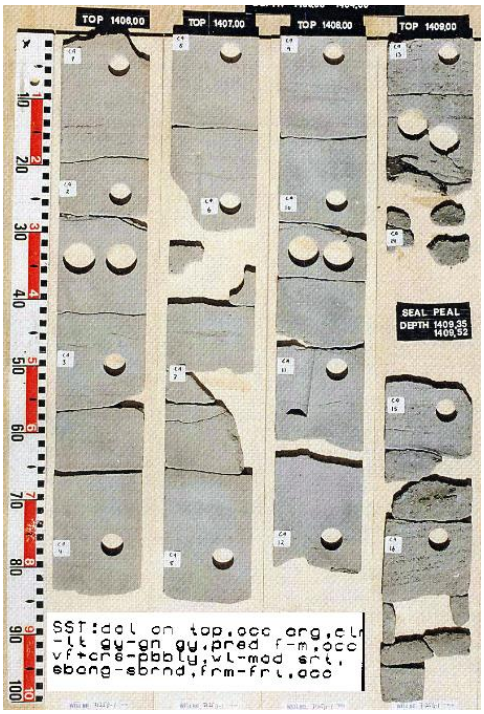

Figure 5.24. Core photo of the Stø Formation sandstone in well 7125/1-1, from depth 1406-1409 m. Description from the drilling company is included along the bottom. Modified from NPD (2015b).

When comparing information gathered from plotting in the V_p-porosity and V_s-porosity domains, i.e. the two plots shown in Figure 5.5, it is apparent that they do not provide entirely consistent information about the smaller scale specifics, like degree of cementation. This could firstly be related to how valid each template is for this dataset, and that they should be calibrated to a specific study area in order to be able to infer percentages of cement volume or an accurate degree of sorting. Secondly, the discrepancy can be related to the fact that the points do not have, and are not expected to have, the same relative positioning to each other in both domains. This would only be the case if the V_p/V_s ratio was constant and there were no hydrocarbon effects to account for. A reason for points in the deep reservoirs plotting below the friable sand model can be an effect of shale/clay content which drags points towards lower velocity (Avseth et al. 1999).

5.2.2 Compaction and cementation

In plots of velocity versus porosity with larger amounts of data from this study, e.g. from entire formations or as in Figure 5.6, it is not possible to clearly separate reservoirs of depths greater than 600-800 m from each other. A possible reason is that the shallowest reservoirs plot differently than all others can be related to uplift effects. Even though present depth of multiple reservoirs are rather shallow (below ~2 km), the maximum burial of these rocks are almost certainly in the domain of chemical compaction. With estimations of uplift in the range of ~1250-1600 m as discussed in chapter 2, the reservoirs which today are situated between 600 and 800 m possibly avoided or was only lightly influenced by chemical compaction even

at maximum burial. This could be a reason for the points plotting in areas of lower velocity, and could also to a certain extent explain the high porosity estimates derived in the petrophysical analysis for these particular reservoirs. Initial quartz precipitation is normally expected to occur at around 2 km depth, although it is largely dependent on the local temperature gradient as the process is controlled by temperature and expected to begin at 70-80^{o}C (Storvoll et al. 2005). The cement model templates (see Figure 5.5 and Figure 5.6) indicate that a small amount of cement is present even in the shallow reservoirs, which points more towards some influence of chemical compaction, and not exclusively mechanical compaction. When displaying all data in a plot of velocity versus depth (Figure C.1), it does not show a clear jump in velocity in well 7222/11-1 or well 7222/6-1 which is often associated with the transition from mechanical to chemical compaction (Mondol 2015b). In well 7223/5-1 this seems to occur slightly above the studied reservoir formations. If restricting the range to only shale data (Figure C.2 to C.9), possible transition lines can more readily be suggested.

The transition from mechanical to chemical compaction appears to occur at ~700 m present depth below sea floor, equal to ~990 m below KB, in well 7224/6-1 (Arenaria, Figure C.9). In well 7222/11-1 it is suggested around 750 mBSF, but in well 7222/6-1 the transition is still hard to interpret. A change in velocity can possibly be pinpointed in the data from well 7223/5-1 slightly above the Stø Formation or in the Kolmule Formation. In the remaining four wells, the same trend is observed as in well 7224/6-1, only with varying depth level for the transition. An interesting point discussed in the article of Storvoll et al. (2005) is that since chemical compaction can continue during exhumation, the deeply buried sediments have been influenced by temperatures above 70-80^{o}C for longer than the shallowly buried sediments. This can consequently increase the difference in cementation (and velocities) between shallow and deep sediments, and the uplift has thereby contributed to making the contrast between the younger and older sediments greater than if the burial was uninterrupted.

Another domain useable for discriminating rocks influenced by mechanical and chemical compaction is in a plot of shear modulus (μ) versus density or porosity (Storvoll and Brevik 2008; Baig et al. 2016). The plot showing data from well 7224/6-1 (Figure 5.7) can to some degree support the interpretation from the velocity-depth plots (Appendix C) in the sense that a certain steepening of the trend in the data with higher density (lower porosity) is observable. An implication of this is that some transitioning from mechanical (or lighter chemical) to chemical compaction should indeed be noticeable in this well, and by extension also in all other wells except possibly 7222/6-1 if the sudden velocity-increases are correctly interpreted. V_s data is unfortunately not available in the remaining four wells where an assumed transition has been observed, which could have been used to further quality control these observations. Assessing the μ versus ρ crossplot of Figure 5.8, it seems more likely that the transition in well 7222/11-1 is just difficult to observe in the V_p-depth domain rather than being non-existent, as there are clearly distinctions in the trend of the data above and below density values ~2.35 g/cm^3.

On closer inspection of the assumed transition in well 7224/6-1 by plotting mainly shale velocity data against depth and comparing to published compaction trends (Figure 5.25), a straight-forward estimate of uplift magnitude (~1400 m) corresponds well with Baig et al. (2016) for the location of this well. In turn, this can be argued to increase the confidence in or validity of using this well as a reference for confirming how the compaction transition would appear. When plotting shale data only from well 7222/11-1, where there was no clearly visible jump in velocity when using all data, a certain change in compaction trend can be

identified also in this well at approximately 750 m depth below sea floor (Figure 5.25). The estimated uplift value of minimum 1500 m from this V_p-depth plot results in slight discrepancy compared to estimates of Baig et al. (2016) of around 1325 m.

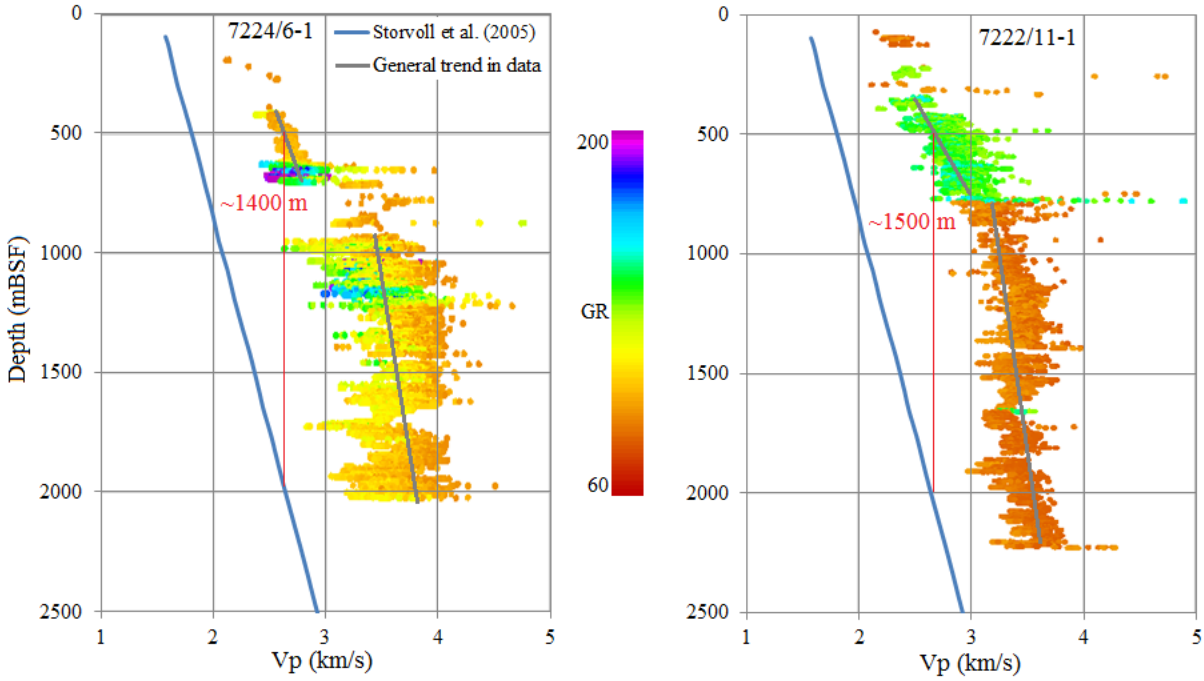

Figure 5.25. Crossplot of V_p versus depth, with a published trend from literature included. Data is from mainly shaley lithology in well 7224/6-1 and 7222/11-1. Note red line indicating difference (m) between published trend and studied data.

Cement volume calculated from velocity data shown in Figure 5.9 is also coherent with observations of low- to no cement volume in the data points from the shallow Snadd reservoirs that plot in areas of low V_p (below ~3 km/s) and higher porosity. As V_p is the only input for the calculation, cement volume increases linearly with increasing V_p and is consequently providing slightly different information than derived from comparing to the cement model templates.

If considering the plot of V_p/V_s versus acoustic impedance in Figure 5.16, where predicted V_s data is used in well 7223/5-1, the positioning of the low-impedance sandstone data (below ~7 km/s*g/cm^3, marked by ellipse) could also be connected to a lower cement volume compared to the remaining higher-impedance sandstone data. The deviating data points belong to the aforementioned shallow Snadd reservoir at less than 800 m depth. As increasing cement volume is assumed to drag data points towards lower V_p/V_s ratios because of the increase cement provides in shear strength (Ødegaard and Avseth 2004; Storvoll and Brevik 2008), this could explain why the sandstone data follow seemingly separate trends. This interpretation is supported by cement volume estimated from the relation of Marcussen et al. (2010) in Figure 5.17.

LMR crossplots of the Snadd and Kobbe reservoir sands in the four wells with measured S-velcocity, displayed in Figure 5.21 and Figure 5.23 respectively, can be of aid in observing

the difference in cementation between wells. Well 7222/11-1 (Caurus) which is assumed to have experienced the least amount of uplift (e.g. Ohm et al. (2008); Baig et al. (2016)) exhibits signs of very variable cement volume in the Snadd Formation, ranging from very low to high degree of cementation. Towards the north, data from well 7223/5-1 and 7222/6-1 (Obesum) indicate slight differences in the Snadd sands judging from a slight reduction in the lower Mu-Rho and cement volume fraction, which can possibly be correlated with higher maximum burial. The difference is mostly observable in well 7222/6-1. In well 7222/6-1 all reservoir data is from below 1100 m present depth (below KB), whereas well 7223/5-1 also include data from shallower reservoirs units at around 600-800 m, similarly to well 7222/11-1. Well 7224/6-1, positioned east of the other three wells and to the far north of the study area, lacks data in the lowest fraction of estimated cement volume and below 15 GPa*g/cm^3 for $\mu\rho$. The shallowest Snadd reservoir data in this well is from around 1200 m present depth. An interpretation of this could be that the Snadd Formation is overall more cemented in this area, if comparing to well 7222/6-1 in particular which encounter reservoirs at most similar depths. The reasons behind are harder to pinpoint, but could possibly be due to differences in paleotopography, higher maximum burial (even though exhumation estimates are approximately equal) or other factors. The Kobbe reservoirs display fewer differences between wells, which could be indicative of less variation in deeper intervals that are more unambiguously influenced by chemical compaction/cementation. All established Kobbe reservoirs are situated between ~1970-2300 m present depth, resonating with the observation that they do not distinguish significantly from each other with regard to compaction and cementation. Note also that a hydrocarbon indication is present to a larger or smaller degree in all eight crossplots, indicating at least some hydrocarbon influence in all four wells for both Snadd and Kobbe if assuming the cutoff value of $\lambda\rho$ = 20 GPa*g/cm^3 to be valid.

5.2.3 Hydrocarbon separation and lithology sensitivity

Revisiting the V_p/V_s-AI domain, the standard template created with generally accepted values for rock properties of sand and shale seems to apply fairly well for the data examined in this study. Even in low saturation intervals of hydrocarbon as in the reservoirs shown from the Snadd and Tubåen formations in Figure 5.14, hydrocarbon separation in the points is clearly visible. Water-bearing sand of the Tubåen reservoir, which from petrophysical analysis is expected to be slightly cleaner than the Snadd reservoir (Figure 5.26), plots relatively similar to the Snadd reservoir data points in relation to the clean water-sand model. This is either indicative of inaccuracies in the petrophysical analysis, or a lack of sensitivity in this rock physics model to small variations in lithology and shale volume.

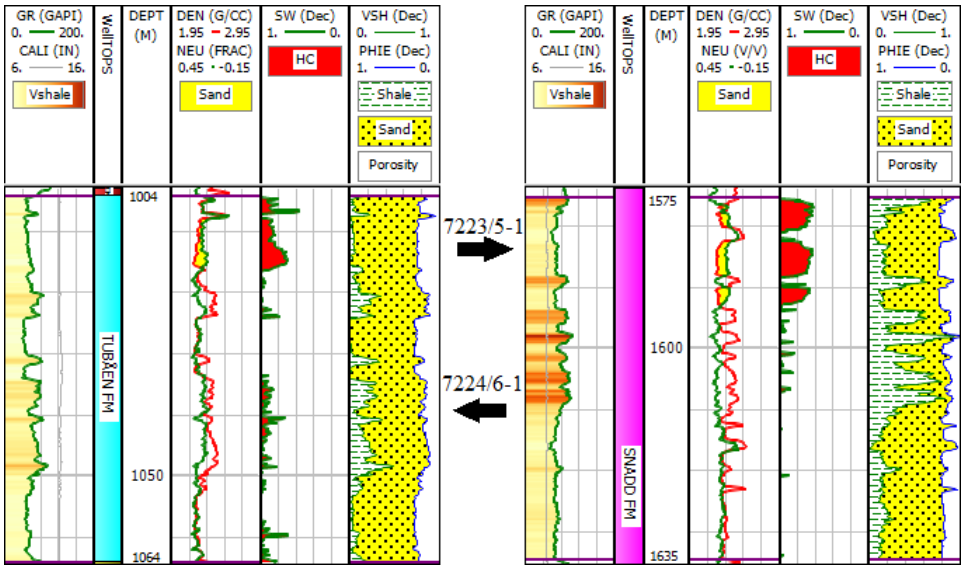

Figure 5.26. Composite log display of the Tubåen reservoir from well 7224/6-1 and the Snadd reservoir from well 7223/5-1 shown in previous V_p/V_s versus AI crossplot.

The accuracy of the V_p/V_s-AI rock physics template is further tested in Figure 5.16, where measured and predicted V_s values are used as input and compared. Data that is interpreted as clean, water-bearing sand plots higher than the model predicts. This could be due to inaccuracy in only using published values for bulk and shear moduli of quartz for this dataset, and the assumption that the matrix is purely quartz will also obviously result in some discrepancy. An interesting feature in the data however, is that using predicted V_s as input shifts the clean sand data higher, away from the water sand model line. A possible explanation for this perhaps lies in the relation derived to predict V_s from V_p using all studied data to get a local fit. If the majority of the data available stem from shaley or heterogeneous lithology (i.e. the V_p-V_s relation is not designed to fit clean sand or pure shale), data points will plot in the area between the clean sand and pure shale models in the V_p/V_s-AI domain, regardless if the data in reality represents shaley or sandy lithology.

Porosity estimates correspond reasonably well to the V_p/V_s-AI template indications (~5% error) in Figure 5.18. All Snadd Formation reservoirs in the wells with measured V_s are shown in Figure D.2. Quantitating water saturation levels based on the same template however appears to be a much more uncertain task. Water saturation estimates, although as discussed may not be precise and comes with uncertainties of its own, are significantly higher than what inferred from where the points plot relative to the template. An explanation for points dragging further upwards in the plot than expected could be due to a certain shale content in the reservoir, as can be seen in the right plot where data is colored to represent shale volume. Data from this reservoir displays the largest separation towards the gas-saturated line of all reservoirs analyzed, and the consequent implication is that the V_p/V_s-AI templates apply poorly to the current database with regard to observing detailed saturation levels. Gas saturation in any case would be poorly separated if increased above 10% due to the nature of this template in the V_p/V_s-AI domain (Ødegaard and Avseth 2004).

LMR crossplots are argued to better separate lithological variations independent on fluid effects, and to provide an increased sensitivity to presence of hydrocarbon (Goodway 2001).

Considering the two Snadd reservoirs in well 7222/11-1 (Caurus), the LMR interpretation indicates that more of the upper reservoir (left plot Figure 5.20) is gas-bearing than what was established in the petrophysical analysis. From 636 m to 690 m almost all data points plot below the cutoff value of Lambda-Rho = 20 GPa*g/cm^3, which in theory indicates gas sand in the top two-thirds of the uppermost Snadd reservoir. This also contrasts the information from the drilling company (NPD 2016), which indicates hydrocarbon presence in only two thin sandstones (~1 m each) in this interval. Additionally, these thin intervals are interpreted to have a rather low hydrocarbon-saturation of maximum ~40%. Mu-Rho values are low, between 5-10 GPA*g/cm^3, which could possibly be related to a low degree or lack of cementation which generally increases shear resistance (Storvoll and Brevik 2008). Sporadic points representing the remaining lower 25 m of this reservoir also fall beneath the cutoff. For the second uppermost reservoir interval in this well (right plot Figure 5.20) practically all data points plot below the cutoff value, which is expected as it is interpreted to be hydrocarbon-filled (gas) in the petrophysical analysis. Some exceptions fall below the cutoff value in this plot as well, i.e. points from 791-798 m which is assumed to be a brine-interval, but also described to have good oil shows by the drilling operator (NPD 2016). The same data from both reservoirs are plotted with water saturation as color code in Figure 5.27 for comparison with the results of petrophysical analysis.

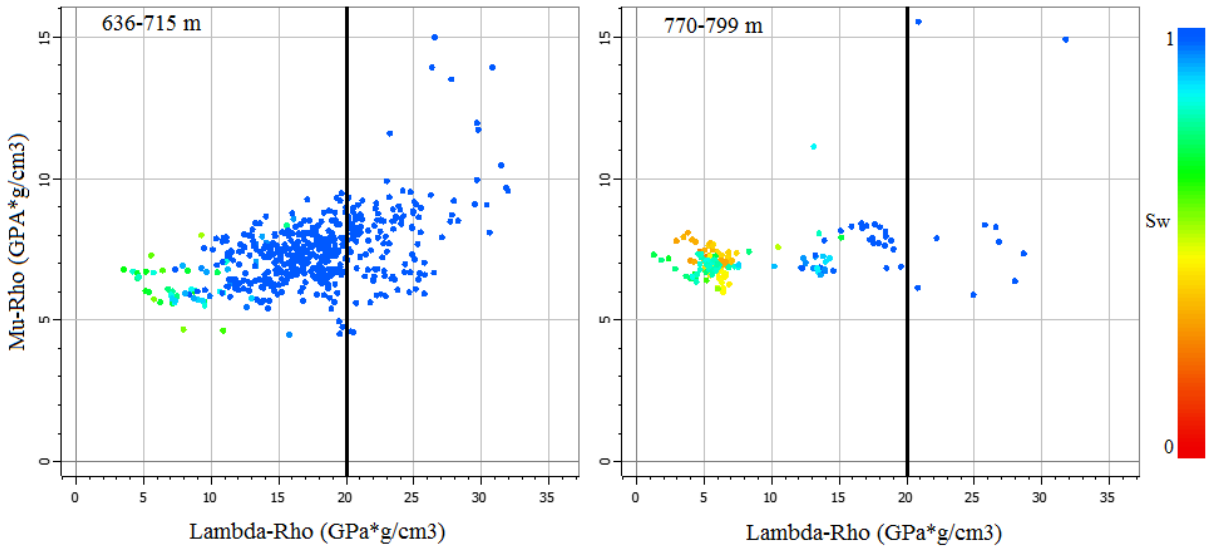

Figure 5.27. LMR crossplot with data from the two upper Snadd reservoirs in well 7222/11-1. Data colored by water saturation. Note discrepancy between gas cutoff line and saturation according to the color coding.

These interpretations can possibly question the universality of the 20 GPa*g/cm^3 cutoff value for Lambda-Rho, and shows that small variations exists in this domain. E.g. based solely on these two particular reservoir intervals, a cutoff value of 10 GPa*g/cm^3 would locally coincide better with the petrophysical analysis and information about the HC-water contact in the lowest reservoir (NPD 2016). This is however only a justifiable statement with additional quality control and confirmation from the encounters made by drilling, and does not rely on water saturation estimates and petrophysical hydrocarbon identification alone.

5.3 Uncertainties

If attempting to identify the boundary between mechanical and chemical compaction in a plot of V_p versus depth, apparent jumps in velocity could be related to lithology effects. On inspection of wells 7224/7-1 and 7224/6-1 (Figure C.5 and C.9), it appears to occur somewhere within the Fuglen Fm, and lithology should consequently not be expected to change that much. An alternative candidate for this boundary could be in the Kolmule Formation in well 7224/6-1. Wells 7124/3-1, 7125/1-1 and 7226/11-1 appear to have a transition somewhere below the Kolmule Formation and above the Tubåen and Stø Formations (Appendix C). An additional uncertainty is related to comparing the estimated transition zone depths with observed data trends, as these estimates are based on present day geothermal gradients which could be different from paleo-geothermal gradients.

Published models and background templates used in this study often comes with the assumption of using clean quartz parameters for modeling sandstone. Especially in the Snadd and Kobbe formations, the mineralogy can be very deviating from this assumption, whereas in the Tubåen and Stø formations it may have a higher validity. E.g. in Ryseth (2014) the composition of Snadd Formation sandstones is characterized by around 30% of other minerals as chert, K-feldspar and plagioclase. Climate changes, changes in provenance areas and the composition of eroded material are explanations for the changing mineralogy between Snadd and later Triassic/Jurassic sediments. Bergan and Knarud (1993) indicate the quartz content in sandstones from Kobbe and Snadd to be less than 60%. The composition of Kobbe and Snadd close to the current study area has also been discussed in Line (2015), as well as the effect of chlorite coating largely inhibiting quartz precipitation. Findings in the mentioned study somewhat contrasts the indications of relatively high cement volumes estimated for particularly the deeper intervals in this thesis. Consequently, assumptions for use of the models and rock physics templates are violated which theoretically leads to higher uncertainty in some results.

When utilizing pre-existing rock physics templates which describes cement models in plots of V_p or V_s versus porosity, significant uncertainty lies in the conditions the templates are created for. Calculating and evaluating own complete models is beyond the scope of this study, but for analyzing uncertainty related to using digitized models some friable sand models at different conditions have been created for comparison. In Figure 5.28 the computed models are shown in different colors, with the digitized models shown in black. The template from Avseth et al. (2005) for V_p versus porosity used in this study is a generalized model, and strictly not valid for doing detailed analysis of the reservoirs being examined. The friable sand line appears to nearly coincide with the calculated friable sand model assuming 1 MPa effective pressure. Assuming a higher effective pressure would shift the model towards higher velocity values, and the interpretation of cementation would slightly change. The template for V_s versus velocity (Avseth et al. 2010) has a friable sand line which is mimicked by the 10 MPa calculated friable sand model, thereby indicating that this model is created for an effective pressure of approximately or slightly less than 10 MPa. The lowest constant cement trend line in this plot is equivalent to a friable sand model computed for 20 MPa effective pressure. Other uncertain parameters that have been used as input for generating these models are coordination number and critical porosity corresponding to each stress level. Relative relations between data points plotted in either domain will however of course remain constant and interpretable, as the uncertainties are related to overlay templates only.

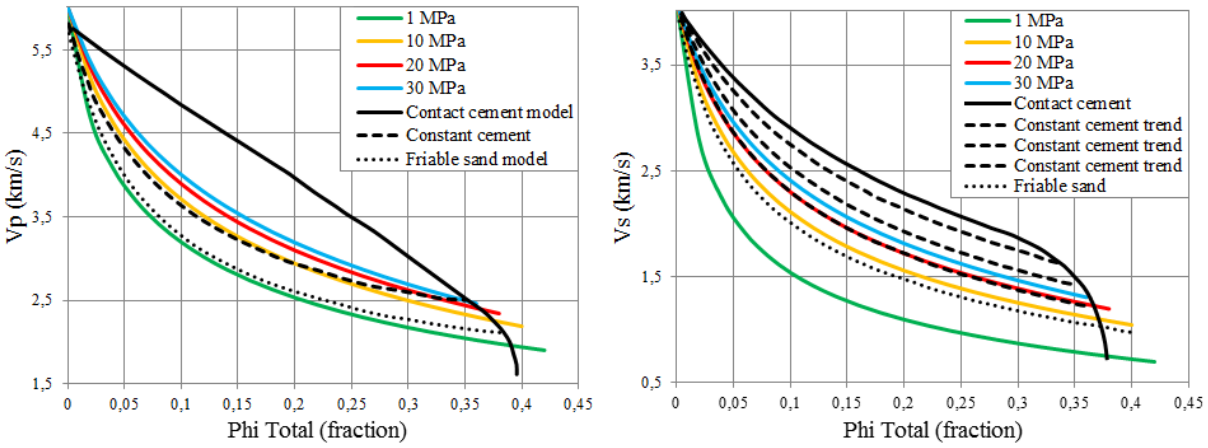

Figure 5.28. Digitized rock physics cement models compared to friable sand models calculated for 1, 10, 20 and 30 MPa expressed in the V_p-porosity and V_s-porosity domains. Published models are from Avseth et al. (2005) and Avseth et al. (2010).

Chapter 6: AVO modeling

The goal of AVO- or AVA modeling is mainly to investigate fluid effects, and preferably lithological effects, on the angle-dependent seismic signatures of reservoir interfaces. In this chapter, a few selected reservoirs are analyzed by creating synthetic gathers from in-situ and fluid-substituted well logs and describing the extracted information. The sensitivity in elastic parameters related to fluid content can also be examined when modeling theoretical fluid contents. Reservoirs used for modeling are of different relative depth levels and quality, and are presented briefly in Table 6.1. One deep and one shallow reservoir interval has been picked from well 7222/11-1 located in the south-western part of the study area. From the more northern part of the study area, reservoirs from well 7224/6-1 have also been chosen for modeling (Figure 6.1). The reasoning behind the selection of these reservoir sections was to compare both as different depth levels as possible as well as testing different locations, while still picking intervals that appear suitable and well defined for AVO modeling results.

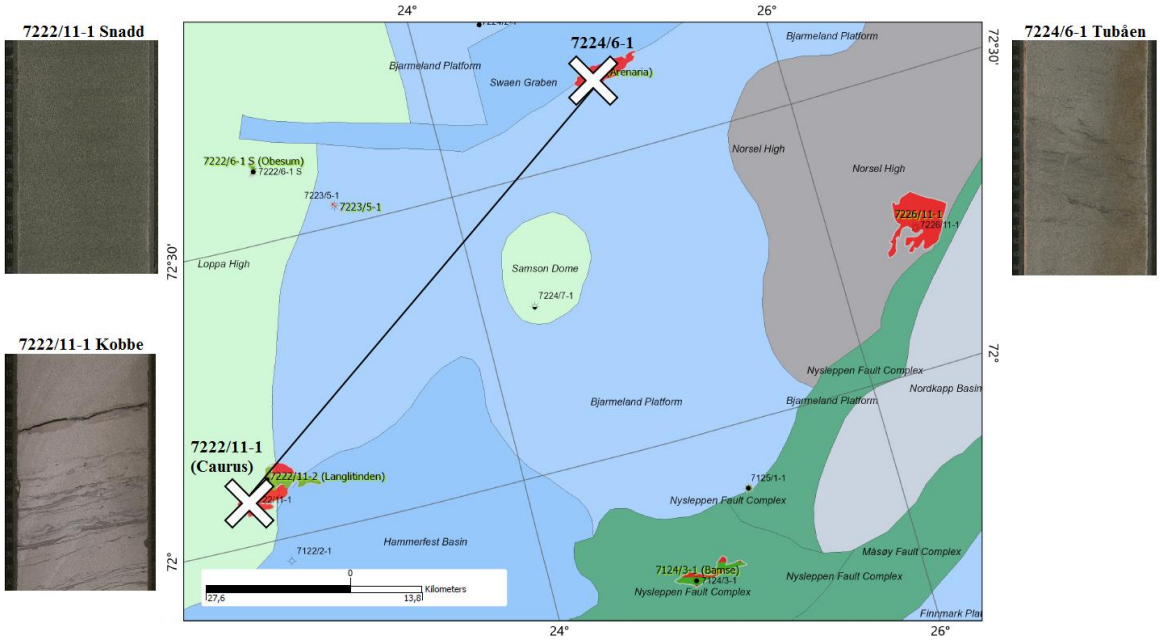

Figure 6.1. Map of the study area (source: NPD Factmaps 2016), indicating wells used for AVO modeling and available core photos from the reservoirs tested (core photos courtesy of Statoil ASA, previously StatoilHydro Petroleum AS).

Table 6.1: Overview of reservoir intervals selected for AVO modeling. Note that only a relevant part of the Kobbe reservoir in well 7222/11-1 and the Snadd reservoir in well 7224/6-1 classified in previous chapters has been examined.

Well	Formation	Depth in mRKB and (mBSF)	In-situ fluid
7222/11-1 (Caurus)	Snadd	770-799 (390-419)	~60% Gas
7222/11-1 (Caurus)	Kobbe	2228-2238 (1848-1858)	~70% Oil and gas
7224/6-1 (Arenaria)	Tubåen	1004-1064 (715-775)	Low saturation (< 20%) gas
7224/6-1 (Arenaria)	Snadd	1808-1838 (1520-1549)	Brine

6.1 Results

6.1.1 Gassmann fluid substitution

Gassmann fluid substitutions of 100% brine, 10% gas and 100% gas were applied through the Fluid Replacement Modeling (FRM) in the Hampson-Russell software, in order to create logs that represent a given reservoir with different fluid content than the in-situ situation. Fluid replacement yields changes in elastic properties such as bulk modulus and density, and by extension P-wave velocity, S-wave velocity and Poisson's ratio. For the shallow Snadd reservoir in well 7222/11-1, these changes are shown in Table 6.2, represented by V_p, V_s, density and Poisson's ratio.

Table 6.2: V_p, V_s, density, saturated bulk modulus and Poisson's ratio values at different levels of saturation in a gas-water system for top reservoir interfaces in well 7222/11-1 and 7224/6-1.

In-situ and fluid replaced values	**V_p (km/s)**	**V_s (km/s)**	**ρ (g/cm3)**	**K_{sat} (GPa)**	**υ (unitless)**
7222/11-1 Snadd					
100% brine	2.481	1.231	2.291	9.397	0.34
10% gas	2.120	1.240	2.258	5.783	0.245
In situ (60% gas)	2.171	1.291	2.084	5.484	0.232
100% gas	2.232	1.329	1.966	5.462	0.231
7222/11-1 Kobbe					
100% brine	3.768	2.143	2.518	20.341	0.261
10% gas	3.614	2.149	2.503	17.266	0.226
In situ (~60% gas)	3.655	2.183	2.427	17.006	0.223
100% gas	3.700	2.210	2.367	16.983	0.222
7224/6-1 Tubåen					
100% brine	3.251	1.788	2.293	14.461	0.283
10% gas	2.980	1.798	2.268	10.361	0.214
In situ (<20% gas)	2.994	1.819	2.216	10.095	0.208
100% gas	3.110	1.893	2.044	9.998	0.206
7224/6-1 Snadd					
In situ (Brine)	4.409	2.602	2.630	27.373	0.233
10% gas	4.218	2.604	2.625	22.972	0.192
100% gas	4.230	2.626	2.582	22.466	0.187

Subsequent changes in the synthetic seismograms and fluid-substituted logs created for all scenarios are shown in Figure 6.2 and Figure 6.3 for well 7222/11-1 and well 7224/6-1 respectively.

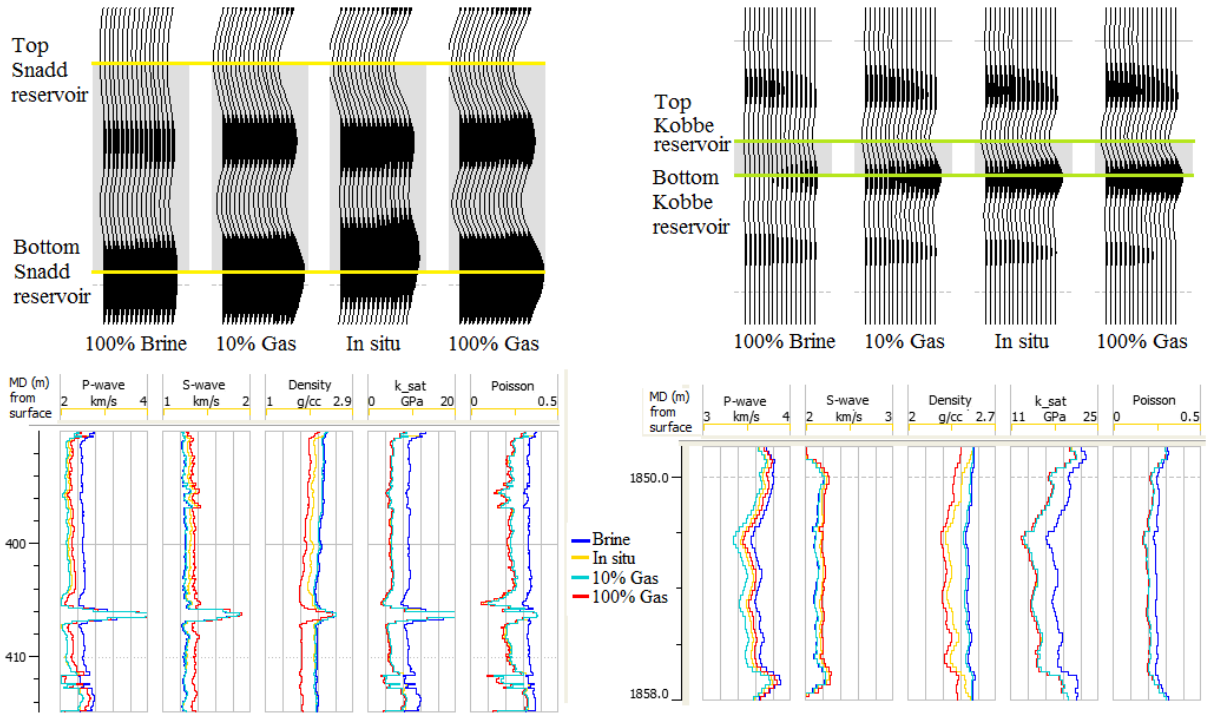

Figure 6.2. Synthetic seismograms for all scenarios of the reservoirs in well 7222/11-1 are shown in the two upper plots. Relevant logs from the reservoir intervals are shown in the two lower plots.

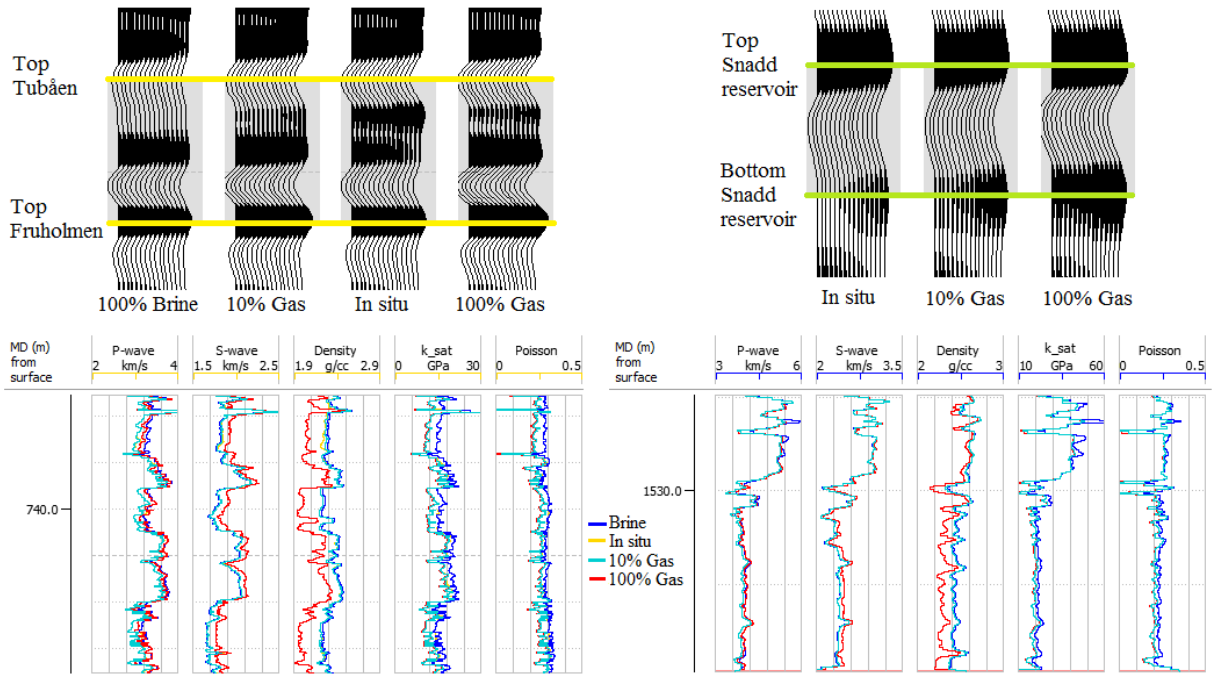

Figure 6.3. Synthetic seismograms for all scenarios of the reservoirs in well 7224/6-1 (upper plots). Relevant logs from the reservoir intervals are shown in the lower plots.

6.1.2 Blocking/upscaling of well log data

Velocity and density logs are used for constructing a model of reflectivity and elastic properties of the subsurface in the studied well locations. Combining this with a wavelet yields a representation of how a seismic wave would propagate through and interact with the rock layers visible in the logs. Logs should consequently be upscaled before generating synthetics in order to correspond better to the resolution expected in seismic data, which is lower than in well logs. The block size and method of averaging being utilized has an effect on the resulting synthetic seismograms' appearance. Blocking is conducted after performing the fluid substitution during creation of synthetics, with an average block size of 3 m, as suggested in e.g. Ross (2000) as a minimum yet reasonable thickness for modeling (example shown in (Figure 6.4). Although different averaging methods are available, the automatic non-uniform blocking algorithm in Hampson-Russell was found to be most adequate to capture important interface contrasts, and has consequently been chosen for this modeling study. This method is based on maximum-likelihood detection of the large events to make sure the main features are emphasized, by varying the block size when necessary while still retaining the average block thickness.

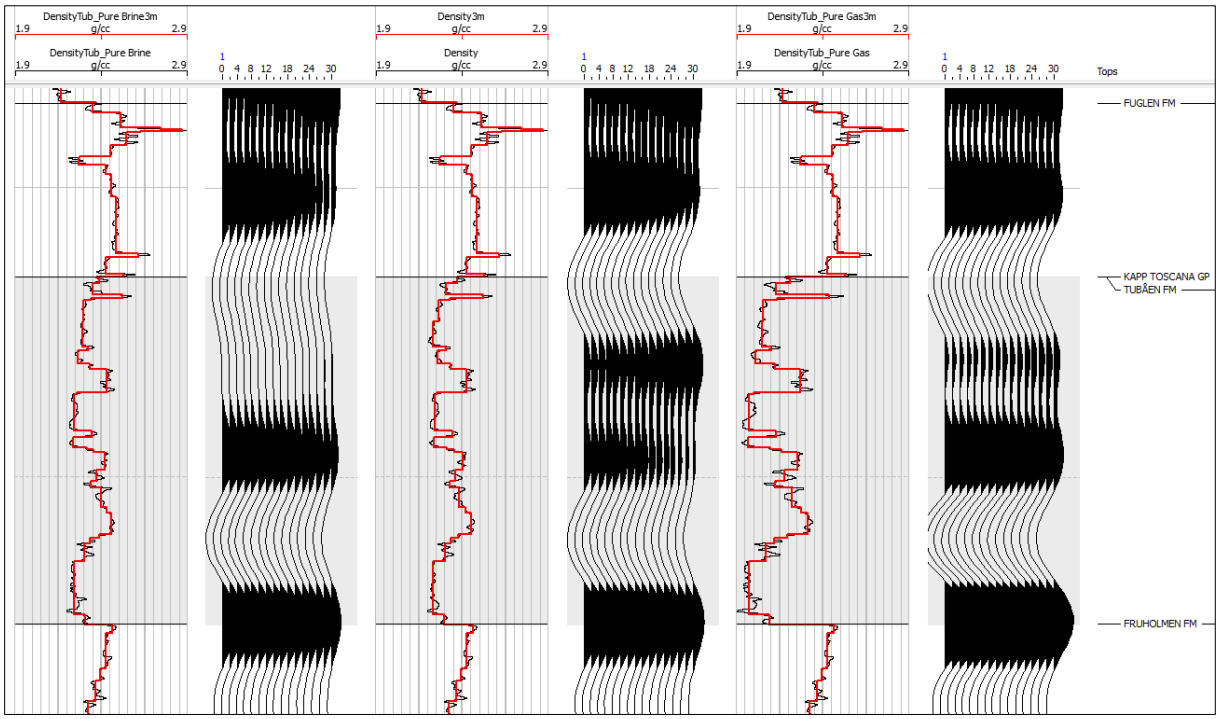

Figure 6.4. Example from the Tubåen Formation in well 7224/6-1 of blocked density logs after fluid substitution with corresponding synthetics created from the blocked logs.

6.1.3 Generation of synthetic seismogram

A linear phase Ricker wavelet (Figure 3.19) has been used in the generation of synthetic seismograms which are created by using the full Zoeppritz equations and show primary events only (Figure 6.2, Figure 6.3). This choice of wavelet is a simple approach which provides good vertical resolution and minimal noise influence, but if the synthetics were intended to compare to real pre-stack seismic data a more realistic wavelet (e.g. extracted from seismic data) would be preferable. Synthetics are presented as angle-domain gathers and classification plots are presented with variable incidence angle rather than offset mainly for a more intuitive understanding of the results.

6.1.4 AVO classification

For gradient analysis and subsequent classification of reservoir AVO-signatures, angles up to 30^o have been included and the Aki-Richards two-term approximation has been used as trend curves in plots of amplitude ($R_{pp}(\theta)$) versus incidence angle. Angles above 30^o were excluded to ensure certainty of the Aki-Richards approximation being valid for comparison to the Zoeppritz equation which was used to create the synthetics (Li et al. 2007; Chopra and Castagna 2014). A standard background trend based on constant V_p/V_s ratio (=2) as described in Castagna et al. (1998) is included as overlay in crossplots of intercept and gradient. For reservoirs originally containing hydrocarbon, the response of substituting with brine is shown, and vice versa. Seeing as the in situ situation is rarely in reality that a reservoir contains 100% gas, this scenario is also included when examining reservoirs with at least a certain level of in-situ hydrocarbon saturation. Effects of even more step-wise differences in water saturation are done by including a 10% gas saturation model.

The in-situ and fluid substituted responses of the Snadd and Kobbe reservoirs in well 7222/11-1 (Caurus) are shown in Figure 6.5 as both $R_{pp}(\theta)$ versus angle and in an intercept-gradient crossplot. Both reservoirs contain hydrocarbons, and have consequently been replaced with brine, 10% gas and 100% gas for comparison.

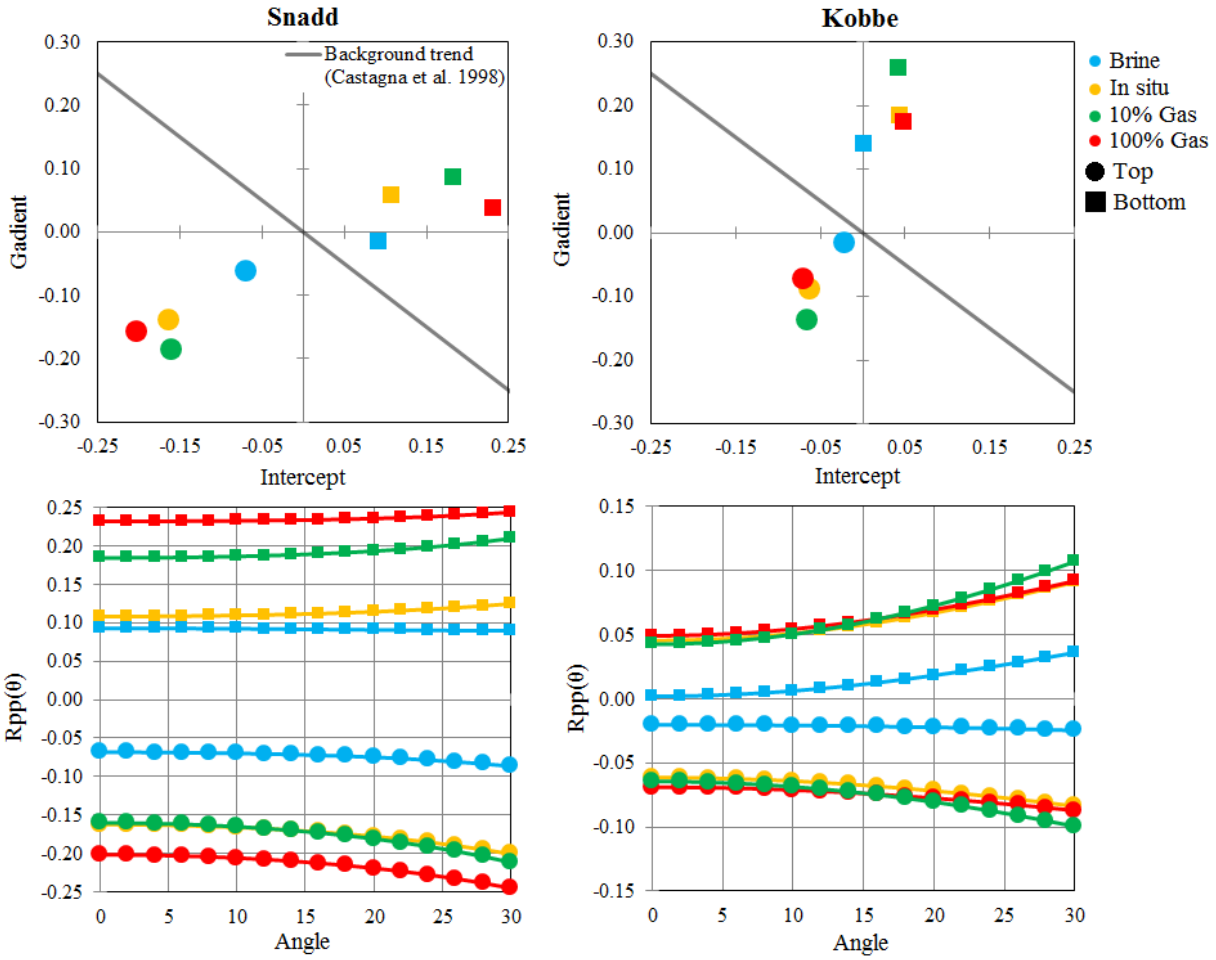

Figure 6.5. Reservoir responses of the Snadd (left) and Kobbe (right) reservoirs from well 7222/11-1 including in situ, brine and gas scenarios (10% & 100%). Top: Intercept versus gradient crossplots. Bottom: P-wave reflection coefficient versus angle. Note that the Y-axis of the two bottom plots are not in the same scale.

There are some differences to note between the Snadd and Kobbe reservoirs found at relatively shallow and deep depth levels, respectively. The in situ top reservoir points in the upper crossplots reveal both a higher intercept (i.e. zero-offset amplitude) and a higher gradient (i.e. change with offset) for the Snadd reservoir. Reflections from the lower reservoir interfaces imply that the Kobbe reservoir base is dimmer at zero offset than the Snadd reservoir, but has on the other hand a higher positive gradient value.

Fluid replacement of brine in the place of in situ hydrocarbons results in a movement towards the center of the plot and the background trend. For the top Snadd reflection, the intercept value increases (gets less negative) from around -0.16 to -0.06 and the gradient changes from -0.14 to -0.06. By increasing gas saturation from in situ values to 100%, the movement is opposite and the values change by approximately -0.04 and -0.02 for intercept and gradient respectively. For the Kobbe reservoir, the three gas-influenced top reservoir points plot very close to each other similarly to the position of the top Snadd brine reflection point. Substituting with brine causes an increase in intercept from around -0.06 to -0.02 (i.e. lower amplitude), and a gradient magnitude decrease of ~0.07.

Corresponding responses of the reservoirs in well 7224/6-1 are presented in Figure 6.6. The shallowest Tubåen Formation reservoir contains low saturation gas, and is therefore modeled with both 100% brine, 10% gas and 100% gas for comparison. The lower reservoir in the Snadd Formation is brine-filled in the in situ condition and is consequently substituted with 10% gas and 100% gas.

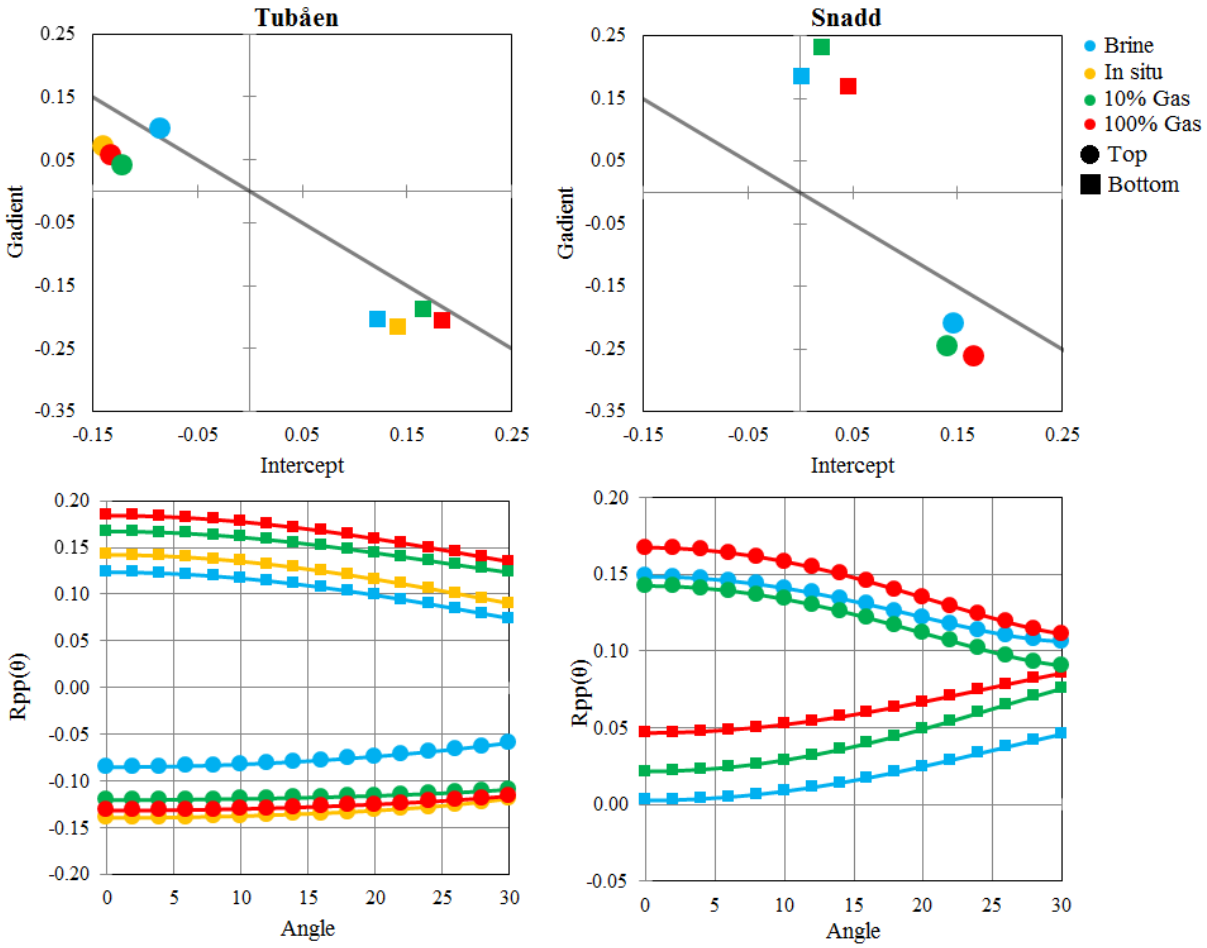

Figure 6.6. Reservoir responses of the Tubåen (left) and Snadd (right) reservoirs from well 7224/6-1 including in situ, brine and gas scenarios. Note in situ fluid in the Snadd reservoir is brine. Top: Intercept versus gradient crossplots. Bottom: Reflection coefficient versus incident angle. Note that the Y-axis of the two bottom plots are not in the same scale.

Both top and bottom reflection point sets for all three scenarios in the Tubåen reservoir plots on or below the background trend in the intercept-gradient crossplot. Substituting in situ gas for brine yields an increase in gradient value of +0.03 and an intercept increase of +0.06. This shifts the response of the top interface up to the background trend line. Increasing the gas saturation to 100% will show a slight decrease in gradient (-0.01) from the in situ point, as well as having a less negative intercept value (+0.01), meaning they have approximately the same signature. For the bottom reservoir levels, all four points have a gradient value of around -0.19 to -0.21, but display stronger intercept values for gas scenarios than for brine (increase from 0.12 to 0.14-0.18).

Considering the top of the Snadd reservoir, moving from in situ brine to pure gas results in a gradient decrease from -0.21 to -0.26 (i.e. stronger negative gradient), and a smaller increase in intercept from ~0.14 to 0.17. 10% gas saturation results in the lowest intercept and intermediate gradient. Bottom Snadd reservoir points plot above the background trend as typically expected. The gas-substituted reservoir model has a slightly stronger intercept response than the in situ brine model, which has a zero offset reflection coefficient of around 0. In the plots of reflection coefficient versus incident angle it can be noted that the Snadd reflections have a positive zero-offset amplitude which decreases at higher angles, while the Tubåen reflections start as negative and display a mirrored behavior by increasing with increasing angle.

6.2 Discussion

If firstly examining Figure 6.5 with regard to classification schemes of reservoir sands described in chapter 3 (based on top reservoir reflections), the in situ gas reservoir in the Snadd Formation displays a class 3 anomaly. Class 3 sands are typically associated with shallow, mostly unconsolidated sediments, which coincide nicely with previously made remarks about this reservoir (Rutherford and Williams 1989; Chopra and Castagna 2014). More surprisingly, however, is that the Kobbe reservoir falls within the same classification even though it is situated around 1450 m deeper and is therefore expected to be significantly more compacted and cemented. A fitting description is perhaps a weak class 3 anomaly, indicating an impedance contrast with the surrounding shale that is lower than what is observed for the Snadd reservoir. The brine substituted top Kobbe reflection approaches a class 2 anomaly (i.e. less than 0.02 in zero offset reflection magnitude). Reflections from the base of the Kobbe reservoir display higher gradient values than do the top reflections, which could be related to the lower boundary being more abrupt and the Poisson's ratio contrast to the underlying shale being stronger (Chopra and Castagna 2014).

In the results from well 7224/6-1, the Tubåen reservoir is classified as a class 4 sand by assessing the in situ top reservoir response in the intercept-gradient crossplot shown in Figure 6.6. Class 4 sands are typically related to the same origin as class 3 sands, or associated with porous sands overlain by a hard, high-velocity cap rock (Castagna et al. 1998). The cap rock overlying this reservoir is a Fuglen Formation shale which exhibits P-velocity values of around 3.5 km/s. Approximate velocity values for the intra-Snadd shale overlying the Snadd gas reservoir in well 7222/11-1 are around 2.6 km/s, and the shale is expected to be less compacted here in addition to having slightly lower density values. These cap rock properties are factors that can contribute to explaining why these two reservoirs classify as two different gas sands, even though their zero-offset reflection coefficients are approximately equal. There are other factors disassociating these reservoirs, but the medium above the reflector being used to classify a given sand is inferred to play an important role (Castagna et al. 1998).

One of the other factors that separate these reservoirs is the compactional difference between the sands related to their burial and exhumation history. Even though only around 300 m separate the top of these reservoirs at present depth, reservoirs in well 7224/6-1 is assumed to have experienced approximately 250 m additional uplift compared to well 7222/11-1 (Baig et al. 2016), increasing the difference in maximum burial further. Findings in this study indicate that the older Snadd reservoir is paradoxically less influenced by chemical compaction than the younger Tubåen reservoir, even though the notation "shallow" has been used for both.

Considering these observations about compaction, depth and differences in surrounding media, the fact that the reservoirs display dissimilar AVO signatures is not unreasonable.

Returning to Figure 6.6, the deeper Snadd reservoir in well 7224/6-1 classifies as a class 1 sand since the in situ top reservoir response (blue triangle) plots in the fourth quadrant of the intercept-gradient crossplot. Consequently, the associated reflector has high positive zero-offset amplitude, which then decreases with increasing angle as observable in the lower plot of (Figure 6.6). Class 1 sands are associated with deeply buried, well consolidated sands with higher impedance than surrounding rocks and relatively lower V_p/V_s ratio, which fits nicely with how this reservoir appears in the log data (Chopra and Castagna 2014). The V_p/V_s ratio drops from around 1.9 in the surrounding shales to 1.6 in this interval.

6.2.1 Fluid vectors and background trend

The movement of data in the intercept-gradient domain, when interpreted to be due to fluid alterations, can be described by fluid vectors. A fluid vector represents movement of AVO reflection coefficients, and is commonly displayed in the case of brine being replaced by gas, resulting in movement away from the given background trend/cluster (Castagna et al. 1998; Ross 2000). Figure 6.7 shows the response of only the trough related to the top of the shallow Snadd reservoir from well 7222/11-1 by plotting only a narrow depth window, with the in-situ gas model displayed as squares and the brine-substituted model as triangles. The points connected by a solid arrow represent the picks interpreted to mainly represent information about the interface, whereas smaller points represent samples from either side of the trough minima. Note that the direction of movement from brine to gas points (which can be tracked individually in this case) is not constant. Closer examination of point-to-point fluid vectors can help explain deviation from the given background trend or possible inaccuracies in the choice of a background line.

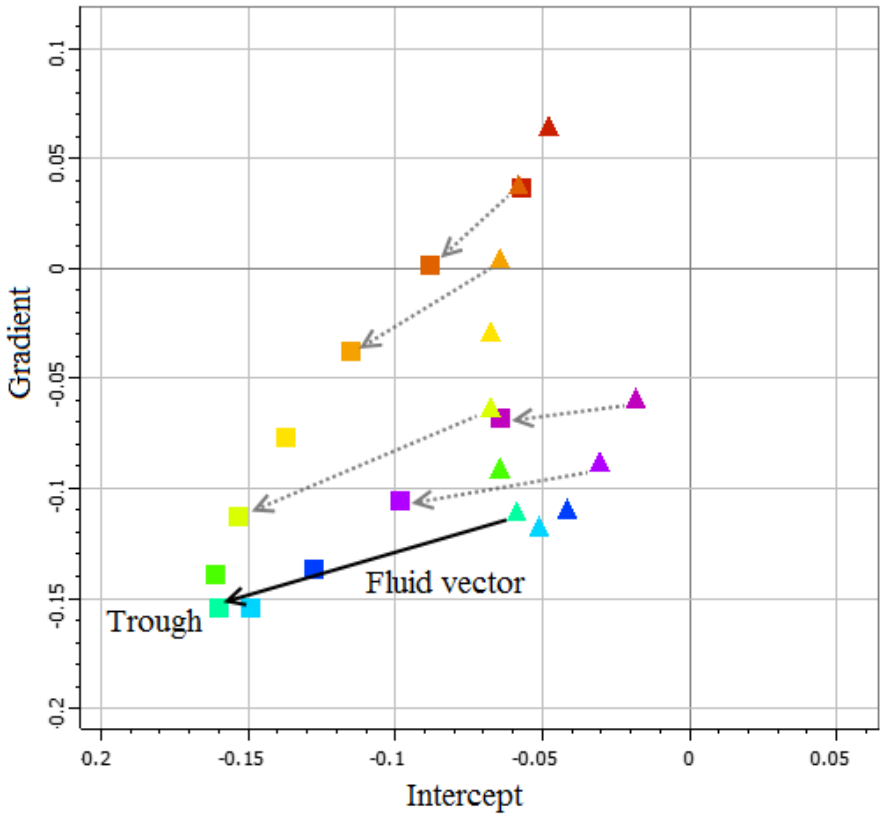

Figure 6.7. Crossplot of intercept versus gradient showing data from the trough associated with top reservoir interface at 770 mRKB in the Snadd Formation in well 7222/11-1. Arrows show the direction of movement in points when changing from brine to in-situ gas saturation.

As the behavior of data expected to act as background (i.e. brine interfaces) can differ with V_p/V_s ratio, the background trend is not constant for all depths and is only valid for a certain restrained time- or depth window (Castagna et al. 1998). Some error (or more accurately - deviation) in the position of brine-interface points relative to the background trend line in an intercept-gradient crossplot is also expected, and interpretation of clusters can be an alternative approach, albeit providing less definitive values (Castagna et al. 1998; Ross 2000). For the same reservoir, visual interpretation of the clustering deviations from the background trend is shown in Figure 6.8. All points from the brine model (blue points) falls within the shaded ellipse, together with most points from the in-situ gas model (red points). The deviation in the data representing the top gas interface is clear and indicated with the solid line ellipse, whereas the bottom in-situ reservoir interface displays a somewhat less clear anomaly (dotted ellipse). This can be an effect of the gas not being present in-situ at significant saturation levels throughout the reservoir, as the lowermost part of the reservoir contains brine and oil shows rather than gas (NPD 2016). Consequently, the contrast of the bottom interface less clear than the upper, well-defined boundary. For this particular reservoir, the background trend line assuming $V_p/V_s = 2$ still seems to provide a good fit with the background data.

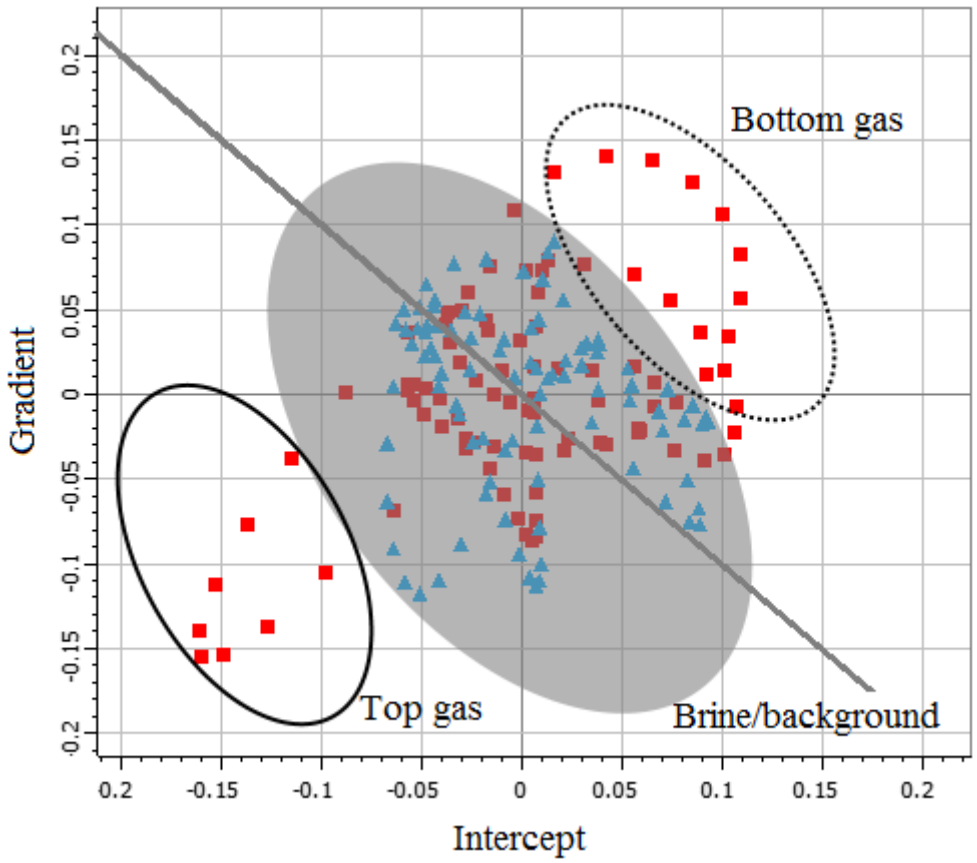

Figure 6.8. Interpretation of deviation from the background cluster trend in the intercept-gradient domain, with data from the shallow Snadd gas reservoir in well 7222/11-1. Note scatter around background trend line for background data of both models.

On the other hand, the odd positioning of the points from the shallow Tubåen reservoir in well 7224/6-1 (Figure 6.6) relative to the trend line could be explained by a different V_p/V_s ratio than what is inferred from the standard background trend. Overall, the background brine-saturated sand and shale's V_p/V_s ratio appears to be lower than 2 – i.e. what is indicated by the overlay background trend line which is based on constant V_p/V_s ratio. This could in turn be explained by the uplift history of the study area, as more compacted, cemented and deeply buried rocks tend to experience a decrease in the overall V_p/V_s ratio, which should lead to a steeper background trend line (Chopra and Castagna 2014). As explored in previous chapters, the shallow reservoirs of well 7222/11-1 are suspected to be more excluded from severe chemical compaction than the other reservoirs examined in this study. This resonates with the argument of suggesting prevalently lower V_p/V_s ratios as a reason for the behavior of the other reservoirs examined in the intercept-gradient domain, such as the Tubåen reservoir in well 7224/6-1. Figure 6.9 shows the top and bottom reflection points of this Tubåen reservoir for the in-situ situation where some low-saturation gas is assumed to be present, the brine-substituted case and the fully gas-saturated case. A depth window of 160 m was plotted to include background trend points for all three models along with the reservoir interval which has a thickness of 60 m. The standard background trend line is shown in grey, whereas the green line indicates what appears to be a more fitting trend for the background data. Note that the base reservoir points now plot above the green trend line. Below, the change in background trend lines with increasing V_p/V_s ratio is shown, assuming constant V_p/V_s for

each individual line and Gardner's relation for density as described in Castagna et al. (1998). Moving from brine-saturated to in-situ or 100% gas in the upper crossplot yields at most a highly discrete deviation from the background and brine-substituted points. Sensitivity to the fluid-substitution appears to be low even though porosity values are high (average effective porosity = 21.6% from petrophysical analysis).

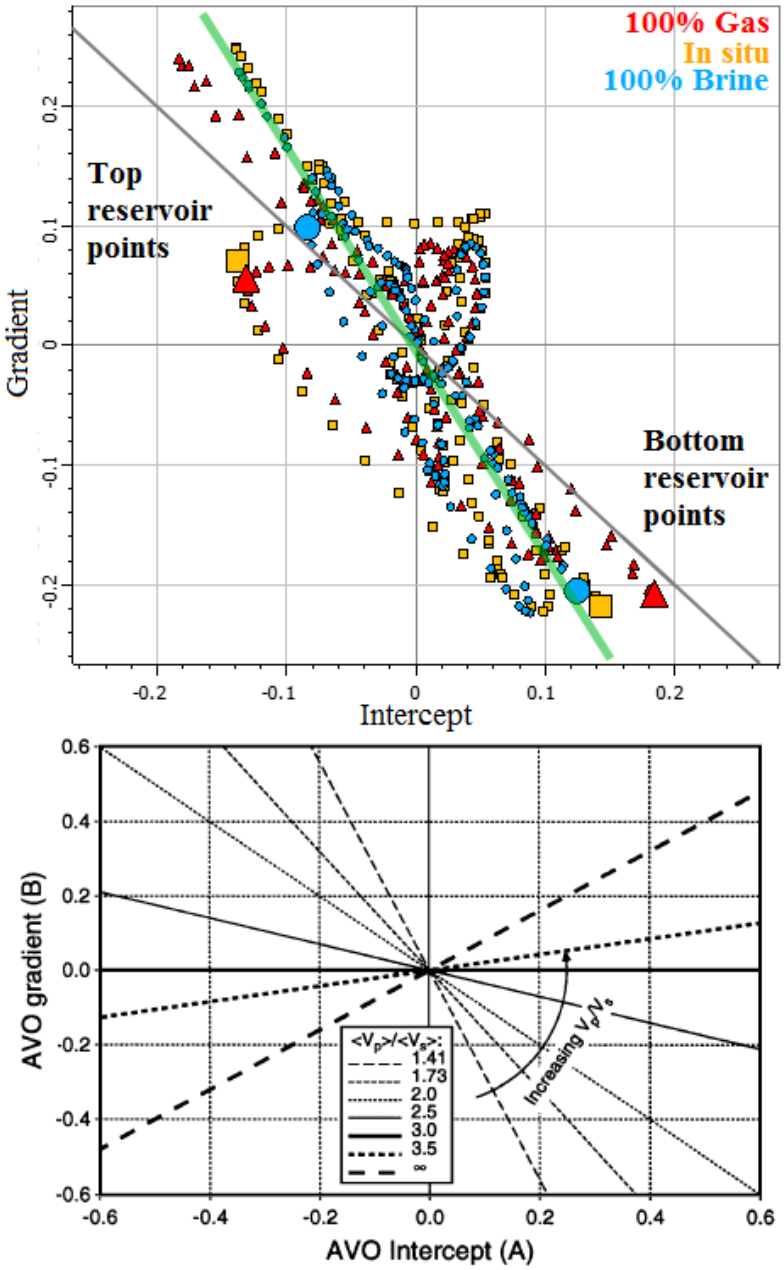

Figure 6.9. Top: Crossplot of intercept versus gradient from the Tubåen reservoir in well 7224/6-1. Points are from a depth window of 160 m centered on the 60 m thick reservoir. The grey line shows the standard background trend ($V_p/V_s = 2$) and the green line indicates what appears to be the actual trend in the background data. Enlarged points are the picks from top and bottom interface of the reservoir. Bottom: The influence of varying the V_p/V_s ratio on the background trend, assuming constant V_p/V_s for each line (adapted from Castagna et al. 1998).

6.2.2 Sensitivity analysis

6.2.2.1 Block size

As an example of how the average block size affects the resulting AVO signature of a reservoir, four different average block sizes were used in the generation of synthetics from the Snadd reservoir in well 7224/6-1 (Figure 6.10). A block size of 3 m or 15 m results in the same trend when substituting gas for in situ brine, only with slightly different values for intercept and gradient. If not applying any blocking to the input logs, the top reservoir point for gas is instead shifted to the lower left of the brine reflection point. What these three response pairs have in common is that they all predict the reservoir to be a class 1 sand. If applying an upscaling with 25 m average block size however, the signature of this reservoir is fundamentally changed. Represented by diamonds in Figure 6.10, these points plot in quadrant 1 above the background trend line and consequently fall outside the classification system of top sand reflections.

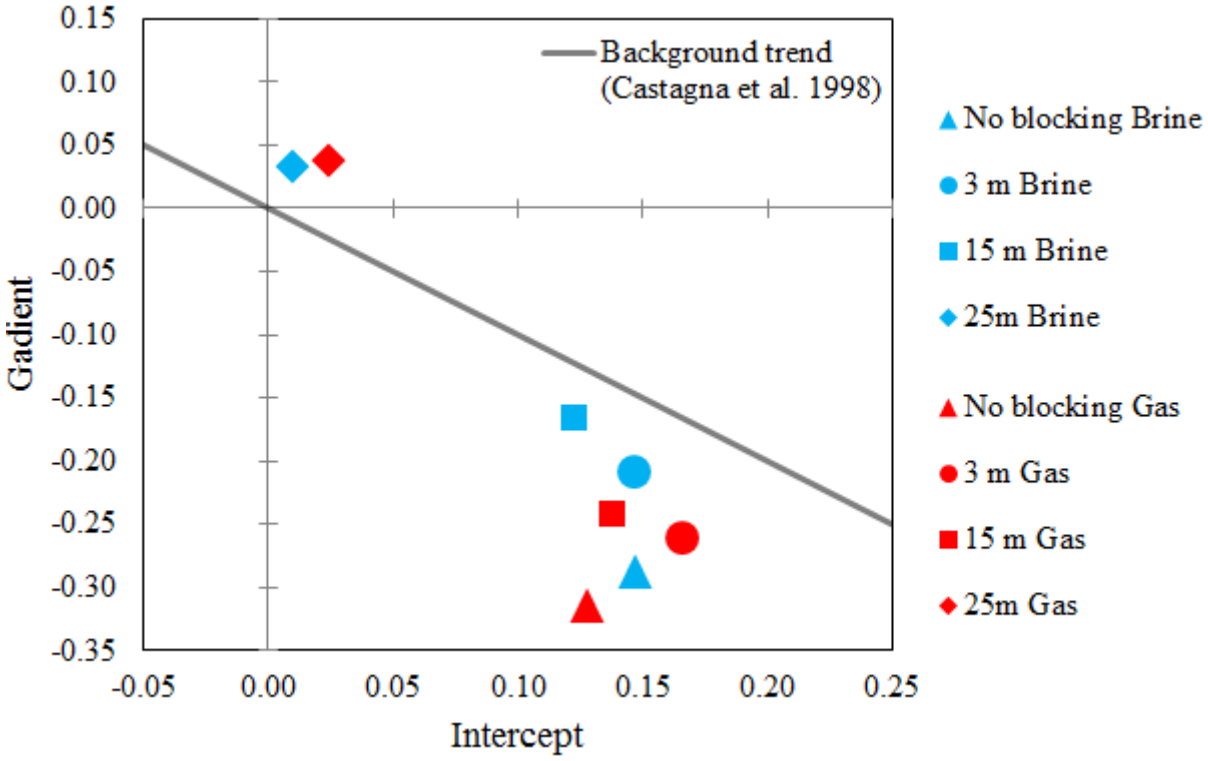

Figure 6.10. The effect of block size variation on the Snadd reservoir in well 7224/6-1 presented in an intercept-gradient crossplot.

A bigger block size will include information from a higher number of smaller scale reflections in each block, and consequently results in a cleaner seismogram with fewer visible events. If the blocks are too large and the events of interest are not highly dominant in the log data however, the synthetics might ignore important reflections or be distorted by multiple reflections canceling each other out. This could possibly explain the erroneous top reservoir signature achieved when using 25 m blocking. Smaller block sizes can, if not used carefully, cause the bigger scale trends to become dimmer amongst many smaller log variations, but in

this study for well 7224/6-1, this seems to affect the resulting synthetics less than having a too large average blocking thickness. Reservoir thickness should also be considered in terms of choosing an appropriate block size.

6.2.2.2 Water saturation

By changing a given pore fluid of a rock to a different pore fluid, corresponding changes take place in the P- and S-velocities of the rock as a result of difference in rock compressibility and bulk density (Avseth 2015). In an example of substituting in-situ brine with gas, shear velocity is expected to increase slightly as an effect of decreased bulk density, and that the shear modulus is theoretically constant. For the same scenario, the rock bulk modulus (denoted 'K' in previously given equations) is predicted from Gassmann's equation to decrease and yield a net decrease in P-velocity. The manner of how P-velocity decreases with increasing water saturation is related to the spatial distributions of fluid phases in the rock (Avseth 2015). In the process of fluid substitution, a decision to be made is whether to assume homogeneous saturation or patchy saturation of the pore fluid. Respective changes in V_p with decreasing water saturation is shown in Figure 6.11 for homogeneous and patchy mixing of gas and water (Reuss lower bound and Voigt upper bound, respectively). The example data is from the shallow Snadd Formation gas reservoir in well 7222/11-1.

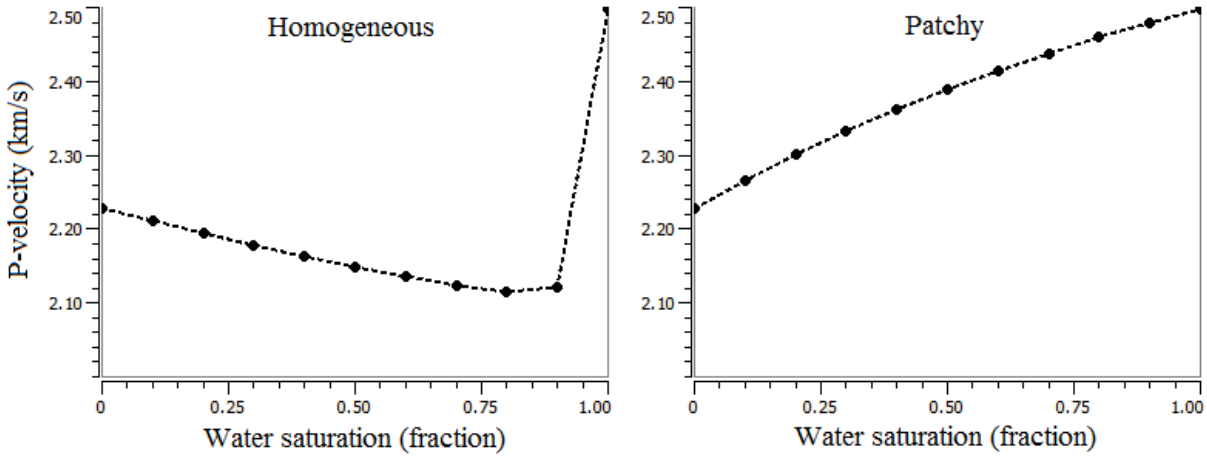

Figure 6.11. Plots showing the change in V_p with changing water saturation depending on homogeneous or patchy mixing of fluids, with data from the top of the shallow Snadd reservoir in well 7222/11-1. Note that velocity slightly increase when water saturation decrease beyond 10-20%.

A gradual increase in gas content can be seen in Figure 6.5 in the responses of the Snadd reservoir in well 7222/11-1. An increase in gas saturation from 0% to only 10% results in a large change in the AVO signature of the top (and bottom) reservoir interface, as shown again with the arrows in Figure 6.12. Further increase in gas content appears to shift points firstly towards slightly less negative gradient values and then towards slightly higher intercept values.

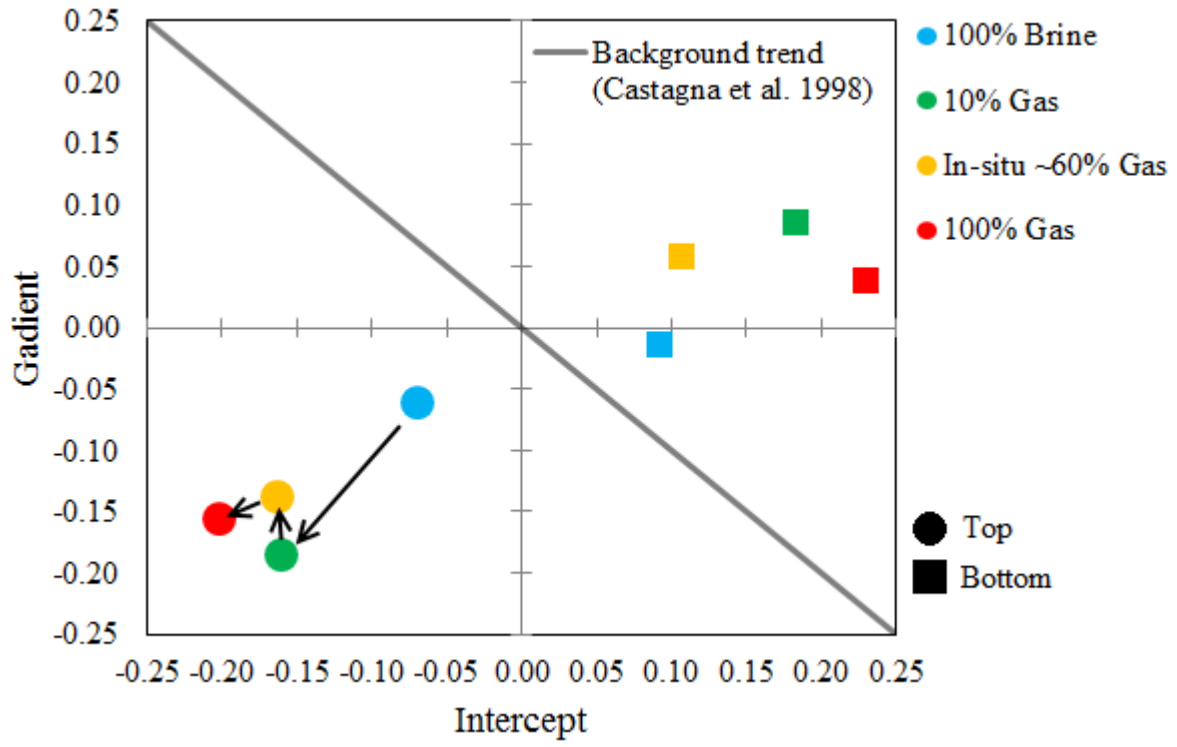

Figure 6.12. Crossplot of intercept versus gradient for the shallow Snadd reservoir in well 7222/11-1, showing the responses of increasing gas saturation from 0% to 10%, in situ 60% and finally 100%.

Table 6.3 shows the quantitative change in rock parameters for the top interface of the reservoirs, namely V_p, V_s, density (ρ), saturated bulk modulus (K_{sat}) and Poisson's ratio (υ) in the case of replacing brine with gas. Values are shown relative to the 100% brine saturated scenario, and the in-situ case of approximately 60% average gas saturation is indicated in the table. Additionally, the assumption of homogeneous mixing of fluids is once again evident from the P-velocity changes as it slightly increases with increasing gas saturation above 10%, after a drop of 14% from the pure brine scenario. Specific values are previously provided in Table 6.2. Table 6.3 also indicates that the biggest change in P-velocity (and Poisson's ratio) occurs by introducing only a small amount of gas to the system, and that subsequent decrease in water saturation only amounts to minor changes. On the other hand, shear-velocity only shows a small percentage increase as a function of lowered bulk density, and is therefore relatively insensitive to fluid content. Density decreases as more gas replaces water. The interplay between these parameters helps explain the somewhat unintuitive relative positioning of the reflection points representing the three gas-influenced scenarios in Figure 6.12. More specifically, it could be an effect of the P-velocity's change from decreasing in the first step to increasing in the subsequent steps, as opposed to the other parameters which show more consistent behavior of only decreasing or increasing with each change in saturation. As V_p is determined by both the rock bulk density and bulk modulus (Eq. 3.25), increasing V_p with increased gas saturation indicate that the density decreases more due to the lower fluid density of gas than does the bulk modulus due to the higher compressibility of gas. This is observable in the values of saturated bulk modulus in Table 6.3. A second effect causing the back-and-forth positioning of points in all reservoirs plotted is that the gas parameters (e.g. density, fluid modulus) are standard values which are constant for the modeled gas saturations

in all cases. Properties assigned to the in situ gas are calculated based on the estimated water saturation and are variable from reservoir to reservoir. If assuming a constant approximate average of the reservoir's in situ water saturation, a more linear fluid trend would appear between 10% and 100% gas saturation in the intercept-gradient plot. Water saturation from petrophysical analysis is in this study preferred to be used as an input parameter, as choosing a constant value would lead to yet another idealization of the results obtained.

Table 6.3: Change in rock parameters due to fluid substitution, from pure brine to pure gas. Data from top shallow Snadd reservoir interface in well 7222/11-1.

Increasing gas saturation from 100% brine model	**ΔV_p (%)**	**ΔV_s (%)**	**$\Delta\rho$ (%)**	**K_{sat} (GPa)**	**$\Delta\upsilon$ (%)**
7222/11-1 Snadd					
10% gas	-14.551	0.731	-1.440	-38.459	-27.941
In situ (60% gas)	-12.495	4.874	-9.035	-41.641	-31.765
100% gas	-10.036	7.961	-14.186	-41.875	-32.059
7222/11-1 Kobbe					
10% gas	-4.087	0.280	-0.596	-15.117	-13.410
In situ (~60% gas)	-2.999	1.867	-3.614	-16.395	-14.559
100% gas	-1.805	3.126	-5.997	-16.509	-14.943
7224/6-1 Tubåen					
10% gas	-8.336	0.559	-1.090	-28.352	-24.382
In situ (<20% gas)	-7.905	1.734	-3.358	-30.192	-26.502
100% gas	-4.337	5.872	-10.859	-30.862	-27.208
7224/6-1 Snadd					
10% gas	-4.332	0.077	-0.190	-16.078	-17.597
100% gas	-4.060	0.922	-1.825	-17.926	-19.742

By examining Figure 6.5, it is apparent that the effect of decreasing water saturation in the intercept-gradient crossplot is markedly smaller for the deeper Kobbe reservoir in well 7222/11-1 than for the shallow Snadd reservoir. Even though porosity values are in a decent range in this particular interval (estimated to ~8-15% in petrophysical analysis), all four points representing top reservoir for the brine-, in situ- and gas scenarios are located around the position of the point representing 100% brine saturation in the Snadd reservoir. The Kobbe brine scenario is to some degree displaced more towards the background trend.

Table 6.3 demonstrates the percentage change in parameters for the top of the Kobbe reservoir. If examining the trends of increasing gas saturation, the progression is the same as seen in the Snadd reservoir. S-wave velocity slightly increase, density and Poisson's ratio decrease, and P-wave velocity initially decreases before slightly approaching the initial value again. However, as an effect of both lower porosity as well as deeper burial and higher degree of cementation which increases the pore space stiffness, the relative change is smaller (Figure 6.5). This can be seen as a display of deeply buried, compacted and cemented sediments having a lower sensitivity to fluid changes than younger, more unconsolidated sediments (Chopra and Castagna 2014; Avseth 2015). Tubåen and Snadd reservoirs in well 7224/6-1 also exhibits less percentage change in parameters than the less consolidated Snadd reservoir in well 7222/11-1. Tubåen appears slightly more sensitive to fluid substitution than the Kobbe and deeper Snadd reservoirs, as expected due to higher porosity, seeing as e.g. the V_p decrease due to 10% gas is double that of the deeper examples (-8.336% versus ~4%). Low porosity values (<5%) is observed in the upper part of the 7224/6-1 Snadd reservoir, whereas porosity

approaches 14% in the lower section. This can explain the very minute change in properties from 10% to 100% gas, as values are extracted from the top of each reservoir.

6.3 Uncertainties

A number of uncertainties in AVO modeling are related to the fluid replacement process. Previously discussed uncertainty in well log measurements are conserved or increased when put through the Gassmann equations for predicting changes in velocity. Predicted log traces for e.g. brine-sand or gas-sand are consequently not absolute, but comes with a certain range of error (Chopra and Castagna 2014). Gassmann's equations have a set of assumptions that can be broken and thereby introducing more uncertainty to the results, e.g. low permeability and/or low porosity reservoirs, or in the case of heterogeneities in fluid distribution and rock components (Chopra and Castagna 2014). Most of the reservoirs considered in this study include a shale-component, which introduces an uncertainty to the fluid replacement modeling. This is partially taken into account in the FRM process where shale volume is input as a parameter for effective medium modeling to represent more realistic conditions, as opposed to assuming pure quartz reservoirs only. If conducting fluid substitution in shaly sands, residual water saturation in gas intervals can be up to 50%. Gassmann's equations are nevertheless strictly only applicable to clean, high-permeability reservoir rocks (Chopra and Castagna 2014).

Many of the reservoirs identified in this study are of limited thickness, e.g. the Kobbe reservoir used for AVO modeling in this chapter (~10m). Reservoirs can cause tuning effects if they are too thin relative to the wavelet length (< ¼*λ), or if intra-reservoir reflectors disturb the response (Mondol 2015a).

Chapter 7: Summary and Conclusions

The overall goal of this study has been to characterize reservoirs of the Triassic and Jurassic successions in the southern part of the Bjarmeland Platform, Norwegian Barents Sea. This has been carried out through the three different, yet intertwined approaches of petrophysical analysis, rock physics diagnostics and AVO modeling, utilizing data from eight (8) exploration wells. The wells included in this study are 7222/6-1 (Obesum), 7223/5-1, 7222/11-1 (Caurus), 7224/7-1, 7124/3-1 (Bamse), 7125/1-1 (Binne), 7226/11-1 and 7224/6-1 (Arenaria). Four formations from these two time periods have been granted the primary focus, namely the Kobbe and Snadd Formations of Triassic age and the Tubåen and Stø Formations of Jurassic age. Combining and comparing the results and observations from each stage of the process has contributed to a more complete understanding of reservoir characteristics, based on data from a number of identified potential reservoir intervals and known hydrocarbon-bearing zones. The applicability and limitations of each approach for this specific database have been discussed, in order to attain an image of how well reservoir variations are captured in this study area.

The study area includes the south-western corner of the Bjarmeland Platform, bounded by the Loppa High to the west, the Swaen Graben to the north, Norsel High and the Nordkapp Basin to the east, and the Nysleppen Fault Complex and the Hammerfest Basin to the south. Two wells are drilled on the eastern margin of the Loppa High, one is positioned on the Norsel High, one in the Nysleppen Fault Complex and one on the Samson Dome. The remaining three wells are located within the Bjarmeland Platform. Hydrocarbons are proven in all wells (if including all formations) except well 7226/11-1 where only shows are documented (NPD 2016).

Results from the petrophysical analysis include calculated estimates of shale volume, porosity, net-to-gross reservoir, net pay, water saturation and, where applicable, pay zone water saturation. Neutron-density crossplots have been used as assistance for lithology discrimination and as a hydrocarbon indicator. Jurassic reservoirs display higher average quality of reservoir properties than Triassic intervals, but are in return very thickness-limited. In the dominantly shaley Snadd Formation, good quality reservoirs have been discussed in relation to shallow marine deposition and fluvial channel deposition in a coastal/delta plain environment. These are suggested to be most frequently found in upper Snadd intervals, but the nature of fluvial, channelized sandstones make correlation across wells difficult. Porosity for the numerous reservoir intervals analyzed is inferred to be within a wide range. Kobbe reservoir sands are generally more shaley than its younger counterparts, and continuous promising intervals are found to be relatively thin, i.e. less than 30 m. On the other hand, reservoirs estimated to fulfill the cutoff demands selected for porosity, shale volume and water saturation (i.e. defined as pay zones based on currently used definitions) were identified in six of eight wells. The Tubåen and Stø formations are recorded with sufficient well log data and analyzed in four (7224/7-1, 7124/3-1, 7226/11-1, 7224/6-1) and three (7224/7-1, 7125/1-1, 7226/11-1) wells, respectively.

Rock physics diagnostics has been used to extract information about reservoir sorting, cementation, hydrocarbon content and lithological influences in relevant crossplot domains, by identifying trends in the data related to depositional-, diagenetic- or fluid effects. The sensitivity of published models to data from this study area is shown to be reasonably valid. Crossplots with relevant templates employed in this study include V_p versus porosity, shear

modulus versus density, V_p versus V_s, V_p/V_s versus acoustic impedance, and Lambda-Rho versus Mu-Rho. A local V_p-V_s relation was derived from all available data, compared to published V_p-V_s trends, and used for estimating V_s in the four wells where it is not measured. Estimated shear velocity values were mainly used for comparison with results obtained when utilizing recorded V_s, e.g. in plots of V_p/V_s versus AI or LMR. V_p-depth trends have been compared to published V_p-depth data and exhumation estimates to compare the validity of more general information to the local data. Uplift estimates based on the approximate difference between how the studied data plots and a linear compaction trend shows good correlation with values from literature. Effort has also been made to identify mechanical to chemical compaction transition zones and reservoir intervals that have experienced a markedly lower degree of chemical compaction.

Separation of data due to hydrocarbon content has been shown in crossplots of V_p versus V_s, rock physics templates (RPTs) used in the V_p/V_s versus acoustic impedance domain and in plots of $\lambda\rho$ versus $\mu\rho$ (LMR). The latter was also utilized together with a published V_p-cement relation to establish across-wells trends where the Snadd Formation reservoirs appear to contain less low-cement data in the northernmost well 7224/6-1 (Arenaria) than in western to southwestern wells 7222/6-1 (Obesum), 7223/5-1 and 7222/11-1 (Caurus). The Kobbe Formation reservoirs display more consistent signs of intermediate to high cementation. Interpretations regarding quantitative cement volume estimates are however approached with caution, as published literature point towards mineral compositions in Snadd and Kobbe that strictly do not coincide with the assumptions for use of rock physics cement model templates or the empirical V_p-cement relation tested. Additionally, if chlorite coating is effectively present in the reservoirs, quartz cementation is assumed to be inhibited.

AVO modeling has been used for analyzing four select reservoirs distributed over two different wells (7222/11-1 Caurus and 7224/6-1 Arenaria) and at varying depths. By creating synthetic seismograms within a reasonably realistic framework, the synthetics generated from well log data can be seen as an indication of how the reservoirs would behave in real pre-stack seismic data. They do, however, provide an idealistic image of the subsurface as practically no noise is incorporated and no multiples are modeled. Fluid substitution is used to create an image of how the same reservoir would appear if saturated with another fluid or a certain level of water saturation. Effects of decreasing water saturation on the seismic properties and AVO signature is discussed, as well as the effect of modifying modeling input parameters - e.g. block size used for upscaling of well logs. Cluster interpretation is shown as an alternative to interpreting only reflection point picks, and the effect of choosing a suitable background trend when interpreting data is commented on. The uncertainties that arise when using the Gassmann equations for fluid replacement modeling and tuning effects in thin reservoir are also expressed.

Final conclusions and main results acquired during this thesis work are summarized below.

- Potential Triassic reservoir intervals are identified at multiple depth levels within the dominantly shaley Snadd and Kobbe formations in the Bjarmeland Platform area, many of them containing hydrocarbon indications. Shale content, low porosity (leading to lower permeability) and limited thickness, however, often degrade their apparent quality. Extensive uplift and erosion, assessed to be in the range of ~1150-1600 m, has contributed to decrease the expected reservoir quality at a given depth.
- Average Kobbe reservoir effective porosity ranges from 2.6-16.4% and net-to-gross reservoir varies between 0.056 and 0.680. The maximum continuous hydrocarbon interval thickness found is 10 m in well 7222/11-1 (Caurus).
- Porosity for the diverse Snadd reservoir intervals analyzed is inferred to be within a wide range, approximately 6 to 30%. Net-to-gross reservoir varies from 30 to 100% and is very dependent on the definition of the gross reservoir thickness identified.
- Reservoir quality in the Tubåen Formation was interpreted as consistently good across all relevant wells with regard to shale volume, porosity and net-to-gross reservoir. Effective porosity ranges from 21.4 to 25.2% and net-to-gross reservoir is close to 100% in all wells based on chosen cutoff values. Hydrocarbons are identified in a 13.9 m pay zone in well 7124/3-1 and as low saturation gas in well 7224/6-1 (Arenaria).
- Stø Formation properties deteriorate and thickness decreases from well 7125/1-1 in the south of the study area towards well 7226/11-1 in the north-east. A thin hydrocarbon zone is identified in the 122 m clean sandstone reservoir in well 7125/1-1 which has a calculated average porosity of 24.6%. Intermediate thickness (~25 m) and properties are found in well 7224/7-1 on the Samson Dome.
- Data has been compared to rock physics cement models and published exhumation estimates to show a distinct difference between reservoirs at less than ~800 m present depth (below KB) and the remaining data. Shallow Snadd Formation reservoir intervals in wells 7222/11-1 (Caurus) and 7223/5-1 distinguish themselves from the rest, and are interpreted to be at most lightly cemented. This is supported by comparison to empirical relations for cement estimation and plots of μ versus ρ.
- V_p/V_s versus AI rock physics templates are shown to detect hydrocarbon saturation both in low saturation gas reservoirs (e.g. Tubåen Formation well 7224/6-1, Snadd Formation well 7223/5-1) and in deeper reservoirs studied (e.g. Kobbe Formation). Separation is however not significant enough to infer saturation levels or to discriminate oil from gas. Data plots between the brine-saturated line and the gas saturated line - but in areas where less 10% gas saturation is assumed - in all cases with one possible exception that has been discussed. Brine data generally plots from slightly above the brine-sand line and up towards the shale line. Tweaking the template to an individual reservoir and depth naturally generates an improved fit.
- LMR interpretation indicated a more generous amount of hydrocarbon-influenced reservoir rock than the petrophysical analysis in the discussed reservoir intervals. Lithological differences and cement effects were clearly observable in studied data, showing more consistent and constrained behavior of Kobbe reservoirs than Snadd reservoirs.
- AVO modeling of reservoirs in different locations, at different depths and with different cap rocks resulted in diverse behavior of the reflection signatures. The Snadd and Kobbe reservoirs in well 7222/11-1 (Caurus) both displayed class 1 anomalies for the in situ top reservoir reflections. A stronger response was observed in the shallow,

less consolidated and less cemented Snadd reservoir, whereas the Kobbe reservoir is interpreted to have a lower impedance contrast to the surrounding shale.

- The top Tubåen Formation interface in well 7224/6-1 exhibits a class 4 anomaly, which is typically associated with shallow, unconsolidated reservoirs. The reservoir is situated at ~1000 m depth and is assumed to have experienced approximately 1500 m uplift, indicating that it has been in the range of quartz cementation. A hard Fuglen Formation cap rock is proposed as an explanation for the atypical reservoir classification, and by extension as an explanation for similar reservoirs exhibiting decreasing reflection magnitude with increasing incident angle.
- Classification of the deeper Snadd reservoir in well 7224/6-1 resulted in a class 1 anomaly associated with well-consolidated hard sands, which corresponds well to the depth and low V_p/V_s ratio of this reservoir.
- Changes in seismic properties are quantitatively shown to be highly reliant on porosity.

Reference list

Aki, K. and Richards, P. G., 1980, Quantitative Seismology: Freeman.

Amante, C. and Eakins, B. W. 2009. *ETOPO1 1 Arc-Minute Global Relief Model: Procedures, Data Sources and Analysis.* National Geophysical Data Center, NOAA.

Archie, G. E. 1942. The Electrical Resistivity Log as an Aid in Determining Some Reservoir Characteristics. Transactions of the AIME, **146,** 54-62.

Asquith, G. and Krygowski, D. A. 2004a. Gamma Ray. Basic Well Log analysis: AAPG Methods in Exploration, **2,** 31-35.

Asquith, G. and Krygowski, D. A. 2004b. Porosity logs. Basic Well Log analysis: AAPG Methods in Exploration, **2,** 37-76.

Asquith, G. and Krygowski, D. A. 2004c. Resistivity logs. Basic Well Log analysis: AAPG Methods in Exploration, **2,** 77-101.

Avseth, P., 2015, Explorational Rock Physics: The Link between Geological Processes and Geophysical Observables, *In* Bjørlykke, K., ed., Petroleum Geoscience. From Sedimentary Environments to Rock Physics - Second Edition. Springer-Verlag Berlin Heidelberg, 455-488.

Avseth, P., Dvorkin, J., Mavko, G. and Rykkje, J. 2000. Rock physics diagnostic of North Sea sands: Link between microstructure and seismic properties. Geophysical Research Letters, **27,** 2761-2764.

Avseth, P., Mavko, G., Dvorkin, J. and Mukerji, T. 1999. Rock Physics and Seismic Properties of Sands and Shales as a Function of Burial Depth. SEG Technical Program Expanded Abstracts**,** 4.

Avseth, P., Mukerji, T. and Mavko, G., 2005, Quantitative Seismic Interpretation: Applying Rock Physics Tools to Reduce Interpretation Risk: Cambridge University Press.

Avseth, P., Mukerji, T., Mavko, G. and Dvorkin, J. 2010. Rock-physics diagnostics of depositional texture, diagenetic alterations, and reservoir heterogeneity in high-porosity siliciclastic sediments and rocks — A review of selected models and suggested work flows. Geophysics, **75,** 75A31-75A47.

Baig, I., Faleide, J. I., Jahren, J. and Mondol, N. H. 2016. Cenozoic exhumation on the southwestern Barents Shelf: Estimates and uncertainties constrained from compaction and thermal maturity analyses. Marine and Petroleum Geology, **73,** 105-130.

Bergan, M. and Knarud, R., 1993, Apparent changes in clastic mineralogy of the Triassic–Jurassic succession, Norwegian Barents Sea: possible implications for palaeodrainage and subsidence, *In* Vorren, T. O., Bergsager, E., Dahl-Stamnes, Ø. A., Holter, E., Johansen, B., Lie, E. and Lund, T. B., eds., Norwegian Petroleum Society Special Publications. Elsevier, 481-493.

Bhuyan, K. and Passey, Q. R. 1994. Clay Estimation From Gr And Neutron -Density Porosity Logs. *SPWLA 35th Annual Logging Symposium.* Society of Petrophysicists and Well-Log Analysts.

Bjørlykke, K., 2015a, Heat Transport in Sedimentary Basins, *In* Bjørlykke, K., ed., Petroleum Geoscience. From Sedimentary Environments to Rock Physics - Second Edition. Springer-Verlag Berlin Heidelberg, 273-277.

Bjørlykke, K., 2015b, Production Geology, *In* Bjørlykke, K., ed., Petroleum Geoscience. From Sedimentary Environments to Rock Physics - Second Edition. Springer-Verlag Berlin Heidelberg, 545-558.

Bjørlykke, K. and Jahren, J., 2015, Sandstones and Sandstone Reservoirs, *In* Bjørlykke, K., ed., Petroleum Geoscience. From Sedimentary Environments to Rock Physics - Second Edition. Springer-Verlag Berlin Heidelberg, 119-149.

Castagna, J. P., Batzle, M. L. and Eastwood, R. L. 1985. Relationships between compressional-wave and shear-wave velocities in clastic silicate rocks. Geophysics, **50,** 571-581.

Castagna, J. P., Batzle, M. L. and Kan, T. K., 1993, Rock physics: The link between rock properties and AVO response, *In* Castagna, J. P. and Backus, M., eds., Offset-dependent reflectivity: Theory and practice of AVO analysis: Investigations in Geophysics. 135-171.

Castagna, J. P. and Swan, H. W. 1997. Principles of AVO crossplotting. The Leading Edge, **16,** 337-342.

Castagna, J. P., Swan, H. W. and Foster, D. J. 1998. Framework for AVO gradient and intercept interpretation. Geophysics, **63,** 948-956.

Chiburis, E., Leaney, S., Skidmore, C., Franck, C. and Mchugo, S. 1993. Hydrocarbon Detection With AVO. Oilfield Review, **5,** 42-50.

Chopra, S. and Castagna, J., 2014, AVO: Society of Explorational Geophysicists.

Crain, E. R. 2015. Crain's Petrophysical Handbook [Online]. Available: https://www.spec2000.net/01-index.htm [Accessed 15. February 2016].

Dalland, A., Worsley, D. and Ofstad, K. 1988. A lithostratigraphic scheme for the Mesozoic and Cenozoic succession offshore mid- and northern Norway. NPD Bulletin, **4,** 1-65.

Doré, A. G. 1995. Barents Sea Geology, Petroleum Resources and Commercial Potential. Arctic, **48,** 207-221.

Doré, A. G. and Jensen, L. N. 1996. The impact of late Cenozoic uplift and erosion on hydrocarbon exploration: offshore Norway and some other uplifted basins. Global and Planetary Change, **12,** 415-436.

Dvorkin, J. 2008. Yet another V_s equation. Geophysics, **73,** E35-E39.

Dvorkin, J. and Nur, A. 1996. Elasticity of high-porosity sandstones: Theory for two North Sea data sets. Geophysics, **61,** 1363-1370.

Ellis, D. V. and Singer, J. M., 2008, Well Logging for Earth Scientists: Springer.

Faleide, J. I., Bjørlykke, K. and Gabrielsen, R. H., 2015, Geology of the Norwegian Continental Shelf, *In* Bjørlykke, K., ed., Petroleum Geoscience. From Sedimentary Environments to Rock Physics - Second Edition. Springer-Verlag Berlin Heidelberg, 603-638.

Faleide, J. I., Gudlaugsson, S. T. and Jacquart, G. 1984. Evolution of the western Barents Sea. Marine and Petroleum Geology, **1,** 123-150.

Faleide, J. I., Vagnes, E. and Gudlaugsson, S. 1993. Late Mesozoic–Cenozoic evolution of the south-western Barents Sea in a regional rift-shear tectonic setting. Marine and Petroleum Geology, **10,** 186-214.

Gabrielsen, R. H., Færseth, R. B., Jensen, L. N., Kalheim, J. E. and Riis, F. 1990. Structural elements of the Norwegian Continental Shelf. Part 1: The Barents Sea Region. NPD Bulletin, **6**.

Gelius, L. J. and Johansen, T. A. 2010. Petroleum Geophysics. UniGEO as.

Glørstad-Clark, E., Birkeland, E. P., Nystuen, J. P., Faleide, J. I. and Midtkandal, I. 2011. Triassic platform-margin deltas in the western Barents Sea. Marine and Petroleum Geology, **28,** 1294-1314.

Goodway, B. 2001. AVO AND LAMÉ CONSTANTS FOR ROCK PARAMETERIZATION AND FLUID DETECTION. CSEG Recorder, **26,** 39-60.

Goodway, B., Chen, T. and Downton, J. 1997. Improved AVO Fluid Detection And Lithology Discrimination Using Lamé Petrophysical Parameters; "λρ", μρ, λμ Fluid Stack", From P And S Inversions. 1997 SEG Annual Meeting.

Greenberg, M. L. and Castagna, J. P. 1992. SHEAR-WAVE VELOCITY ESTIMATION IN POROUS ROCKS: THEORETICAL FORMULATION, PRELIMINARY VERIFICATION AND APPLICATIONS. Geophysical Prospecting, **40,** 195-209.

Halland, E. K., Bjørnestad, A., Gjeldvik, I. T., Bjørheim, M., Magnus, C., Meling, I. M., Mujezinović, J., Riis, F., Sande Rød, R., Pham, V. T. H. and Tappel, I. 2014. Geology of the Barents Sea. *CO2 Storage Atlas.* Norwegian Petroleum Directorate.

Han, D. 1986. Effects of porosity and clay content on acoustic properties of sandstones and unconsolidated sediments. PhD Thesis, Stanford University.

Henriksen, E., Bjørnseth, H. M., Hals, T. K., Heide, T., Kiryukhina, T., Kløvjan, O. S., Larssen, G. B., Ryseth, A. E., Rønning, K., Sollid, K. and Stoupakova, A. 2011a. Chapter 17 Uplift and erosion of the greater Barents Sea: impact on prospectivity and petroleum systems. Geological Society, London, Memoirs, **35,** 271-281.

Henriksen, E., Ryseth, A. E., Larssen, G. B., Heide, T., Rønning, K., Sollid, K. and Stoupakova, A. V. 2011b. Chapter 10 Tectonostratigraphy of the greater Barents Sea: implications for petroleum systems. Geological Society, London, Memoirs, **35,** 163-195.

Hook, J. R. 2003. An Introduction to Porosity. Petrophysics, **44,** 205-212.

Kennedy, M., 2015, Practical Petrophysics: Elsevier B. V.

Klausen, T. G., Ryseth, A. E., Helland-Hansen, W., Gawthorpe, R. and Laursen, I. 2015. Regional development and sequence stratigraphy of the Middle to Late Triassic Snadd Formation, Norwegian Barents Sea. Marine and Petroleum Geology, **62,** 102-122.

Krief, M., Garat, J., Stellingwerf, J. and Ventre, J. 1990. A Petrophysical Interpretation Using The Velocities Of P and S Waves (Full-Waveform Sonic). The Log Analyst, **31,** 355-369.

Li, Y., Downton, J. and Xu, Y. 2007. Practical aspects of AVO modeling. The Leading Edge, **26,** 295-311.

Line, H. L. 2015. Reservoir characterization of the Middle – Upper Triassic Kobbe and Snadd Formations in the southwestern Barents Sea - The role of chlorite coating. Master Thesis, University of Oslo.

Lundschien, B. A., Høy, T. and Mørk, A. 2014. Triassic hydrocarbon potential in the Northern Barents Sea; integrating Svalbard and stratigraphic core data. Norwegian Petroleum Directorate Bulletin, **11,** 3-20.

Magoon, L. B. and Dow, W. G. 1994. The Petroleum System - from source to trap. AAPG Memoir, **60,** 3-24.

Marcussen, Ø., Maast, T. E., Mondol, N. H., Jahren, J. and Bjørlykke, K. 2010. Changes in physical properties of a reservoir sandstone as a function of burial depth – The Etive Formation, northern North Sea. Marine and Petroleum Geology, **27,** 1725-1735.

Mavko, G., Mukerji, T. and Dvorkin, J., 1998, The Rock Physics Handbook: Tools for Seismic Analysis in Porous Media: Cambridge University Press.

Mavko, G., Mukerji, T. and Dvorkin, J., 2009, The Rock Physics Handbook: Tools for Seismic Analysis of Porous Media: Cambridge University Press.

Mondol, N. H., 2015a, Seismic Exploration, *In* Bjørlykke, K., ed., Petroleum Geoscience. From Sedimentary Environments to Rock Physics - Second Edition. Springer-Verlag Berlin Heidelberg, 427-454.

Mondol, N. H., 2015b, Well logging: Principles, Applications and Uncertainties, *In* Bjørlykke, K., ed., Petroleum Geoscience. From Sedimentary Environments to Rock Physics - Second Edition. Springer-Verlag Berlin Heidelberg, 385-425.

Mondol, N. H., Bjørlykke, K. and Jahren, J. 2008. Experimental compaction of clays: relationship between permeability and petrophysical properties in mudstones. Petroleum Geoscience, **14,** 319-337.

Mondol, N. H., Bjørlykke, K., Jahren, J. and Høeg, K. 2007. Experimental mechanical compaction of clay mineral aggregates—Changes in physical properties of mudstones during burial. Marine and Petroleum Geology, **24,** 289-311.

Mondol, N. H., Grande, L., Aker, E., Berre, T., Ørbech, T., Duffaut, K., Jahren, J. and Bjørlykke, K. 2010. Velocity anisotropy of a shallow mudstone core. EAGE Extended Abstract, EarthDoc, C03, EAGE Shale Workshop: Shale-Resource & Challenge, 26-28 April 2010, Nice, France.

Mørk, A., Dallmann, W. K., Dypvik, H., Johannessen, E. P., Larssen, G. B., Nagy, J., Nøttvedt, A., Olaussen, S., Pčelina, T. M. and Worsley, D., 1999, Mesozoic lithostratigraphy, *In* Dallmann, W. K., ed., Lithostratigraphic Lexicon of Svalbard. Review and recommendations for nomenclature use. Upper Palaeozoic to Quaternary bedrock.: Norwegian Polar Institute, 127-214.

Norwegian Petroleum. 2016. Areas on the Norwegian continental shelf [Online]. Norwegian Petroleum Directorate & Norwegian Ministry of Petroleum and Energy. Available: http://www.norskpetroleum.no/en/exploration/licensing-position-for-the-norwegian-continental-shelf/ [Accessed 15. May 2016].

Npd 2011. The Resource Report 2011. Norwegian Petroleum Directorate.

Npd. 2014. Geological Plays [Online]. Norwegian Petroleum Directorate. Available: http://www.npd.no/en/Topics/Geology/Geological-plays/ [Accessed 02. November 2015].

Npd. 2015. 23rd licensing round - announcement [Online]. Norwegian Petroleum Directorate. Available: http://www.npd.no/en/Topics/Production-licences/Theme-articles/Licensing-rounds/23rd-Licencing-round/Announcement/ [Accessed 14. December 2015.

Npd. 2016. FactPages [Online]. Norwegian Petroleum Directorate. Available: http://factpages.npd.no/FactPages/Default.aspx?culture=en.

Npd Factmaps. 2016. Norwegian Petroleum Directorate. Available: http://gis.npd.no/factmaps/html_20/ [Accessed 15. May 2016].

Ohm, S. E., Austin, T. J. F. and Karlsen, D. A. 2008. Geochemically driven exploration models in uplifted areas: Example from the Norwegian Barents Sea. AAPG Bulletin, **92,** 1191-1223.

Petrowiki. 2015a. Determination of saturation [Online]. Society of Petroleum Engineers. Available: http://petrowiki.org/index.php?title=Well_log_interpretation&printable=yes [Accessed 08. January 2016].

Petrowiki. 2015b. Permeability determination [Online]. Society of Petroleum Engineers. Available: http://petrowiki.org/Permeability_determination [Accessed 08. March 2016].

Ross, C. P. 2000. Effective AVO crossplot modeling: A tutorial. Geophysics, **65,** 700-711.

Ross, C. P. and Kinman, D. L. 1995. Nonbright-spot AVO: Two examples. Geophysics, **60,** 1398-1408.

Rutherford, S. R. and Williams, R. H. 1989. Amplitude-versus-offset variations in gas sands. Geophysics, **54,** 680-688.

Ryseth, A., 2014, Sedimentation at the Jurassic–Triassic boundary, south-west Barents Sea, From Depositional Systems to Sedimentary Successions on the Norwegian Continental Margin. John Wiley & Sons, Ltd, 187-214.

Shuey, R. T. 1985. A simplification of the Zoeppritz equations. Geophysics, **50,** 609-614.

Smelror, M., Petrov, O., Larssen, G. B. and Werner, S., 2009, Geological history of the Barents Sea: Norges Geologiske undersøkelse.

Storvoll, V., Bjørlykke, K. and Mondol, N. H. 2005. Velocity-depth trends in Mesozoic and Cenozoic sediments from the Norwegian Shelf. AAPG Bulletin, **89,** 359-381.

Storvoll, V. and Brevik, I. 2008. Identifying time, temperature, and mineralogical effects on chemical compaction in shales by rock physics relations. The Leading Edge, **27,** 750-756.

Williams, D. M. 1990. The Acoustic Log Hydrocarbon Indicator. Society of Petrophysicists and Well-Log Analysts 31st Annual Logging Symposium**,** 1-22.
Worsley, D. 2008. The post-Caledonian development of Svalbard and the western Barents Sea. Polar Research, **27,** 298-317.
Worthington, P. F. and Cosentino, L. 2005. The Role of Cutoffs in Integrated Reservoir Studies. SPE Reservoir Evaluation & Engineering, **8,** 276-290.
Ødegaard, E. and Avseth, P. 2004. Well log and seismic data analysis using rock physics templates. First Break, **23,** 37-43.

Appendix A. Composite log displays

Kobbe Formation

Reservoir intervals are indicated by purple lines, and are numbered according to the order of reservoirs in Table 4.2.

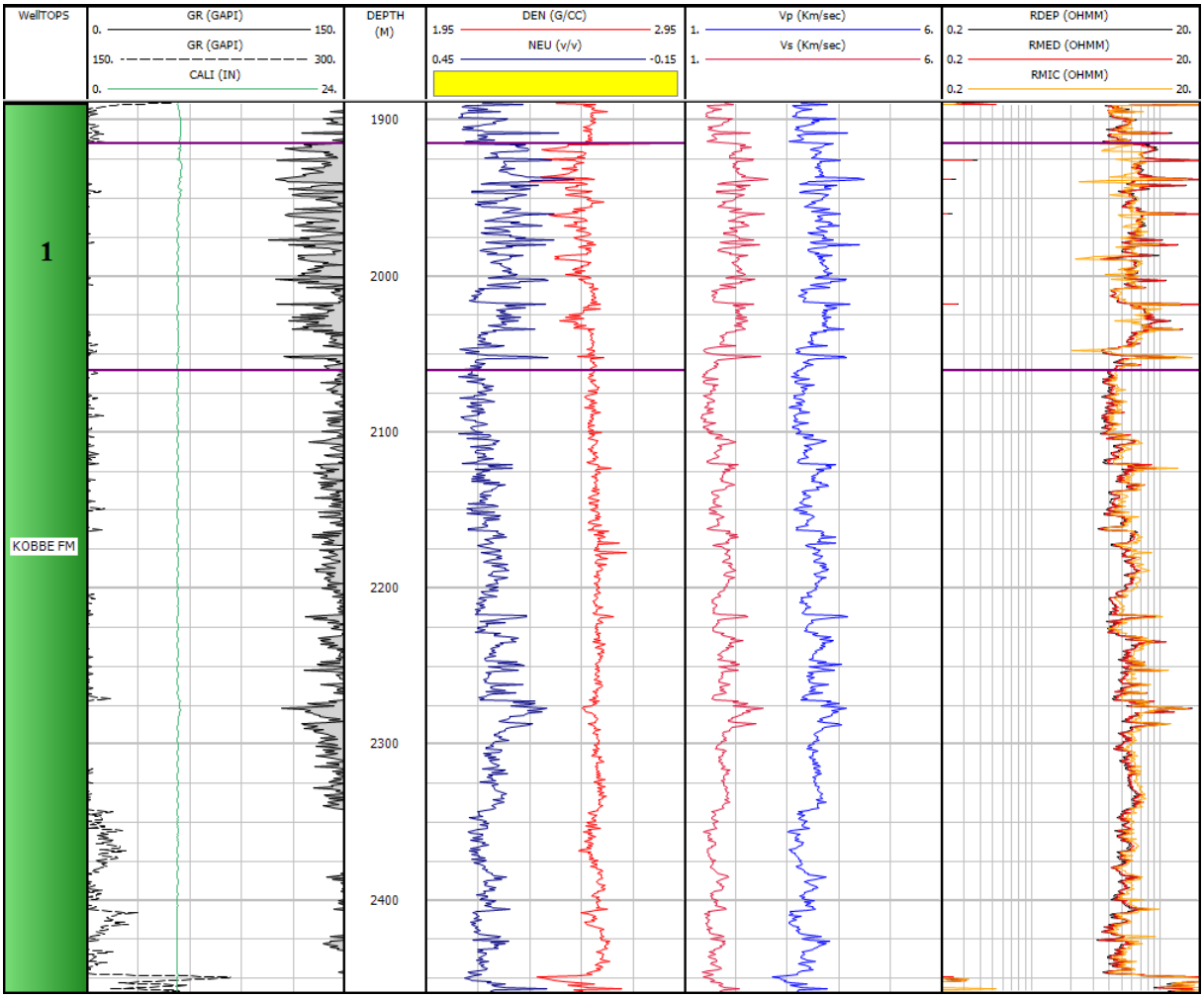

Figure A.1: Composite log display of the Kobbe Formation, well 7222/6-1.

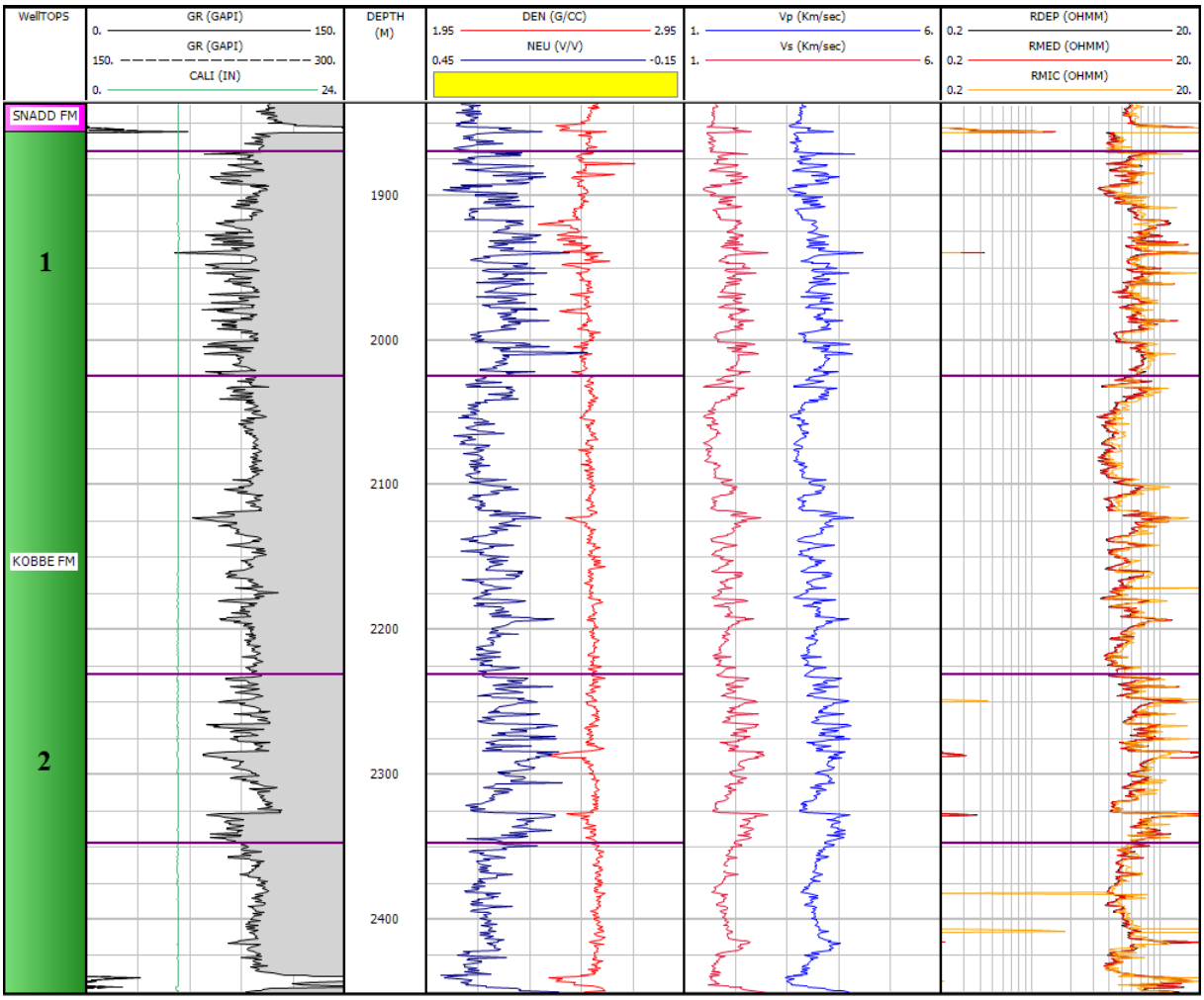

Figure A.2: Composite log display of the Kobbe Formation, well 7223/5-1.

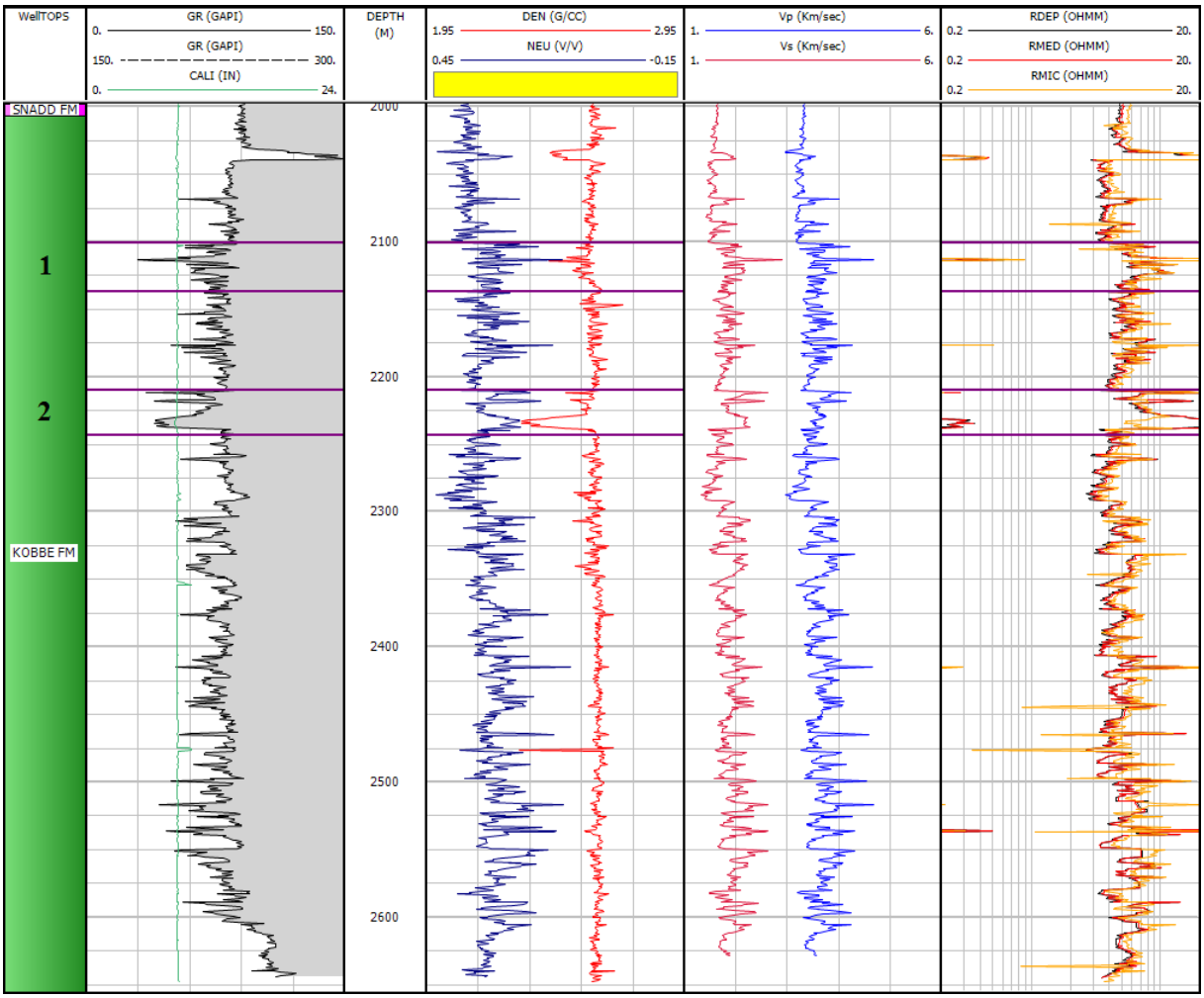

Figure A.3: Composite log display of the Kobbe Formation, well 7222/11-1.

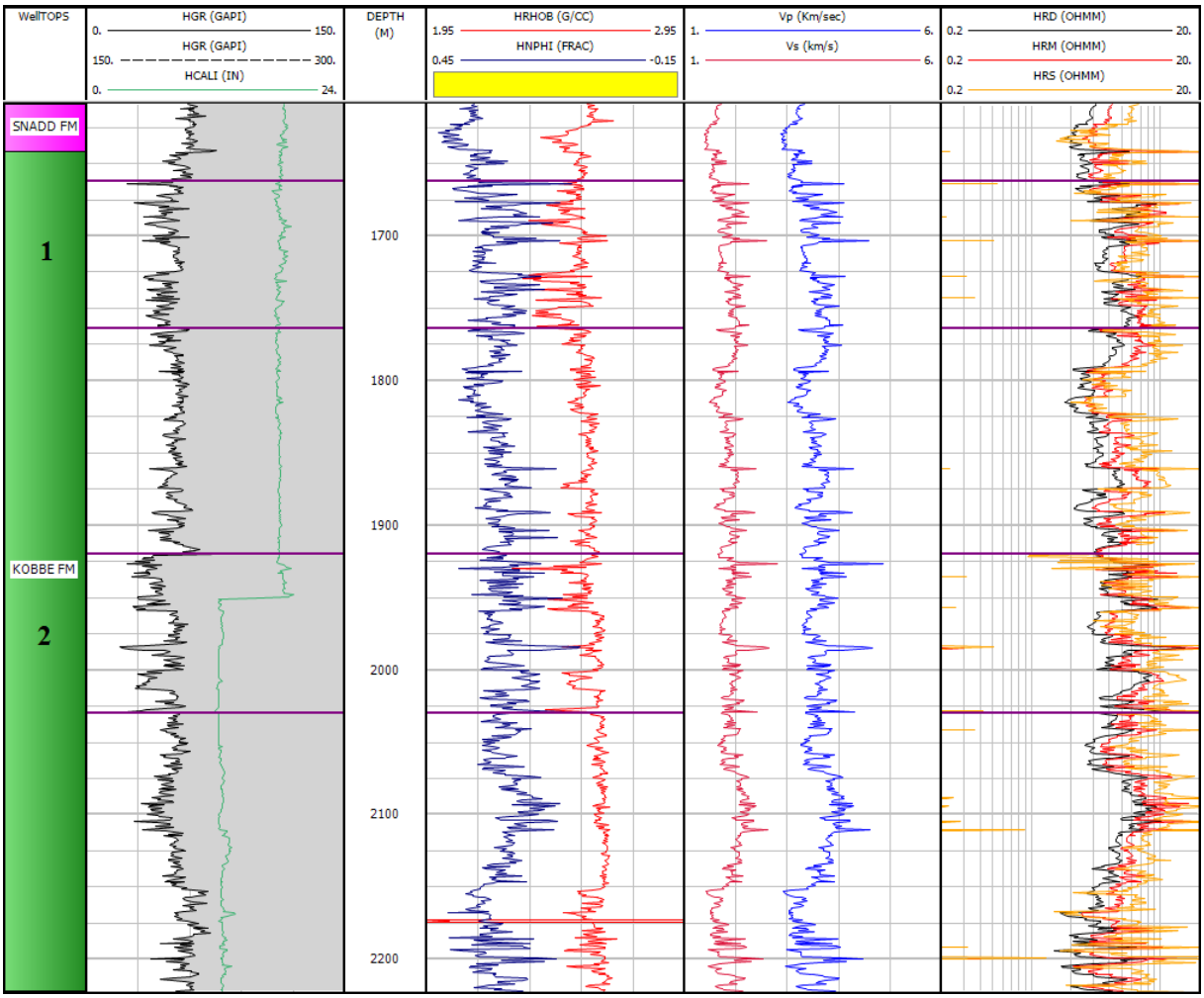

Figure A.4: Composite log display of the Kobbe Formation, well 7224/7-1.

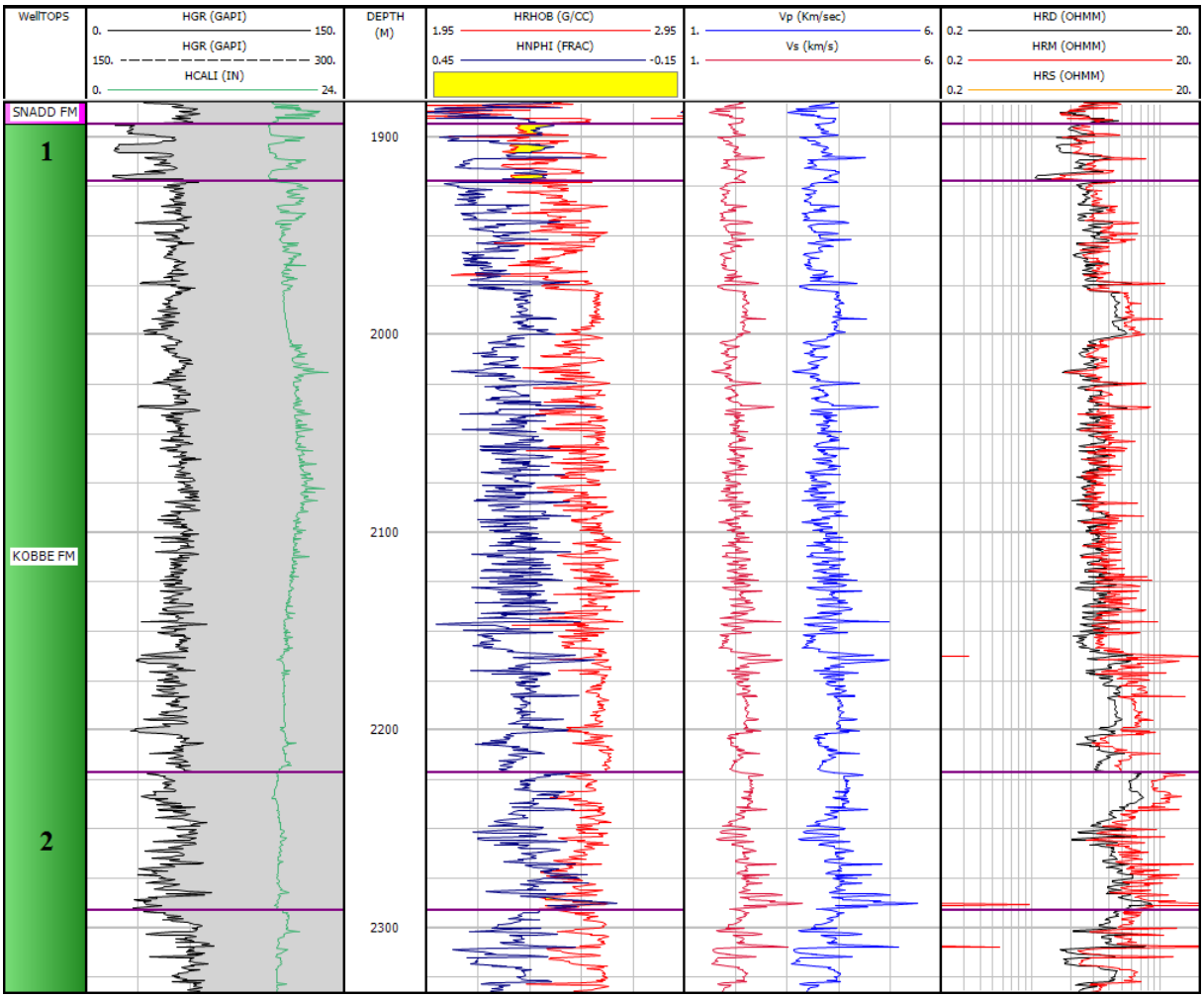

Figure A.5: Composite log display of the Kobbe Formation, well 7124/3-1.

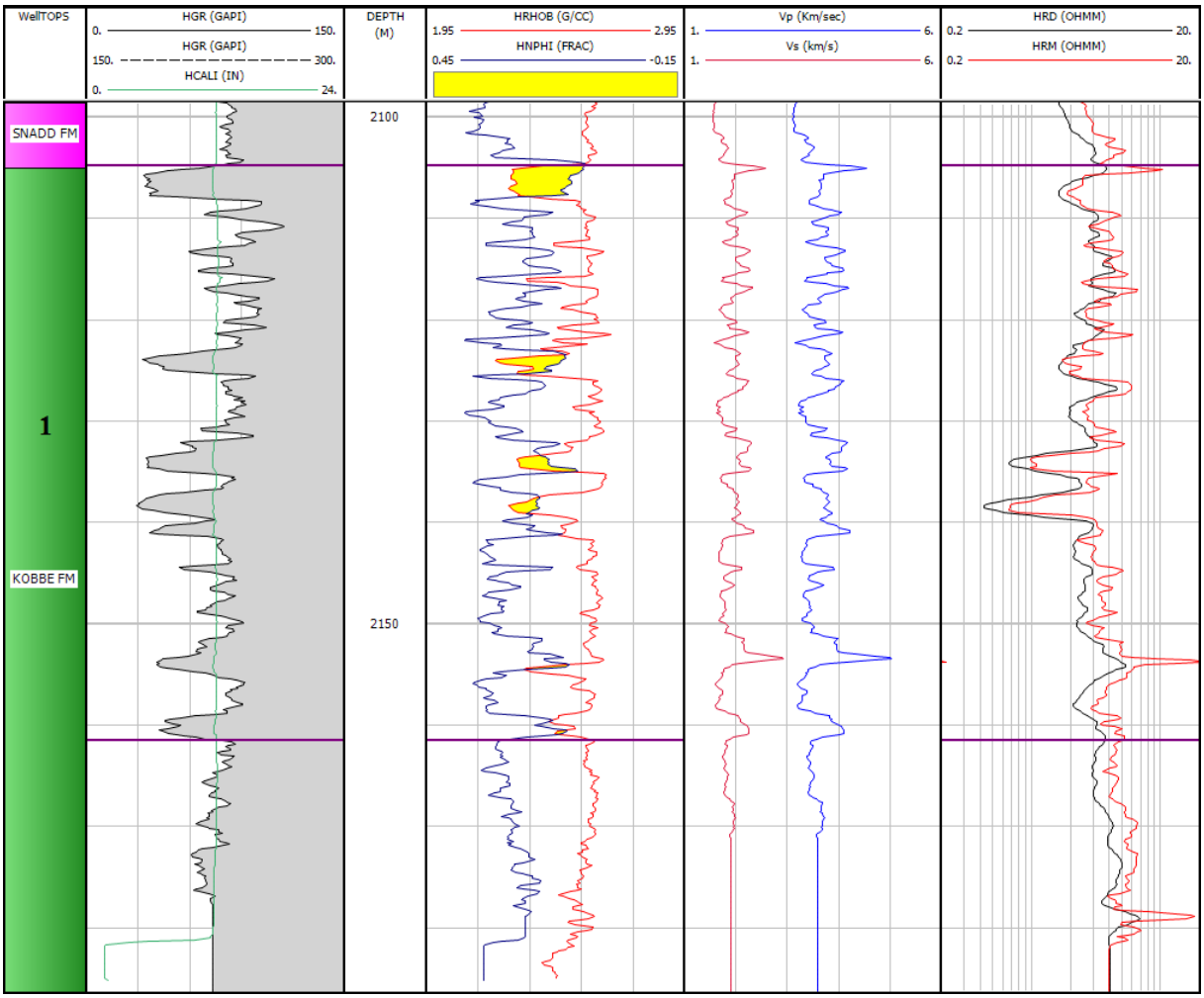

Figure A.6: Composite log display of the Kobbe Formation, well 7125/1-1.

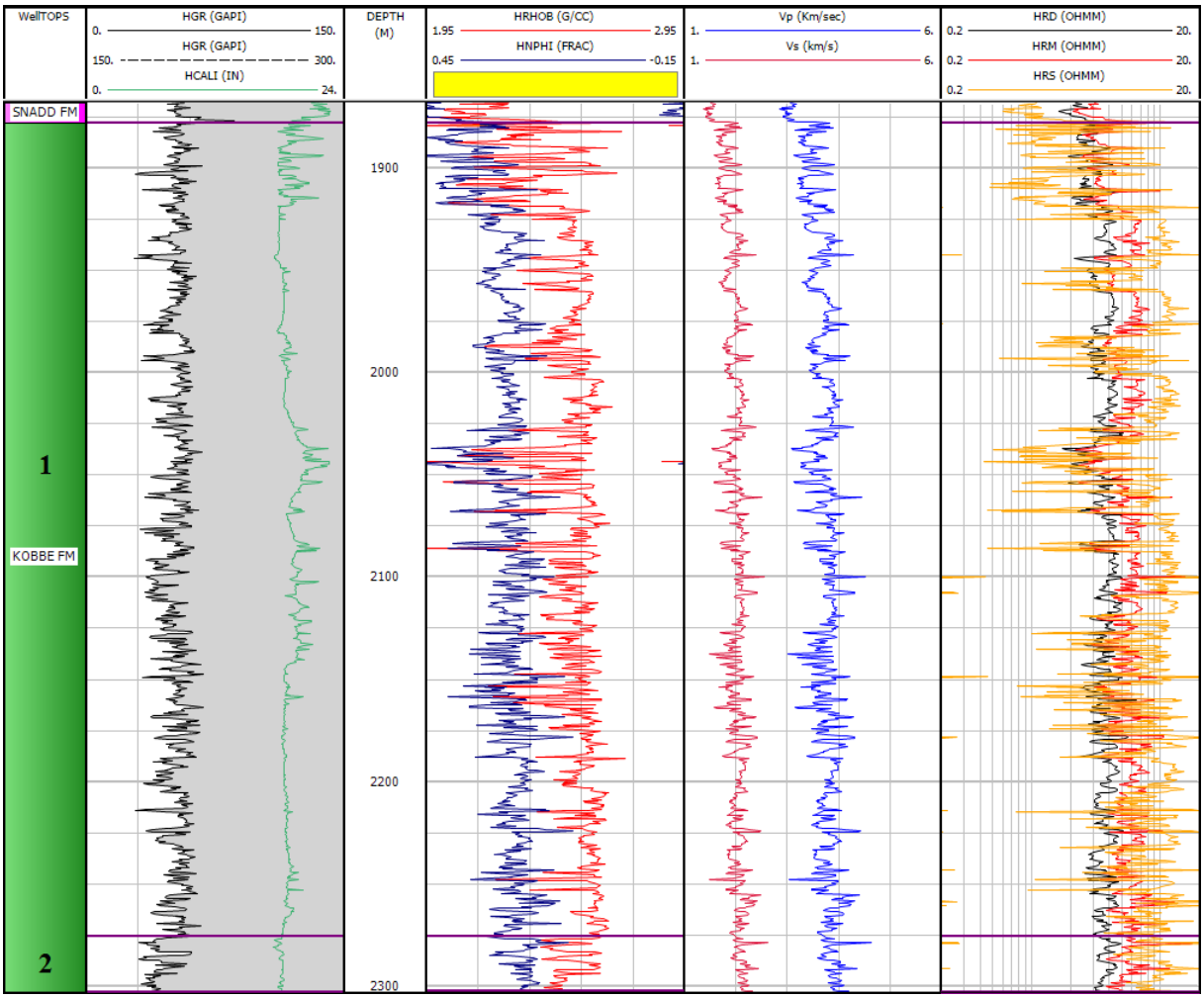

Figure A.7: Composite log display of the Kobbe Formation, well 7226/11-1.

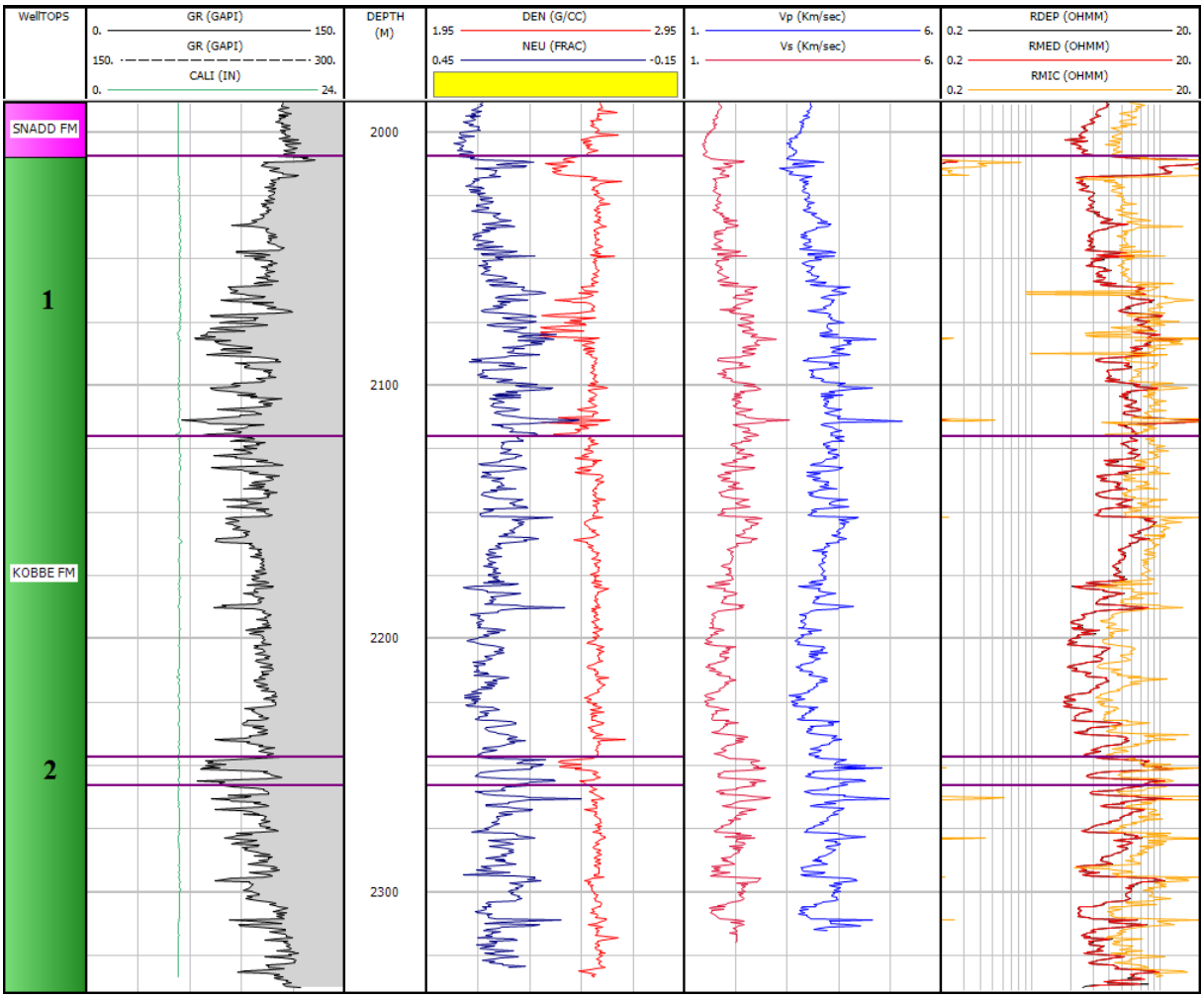

Figure A.8: Composite log display of the Kobbe Formation, well 7224/6-1.

Snadd Formation

Reservoir intervals are indicated by purple lines, and are numbered according to the order of reservoirs in Table 4.3.

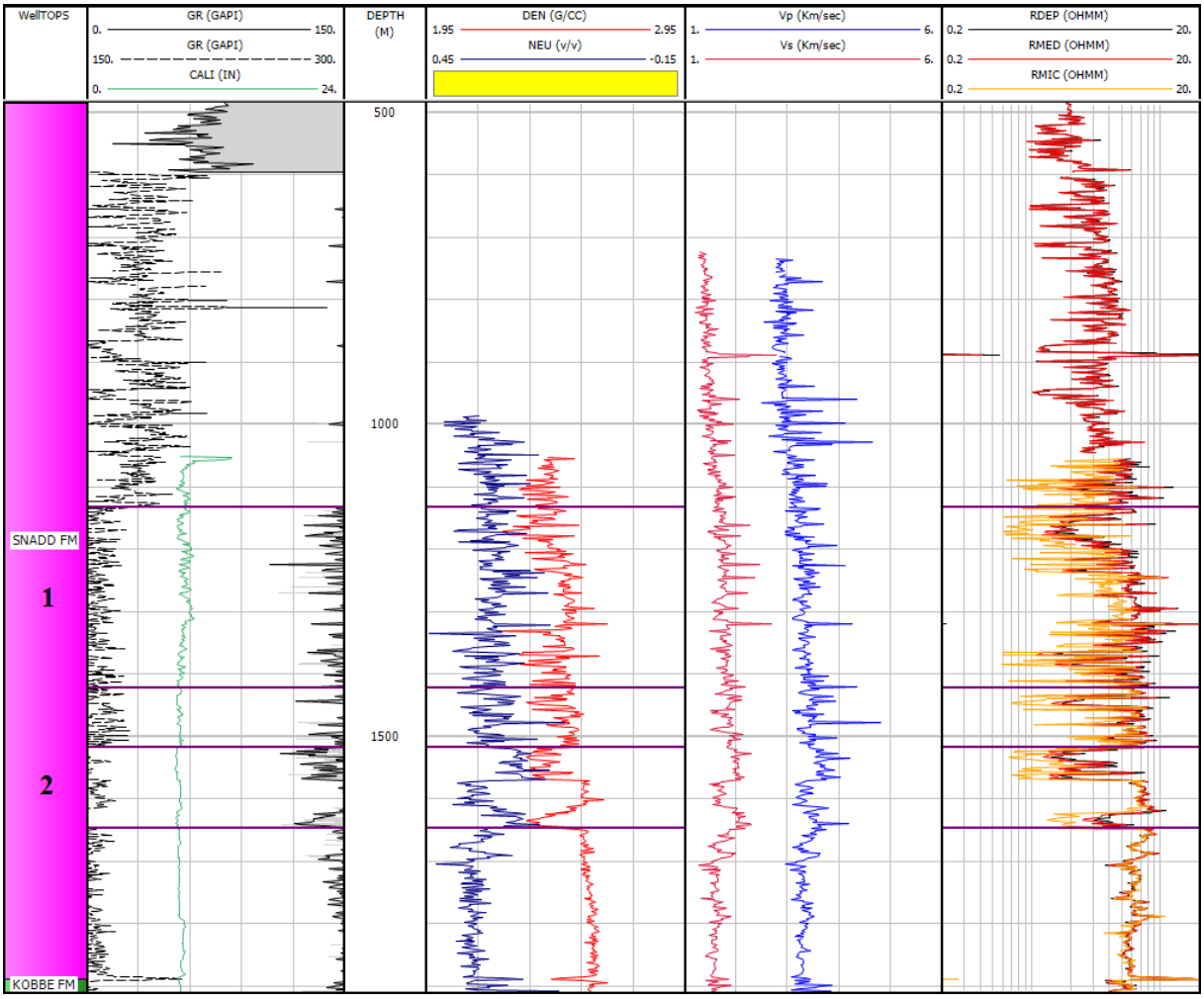

Figure A.9: Composite log display of the Snadd Formation, well 7222/6-1.

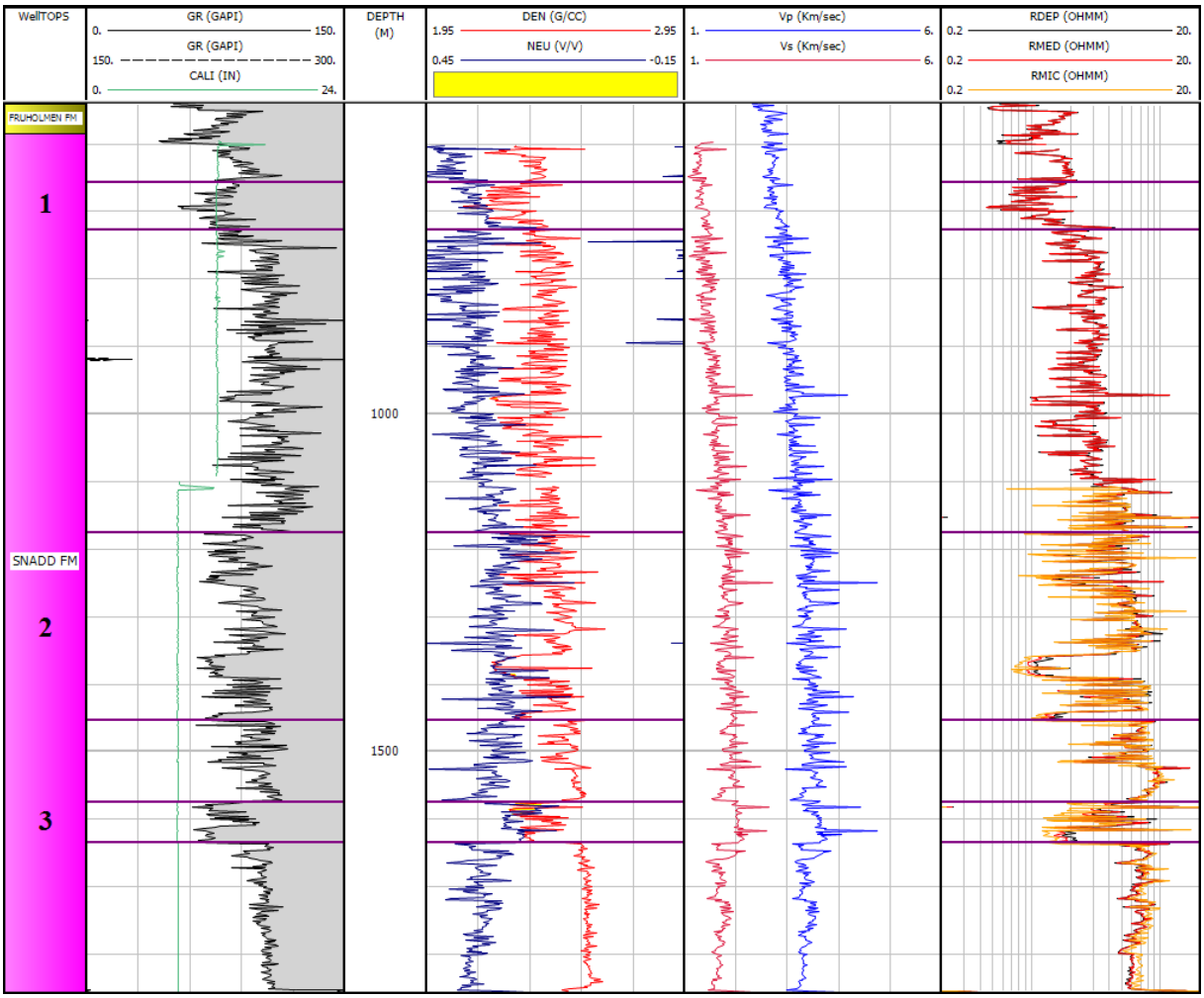

Figure A.10: Composite log display of the Snadd Formation, well 7223/5-1.

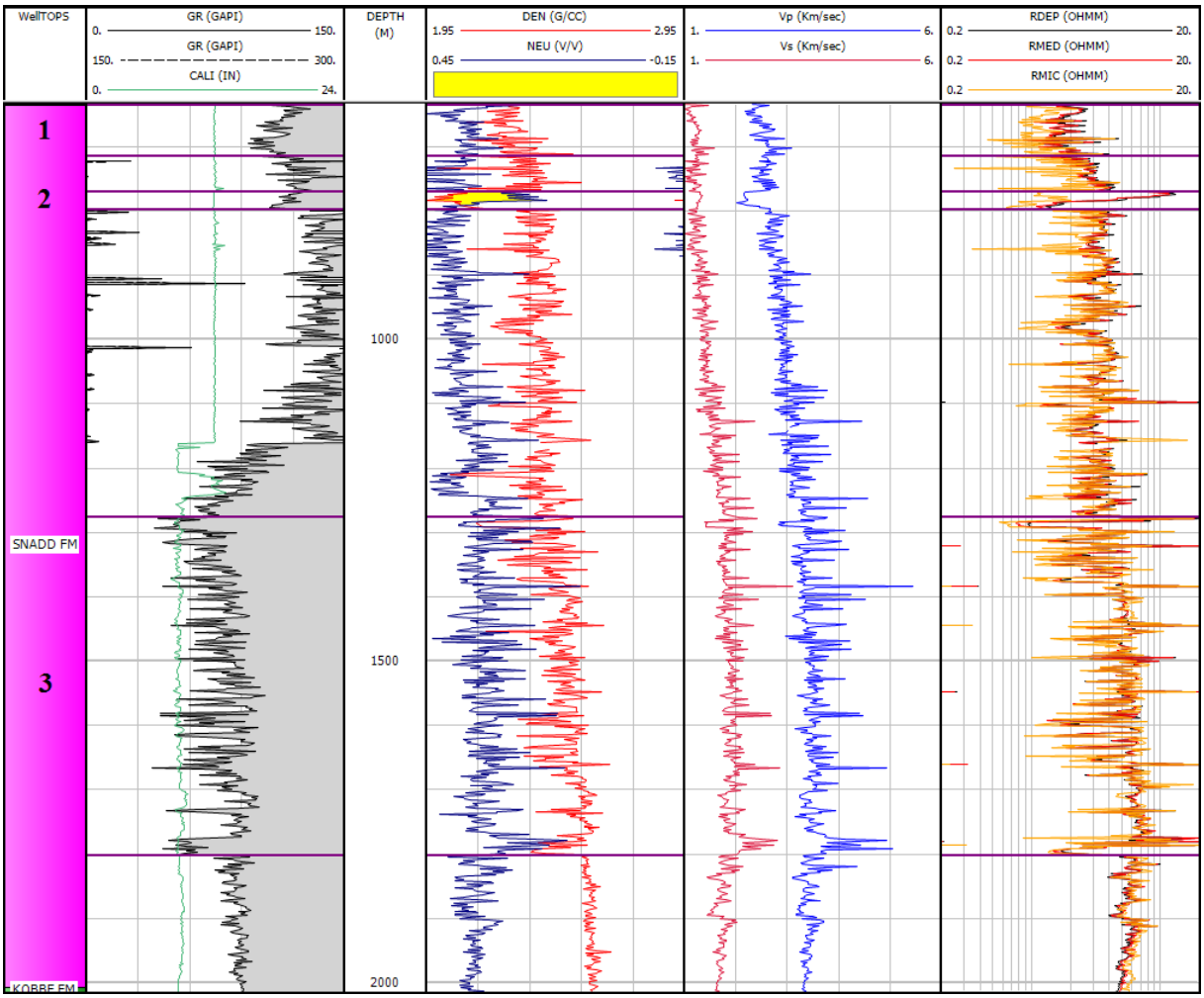

Figure A.11: Composite log display of the Snadd Formation, well 7222/11-1.

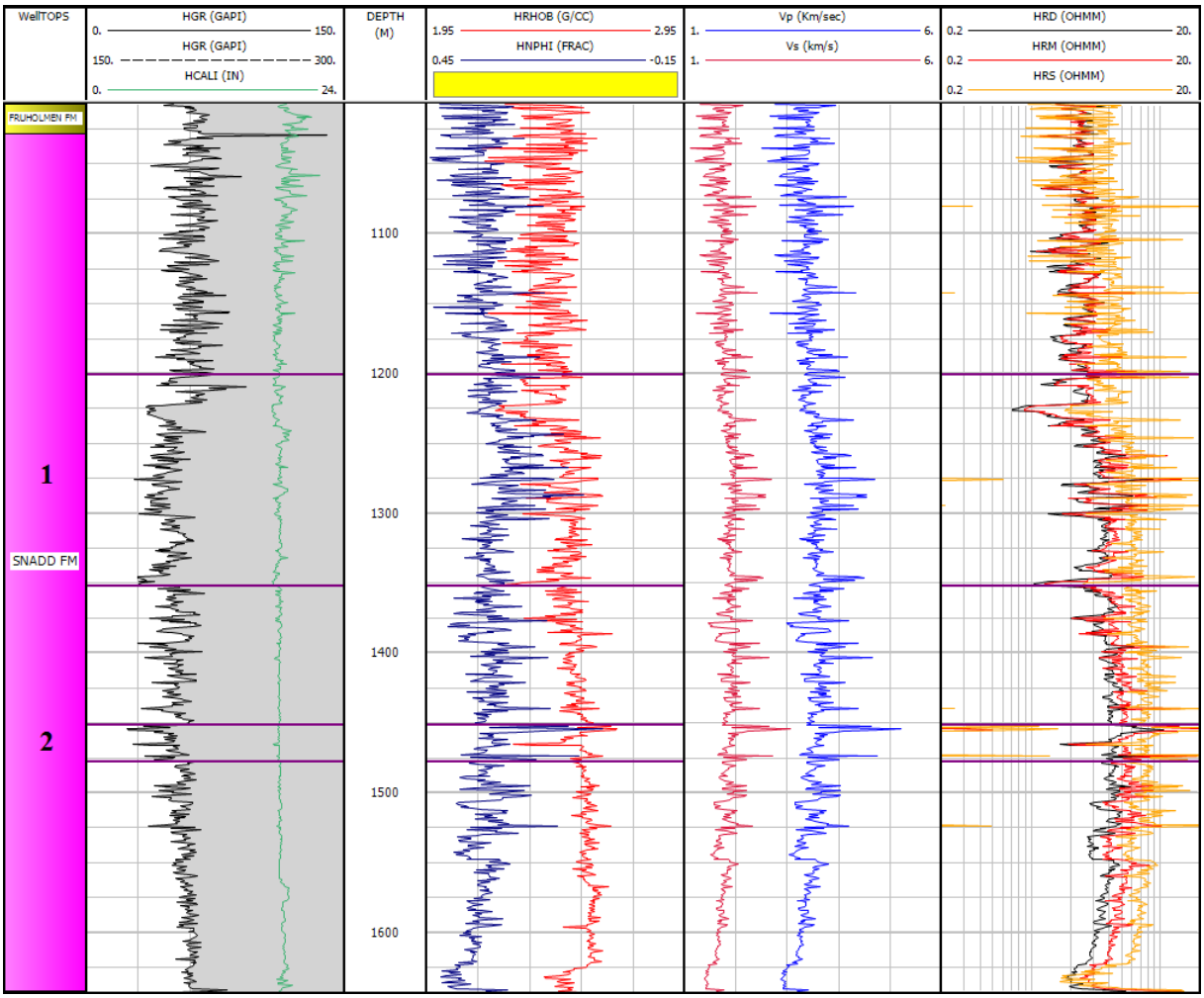

Figure A.12: Composite log display of the Snadd Formation, well 7224/7-1.

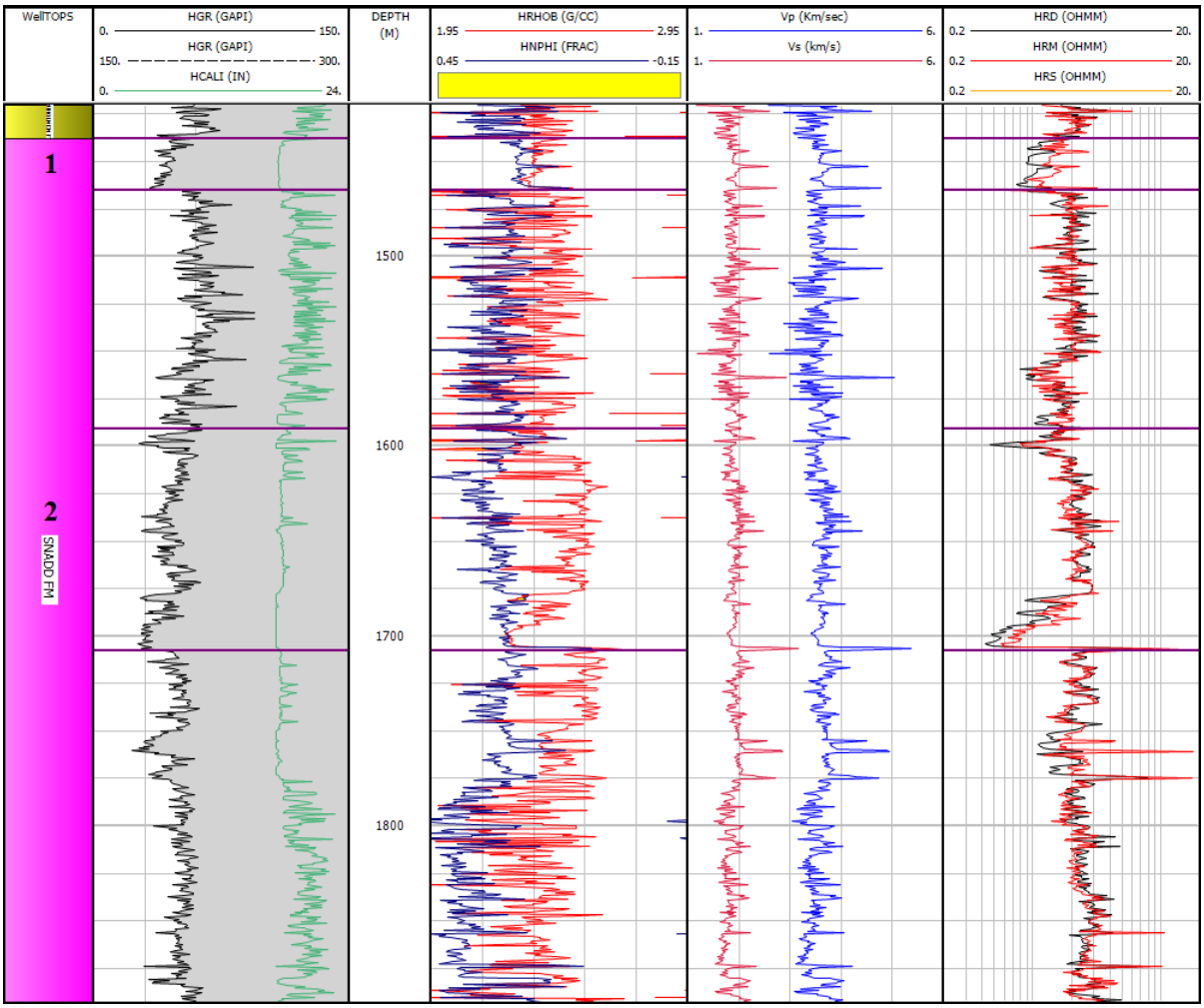

Figure A.13: Composite log display of the Snadd Formation, well 7124/3-1.

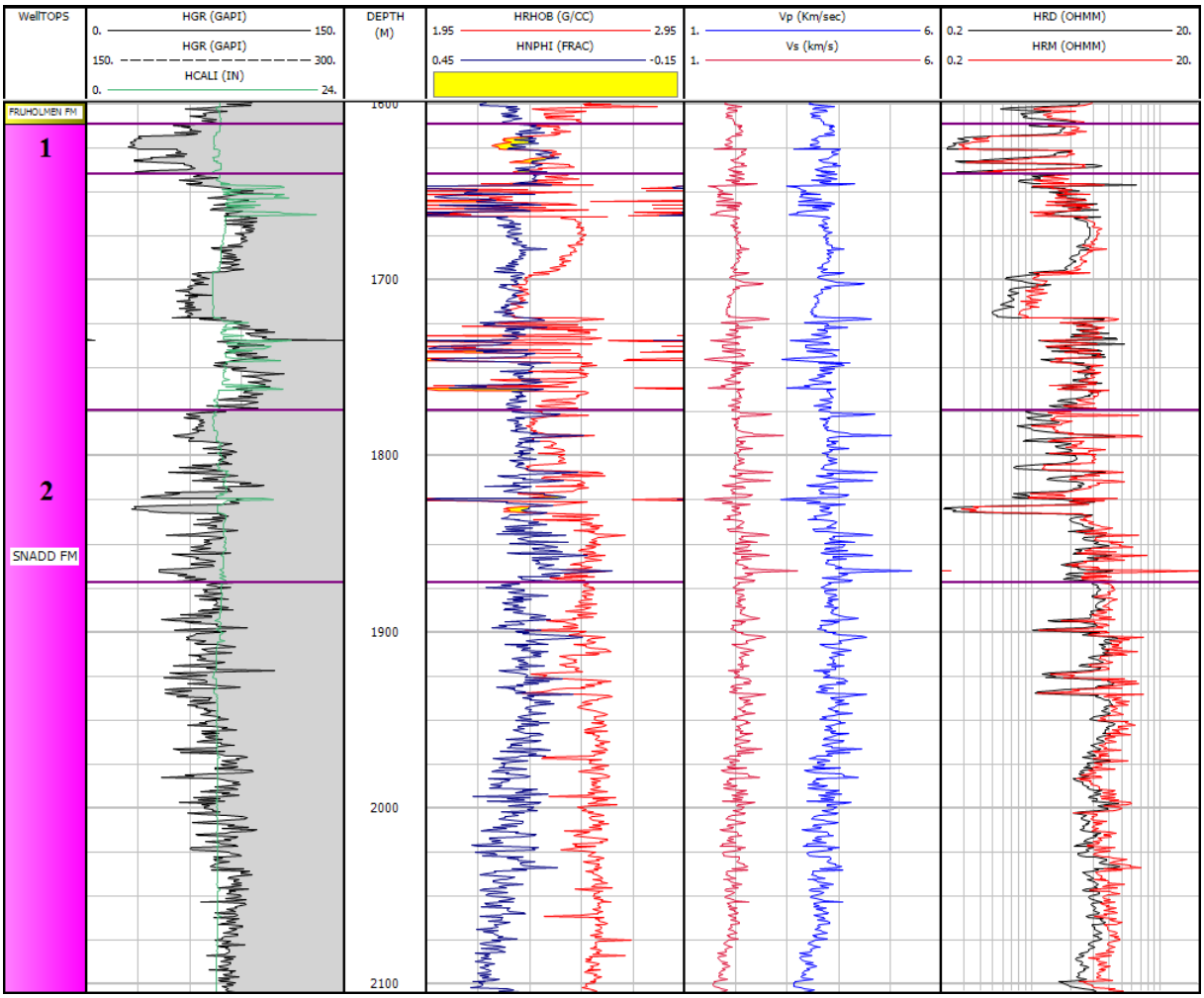

Figure A.14: Composite log display of the Snadd Formation, well 7125/1-1.

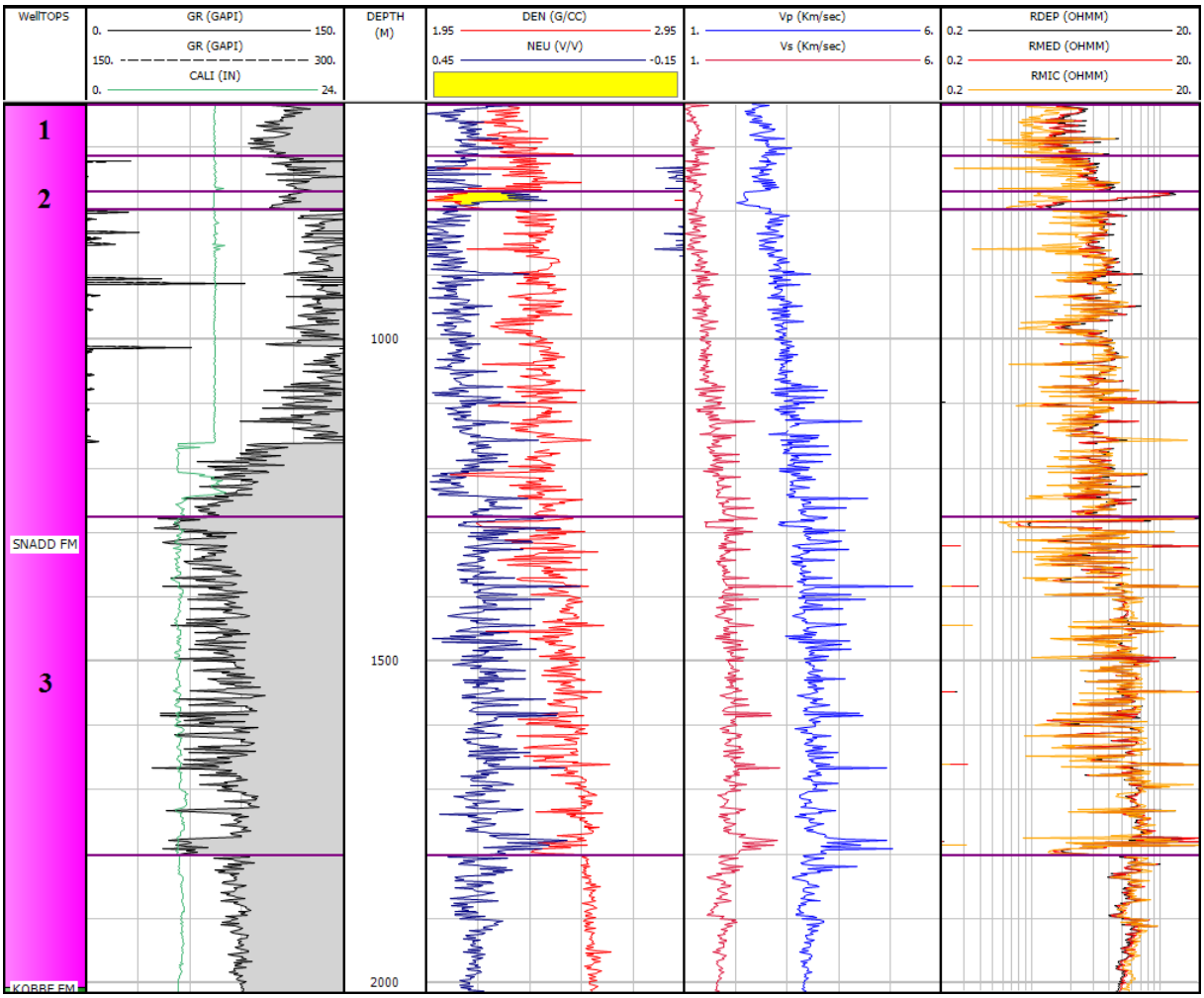

Figure A.15: Composite log display of the Snadd Formation, well 7226/11-1.

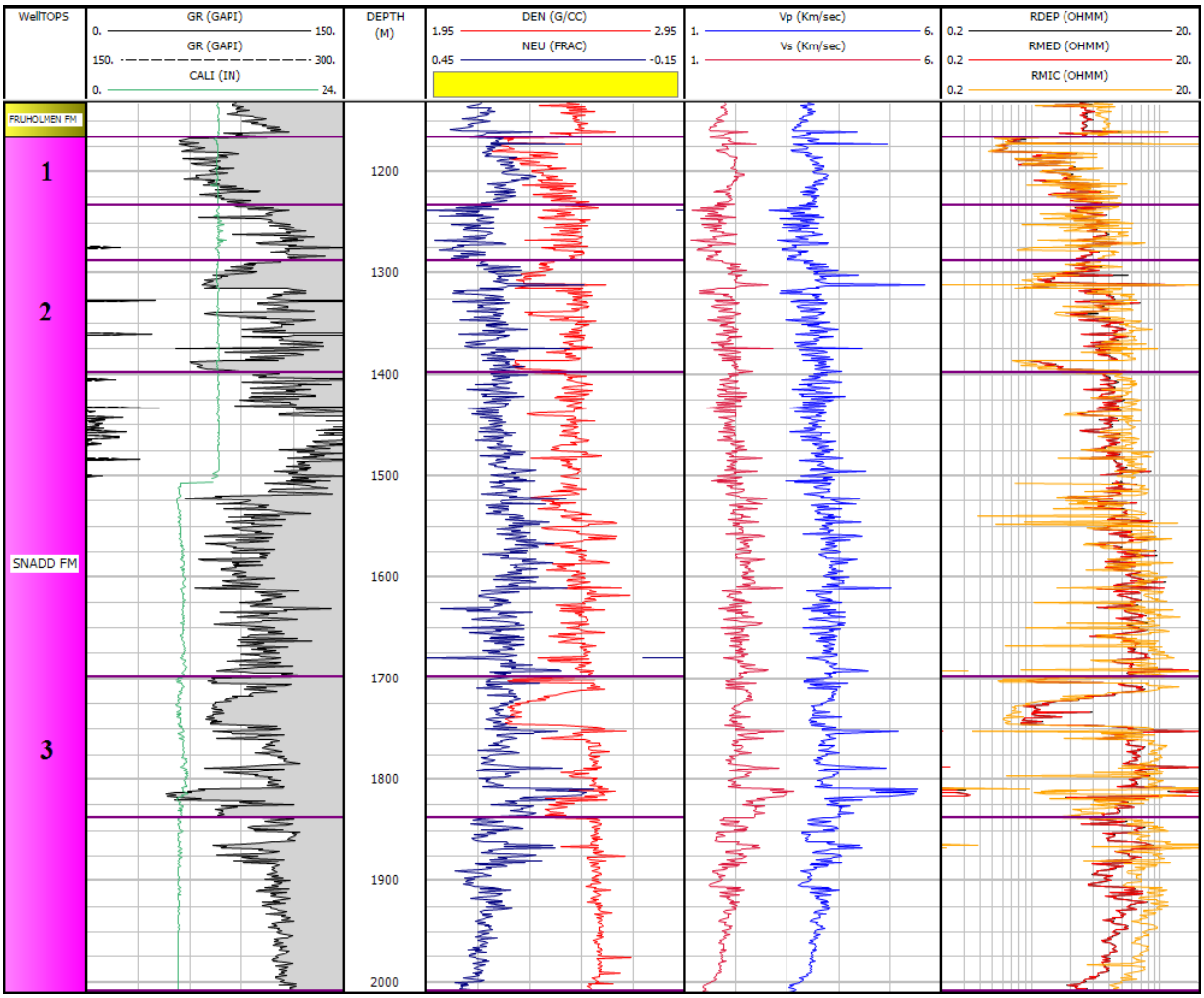

Figure A.16: Composite log display of the Snadd Formation, well 7224/6-1.

Tubåen and Stø Formations

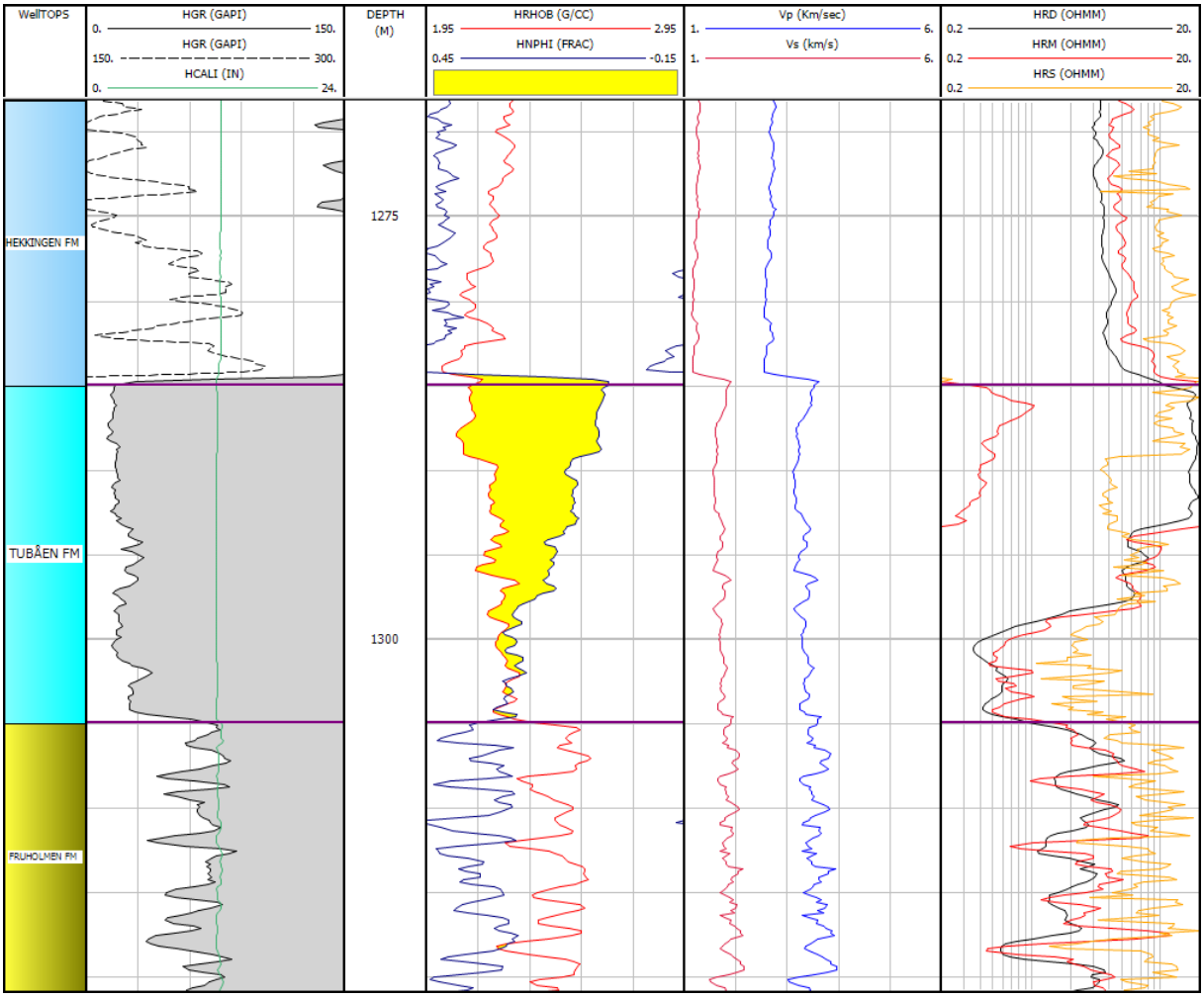

Figure A.17: Composite log display of the Tubåen Formation, well 7124/3-1.

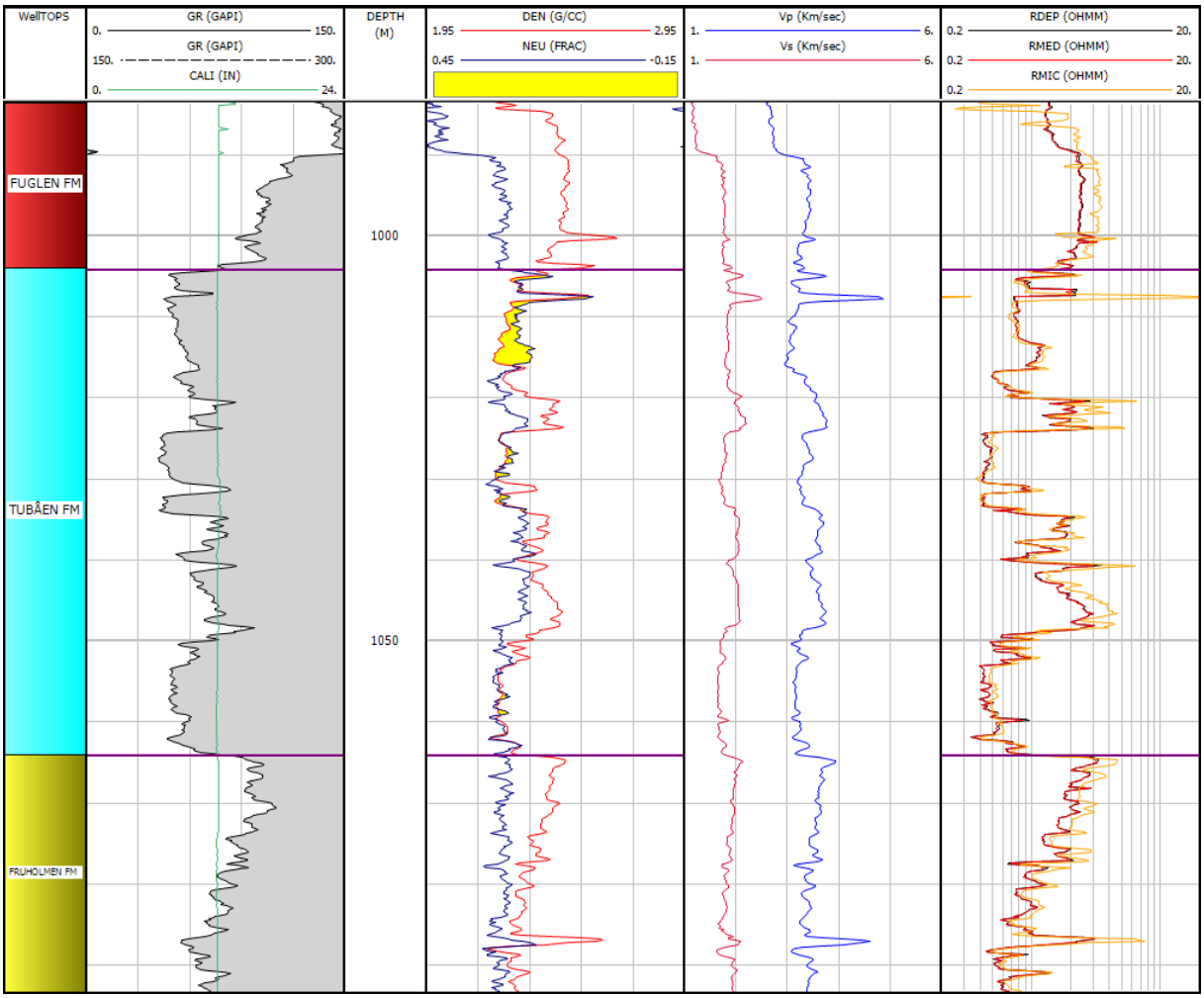

Figure A.18: Composite log display of the Tubåen Formation, well 7224/6-1.

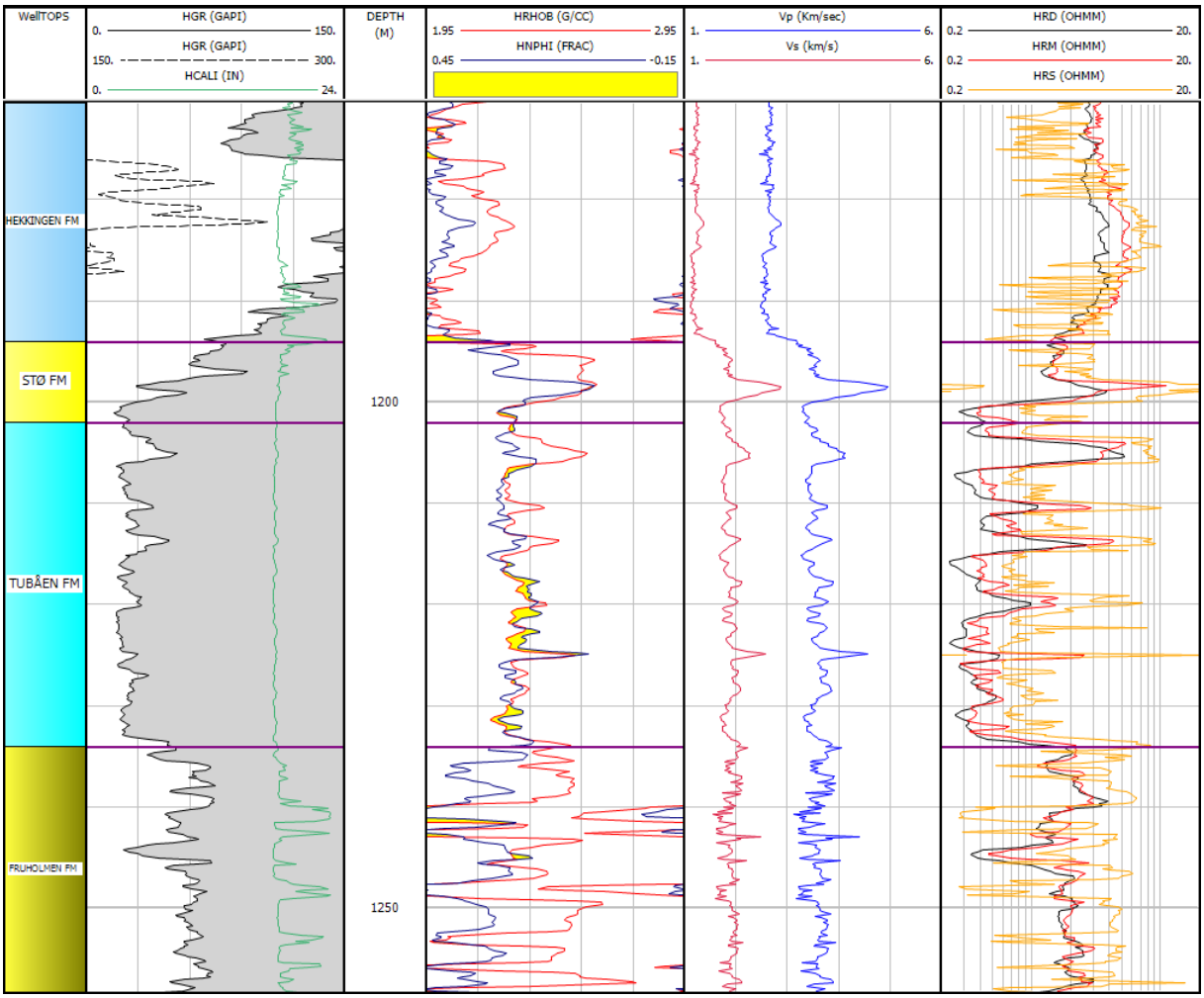

Figure A.19: Composite log display of the Tubåen and Stø Formations, well 7226/11-1.

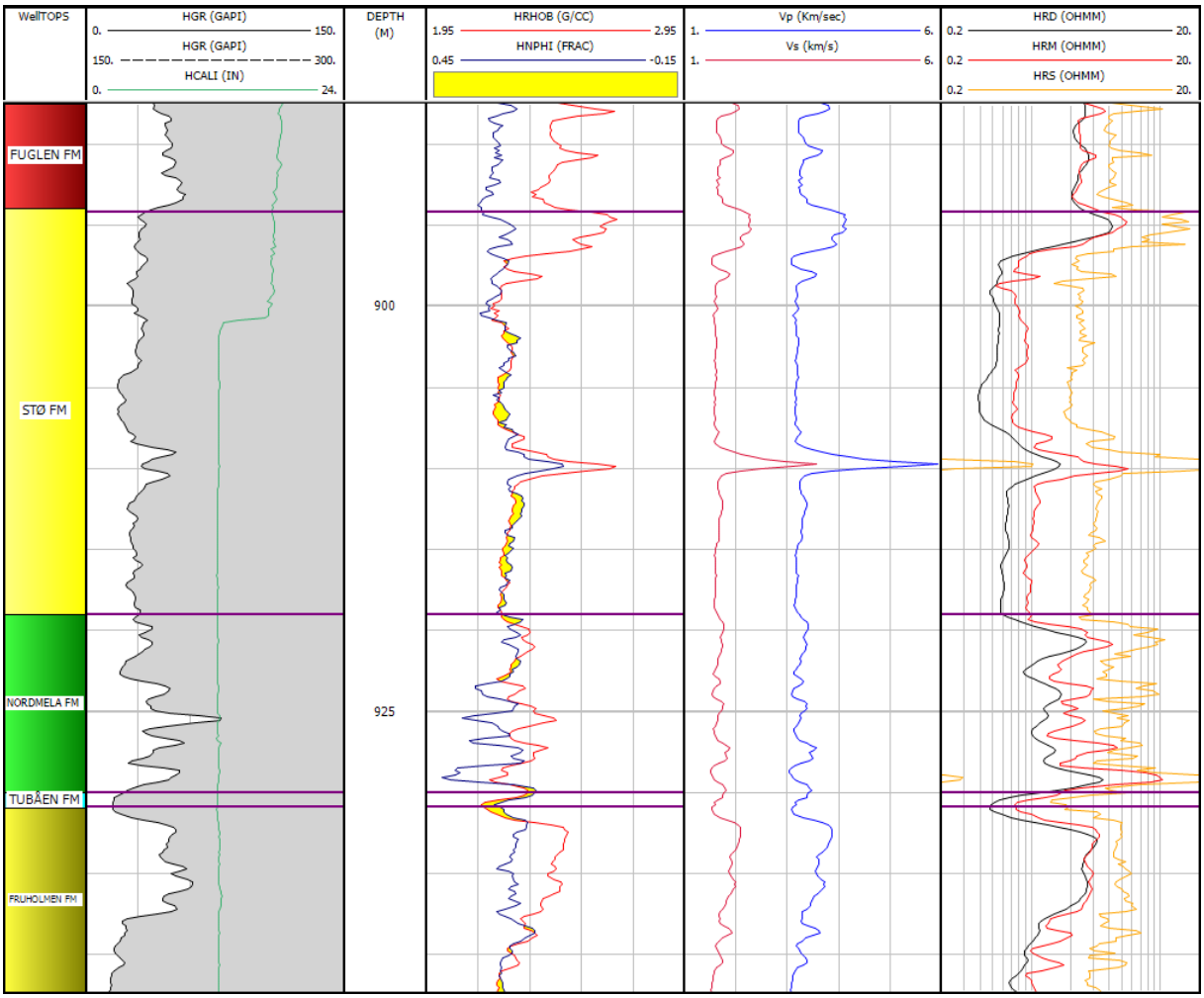

Figure A.20: Composite log display of the Tubåen and Stø Formations, well 7224/7-1.

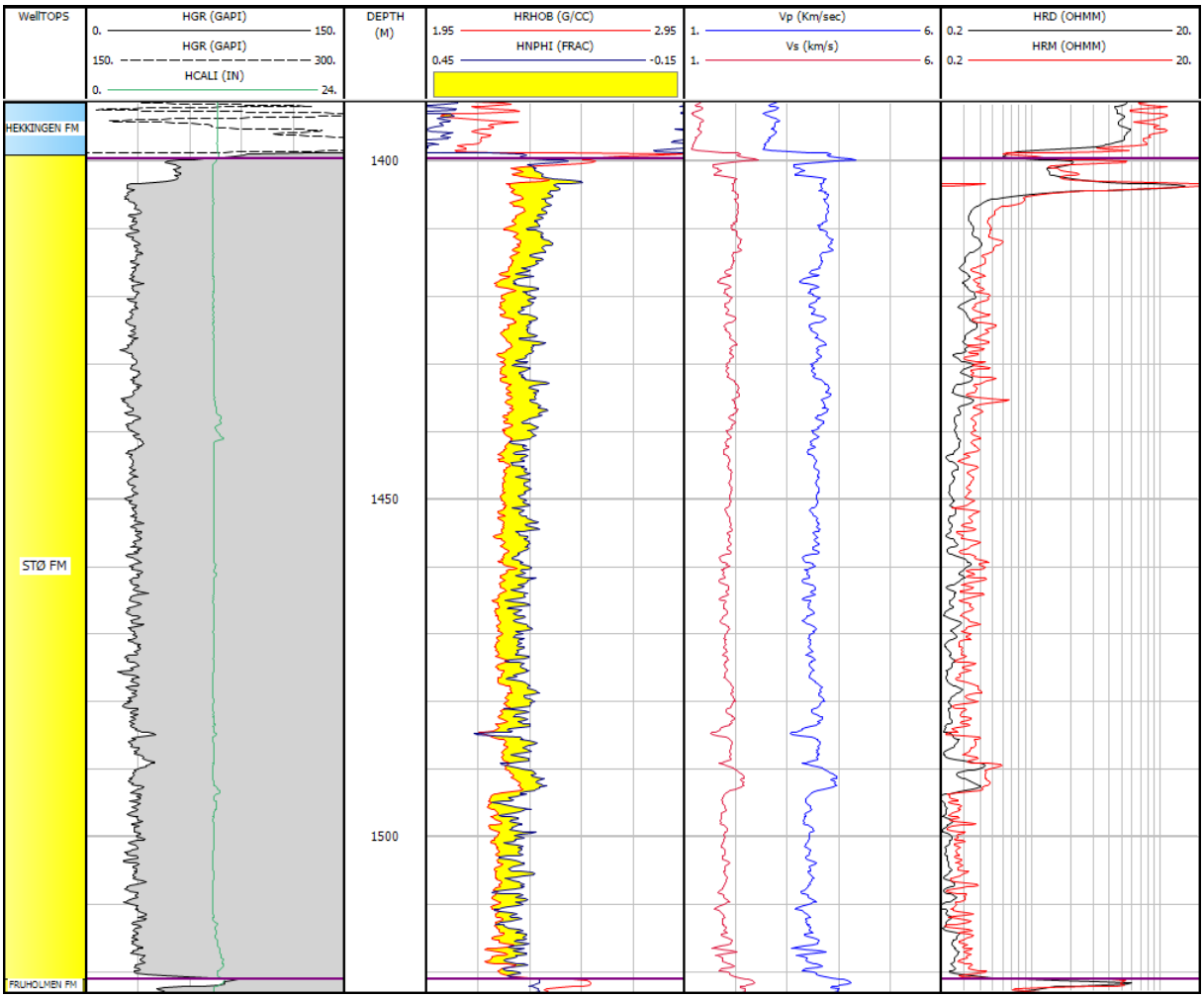

Figure A.21: Composite log display of the Stø Formation, well 7125/1-1.

Appendix B. Reservoir interval correlation panels

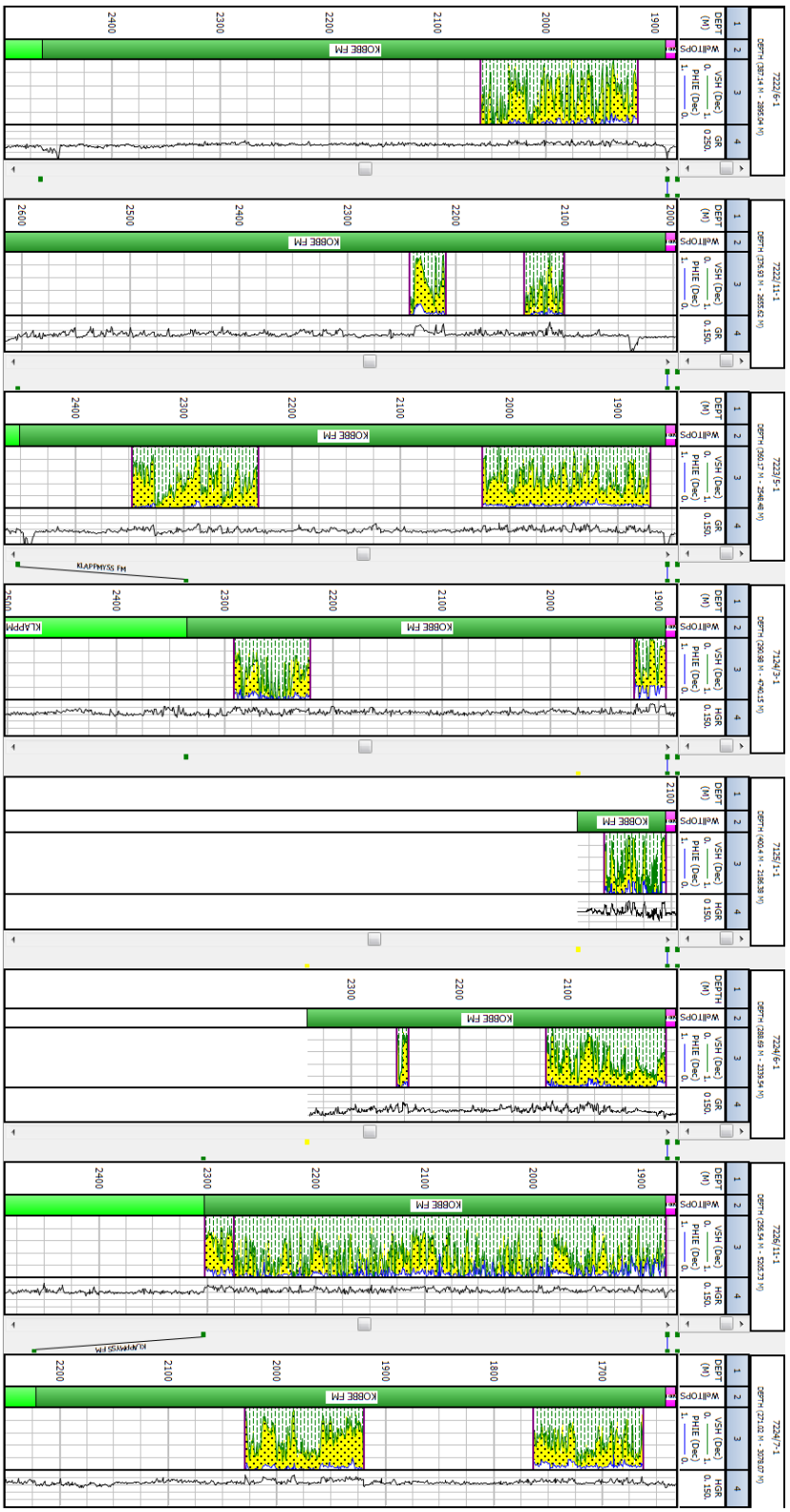

Figure B.1: Reservoir intervals in the Kobbe Formation, correlation panel flattened on Top Kobbe.

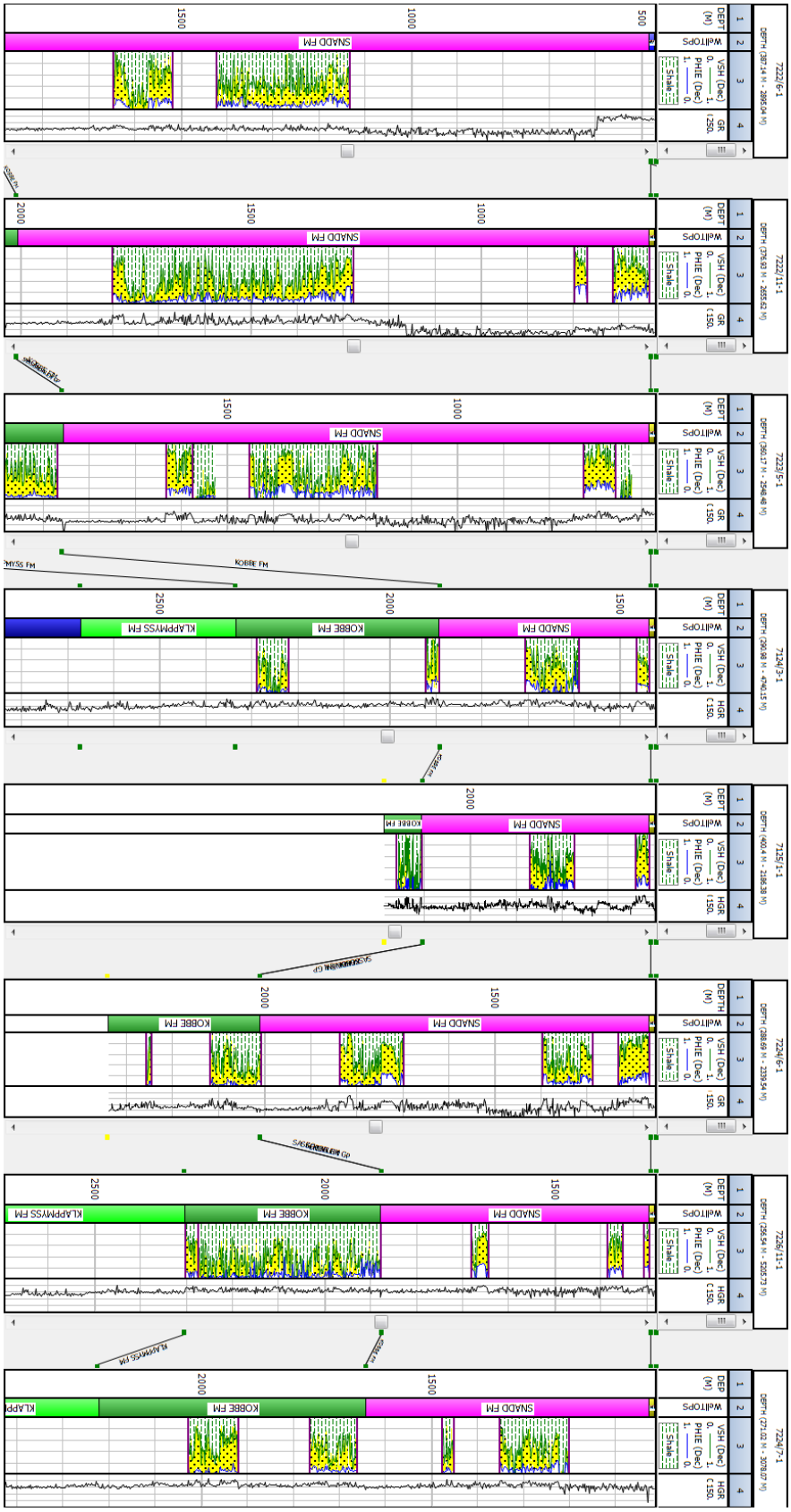

Figure B.2: Reservoir intervals in the Snadd Formation, correlation panel flattened on Top Snadd.

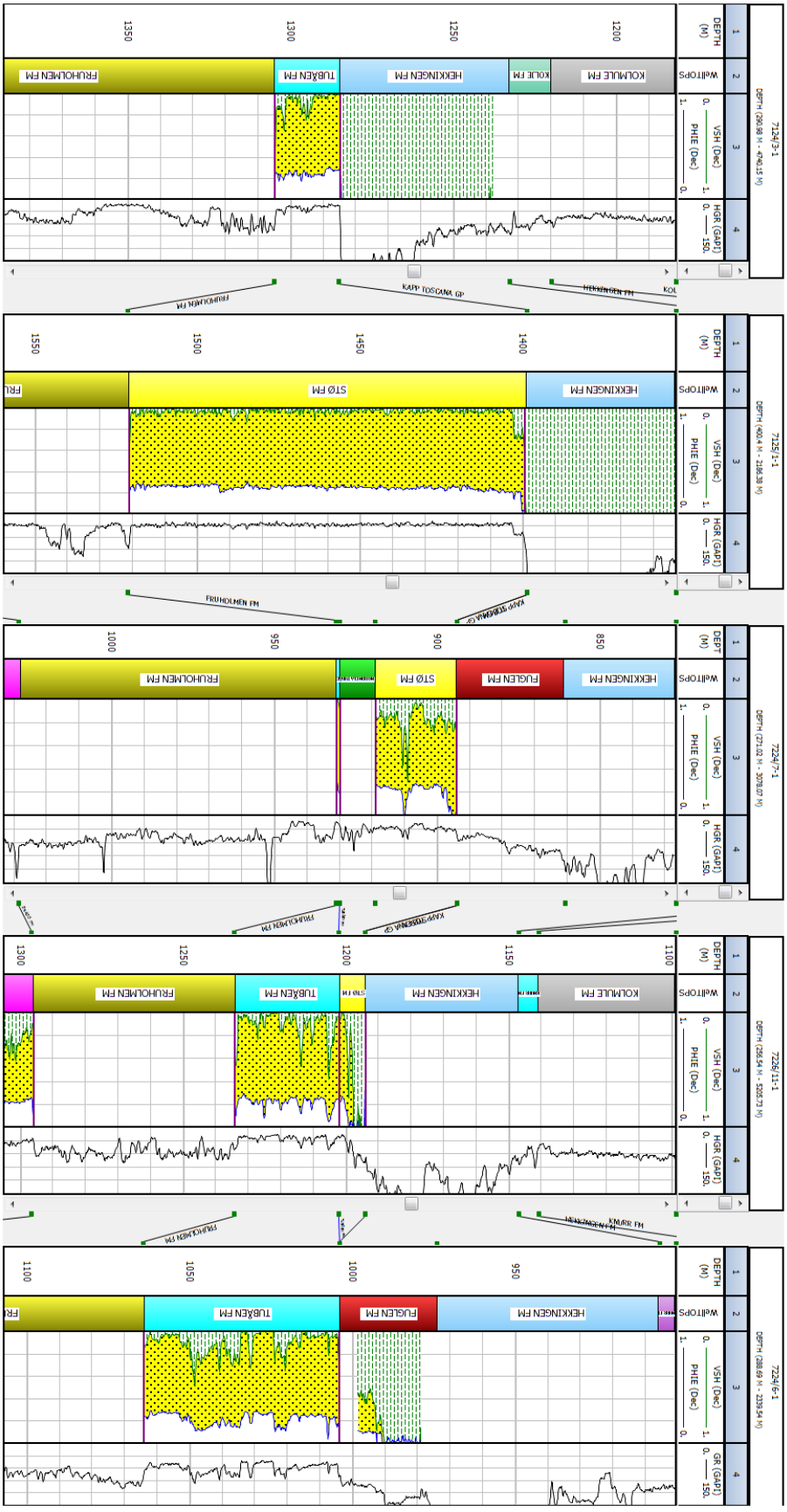

Figure B.3: Reservoir intervals in the Jurassic Tubåen and Stø Formations.

Appendix C. Compaction trends and transition lines

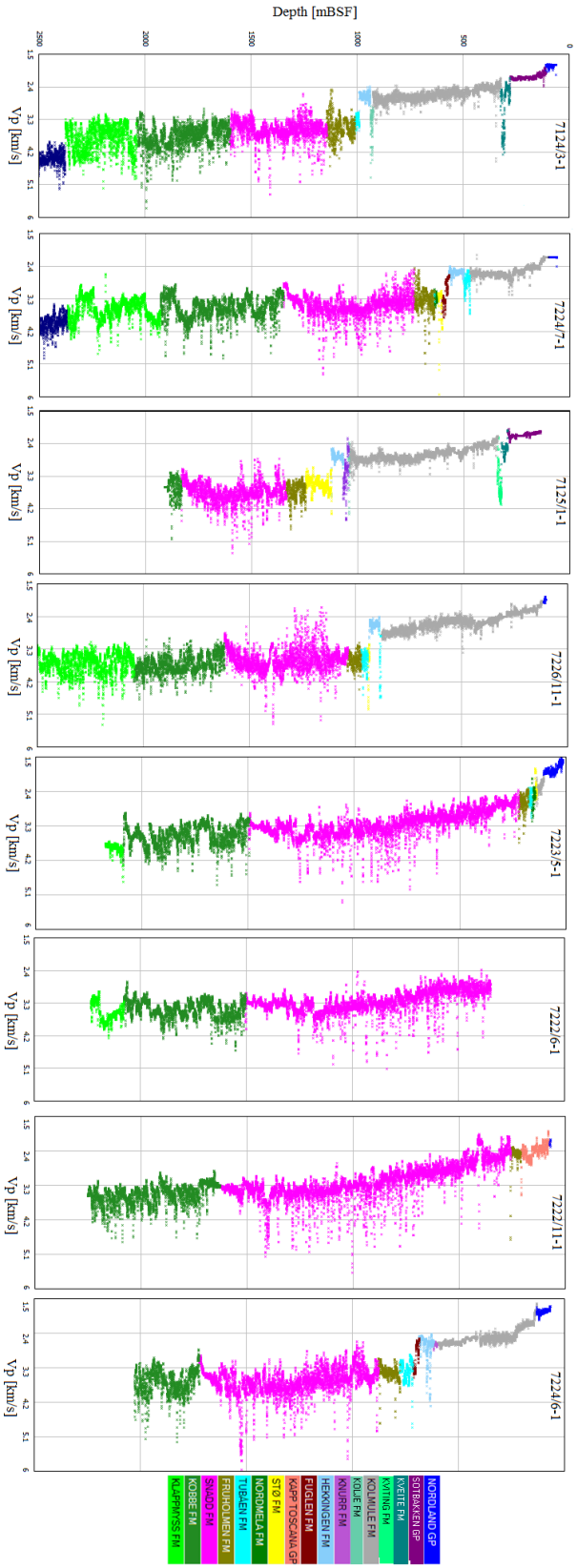

Figure C.1: V_p-depth plot of all data from studied wells. Color coded by formation.

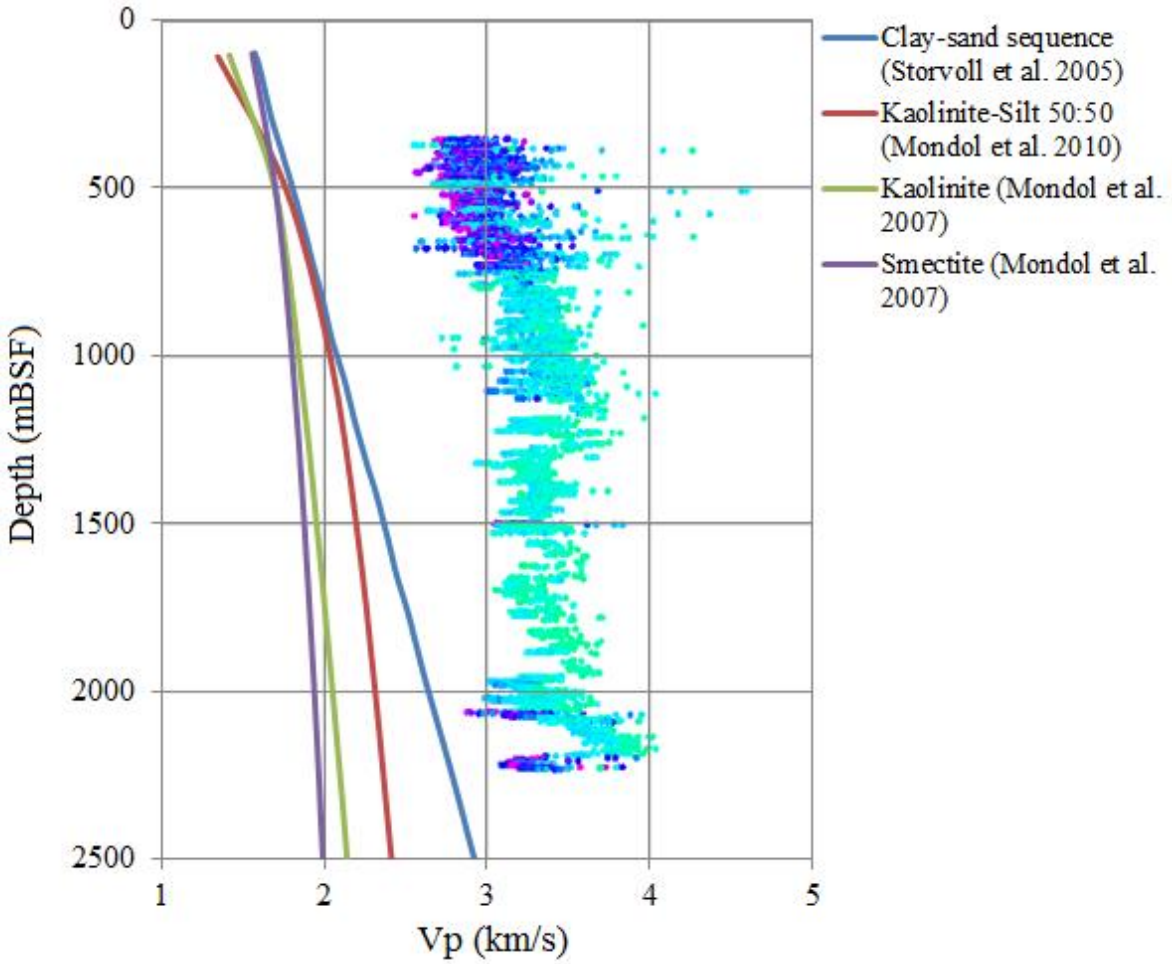

Figure C.2: V_p-depth plot showing shale data from well 7222/6-1, compared to published V_p-depth trends.

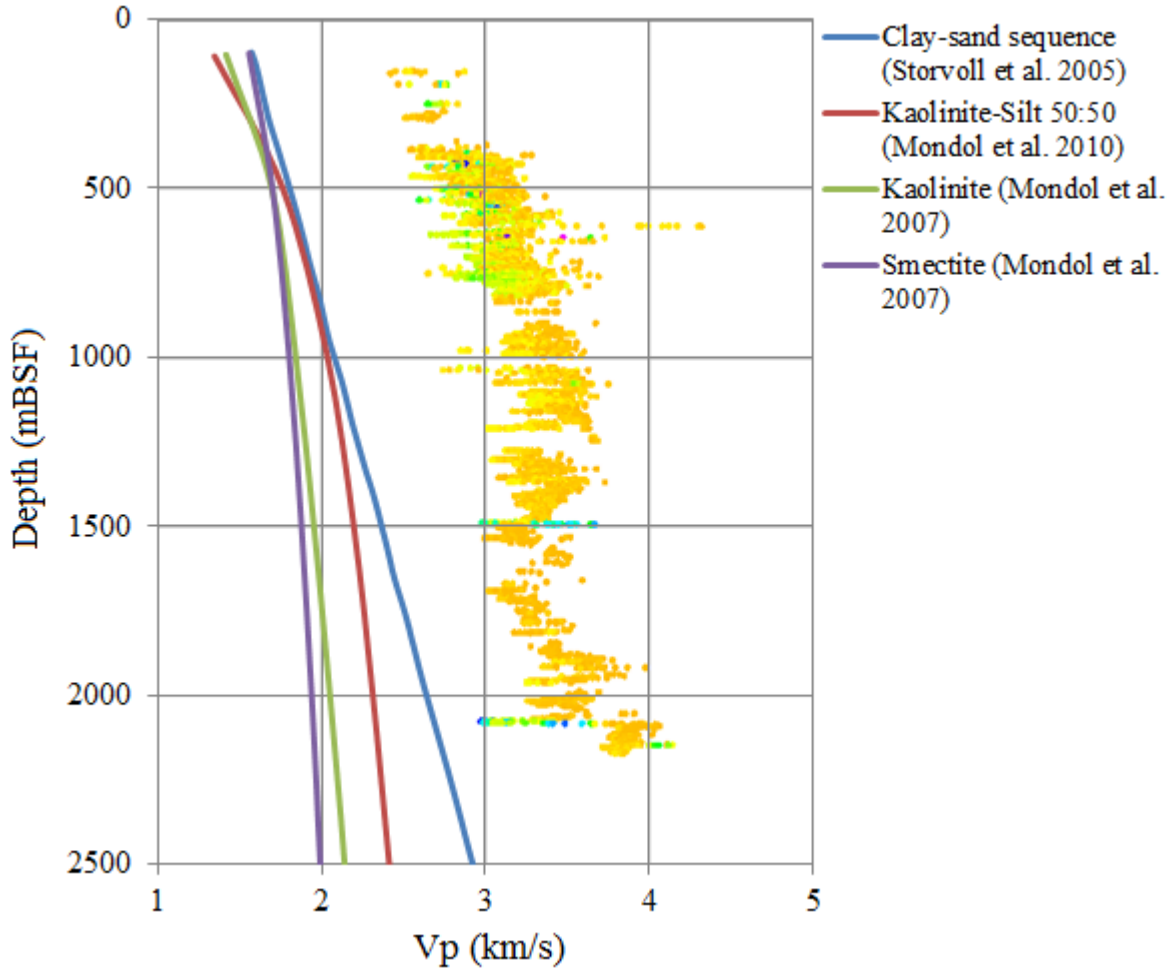

Figure C.3: V_p-depth plot showing shale data from well 7223/5-1, compared to published V_p-depth trends.

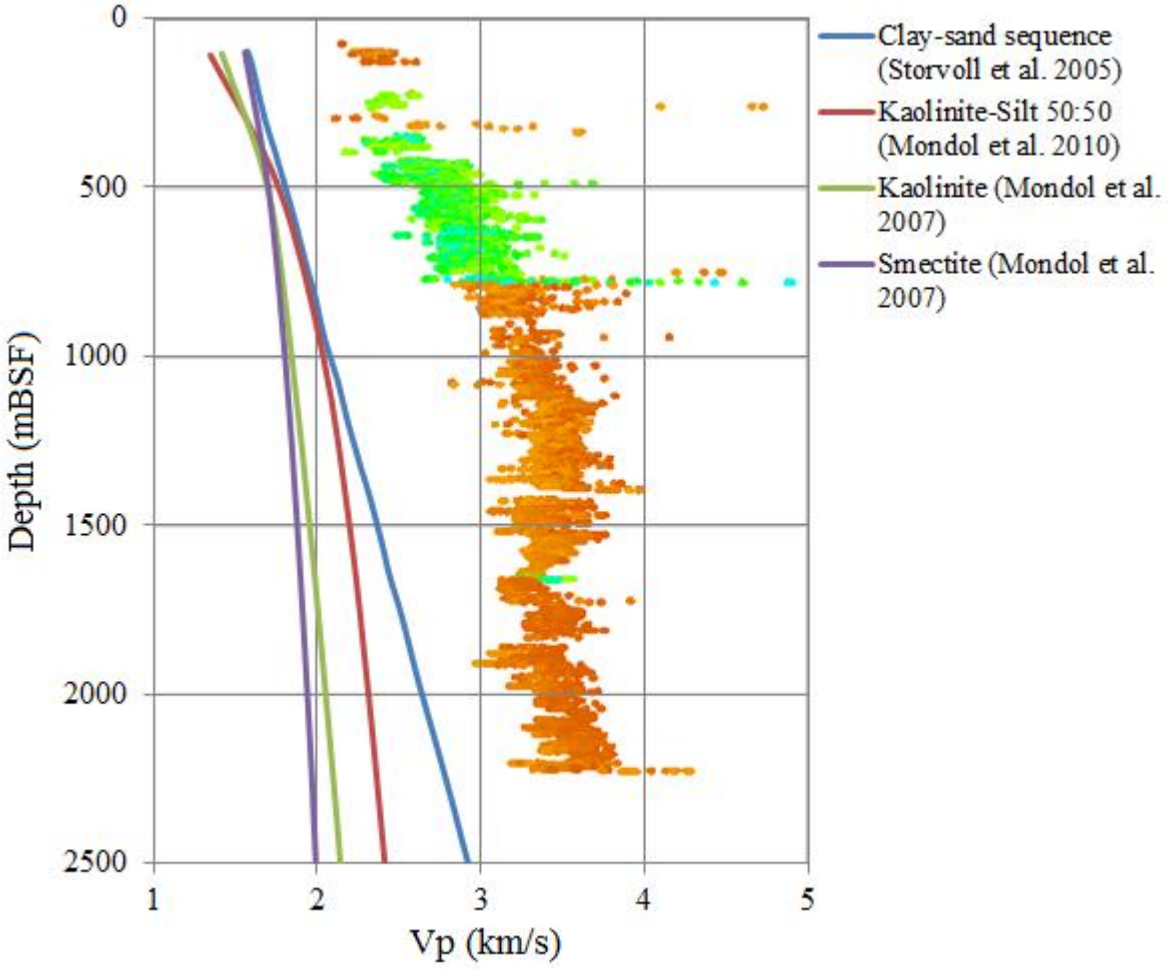

Figure C.4: V_p-depth plot showing shale data from well 7222/11-1, compared to published V_p-depth trends.

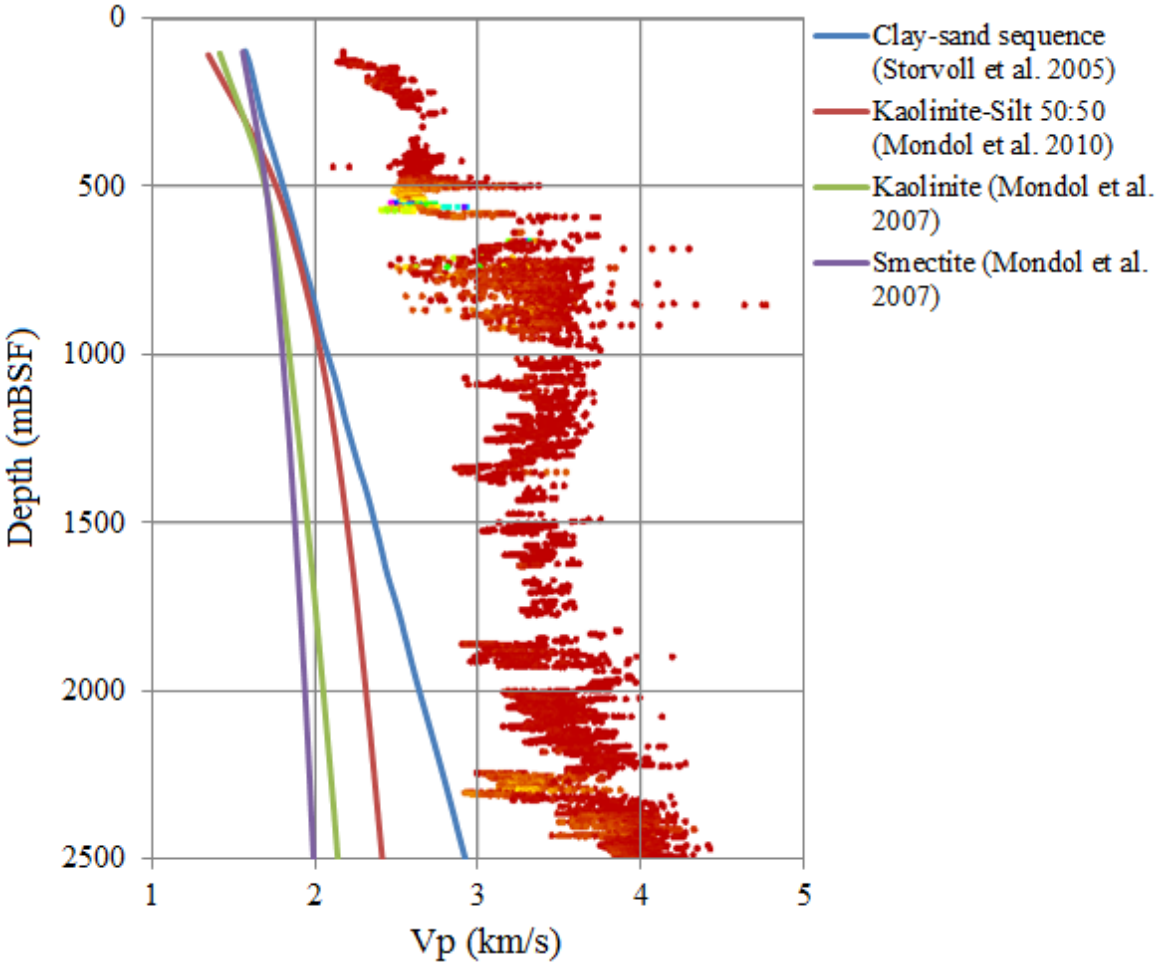

Figure C.5: V_p-depth plot showing shale data from well 7224/7-1, compared to published V_p-depth trends.

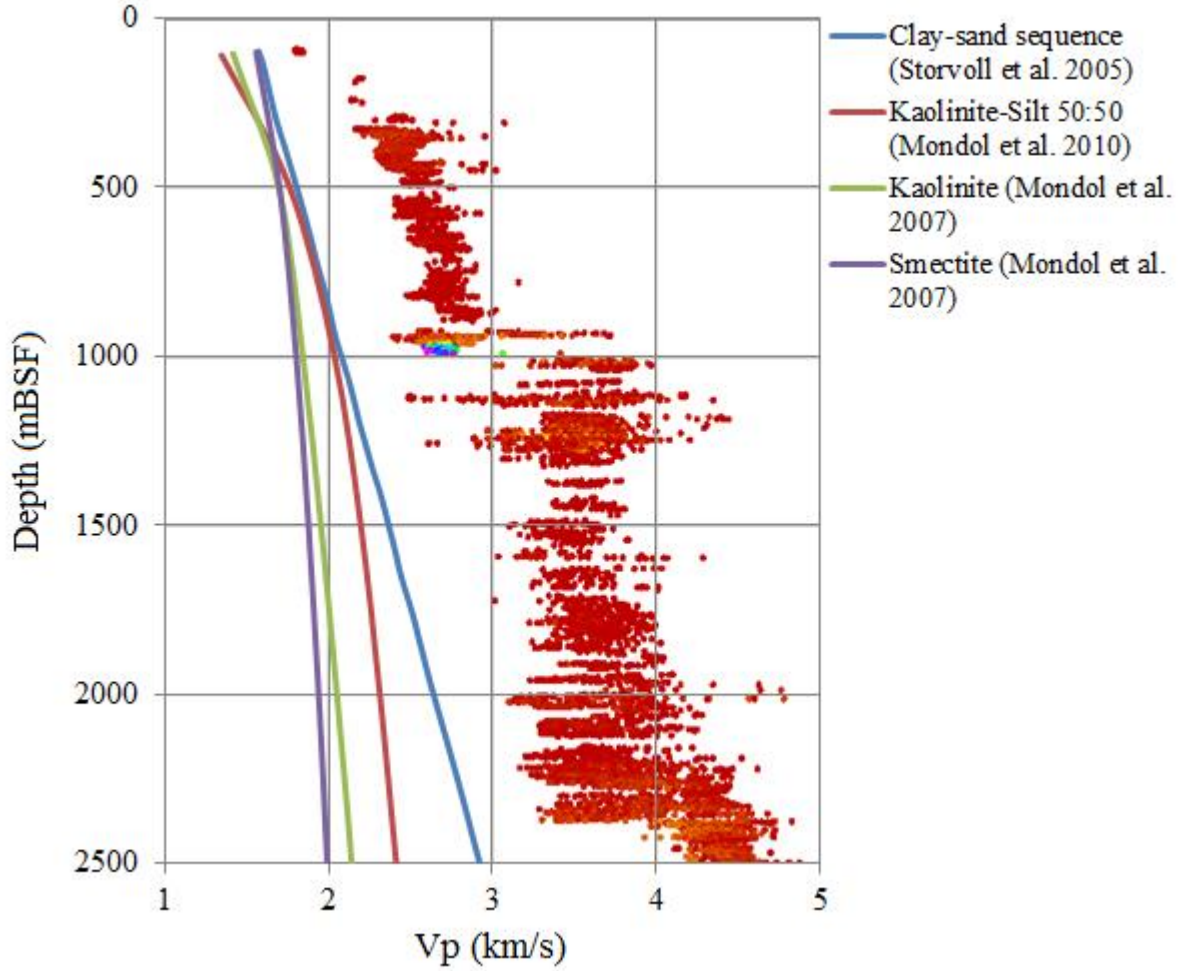

Figure C.6: V_p-depth plot showing shale data from well 7124/3-1, compared to published V_p-depth trends.

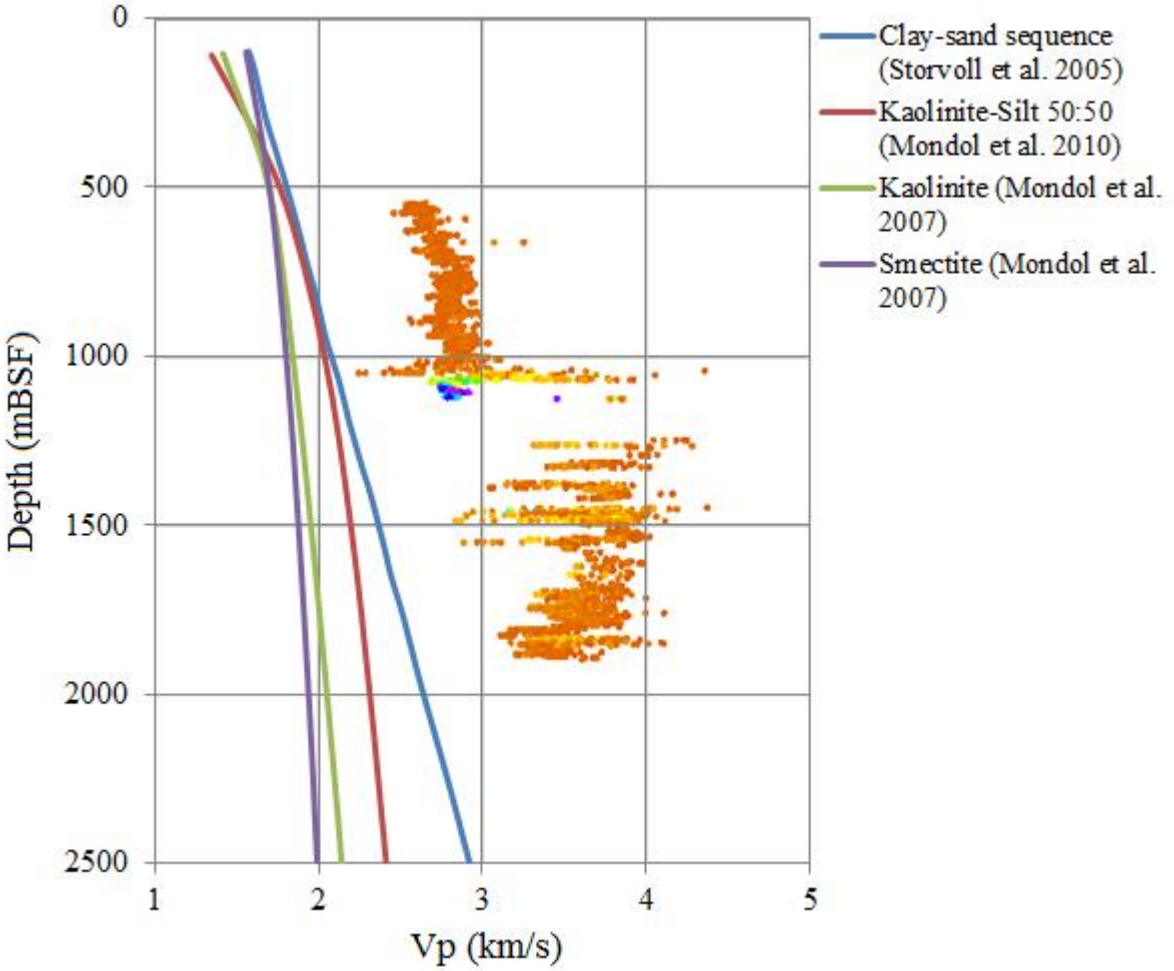

Figure C.7: V_p-depth plot showing shale data from well 7125/1-1, compared to published V_p-depth trends.

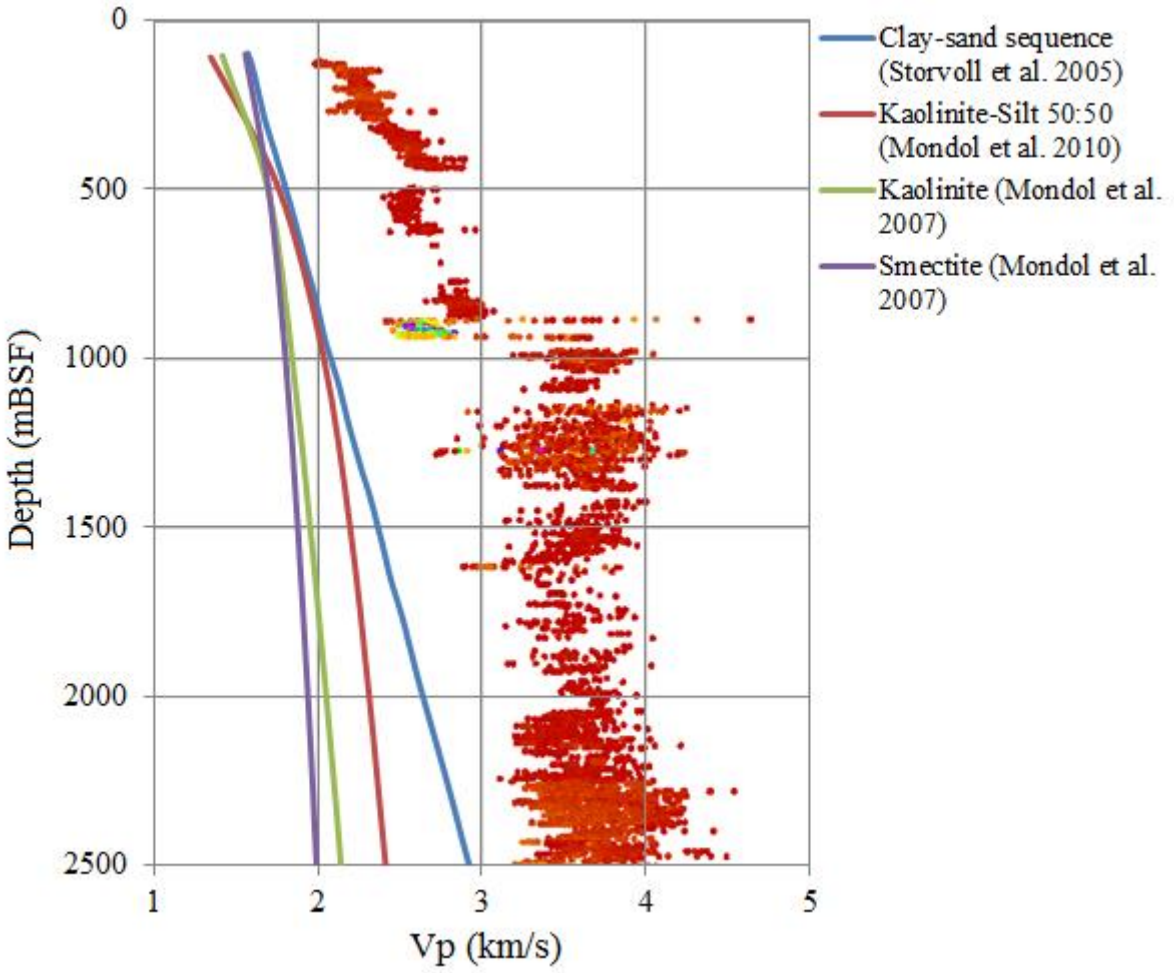

Figure C.8: V_p-depth plot showing shale data from well 7226/11-1, compared to published V_p-depth trends.

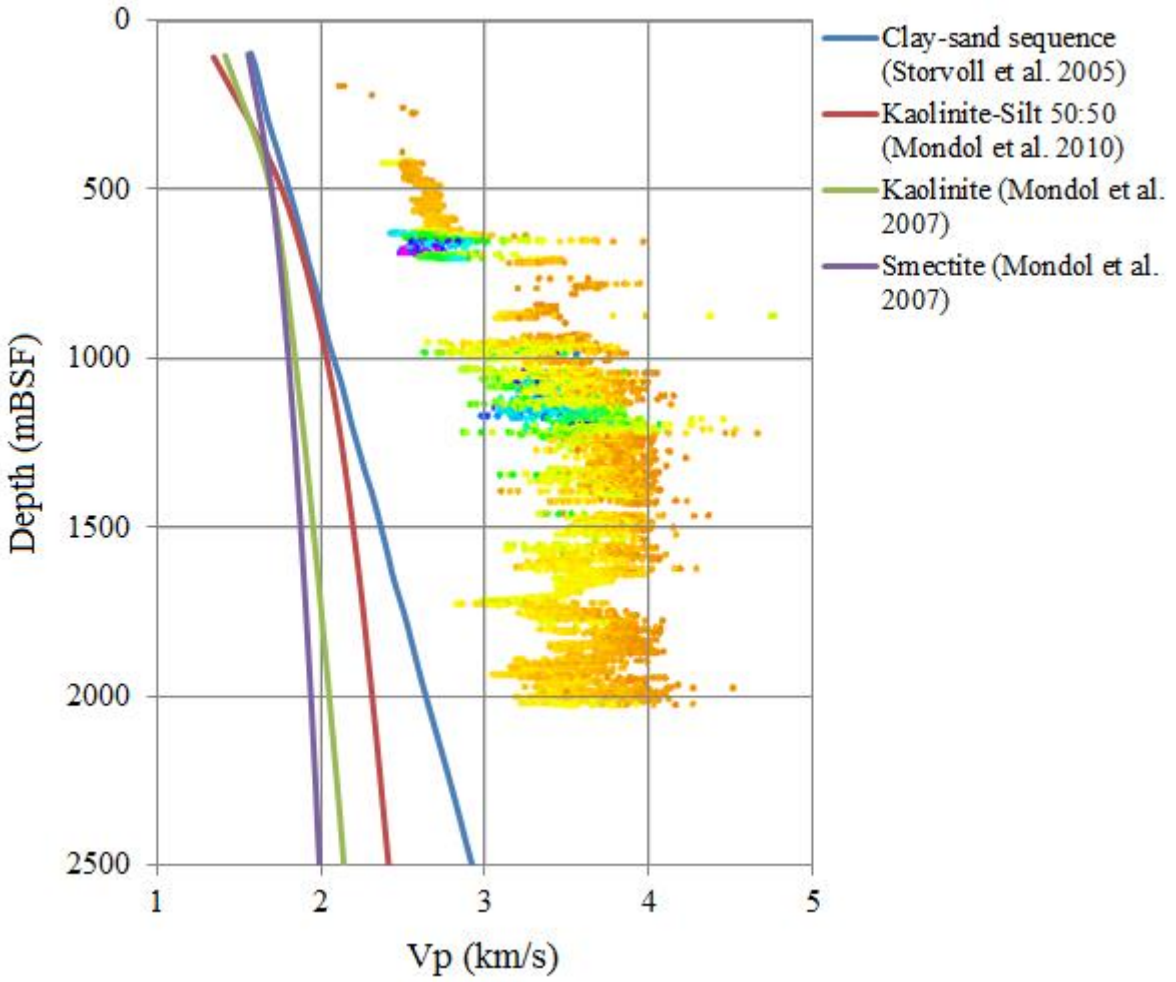

Figure C.9: V_p-depth plot showing shale data from well 7224/6-1, compared to published V_p-depth trends.

Appendix D. Additional Rock Physics Diagnostic plots

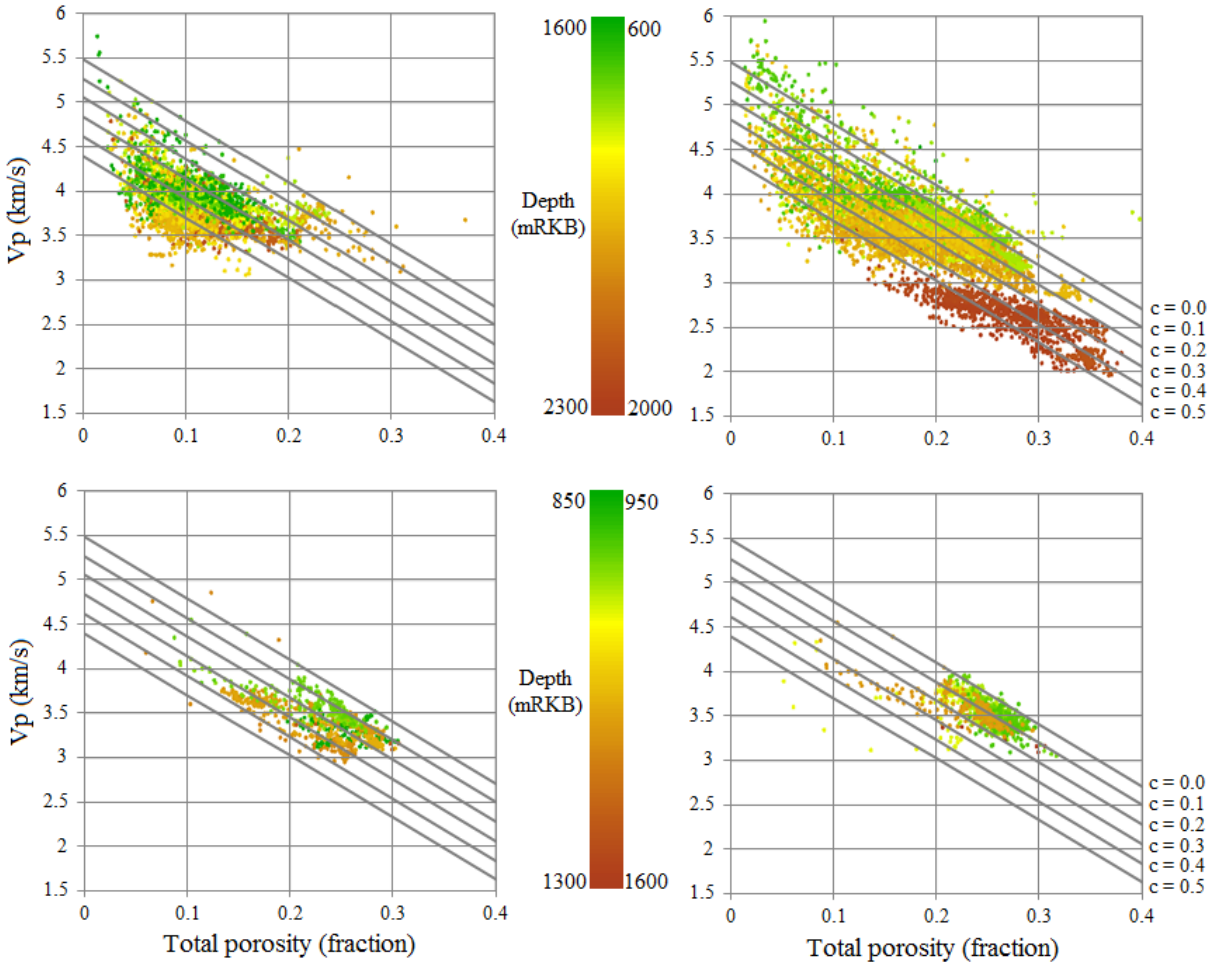

Figure D.1: Comparison of all reservoirs separated into formations, relative to Han's (1986) empirical equations valid for 20 MPa effective pressure. Color coded by measured depth from KB, note different color scale for all four plots.

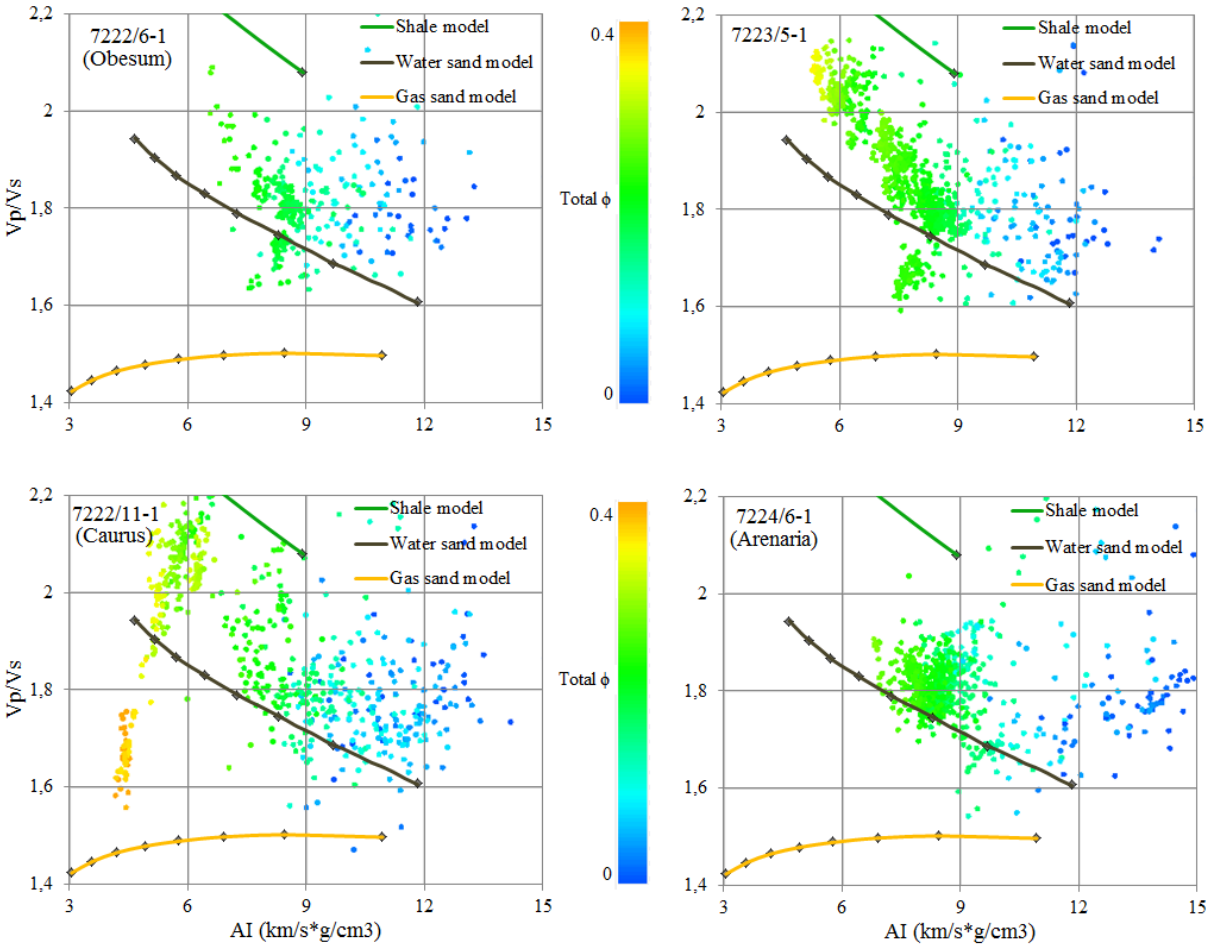

Figure D.2: V_p/V_s-AI crossplots showing all Snadd Formation reservoir data from wells that have V_s.